

**Structural Performance of Fiber-Placed,  
Variable-Stiffness Composite Conical  
and Cylindrical Shells**

A.W. Blom



# **Structural Performance of Fiber-Placed, Variable-Stiffness Composite Conical and Cylindrical Shells**

## **Proefschrift**

ter verkrijging van de graad van doctor  
aan de Technische Universiteit Delft,  
op gezag van de Rector Magnificus prof.ir. K.C.A.M. Luyben,  
voorzitter van het College voor Promoties,  
in het openbaar te verdedigen op maandag 1 november 2010 om 15:00 uur  
door Adriana Willempje BLOM,  
ingenieur Luchtvaart en Ruimtevaart,  
geboren te Leiderdorp

Dit proefschrift is goedgekeurd door de promotor:  
Prof.dr. Z. Gürdal

Samenstelling promotiecommissie:

Rector Magnificus	voorzitter
Prof.dr.ir. Z. Gürdal	Technische Universiteit Delft, promotor
Prof.dr. V. Giurgiutiu	University of South Carolina
Prof.dr.-Ing. R. Degenhardt	Göttingen Private University/DLR
Prof.dr.ir. M.J.L. Van Tooren	Technische Universiteit Delft
Prof.dr.ir. R. Akkerman	Universiteit Twente
Dr. P.B. Stickler	University of Washington/Boeing
Dr. T.K. Henriksen	ESA/ESTEC
Prof.dr.ir. R. Benedictus	Technische Universiteit Delft, reservelid

The research described in this thesis was supported by Delft University of Technology, NLR (National Aerospace Laboratory in the Netherlands), Fokker Aerostructures, and The Boeing Company.

ISBN 978-90-9025563-7

Keywords: Composites, Advanced Fiber Placement, Variable Stiffness, Cylinder, Cone, Optimization, Modal Test, Bending Test

Printed by Wöhrmann Print Service, Zutphen, The Netherlands

Copyright © 2010 by A.W. Blom

All rights reserved. No part of the material protected by this copyright notice may be reproduced or utilized in any form or by any means, electronic or mechanical, including photocopying, recording or by any information storage and retrieval system, without written permission of the author.



# Summary

The use of fiber-reinforced composites in aerospace structures has increased dramatically over the past decades. The high specific strength and stiffness, the tailorability, and the possibilities to integrate parts and reduce the number of fasteners give composites an advantage over metals. Automation of the production process enables large-scale production of composites in a repeatable, reliable fashion. Fiber-reinforced composite laminates are traditionally made of  $0^\circ$ ,  $90^\circ$  and  $\pm 45^\circ$  plies. Automated manufacturing techniques, such as advanced fiber placement, allow for fiber orientations other than  $0^\circ$ ,  $90^\circ$  and  $\pm 45^\circ$ , and for the placement of curved fibers such that the fiber orientation within a ply is continuously varied. Laminates that contain plies with spatially varying fiber orientations have a spatially varying stiffness and are called *variable-stiffness composites*. Tailoring the stiffness variation can be used to improve the structural efficiency of a composite.

Analytical and experimental work on flat variable-stiffness composite panels with and without central holes has shown that large improvements in structural efficiency are feasible, such as increasing the panel strength or buckling load while maintaining the same overall weight. The research presented in this dissertation expands the work on variable-stiffness composite laminates from flat panels to conical and cylindrical shells. Variable-stiffness plies with either an axial or a circumferential stiffness variation are defined based on the shifted course principle, where a full ply is formed by shifting identical courses in the direction perpendicular to the direction in which the fiber angle is varied. Four different types of fiber paths are discussed: i) geodesic paths, ii) constant angle paths, iii) paths with a linearly varying fiber angle, and iv) paths with a constant curvature. General mathematical descriptions to define the coordinates of these paths on a conical or cylindrical shell and expressions for the in-plane curvature are derived. The in-plane curvature is limited to a maximum value to ensure a good laminate quality, assuming the variable-stiffness laminate is manufactured using advanced fiber placement. A procedure to determine the exact stacking sequence for a given location within a laminate is given.

Structural analyses were carried out using the finite element program ABAQUS. The stiffness variation was implemented in the finite element shell model as a user-written FORTRAN subroutine, such that each element was uniquely defined. Two design studies were carried out, using the ABAQUS models to evaluate the structural performance of variable-stiffness composite laminates.

The first design study was the optimization of conical and cylindrical shells with different dimensions for maximum fundamental frequency. The 8-ply laminates had a  $[\pm 45 \pm \varphi(x)]_s$  layup, where  $\varphi(x)$  denotes a ply with an axially varying fiber angle, and the laminate thickness was assumed to be constant. Manufacturability of the variable-stiffness plies was

judged based on the maximum in-plane path steering allowed by the fiber placement process. Numerical examples showed that manufacturability can have a large influence on the value of the maximum fundamental frequency of conical and cylindrical composite shells with an axial stiffness variation, and that it is necessary to take the manufacturing constraints into account in the design phase of a variable-stiffness laminate. It was shown that the fundamental frequency of conical and cylindrical shells can be improved up to 30 percent by using variable-stiffness laminates, especially for larger cones.

The second design study covered the maximization of the buckling load of a variable-stiffness composite cylinder loaded in bending. It was shown that the use of variable-stiffness constant-thickness laminates may improve the buckling load of a cylinder under pure bending because it allows the redistribution of in-plane loads between the compression and tension parts around the circumference by tailoring the circumferential in-plane stiffness distribution in the cylinder skin. The compressive loads were reduced and spread out over a larger part of the cylinder circumference thus increasing the buckling load and changing the buckling mode shape. Loading was also shifted from buckling-critical compression loads into buckling-noncritical tension loads. The redistributed loads caused the first buckling mode to change such that a larger part of the cylinder participated in the buckling deformations.

Introduction of curvature, strength and stiffness constraints caused a small reduction in buckling load carrying capability of the variable-stiffness designs. These manufacturable and more practical laminates showed improvements of up to 18 percent compared to the optimized baseline consisting of  $0^\circ$ ,  $90^\circ$  and  $\pm 45^\circ$  plies.

The buckling load carrying capability of variable-stiffness designs that included overlapping fiber courses was optimized by increasing the laminate thickness on the compression side of the cylinder. The larger laminate thickness, which is coupled to the fiber angle variation, was achieved by having a small fiber orientation on the compression side of the cylinder and a large fiber orientation near the neutral axis. The increased laminate thickness and the small fiber orientation caused high axial stiffness, resulting in high axial loads on the compression side of the cylinder. The laminate bending stiffness on the compression side increased more than the in-plane laminate stiffness, however, such that it compensated for the higher axial loads and dominated the response.

Including the curvature and strength constraints had a higher impact on the variable-stiffness designs with overlap than on the ones with a constant thickness. The amount of thickness buildup on the compression side was limited, because the shift of the neutral axis associated with the high axial laminate stiffness on the compression side caused failure on the tension side of the cylinder. The laminate stiffness and thickness on the tension side became similar to those on the compression side.

One constant-thickness, variable-stiffness specimen and two baseline specimens were manufactured using advanced fiber placement technology. Both designs were optimized for maximum buckling load carrying capability under bending. The small dimensions of the cylinder required a small turning radius, causing puckers to form during lay-down which were not visible in the end product. The amount of small triangular gaps and overlaps within the constant-thickness laminate was minimized by using a 50 percent coverage parameter, while long gaps between parallel courses were avoided by adjusting the shift between courses. The minimum cut length requirement was taken into account during the design, preventing any deficiencies in placing tows on the surface. Cutting tows on the outside of a

steered course caused the tows to straighten, because the outer tows were not restrained and thus followed a geodesic path. Adjustments are needed in future variable-stiffness designs to avoid fiber straightening.

A modal test was carried out on the variable-stiffness and on one of the baseline fiber-reinforced composite cylinders that were optimized for bending. An ABAQUS finite element model was used to predict the modal behavior of the cylinders. The analytically predicted mode shapes and modal frequencies showed a good agreement with the experimental results, both for the baseline and for the variable-stiffness cylinder. The modal frequencies of the variable-stiffness cylinder were lower than those of the baseline cylinder due to the lower laminate bending stiffness in the circumferential direction, which plays an important role in the formation of waves in the circumferential direction. The larger axial stiffness of the variable-stiffness cylinder became apparent for modes with an increasing number of axial half waves and the modal frequency of the variable-stiffness cylinder approached or even exceeded the modal frequency of the baseline cylinder. The modal response simulations executed in ABAQUS matched the experimental results both for location and amplitude of the response. Although only 2 cylinders were tested, the presented results indicated that the finite element model for the variable-stiffness cylinder provides a good representation of the cylinder in terms of mass and stiffness distributions.

A fixture was designed to test the baseline and the variable-stiffness cylinders in pure bending. Strains and displacements were measured using strain gauges, digital image correlation, LVDT's and lasers. Three carbon fiber-reinforced cylinders were tested: two with a baseline laminate and one with circumferentially varying laminate stiffness. The variable-stiffness cylinder was tested in two configurations: i) it was tested in the orientation for which it was optimized, called the preferred configuration, and ii) it was tested while rotated  $180^\circ$  about the longitudinal axis, such that the loading on the cylinder was reversed, this was called the reversed configuration. This resulted in three test configurations: the baseline, the variable-stiffness in the preferred orientation and the variable-stiffness in the reversed orientation.

A comparison of the experimental response of the two baseline cylinders with the finite element predictions revealed that the experimental boundary conditions were more flexible than originally modeled in the finite element model. The introduction of flexible boundary conditions in the finite element model resulted in good agreement between the experimental and the analytical results. A final improvement of the finite element predictions was achieved by including geometric imperfections in the model and by performing a Riks analysis. The latter model was used to make a prediction for the variable-stiffness test results.

A comparison of the experimental results with the finite element predictions of the Riks analysis in general showed a good agreement for all three configurations. The match of the end rotations and strains was equally good for the variable-stiffness cylinder and the baseline cylinder. The variable-stiffness cylinder was stiffer than the baseline cylinder when comparing the global behavior in terms of end rotations, which was to be expected because of the larger laminate stiffness of the variable-stiffness cylinder. The variable-stiffness cylinder response was stiffer in the reversed orientation than in the preferred orientation due to the boundary condition effects.

The most important observation resulted from the strain distribution with the vertical coordinate of the cylinder: at equal load level the maximum compressive strains of the variable-stiffness cylinder in the preferred orientation were about 10 percent lower than

those of the baseline cylinder; the tensile strains were 35 percent smaller. This difference in extreme strain values is a large improvement in performance when strain-based strength criteria are applied. In addition, the circumferential stiffness variation resulted in a redistribution of the loads, such that the tension side was more effective in carrying loads, the compressive loads were carried by a larger part of the cylinder and the compressive load peak at  $\theta = 180^\circ$  was reduced by 25 percent compared to the baseline cylinder. The adjusted finite element model predicted an increase in buckling load of 18 percent compared to the baseline cylinder as a result of this load redistribution.

# Samenvatting

Het gebruik van vezelversterkte composieten in luchtvaartconstructies is in de afgelopen decennia drastisch toegenomen. De grote specifieke sterkte en stijfheid, de vrijheid om effectieve materiaaleigenschappen aan te passen en de mogelijkheid om onderdelen te integreren en het aantal verbindingen te reduceren werken in het voordeel van vezelversterkte composieten ten opzichte van metalen. Automatisering van het productieproces maakt het mogelijk om op grote schaal composieten te produceren op een herhaalbare, betrouwbare manier. Vezelversterkte laminaten bestaan traditiegetrouw uit lagen met een vezelhoek van  $0^\circ$ ,  $90^\circ$  en  $\pm 45^\circ$ . Geautomatiseerde productiemethoden zoals advanced fiber placement maken het mogelijk om lagen met andere hoeken dan  $0^\circ$ ,  $90^\circ$  en  $\pm 45^\circ$  neer te leggen. Het is zelfs mogelijk om gekromde vezels neer te leggen, waarbij de vezeloriëntatie continu varieert. Laminaten die lagen bevatten met variabele vezelhoeken hebben een variabele laminaatstijfheid en worden *variabele-stijfheidslaminaten* genoemd. Het is mogelijk de mechanische efficiëntie van een composieten constructie te verbeteren door de stijfheid aan te passen.

Analytisch en experimenteel werk op het gebied van vlakke, variabele-stijfheidslaminaten met en zonder gaten heeft aangetoond dat er grote verbeteringen in structurele efficiëntie mogelijk zijn, zoals het verbeteren van de sterkte of de kniklast van een paneel bij hetzelfde gewicht. Het onderzoek dat in deze dissertatie gepresenteerd wordt breidt het werk aan variabele-stijfheidscomposieten uit van vlakke platen naar conische en cilindrische schalen. Variabele-stijfheidslagen met een vezelhoekvariatie in lengterichting of in omtreksrichting zijn gedefinieerd op basis van het *verschoven band* principe, waarbij een volledige laag wordt gecreëerd door identieke paden te verschuiven in de richting loodrecht op de richting waarin de vezelhoek wordt gevarieerd. Vier verschillende soorten vezelpaden worden besproken: i) geodetische paden, ii) constante hoekpaden, iii) paden met een lineaire variatie van de vezelhoek en iv) paden met een constante kromming. Algemene mathematische uitdrukkingen zijn afgeleid om de coördinaten van deze paden op een conische of cilindrische schaal te definiëren en om de kromming van het pad in het vlak te bepalen. De kromming in het vlak is gebonden aan een maximum waarde om een goede laminaatkwaliteit te waarborgen, aangenomen dat het variabele-stijfheidslaminaat gemaakt wordt met fiber placement. De methode om de exacte laminaatopbouw voor een gegeven punt te bepalen is gepresenteerd.

Structurele berekeningen zijn met het eindige-elementenprogramma ABAQUS uitgevoerd. De stijfheidsvariatie is als FORTRAN subroutine in het eindige-elementenschaalmodel geïmplementeerd, zodat elk element unieke gedefinieerd is. Twee ontwerpstudies zijn uitgevoerd, waarbij de ABAQUS modellen gebruikt zijn om de structurele prestaties van de

variabele-stijfheidscomposieten te beoordelen.

De eerste ontwerpstudie was de optimalisatie van conische en cilindrische schalen met verschillende afmetingen voor maximale eigenfrequentie. Het 8 lagen tellende laminaat had een laminaatopbouw van  $[\pm 45 \pm \varphi(x)]_s$ , waarbij  $\varphi(x)$  een laag met een vezelhoekvariatie in axiale richting aanduidt, en had een constante dikte. Produceerbaarheid van de variabele-stijfheidslagen werd beoordeeld aan de hand van de maximaal toelaatbare kromming van het vezelpad in het vlak bij fiber placement. Numerieke voorbeelden tonen aan dat produceerbaarheid grote invloed kan hebben op de waarde van de maximale eigenfrequentie van conische en cilindrische composiete schallen met een axiale stijfheidsvariatie en dat het noodzakelijk is de produceerbaarheidseisen in een vroeg stadium in het ontwerp mee te nemen. De laagste eigenfrequentie van conische en cilindrische schalen kan met 30 procent toenemen door het gebruik van variabele-stijfheidslaminaten, dit geldt vooral voor grotere kegels.

De tweede ontwerpstudie richtte zich op de maximalisatie van de kniklast van een variabele-stijfheidscomposiete cilinder belast op buiging. Het is aangetoond dat het gebruik van variabele-stijfheids laminaten met een constante dikte de kniklast van een cilinder kan verhogen doordat de interne belastingen van de druk- naar de trekkant van de cilinder kunnen worden geleid door het aanpassen van de laminaatstijfheid in de omtreksrichting van de cilinder. De drukbelasting nam af en werd over een groter deel van de omtrek verdeeld, waardoor de kniklast toenam en de knikvorm veranderde. Belasting werd ook van de knikkritische drukkant naar de niet-kritische trekkant geleid. De herverdeling van de belasting veroorzaakte een verandering in knikvorm zodat een groter deel van de cilinder vervormde.

Het introduceren van restricties voor de kromming van het vezelpad, de sterkte en stijfheid van het laminaat veroorzaakte een kleine afname in de capaciteit van de variabele-stijfheidsontwerpen om kniklasten in buiging te dragen. Deze ontwerpen, die produceerbaar en praktisch zijn, waren tot 18 procent beter dan de geoptimaliseerde referentiecilinder bestaande uit  $0^\circ$ ,  $90^\circ$  en  $\pm 45^\circ$  lagen.

De capaciteit van variabele-stijfheidsontwerpen met overlappingsen voor het dragen van knikbelasting in buiging was optimaal door de toename van de laminaatdikte aan de drukzijde van de cilinder. De grotere laminaatdikte, die gekoppeld is aan de vezelhoekverandering, kwam tot stand door een kleine vezelhoek aan de drukzijde en een grote hoek bij de neutrale as van de cilinder. De toename in laminaatdikte en de kleine vezelhoek resulteerden in een hoge axiale laminaatstijfheid, waardoor de axiale belasting aan de drukzijde toenam. De buigstijfheid van het laminaat nam echter meer toe dan de laminaatstijfheid in het vlak en domineerde de respons, waardoor de hogere axiale belasting werd gecompenseerd.

Het beperken van de vezelpadkromming en de introductie van de sterkte-eis had een grotere invloed op de variabele-stijfheidsontwerpen met overlap dan op die met een constante dikte. De hoeveelheid dikteopbouw aan de drukzijde werd beperkt, doordat de verschuiving van de neutrale as als gevolg van grote laminaatdikte aan de drukzijde materiaalbreuk aan de trekzijde veroorzaakt. De laminaatstijfheid en de dikte aan de trekzijde werden vergelijkbaar aan die van de drukzijde.

Eén optimaal variabele-stijfheidsontwerp met een constante dikte en twee referentiecilinders, beide geoptimaliseerd om een maximale kniklast in buiging te dragen, zijn gebouwd met fiber placement. De kleine afmetingen van de cilinder vereisten een grote kromming van de vezelpaden, waardoor er tijdens de productie hobbels werden gevormd, die

niet zichtbaar waren in het eindproduct. De hoeveelheid kleine driehoekige gaten en overlaps die nodig waren om een constante dikte te verkrijgen was geminimaliseerd door een dekkingsparameter van 50 procent te gebruiken, terwijl lange gaten tussen parallelle banen vermeden werden door de afstand tussen twee banen aan te passen. Tijdens het ontwerp is er rekening gehouden met de minimale kniplengte om afwijkingen tijdens het plaatsen van de vezelstrips te voorkomen. Het knippen van vezelstrips aan de buitenkant van een bocht resulteerde in rechte vezelstrips, omdat de buitenste vezelstrips niet begeleid werden en daardoor een geodetisch pad volgden. In de toekomst zijn er aanpassingen in het ontwerp nodig om dit te voorkomen.

Een trillingstest is uitgevoerd voor de variabele-stijfheids- en één van de referentiecilinders die geoptimaliseerd waren voor buiging. Een ABAQUS eindige-elementmodel is gebruikt om het trillingsgedrag van de cilinders te voorspellen. De analytische voorspelde eigenvormen en eigenfrequenties kwamen goed overeen met de experimentele resultaten, zowel voor de referentiecilinder als voor de variabele-stijfheidscilinder. De eigenfrequenties van de variabele-stijfheidscilinder waren lager dan die van de referentiecilinder vanwege de lagere buigstijfheid van het laminaat in de omtreksrichting, welke een belangrijke rol speelt voor de formatie van golven in de omtreksrichting. De grotere axiale stijfheid van de variabele-stijfheidscilinder werd zichtbaar bij eigenvormen met een toenemend aantal halve golven in axiale richting en de eigenfrequentie van de variabele-stijfheidscilinder benaderde of overtrof de eigenfrequentie van de referentiecilinder. De simulaties van de trillingsrespons in ABAQUS correspondeerden goed met de experimentele resultaten, zowel voor de locatie als voor de amplitude van de respons. Hoewel slechts 2 cilinders getest zijn tonen de gepresenteerde resultaten aan dat het eindige-elementenmodel voor de variabele-stijfheidscilinder de stijfheids- en massadistributie goed weergeven.

Er is testopstelling ontworpen om de referentiecilinder en de variabele-stijfheidscilinder op buiging te testen. Rekken en verplaatsingen werden door middel van rekstrookjes, digital image correlation, verplaatsingsopnemers en lasers gemeten. Drie koolstofvezelversterkte cilinders zijn getest: twee met het referentielaminaat en één met een laminaatstijfheid die in omtreksrichting varieerde. De variabele-stijfheidscilinder is in twee configuraties getest: i) in de richting waarvoor hij ontworpen was, de voorkeursorientatie genoemd, en ii)  $180^\circ$  geroteerd om de langsas, zodat de belastingsrichting omgedraaid werd, de omgekeerde richting genoemd. Dit resulteerde in drie test configuraties: de referentiecilinder, de variabele-stijfheidscilinder in voorkeursrichting en de variabele-stijfheidscilinder in omgekeerde richting.

Een vergelijking van de experimentele respons van de twee referentiecilinder met de eindige-elementvoorspelling toonde aan dat de experimentele randvoorwaarden flexibeler waren dan in eerste instantie gemodelleerd in het eindige-elementmodel. Het introduceren van flexibele randvoorwaarden in het eindige-elementenmodel resulteerde in een goede overeenkomst tussen de experimentele en analytische resultaten. Een andere verbetering van het eindige-elementenmodel werd behaald door geometrische imperfecties in het model te introduceren en een Riks analyse uit te voeren. Dit model werd vervolgens gebruikt om de test resultaten van de variabele-stijfheidscilinder te voorspellen.

Een vergelijking van de experimentele resultaten met de eindige-elementvoorspelling met de Riks analyse vertoont over het algemeen goede overeenkomsten voor alle drie de configuraties. De overeenkomst tussen de voorspelde en gemeten eindrotaties en rekken was net zo goed voor de variabele-stijfheidscilinder als voor de referentiecilinder. De variabele-

stijfheidscilinder was stijver dan de referentiecilinder wanneer de globale respons wordt vergeleken. Dit was te verwachten omdat de variabele-stijfheidscilinder een grotere lami-naatstijfheid heeft. De respons van de variabele-stijfheidscilinder was stijver in de omge-keerde richting dan in de voorkeursrichting vanwege de invloed van de randvoorwaarden.

De belangrijkste observatie komt van de vergelijking van de rekken als functie van de verticale coördinaat van de cilinder: bij hetzelfde belastingsniveau zijn de maximale compressieve rekken van de variabele-stijfheidscilinder in de voorkeursrichting 10 procent lager dan die van de referentiecilinder; de positieve rekken waren 35 procent kleiner. Dit verschil in uiterste rekwaarden is een grote prestatieverbetering wanneer de sterkte criteria op rekken worden gebaseerd. Bovendien resulteerde de stijfheidsvariatie in omtreksrichting in een herverdeling van de belastingen: de drukbelastingen werden door een groter deel van de cilinder gedragen en de piek van de drukbelasting op  $\theta = 180^\circ$  werd met 25 procent teruggebracht ten opzichte van de referentiecilinder. Het aangepaste eindige-elementmodel voorspelde een verbetering van 20 procent in kniklast ten opzichte van de referentiecilinder als gevolg van de herverdeling van de belasting.



# Preface

While reading the preface of other books I thought so many times: "Why do authors always have to thank so many other people?" Over the past four years I started realizing that I would also be one of those authors who would thank a lot of people in the preface of my book. I discovered that even though most of the hard work had to be done by myself, I would never have been able to finish my dissertation without the help of all the people I will mention below. If I forget to acknowledge someone, it is not because I am not graceful, but because of a side-effect of doing a PhD: degradation of the memory.

Let me start telling you how I got interested in the topic of variable-stiffness composites. One afternoon in the summer of 2004, just before leaving for my internship at Boeing Helicopters in Mesa, I had a meeting with the new head of the Aerospace Structures chair, professor Zafer Gürdal, about a possible subject for my internship. He started talking about fiber-reinforced composites with varying fiber angles and what amazing things you could do with them. To be honest: I didn't have a clue what he was talking about! So even though it all sounded like abacadabra I agreed that would be the subject of my internship project. For some reason I ended up doing something else during my internship and instead it turned into my Masters thesis project. After reading some literature the abracadabra started to make sense, and Zafer's enthusiasm passed over to me. When I was about to finish my Masters thesis Zafer invited me to continue my research by doing a PhD with the Aerospace Structures group. After some initial doubts I decided to accept the offer, only because the topic was so challenging that I couldn't resist. Now, more than four years later, I can say that I am really happy that I did accept that offer. I don't think anything could've surpassed the experiences, adventures and challenges I've had in the past four years! So I'd like to start by thanking Zafer for introducing me to the topic, for offering me the PhD position and for being my advisor for the past five years. Also I would like to thank Jan Hol, who was such an excellent MSc advisor that I decided to stay at TUDelft for another four years after my Masters. His straightforward advice often pointed me in the right direction.

I would like to continue by thanking Joost List, Patrick Stickler and Mostafa Rassaian, for making my Boeing Fellowship and consequently my PhD work such a success! Joost, I really enjoyed all our discussions, not only the ones related to my own work, but also the general engineering and the personal discussions! Patrick, thank you for adopting my project as your own and for all the effort you spent in securing funding and defending the existence of my project internally! And Mostafa, your critical questions often made me rethink my explanations and definitely improved the quality of my work! Of course the fellowship program would not have existed without the support of Al Miller, Vanessa Gemmell, Peter Kortbeek and Peter Flinkerbusch, to whom I would like to extend my sincere

gratitude! For the extension of the program I would like to thank Randy Coggeshall.

I had the help of many different people in different stages of my project, whom I'd like to acknowledge here. I would like to thank Brian Tatting for the fruitful discussions we had and for the advice you gave me over the course of my project. Every time we talked I was so full of ideas that I couldn't stop working for the weeks after! My first fiber-steered cylinder ever was built with the help of Bert Thuis, Wilco Gerrits, Bert Bron, and Chris Groenendijk from NLR. Thank you guys: it made me feel so proud to see that first fiber-steered cylinder being built!

My time at Boeing was enriched by the meetings I had with Dave Morgan, Geri Mabson, and Eric Cregger. Dave, thank you for making me feel at home and for introducing me to many other interesting people! Geri and Eric, you made me understand that building an airplane encompasses so much more than what I learnt in college! I am proud to say I got advised by the best! For providing me the program and help to determine the optimum laminate designs I would like to thank Andrew Booker and Evin Cramer. Then of course Brice Johnson and Bob Kisch: Brice, I can't believe you had the patience to answer all my questions and to reply to all the emails I kept bugging you with! Both you and Bob taught me many things about fiber placement and without you guys it would not have been possible to realize this awesome project! For the manufacturing of the shells at Boeing I would also like to thank Massimiliano Moruzzi and Daniel Shugan from IMT, who were instrumental in programming the AFP machine to build my cylinders. The actual fiber placement work was done by Heinz Holzinger, Neil Wilson, Randy Darras and John Knudsen: thank you for hosting my visits to the development center and for doing a great job with fixing the straightened tows! I would also like to acknowledge the help of Don Powers, who performed the modal experiments and explained me everything I had to know about it! Finally I would like to thank Geoff Butler. As you can see the thermal analysis didn't make it into this thesis, but I appreciate all the time and effort you spent in trying to make it work!

When the composite shells were built in Seattle and shipped to the Netherlands the next phase of the project required the help of another big group of people. Luc Hootsmans, Niek Fraterman, Arnt Offringa, John Teunissen and Klaas Kiewiet were of great help in the design and development phase of the test fixture. The dirty work was done by Sake Bremer: Sake, you did a great job and I think you were one of the most important people to make the tests such a success! The team of the aerospace testing lab (vliegtuighal) at the TUDelft was also indispensable: Berthil Grashof, Bob de Vogel, Hans Weerheim and Johan Boender. Berthil and Bob: thank you for answering all my questions about the lab, while Hans is the best instructor ever for instrumenting a test setup! Johan, thank you for the many hours you spent setting up my tests. I always had a lot of fun working with you! I'd also like to thank Serge van Meer for explaining to me how to scan a composite. In addition, I would like to thank all the others in the lab who, one way or another, contributed to my project!

I would like to acknowledge the *NLR*, *the Boeing Company*, *Fokker Aerostructures*, *TUDelft* for their financial contributions to my PhD project.

I am also grateful to Zonta International for granting me the Amelia Earhart Fellowship and to SIMULIA B.V. for covering part of the printing cost of this thesis.

Even though I think I have quite an extensive list already, this preface would not be complete without a word of thanks to all the (current and former) members of the Aerospace Structures group. Gillian, Christian, Julien, Sam, Attila, Ali, Paolo, Roeland, Matthieu, Christos, Mostafa, Glenn, Mohammed, Terry, Farid, Martin, Marcus, prof Arbocz, prof

Rothwell, Jaap Wijker. Thank you for this great group, where I always felt at home! Pooria, Claudio and Sonell, of course I didn't forget about you! I wanted to let you, as my office mates, know that I couldn't have wished any better friends to share the office with! I really enjoyed it and will definitely miss you! Annemarie, Angela and Laura: thanks for always taking good care of me and the rest of the group! Miranda, thank you for helping me to make this thesis readable for others!

Finally, a couple of words of gratitude in English to all my friends in Seattle, who were there for me when I needed them and who became a second family to me: Marian and Brian, Ruth and Fredy Andres, Jeri, Neida and Scott, and Soufiane, thanks for everything!

Tenslotte een paar woorden in het Nederlands:

*Lieve pap en mam, Mariska, Gerard, Simone, Margreet, schoonfamilie, neefjes en nichtjes, dankjulliewel voor jullie steun en liefde! Ik kan alles met jullie delen: wanneer ik het moeilijk heb zijn jullie er voor me, wanneer ik verdrietig ben beuren jullie me op en wanneer ik blij ben zijn jullie blij voor mij. Zonder jullie had ik dit niet kunnen doen! Ik ben trots op onze familie en daarom draag ik mijn proefschrift op aan jullie!*

Agnes

Delft, September 2010



Voor mijn familie:

Pap en mam, Mariska en Henri, Femke, Demi, Esmée en Sjefke, Gerard en Debbie, Lars en Inge, Simone en Bart, Martijn en Nikki, Margreet en Jean-Willem.



# Contents

<b>Summary</b>	<b>i</b>
<b>Samenvatting</b>	<b>v</b>
<b>Table of Contents</b>	<b>xv</b>
<b>List of Symbols</b>	<b>xix</b>
<b>1 Introduction</b>	<b>1</b>
1.1 Brief History of Aerospace Structures . . . . .	1
1.2 Fiber-Reinforced Composites . . . . .	3
1.3 Variable-Stiffness Composites . . . . .	5
1.4 Challenges in Composite Design . . . . .	6
1.5 Research Outline and Overview . . . . .	7
<b>2 Advanced Fiber Placement and Laminate Tailoring</b>	<b>9</b>
2.1 Advanced Fiber Placement . . . . .	10
2.1.1 Fiber Placement Principles . . . . .	10
2.1.2 Restrictions on Manufacturing . . . . .	12
2.1.3 Fiber Placement Applications in the Aerospace Industry . . . . .	14
2.2 Laminate Tailoring . . . . .	15
2.2.1 Tailoring by Discrete Stiffness Changes . . . . .	16
2.2.2 Tailoring by Spatially Varying Fiber Orientations . . . . .	17
2.2.3 Stiffness Tailoring using Lamination Parameters . . . . .	26
2.3 Context of Current Work . . . . .	29
<b>3 Variable-Stiffness Laminate Definition</b>	<b>31</b>
3.1 Variable-Stiffness Laminate Construction . . . . .	31
3.2 Paths on Conical and Cylindrical Shells . . . . .	33
3.2.1 Geometry of a Conical Shell . . . . .	33
3.2.2 Paths on the Shell Surface . . . . .	35
3.3 Ply Construction and Property Tracing . . . . .	36
3.3.1 Axial Angle Variation on Conical Shells . . . . .	36
3.3.2 Axial Angle Variation on Cylindrical Shells . . . . .	41
3.3.3 Circumferential Angle Variation on Cylindrical Shells . . . . .	43

3.4	Path Candidates . . . . .	45
3.4.1	Geodesic Path . . . . .	46
3.4.2	Constant Angle Path . . . . .	47
3.4.3	Path with Linearly Varying Fiber Angles . . . . .	47
3.4.4	Constant Curvature Path . . . . .	49
3.4.5	Multiple Segment Angle Variation . . . . .	50
3.5	Examples of Fiber Paths and Curvature Constraints . . . . .	52
3.6	Conclusions . . . . .	55
<b>4</b>	<b>Optimization of the Fundamental Frequency</b>	<b>57</b>
4.1	Introduction . . . . .	57
4.2	Problem Definition and Optimization Procedure . . . . .	58
4.3	Finite Element Analysis . . . . .	59
4.4	Numerical Results . . . . .	60
4.4.1	Influence of the Curvature Constraint on Design Feasibility . . . . .	62
4.4.2	Influence of the Curvature Constraint on the Optimum Design . . . . .	64
4.4.3	Frequency Results . . . . .	66
4.5	Conclusions . . . . .	67
<b>5</b>	<b>Optimization of a Cylinder in Bending</b>	<b>69</b>
5.1	Introduction . . . . .	69
5.2	Design and Optimization Formulation . . . . .	70
5.2.1	Definition of the Optimization Problem . . . . .	70
5.2.2	Optimization Using a Surrogate Model . . . . .	72
5.2.3	Laminate Design . . . . .	73
5.3	Optimization Results for Laminates with a Constant Thickness . . . . .	75
5.3.1	Optimization Case 1 . . . . .	75
5.3.2	Optimization Case 2 . . . . .	83
5.3.3	Optimization Case 3 . . . . .	88
5.3.4	Variable-Stiffness Design for Manufacturing and Testing . . . . .	92
5.4	Optimization Results for Laminates with Overlaps . . . . .	95
5.4.1	Optimization Case 1 . . . . .	95
5.4.2	Optimization Case 2 . . . . .	102
5.5	Conclusions . . . . .	105
<b>6</b>	<b>Manufacturing</b>	<b>107</b>
6.1	Cylinders with Circumferential Stiffness Variation . . . . .	107
6.1.1	Curvature Constraint . . . . .	108
6.1.2	Compaction Pressure . . . . .	109
6.1.3	Coverage Parameter and Parallel Courses . . . . .	111
6.1.4	Minimum Cut Length and Fiber Straightening . . . . .	115
6.2	Cylinder with Axial Stiffness Variation . . . . .	118
6.3	Conclusions . . . . .	120



<b>7</b>	<b>Modal Test</b>	<b>121</b>
7.1	Description of Specimens . . . . .	121
7.2	Test Configuration . . . . .	121
7.3	Comparison of Modal Frequencies and Mode Shapes . . . . .	123
7.4	Comparison of Physical Response . . . . .	127
7.5	Conclusions . . . . .	130
<b>8</b>	<b>Bending Test</b>	<b>131</b>
8.1	Test Setup . . . . .	131
8.1.1	Design of the Test Fixture . . . . .	131
8.1.2	Test specimens, Preparation and Installation of the Test Article . . .	134
8.2	Data Acquisition and Instrumentation . . . . .	135
8.2.1	Geometric Imperfection Data . . . . .	137
8.2.2	Determining the Applied Bending Moment . . . . .	137
8.2.3	Displacements . . . . .	138
8.2.4	Strain measurements . . . . .	140
8.3	Test Procedure . . . . .	140
8.4	Finite Element Predictions . . . . .	141
8.4.1	Simple Linear and Nonlinear Finite Element Models . . . . .	141
8.4.2	Finite Element Model with Flexible Boundary Conditions and Test Mechanism . . . . .	144
8.4.3	Riks Analysis: Finite Element Model Including Imperfections . . .	147
8.5	Test Results . . . . .	148
8.5.1	Global Response . . . . .	150
8.5.2	Geometric Imperfections . . . . .	151
8.5.3	Strain Gauge Results . . . . .	153
8.5.4	Digital Image Correlation Results . . . . .	161
8.5.5	Deflection and Ovalization . . . . .	165
8.5.6	Comparison of the Buckling Load Predicted by the Different Finite Element Models . . . . .	170
8.6	Discussion and Outlook . . . . .	170
<b>9</b>	<b>Conclusions and Recommendations</b>	<b>173</b>
9.1	Design . . . . .	173
9.2	Finite Element Analysis . . . . .	174
9.3	Optimization Methods . . . . .	175
9.4	Optimization Results . . . . .	176
9.5	Manufacturing using Advanced Fiber Placement . . . . .	178
9.6	Experimental Validation . . . . .	178
9.7	Remaining Challenges . . . . .	180
9.8	Final Conclusions . . . . .	181
<b>A</b>	<b>Derivation of the Curvature Vector</b>	<b>183</b>
<b>B</b>	<b>Derivation of the Constant Curvature Path for Conical Shells</b>	<b>185</b>
<b>C</b>	<b>The Effect of Course Width Variation</b>	<b>189</b>

---

<b>D Bending Optimization Results</b>	<b>193</b>
<b>E Strain-Equivalent Tsai-Wu Strength Constraint</b>	<b>199</b>
<b>F Miscellaneous Modal Test Results</b>	<b>203</b>
<b>G Test Mechanism Loads</b>	<b>207</b>
<b>H Measurements of the End Rotations using DIC and LVDT's</b>	<b>211</b>
<b>I Optimization of Boundary Conditions</b>	<b>213</b>
<b>J Miscellaneous Bending Test Results</b>	<b>217</b>
<b>Bibliography</b>	<b>225</b>
<b>Curriculum Vitae</b>	<b>237</b>

# List of Symbols

## Greek Symbols

$\alpha$	Semi-cone angle	deg, rad
$\beta$	Circumferential surface coordinate on a developed cone	deg, rad
$\delta$	Displacement	m
$\delta$	Tow deviation	m
$\gamma$	Additional variable for bound formulation	Hz
$\gamma$	End rotation	deg,rad
$\kappa$	In-plane curvature	m <sup>-1</sup>
$\kappa$	Out-of-plane laminate curvature	m <sup>-1</sup>
$\lambda$	Fundamental eigenvalue	s <sup>-2</sup>
$\mu$	Fraction of total head width	-
$\Omega$	Ovalization	m
$\rho$	Radius of curvature	m
$\theta$	Circumferential coordinate	deg, rad
$\varepsilon$	Strain	m/m
$\varphi$	Fiber angle orientation	deg, rad

## Latin Symbols

$\bar{M}$	Specific bending moment	Nmkg <sup>-1</sup>
$\bar{w}$	Machine head width	m
$A$	Axial length	m
$A$	Cross-sectional area	m <sup>2</sup>
$a$	Acceleration	ms <sup>-2</sup>
$C$	Constant	-
$c$	Conformance distance of the compaction roller	m
$d$	Distance from the laminate outer surface to the cylinder axis	m
$d$	Moment arm	m
$E$	Modulus of elasticity	Nm <sup>-2</sup>
$F$	Forcing function	N
$f$	Fundamental eigenfrequency	Hz

$f$	Help function	-
$g$	Help function	-
$H$	Frequency response function	$ms^{-1}N^{-1}$
$I$	Moment of inertia	$m^4$
$k$	Spring stiffness	$Nm^{-1}$
$L$	Length	m
$l$	Arc length	m
$l$	Length over which a tow is straightened	m
$M$	Bending moment	Nm
$m$	Mass	kg
$m$	Number of half waves in axial direction	-
$N$	Number of layers in a laminate	-
$N$	Total number of courses in a ply	-
$n$	Course identifier	-
$n$	Number of full waves in longitudinal direction	-
$N_x$	Axial load	$Nm^{-1}$
$P$	Applied load	N
$p$	Distance to the central path	m
$R$	Cylinder radius	m
$r$	Radius	m
$s$	Longitudinal surface coordinate on a developed cone	m
$t$	Laminate thickness	m
$u$	Deformation	m
$V$	Velocity	$ms^{-1}$
$w$	Course width	m
$w$	Geometric imperfection	m
$w_e$	Effective course width in the direction of shift	m
$X$	Global coordinate axis	m
$x$	Longitudinal coordinate along the shell surface	m
$Y$	Global coordinate axis	m
$Z$	Global coordinate axis	m

## Subscripts

$b$	Baseline
$cr$	Critical
$c$	Center
$c$	Clamped boundary conditions
$c$	Composite
$e$	Edge
$f$	Flexible boundary conditions

$f$	Material failure
$i$	Inside of the laminate
$l$	Left
$NA$	Neutral axis
$o$	Outside of the laminate
$p$	Perpendicular to the cylinder surface
$p$	Preferred loading direction
$r$	Reversed loading direction ( $180^\circ$ rotated about the cylinder axis w.r.t. $p$ )
$r$	Right
$st$	Steel
$s$	Spring
$th$	Theoretical
$t$	Total
$t$	Tow
$v$	Variable-stiffness

## Superscripts

$+$	Tension
$-$	Compression

## Vectors

$\hat{\tau}$	Tangent unit vector
$\hat{\xi}$	In-plane path normal unit vector
$\hat{a}$	Longitudinal surface unit vector
$\hat{c}$	Circumferential surface unit vector
$\hat{i}$	Cartesian unit vector
$\hat{j}$	Cartesian unit vector
$\hat{k}$	Cartesian unit vector
$\hat{n}$	Surface normal unit vector
$\vec{\zeta}$	Modal displacement vector
$\vec{K}$	Global stiffness matrix
$\vec{M}$	Global mass matrix
$\vec{R}$	Vector pointing to a point in space
$\vec{T}$	Vector with design variables



# Chapter 1

## Introduction

### 1.1 Brief History of Aerospace Structures

Since the early days of the aerospace industry structures have been an important part of airplane and spacecraft design. The structure of a craft serves to carry all the loads on the aircraft or spacecraft, protect passengers and payload, and provide a comfortable environment for the passengers.

The first powered airplane, the Wright Flyer, was made of fabric, wood and wire. The fabric carried the aerodynamic loads, while the wood and wires were used to support the fabric and to transfer the loads from the wings to the primary carriage. During the First World War Anthony Fokker started replacing wooden frames with steel frames (century-of-flight website, 2010). Junkers then designed the first all metal airplane, consisting of sheet iron, later replaced by duralumin. In the 1920's more metal airplanes started to appear, but buckling, corrosion and fatigue were problems that undermined the competitiveness of metal airplanes against the traditional fabric, wood and wire airplanes. In the 1930's newer types of aluminum were developed, which were more resistant to corrosion, and metal airplanes began to be more popular. It was not until after the Second World War that metal airplanes became the norm. A major conceptual change that came with the introduction of metal in airplane design was a change from a wire-braced truss structure to a stressed-skin semi-monocoque design in which the skin became an integral working part of the structure. A typical stressed-skin semi-monocoque fuselage is shown in figure 1.1. The current generation of aircraft is still being designed according to this principle.

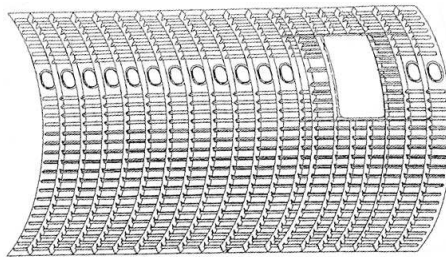


Figure 1.1: Typical stressed-skin semi-monocoque fuselage structure (Smith et al., 1995)

The main drivers behind the changes in material and design concepts were the need to reduce structural weight, whilst increasing safety, durability, and performance of an airplane. Saving structural weight allows fuel to be saved, which in turn allows the payload of the craft to be increased or the range of the aircraft to be extended. Depending on the application, one kilogram of weight saving can be expressed as a monetary value, some examples of which are given in table 1.1 (Jones, 1999).

Table 1.1: Value of weight savings in structures (Jones, 1999)

Small civil aircraft	\$55/kg
Helicopter	\$110/kg
Aircraft engines	\$440/kg
Fighters	\$440/kg
Commercial aircraft	\$880/kg
Supersonic transport	\$1,100/kg
Near-orbit satellites	\$2,200/kg
Synchronous satellites	\$22,000/kg
Space shuttle	\$33,000/kg

The demand for weight savings in the aerospace industry has led to the introduction of light fiber-reinforced composites as an alternative for metals. The first composite parts flew on military airplanes in the late 1960's and early 1970's, on airplanes like the General Dynamics F-111, the Vought A-7, and S-3A and the Harrier (Jones, 1999). As their use in the military sector steadily grew, composites also made their way onto commercial airplanes. The first composite parts on commercial airplanes mainly consisted of secondary structures, engine cowlings and control surface type structures, e.g. elevators, rudders and ailerons. An overview of the increased use of composite structures in the aerospace industry is given in figure 1.2 (Roeseler et al., 2007). Today (2010) the first *full-composite* commercial airplanes

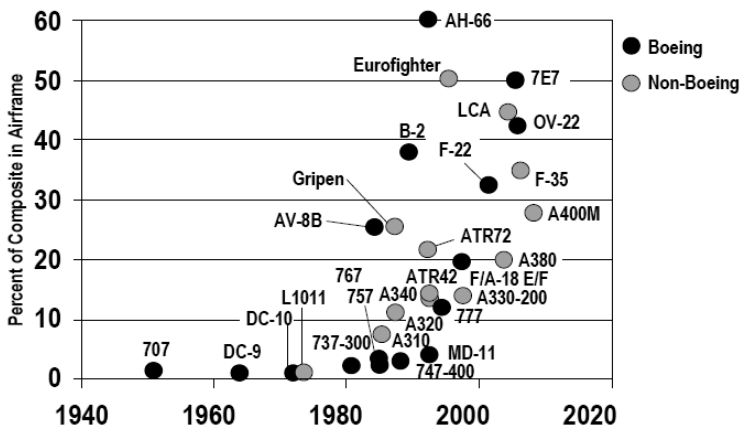


Figure 1.2: Use of composite structures in the aerospace industry (Roeseler et al., 2007)

are being assembled, the Boeing 787 Dreamliner and the Airbus A350. Approximately 50



percent of their structure in terms of weight will consist of composite materials, as shown for the Boeing 787 in figure 1.3 (Roeseler et al., 2007).

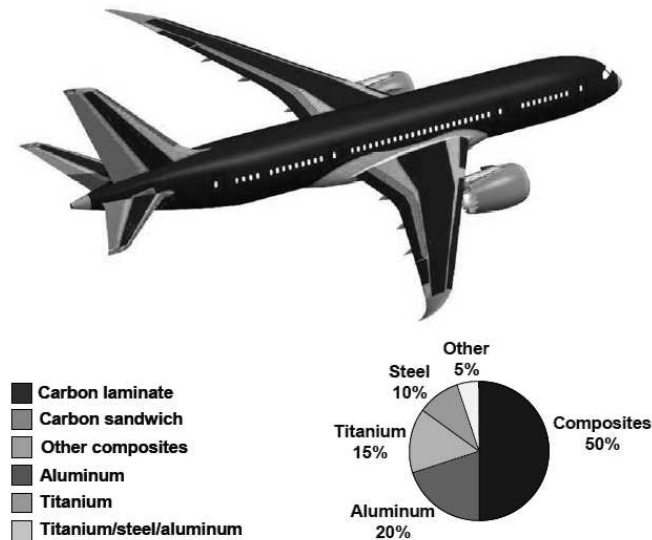


Figure 1.3: Use of composites in the Boeing 787 Dreamliner (Roeseler et al., 2007)

## 1.2 Fiber-Reinforced Composites

Fiber-reinforced composites are materials that consist of fibers that are embedded in a matrix material (Jones, 1999). The function of the fibers within the composite are to carry loads and to provide strength and stiffness. The matrix has to bond the fibers together and provide stress transfer between fibers. In the aerospace industry carbon and glass fibers are most commonly used reinforcements. Thermoset and thermoplastic polymer resins usually serve as the matrix material.

An important feature of fiber-reinforced composites is that the material properties depend on the orientation of the material (Jones, 1999). A composite has high strength and stiffness in the direction of the fiber, but a much lower strength and stiffness in the directions perpendicular to the fiber. This characteristic is called orthotropy. Orthotropy distinguishes composites from metals, the properties of which are independent of the material orientation, and provides a structural engineer extra design options. She can now make use of the directionality of the material by tailoring the mechanical properties to the loads being exerted on the structure, resulting in lighter structures.

The possibility of tailoring material properties is an important advantage that composites have over metals, but it is not the only one. When comparing strength and stiffness per kilogram of material, i.e. the specific strength and specific stiffness, some advanced composites are as much as three times as stiff as aluminium. This results in lighter structures, lowering the raw material costs and importantly, requiring less fuel when used in aerospace

structures. Another advantage of composites is that it is easier to integrate parts, which means a lower part count, less fasteners, and less effort and cost needed for assembly. An example is shown in figure 1.4, where the stringers and skin of the Boeng 787 fuselage are integrated into one part. Maintenance costs of composite structures can also be lower, because composites are less sensitive to fatigue and corrosion than metal structures.

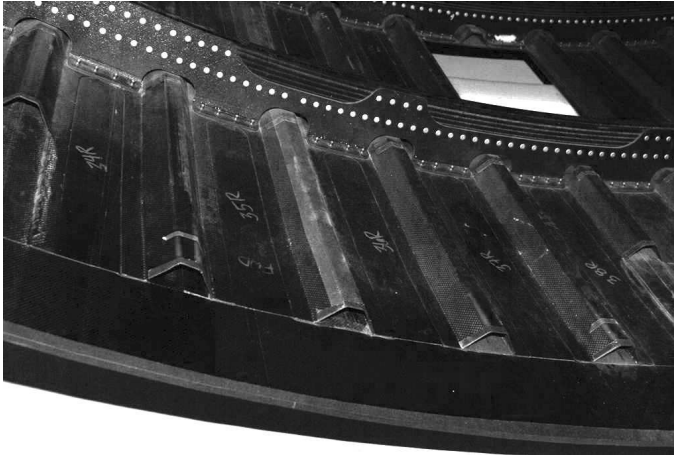


*Figure 1.4: Integrated skin and stringers in a composite fuselage (photo: Blom)*

Fiber-reinforced composites exist in different forms: the fibers can be woven, either as a fabric, or in a 3-dimensional shape; the fibers can be chopped and randomly distributed in a mould; they can be wound continuously around a mandrel; or the fibers can be laid down in tape form, basically forming sheets, called plies, that can be layered. The latter are referred to as composite laminates. Within each layer of the laminate the fiber orientation is typically held constant. The stiffness and strength properties of the laminate can be changed by combining layers with different orientations within one laminate and by varying the total number of layers.

Traditionally composite laminates were manufactured by manually laying layers of fabric, woven fibers, on a mandrel, after which the matrix material was applied, and the entire assembly was cured. For axisymmetric parts, such as pressure vessels and tubes the deposition of the fibers can be automated by the use of a filament winder. Tape laying is an automated process which is very suitable for manufacturing large, low-contoured parts. Large sheets of uni-directional prepreg material are placed on the surface, considerably reducing layup time compared to hand layup. Prepreg material already contains both the fibers and the matrix, so that the fibers do not need to be impregnated after laydown, and the product can be cured directly after layup. A third automated process for the production of composite laminates is advanced fiber placement. This production form bridges the gap between filament winding and tape laying because it can be used to manufacture highly contoured, non-convex shapes. With fiber placement multiple small strips of prepreg tape are placed on the surface, making it possible to curve the fibers and to cut and restart the strips individually. A more detailed description of the fiber placement process will be given in chapter 2. The versatility of advanced fiber placement opens up a number of design possibilities that are not available with any of the other composite manufacturing

techniques commonly used in aerospace.

### 1.3 Variable-Stiffness Composites

The composite laminates that are currently applied in the aerospace industry typically consist of layers with  $0^\circ$ ,  $90^\circ$ ,  $+45^\circ$  and  $-45^\circ$  fiber orientations. This practice originates from the time that composites were being made by hand, which made it hard to align fibers accurately with a direction other than  $0^\circ$ ,  $90^\circ$ ,  $+45^\circ$  or  $-45^\circ$ . Plies were made in the form of orthogonally woven fibers to improve handling qualities. Composites could be made suitable for most load cases by placing these plies at  $0/90^\circ$  and  $\pm 45^\circ$  with respect to the main loading directions. Changes in stiffness were made by locally increasing or decreasing the number of plies and by changing the stacking sequence within the laminate.

The limits on manufacturing laminates with other fiber orientations than  $0^\circ$ ,  $90^\circ$  and  $\pm 45^\circ$  disappeared with the introduction of automated production processes. Yet many composite design rules in the aerospace industry are based on these four fiber orientations, which makes it difficult to change the design philosophy to include other fiber orientations. The current design rules are supported by innumerable coupon tests, so unless there is a strong incentive in terms of possible weight savings, the cost of developing rules for different fiber orientations is a major factor in preventing large changes in this field.

A possible game changer in the application of fiber-reinforced composites in the aerospace industry is the concept of *variable-stiffness* composites. Variable-stiffness composites consist of plies that do not have a constant fiber orientation. For a long time variable-stiffness composites only existed in theory, but advanced fiber placement has made it possible to steer fibers in the plane of the laminate, as shown in figure 1.5. The stiffness of a laminate depends on the orientation of its plies, such that varying the fiber orientation within plies causes a varying laminate stiffness. In addition the stiffness can be varied by designing the fibers to overlap.



Figure 1.5: Steered fibers laid down by an advanced fiber placement machine (photo: IMT)

In a variable-stiffness composite the stiffness can be tailored to create more efficient load paths, resulting in weight savings that can not be achieved using traditional laminates. A literature review of the research on the weight saving potential of variable-stiffness composites is given in chapter 2. One example that covers the full cycle of geometric design, analysis, optimization, manufacturing and testing of a variable-stiffness composite is presented in the work of Gürdal et al. (2005, 2008), Tatting and Gürdal (2002, 2003), Wu et al (2001; 2002) and Jegley et al. (2003, 2005). These researchers optimized flat panels for in-plane compression and shear, taking into account manufacturability based on advanced fiber placement. Improvements in load carrying capability ranged from a couple of percent up to 100 percent when compared to traditional laminates (Gürdal et al., 2005, 2008; Jegley et al., 2003, 2005; Tatting and Gürdal, 2002, 2003; Wu and Gürdal, 2001; Wu et al., 2002), depending on the panel configuration, loading condition and design method. A picture of one of the panels that was built as part of this project is shown in figure 1.6. The fact that Gürdal et al. manufactured variable-stiffness panels and validated their predictions by experiments shows that the weight saving potential can be realized using fiber placement technology.

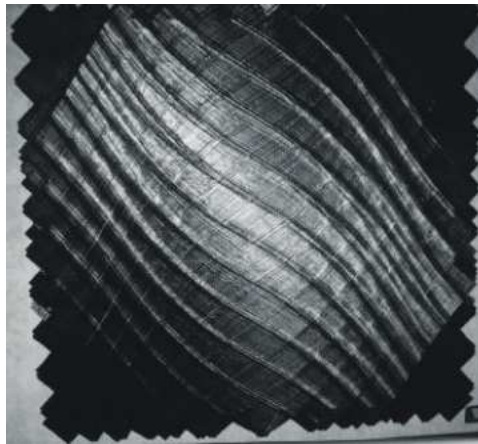


*Figure 1.6: One of the first fiber-steered panels built by Tatting and Gürdal (2002)*

## 1.4 Challenges in Composite Design

The use of composites in the aerospace industry has demonstrated clear advantages over the use of metals. At the same time many aspects that are fundamental to these advantages also cause concerns and problems in composite design and analysis.

The first challenge is to predict the structural behavior of composites reliably. The structural response can be divided in two areas: the stiffness response and the strength response. In general fairly good predictions can be made for the stiffness of thin laminates by applying the Classical Lamination Theory (CLT) (Jones, 1999). A combination of the CLT and a closed-form analytical solution or a finite element analysis is often used to predict the stiffness response of a structure. The orthotropy of the material makes it more complicated

to predict the strength response of a composite compared to a metal, moreover, the response changes with changing stacking sequence.

Predicting the strength of composites is not as straightforward as predicting their stiffness. The presence of multiple materials, the interface between the fibers and the matrix, and the interface between plies create many different failure modes that are often coupled. In the aerospace industry strength criteria are usually empirically based, requiring extensive and thus expensive test programs. In the academic world first-ply-failure theories such as the Hoffman, Tsai-Wu or Tsai-Hill criteria (Jones, 1999) are most commonly used to predict composite failure. The World Wide Failure Exercise (WWFE) was established in an effort to increase the understanding of composite failure mechanisms (Soden et al., 2004). Here the knowledge of experts from industry and academia around the world is brought together to develop reliable models to predict the strength of composite laminates. Some investigators taking part in the WWFE are able to capture several failure mechanisms in their model, but none of the models cover all failure mechanisms simultaneously. The composite world is thus still in need of a reliable model for the prediction of composite failure.

The second challenge in composite design and analysis is to exploit all the opportunities that composites have to offer. Automating the manufacturing process substantially increased the number of design possibilities, making it impossible for an engineer to design a composite without the proper tools. Hundreds of design options already exist for the design of a single variable-stiffness ply. These options need to be limited to make the design problem manageable. Yet the possible advantages of composite use in aerospace structures might disappear if the options are limited too much.

Manufacturability is one limiting factor that can not be ignored in the design of composite laminates. In the past hand layup limited the design of composites to combinations of  $0^\circ$ ,  $90^\circ$ ,  $+45^\circ$  and  $-45^\circ$ , while nowadays fibers can even be curved using fiber placement machines. Fiber placement technology also has limitations, some of which need to be taken into account in the early design phases of a composite structure, while others can be dealt with at a later stage. For the time being the current generation of design and analysis tools do not include the option to use curved fibers, thereby limiting the designer who will not be able to take full advantage of the capabilities of fiber placement technology.

A condition for a good structural design using composite laminates is that the designer understands the behavior of the composite structure, and how certain design changes influence the structural response. Once this condition is met, the best design can be determined using optimization tools that are coupled to the design and analysis tools.

## 1.5 Research Outline and Overview

The research described in this thesis will cover only a small part of the challenges outlined above. The work is focused on extending the variable-stiffness laminate design concept to conical and cylindrical shells. At the end of the thesis the following two questions should be answered:

1. *'Can fiber-placed, variable-stiffness composites be used to reduce the weight of conical and cylindrical aerospace structures?'*
2. *'How does the varying stiffness influence the mechanical behavior of these structures?'*

Before these two questions can be answered the current design and analysis tools need to be extended to cover variable-stiffness conical and cylindrical shells. The experience of other researchers and knowledge about the fiber-placement manufacturing process serve as the starting point for the extension of these tools. A literature survey of variable-stiffness composite research, and a historical and technological perspective on fiber placement are given in chapter 2.

Variable-stiffness ply definitions for conical and cylindrical shells are developed in chapter 3, where a distinction is made between axial stiffness variation on generic conical shells and circumferential stiffness variation on cylinders. Restrictions on the advanced fiber placement process are included in the ply definitions, and effects resulting from the manufacturing process such as fiber angle deviations and course overlaps are discussed.

A series of conical shells is optimized for maximum fundamental frequency in chapter 4. A stiffness variation in axial direction is assumed for these optimizations. Different ply definitions are compared side by side and the influence of the manufacturing constraints on the obtainable improvements is discussed.

A circumferential stiffness variation was applied to study the possible improvements in buckling load of a cylinder in bending, which is discussed in chapter 5. A distinction is made between laminates that have a constant thickness and laminates in which course overlaps are allowed. Again, manufacturability constraints are included. Additionally, strength and local stiffness constraints are imposed on the optimization and their influence on the optimum design is discussed.

Based on the cylinder optimization of chapter 5 one traditional and one variable-stiffness design were selected to be manufactured using an Ingersoll fiber placement machine located at Boeing in Seattle (Blonigen and Johnson, 2006). The design details and the problems encountered during manufacturing are described in chapter 6. This chapter also contains a section on the manufacturing of a cylinder with axial stiffness variation with overlapping courses.

Once the cylinders are manufactured it is essential to know if the mechanical behavior of the manufactured design corresponds to the predicted behavior. Therefore a modal test was performed on the variable-stiffness cylinder and on the baseline cylinder. A modal test provides information about the mass and stiffness distribution in a structure. A comparison of the eigenfrequencies, mode shapes and physical responses of the shells between the ABAQUS model and the experiment therefore serves as a first evaluation of the accuracy of the finite element model. The modal test setup is described and the analytical and test results are discussed in chapter 7.

A second assessment of the accuracy of the finite element prediction was made using a mechanical bending test. A test fixture was designed to test the manufactured shells in pure bending. A description of the test fixture, the data acquisition system and the test procedure, and an extensive discussion of the test results are presented in chapter 8.

Finally, conclusions about the presented work and recommendations for future research will be given in chapter 9.

## Chapter 2

# Advanced Fiber Placement and Laminate Tailoring

An overview of advanced fiber placement technology and composite tailoring, two areas closely related to the subject of this thesis, will be presented in this chapter. First a description of the advanced fiber placement process will be given, with a short description of the limitations and an overview of the past and current applications of advanced fiber placement in the aerospace industry. Then the concept of composite tailoring and previous work on composite tailoring will be discussed. Other references, more related to a specific chapter will be cited throughout the thesis.



*Figure 2.1: General view of an Ingersoll AFP machine (photo: Boeing)*

## 2.1 Advanced Fiber Placement

### 2.1.1 Fiber Placement Principles

Advanced fiber placement (AFP) is a fully automated process for the production of composite laminates that combines the differential payout capability of filament winding and the compaction and cut-restart capabilities of automated tape laying (Evans et al., 1989; Evans, 2001). A variety of machines exist that can deposit different kinds of materials: thermoset prepreg (pre-impregnated) materials, thermoplastic materials, or dry fibers. Carbon fibers pre-impregnated with thermoset resin are most commonly used in the aerospace industry and therefore the fiber placement process will be described assuming a thermoset material system.

Most fiber placement systems have seven axes of motion and are computer controlled. The axes of motion, i.e. three position axes, three rotation axes and an axis to rotate the work mandrel, provide the fiber placement machine flexibility to position the fiber placement head onto the part surface, enabling the production of complicated composite parts. A picture of an Ingersoll AFP machine is shown in figure 2.1.

During the fiber placement process tows of slit prepreg tape are placed on the surface in bands of parallel fibers, called courses. Typical tow widths are 3.175 mm, 6.35 mm, and 12.7 mm (1/8 in, 1/4 in and 1/2 in). For a tow width of 3.175 mm a maximum of 32 tows can be placed on the surface simultaneously, resulting in a maximum course width of 101.6 mm (4 in).

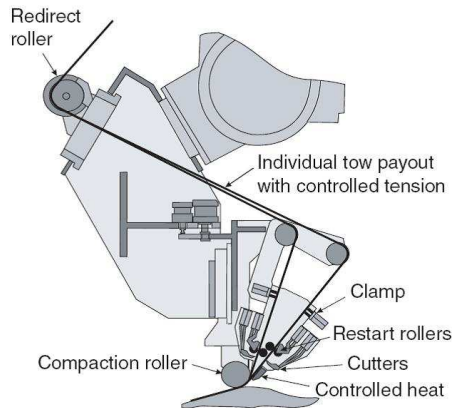


Figure 2.2: Schematic view of an AFP machine head (Evans, 2001)

Each tow originates from an individual spool, seen in the top left corner of figure 2.1, and is started by pinching rollers that move the tow forward until it reaches the tool/part surface, see figures 2.2 and 2.3. The tow is heated before it reaches the tool or part surface to increase the tackiness of the material, needed to overcome the slight tension present in the tow, and compressed by a compaction roller to get the tows to adhere to the surface and to remove trapped air. Once the tow reaches the surface the pinching rollers are released and the tow is pulled forward by the friction of the compaction roller and the tool surface, allowing the tow to move at its own speed. The individual payout of tows, the tackiness



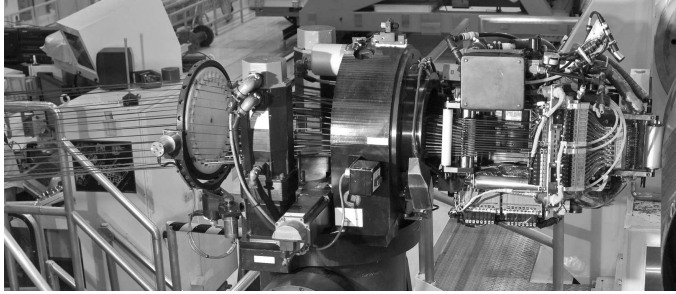
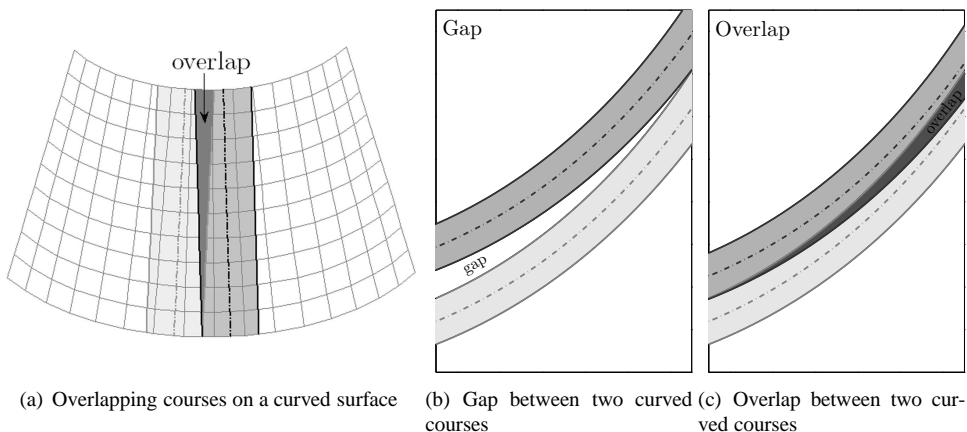


Figure 2.3: Close-up view of the head of an Ingersoll AFP machine (photo: Boeing)

of the material and the compaction of tows at the surface enable placement of curved fiber courses and placement of fibers on concave surfaces.

Tows can also be cut and restarted individually, making it possible to manufacture parts that are close to their final shape, thus reducing scrap rates. The tow cut and restart capability of fiber placement machines also enables variation of the course width, which can be used to eliminate gaps or overlaps between adjacent courses that are caused by geometry and steered fiber courses. For example, courses laid down in the axial direction on a conical shell would start overlapping at the small radius if the course width is kept constant, see figure 2.4(a). A constant-thickness ply can be obtained by cutting (or dropping) tows on the outside of the course when going from the large radius to the small radius. Steered courses can cause overlaps even if the part geometry does not play a role. In general course edges of two steered courses will not match, unless the courses are exactly parallel, and either gaps or overlaps are formed. Gaps can be avoided by reducing the distance between the course centerlines, while overlaps can be eliminated by cutting and restarting tows. An example of a gap between two courses is shown in figure 2.4(b), the same two courses overlap in figure 2.4(c) due to a smaller distance between the centerlines.



(a) Overlapping courses on a curved surface

(b) Gap between two curved courses

(c) Overlap between two curved courses

Figure 2.4: Overlaps and gaps between courses

## 2.1.2 Restrictions on Manufacturing

Advanced fiber placement has substantially increased the capabilities for manufacturing composite laminates, but it also has a number of limitations, some of which will be discussed below.

### Minimum turning radius

When a fiber course is steered the individual tows are bent in the plane of the surface causing the fibers at the inner radius of the tow to be in compression. These fibers might start buckling out-of-plane if the turning radius is too small, as shown in figure 2.5. The presence of buckled tows could lead to a reduction in laminate quality. Therefore a limit on the turning radius is imposed, usually defined in terms of a minimum radius for the centerline of the course. A typical value for the minimum turning radius for a 32 tow course with 3.175 mm wide tows is 635 mm (25 in). Smaller radii are possible, depending on the material system, layup rate, and compaction pressure used. Increasing the tow width increases the amount of compression of the fibers on the inside of the curve, requiring a larger turning radius for courses with larger tow widths. Values for the minimum turning radius of a typical AFP machine for different tow widths are given in table 2.1. The minimum turning radius constraint is often referred to as the curvature constraint, where the maximum curvature is the inverse of the minimum turning radius allowed.

*Table 2.1: Variation of minimum turning radii with tow width for a 102 mm course width*

tow width		typical minimum turning radius	
3.175 mm	(1/8 in)	635 mm	(25 in)
6.35 mm	(1/4 in)	1778 mm	(70 in)
12.7 mm	(1/2 in)	8890 mm	(350 in)

### Minimum cut length

Another important constraint in the manufacturing of fiber-placed composites is the minimum cut length. The minimum cut length refers to the minimum tow length that needs to be laid down before a tow can be cut after it has been started and varies between 63 and 152 mm (2.5 and 6 inches), depending on the machine configuration. When a tow is started by the pinching rollers it needs to travel a certain distance before it reaches the surface. If a tow is cut before the surface is reached it cannot be properly controlled and therefore fiber placement machines are programmed not to place any tows that are shorter than the minimum cut length. The designer might decide to place a longer piece of tow and trim the excess material later if a tow shorter than the minimum cut length is needed at the boundary of a part. An example of tows that are too short to be placed can be seen on the top left and bottom right of figure 2.6(a). How tows could be extended past the part boundary to solve this problem is shown at the top left of figure 2.6(a). Sometimes the minimum cut length requirement is violated within a part. For example, it is not possible to extend the tow when a local rectangular patch with a 45 degree fiber angle orientation like the one shown in figure 2.6(a) is placed on the surface. Another occasion in which tows might need to be cut within

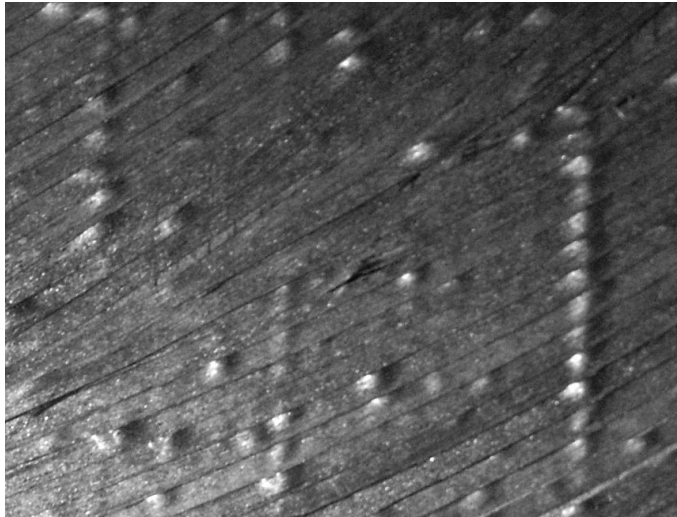


Figure 2.5: Buckled tows in a laminate with steered fiber courses (photo: A.W. Blom)

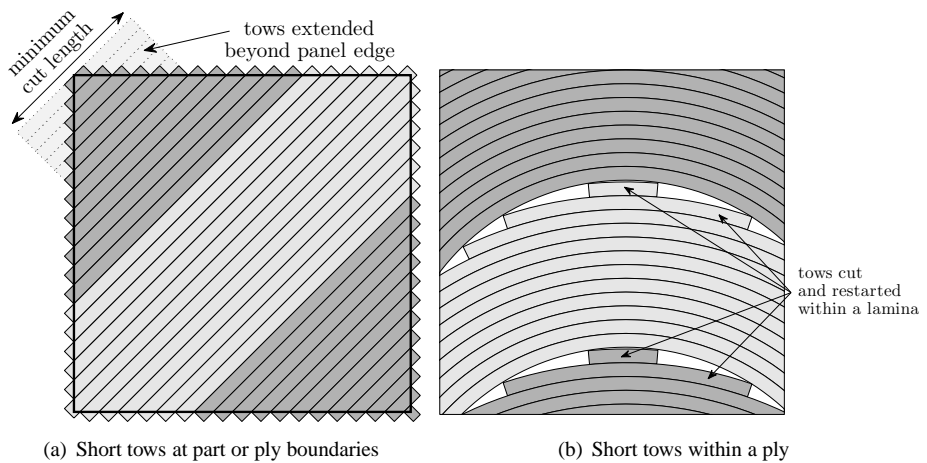


Figure 2.6: Possible minimum cut length issues

a part is when the width of a course is first increased and then decreased to avoid overlaps with adjacent courses, as shown in figure 2.6(b). In these cases either the design needs to be adjusted or the missing tows need to be filled in by hand.

**Coverage parameter**

The coverage parameter determines where tows are terminated and restarted with respect to a boundary, e.g. the boundary of a part or the edge of an adjacent course. Tows are cut perpendicular to the fiber direction and therefore small gaps or overlaps or a combination of gaps and overlaps are created when tows are cut or restarted to match the edge of a

neighboring course. A coverage of 0 percent indicates that a tow is cut as soon as one edge of the tow reaches the boundary of the adjacent course, resulting in a small triangular area without fibers. An example is shown in figure 2.7. A small rectangular overlap is created when a coverage parameter of 100 percent is applied, which is the case as soon as both edges of the tow to be cut have passed the boundary of the adjacent course. Coverage values between 0 and 100 percent represent the intermediate cases.

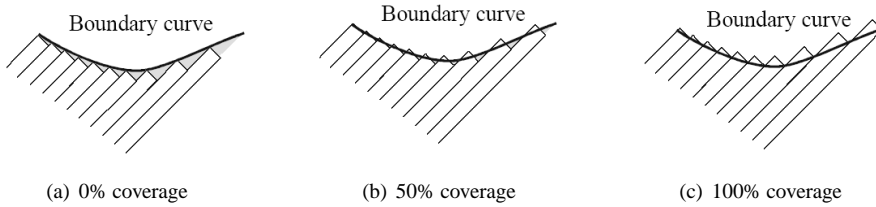


Figure 2.7: Tow dropping with different coverage parameters (Tatting and Gürdal, 2003)

The choice of coverage parameter is expected to have an influence on the strength and surface quality of a laminate. The gaps created with a 0 percent coverage parameter cause resin rich areas in a laminate and these can locally weaken the composite. A theoretical study by Blom et al. (2009) showed that the strength and stiffness of a laminate are reduced by the presence of small triangular gaps when compared to a laminate with smooth course boundaries. The strength was reduced because the resin rich areas acted as failure initiation spots. Using wider tows increases the size of the resin rich areas and is therefore more detrimental for the strength of a laminate with tow drops. This negative effect can be somewhat alleviated by spreading out the tow-drop locations of subsequent plies with the same ply definition. A coverage of 100 percent could lead to ridges of larger thickness, which might also influence the laminate strength. In addition, ridges would be undesirable if the laminate is used as an aerodynamic surface or if it interfaces with other parts. No test data on the influence of the coverage parameter on the strength of fiber-placed composites with cut tows is publicly available, and therefore it is assumed that a coverage parameter close to 50 percent is the least harmful.

### 2.1.3 Fiber Placement Applications in the Aerospace Industry

Advanced fiber placement (AFP) technology, also known as *tow placement technology* or *automated tow/fiber placement* was developed in the late 1980's. The first studies were done as part of the NASA/Hercules ACT and the Boeing ATCAS programs (Anderson and Grant, 1991; Grant and Benson, 1992), for which stiffened panels were built using Hercules AFP machines. Some of the first production parts were the F/A-18E/F horizontal stabilizer skins and the Bell/Boeing V-22 Osprey aft fuselage (Kisch, 2006; Pinckney, 1991), followed by the V-22 grip (Martin et al., 1997; Measom and Sewell, 1996; Mondo et al., 1997; Pasanen et al., 1997). Slowly AFP technology found its way into other aerospace applications such as the Boeing JSF inlet duct, the C17 landing gear pod fairings and the C17 engine nacelle doors (Buchanan et al., 1999; Kisch, 2006) and fuselage sections of the Raytheon Premier I and Hawker Horizon business jets (Evans, 2001). Costs were reduced on all programs

compared to hand layup as a result of a reduction in part count, a reduction in layup time and smaller scrap rates. Most recently AFP is applied on a large scale for the production of the Boeing 787 Dreamliner, the aft fuselage of the A380 and for the Airbus A350 XWB (McCarville et al., 2008; Morey, 2008), while efforts to improve the process and design tools for the AFP process are ongoing.

Developments in the AFP process are mainly focused on increasing the material lay-down rate and improving the reliability of the process. Increasing the speed and reliability at which tows can be cut and restarted (DeVlieg et al., 2007; Izco et al., 2006) and precise application of heat to the tows (Calawa and Nancarrow, 2007; Schledjewski and Schlarb, 2006) are two factors that greatly contribute to increasing the laydown rate and improving the process reliability. In addition, improved material qualities have resulted in less resin and fiber fuzz build up in the fiber redirects and delivery systems of AFP machines, thereby contributing to a higher reliability of the process (Benson and Arnold, 2006). Furthermore, the process has been made suitable for high temperature materials (Benson and Arnold, 2006), e.g. BMI, and in situ consolidation of thermoplastics has become possible (Schledjewski and Schlarb, 2006). Finally, smaller, more affordable machines are developed which are tailored for making specific products so that fiber placement machines become more widely available (Grant, 2006; Martin and Hennings, 2008).

Integrating geometric design tools such as CATIA with structural analysis tools and fiber placement simulation software is necessary to improve part design. Costs can be reduced and eventually lay down rates can be increased by taking the manufacturing process into account early in the design the pre-production development (Hale and Schueler, 2002; Moruzzi et al., 2006; Wyatt and Haj-Hariri, 2008).

## 2.2 Laminate Tailoring

The term *laminata tailoring* refers to adjusting the properties of a composite laminate to meet given performance requirements most efficiently, where performance is expressed in terms of minimum structural weight for given loads or maximum strength or stiffness for a given weight. The stiffness of laminated composites are tailored by changing the number and composition of plies. Laminate membrane properties are changed by varying the number of layers with different orientation angles, while bending properties are influenced by the sequence in which the plies are stacked in addition to the laminate composition.

Traditionally the fiber angle orientation per ply is kept constant, and stacking sequences are varied on a panel by panel basis to comply with the structural requirements. Over the past decades research has shown that a stiffness variation in the plane of a laminate, i.e. spatial stiffness tailoring, can be beneficial for structural performance due to the added capability of internal load redistribution. Spatial stiffness tailoring can be achieved by discretely changing the stacking sequence and number of plies over the plane of a laminate or by spatially varying the fiber orientation angles within plies.

## 2.2.1 Tailoring by Discrete Stiffness Changes

### Flat Panels

An example of improved strength performance of compression-loaded composite plates with central holes by spatial stiffness tailoring is given in the research of Haftka and Starnes (1988). In this work the cross-sectional stiffness is tailored to soften the area around the hole. This was achieved through a redistribution of 0 degree fibers from the center of the panel to the edges of the panel in carbon-fiber-reinforced panels, or by replacing the 0 degree glass fibers at the edges of a glass-fiber-reinforced panel by stiffer carbon fibers. Significant improvements in strength-to-mass ratio were found and validated by experimental work.

The compression and shear buckling responses of rectangular composite plates have been improved in a similar fashion by Biggers and Pageau (1994); Biggers and Srinivasan (1993). A redistribution of uni-directional lamina from the central region to the supported edges results in an increase in buckling load of 200 percent for thin laminates in compression and an increase of more than 50 percent for thick laminates in compression. The shear buckling load increased by 75 percent by rearranging the  $\pm 45$  degree plies in a doubly symmetric diagonal pattern over the planform.

A laminate tailoring concept in the form of multiple concentric rectangular layups has also proved to be beneficial for improving the buckling load of panels subjected to shear loads and in-plane compression, as has been shown by Papadopoulos and Kassapoglou (2004; 2007; 2008).

An experimental and analytical investigation of the buckling and post-buckling behavior of composite plates with a stiffness change at the centerline of the plate has been done by DiNardo and Lagace (1989), here the stiffness was changed by either a ply drop-off or by a discrete angle change of several plies and both showed a marked effect on plate buckling and post-buckling behavior.

### Cylinders

The response of segmented-stiffness cylinders to end shortening and internal pressure has been studied by Riddick and Hyer (1998; 1999; 2002; 2004). In their work the cylinders are divided in 4 segments: a keel and a crown section which have identical stiffnesses and two sides of identical stiffnesses, but which differs from the first stiffness. Exact, approximate and finite element solutions are used to predict the geometrically nonlinear response. The segmented-stiffness cylinders differ from uniform-stiffness cylinders due to the existence of circumferential displacements, caused by the difference in Poisson's ratios from one segment to the next when axial end shortening is applied (Riddick and Hyer, 1998) and by the mismatch in extensional moduli when the cylinder is under internal pressure (Hyer and Riddick, 1999).

The buckling loads and modes of two segmented-stiffness cylinders under axial end shortening were compared using STAGS (Rankin et al., 2000) finite element models by Riddick and Hyer (2004). One segmented-stiffness cylinder had an axially stiff keel and crown section and the other had a circumferentially stiff keel and crown section, both had identical side sections. The axial stress resultants in each segment were uniform and highly dependent on the axial stiffness of each segment. In the nonlinear pre-buckling range the more highly loaded segments of the cylinder started to develop wrinkles in the axial direc-

tion, the other segments remained wrinkle free. When loaded in the post-buckling range the stiffness decreased such that the axial load dropped by 57 percent for the circumferentially-stiff cylinder and 20 percent for the axially-stiff cylinder. Riddick and Hyer showed that the post-buckling stiffness of the circumferentially-stiff cylinder was also reduced more compared to the axially-stiff cylinder. These differences in load drop and stiffness reduction are caused by the difference in buckling mode: the axially stiff cylinder only buckled in the stiff segments, whereas the circumferentially stiff cylinder buckled in all four segments.

Riddick and Hyer (2002) also included the effect of geometric imperfections, i.e. out-of-roundness of the cylinder, on the response of segmented-stiffness cylinders. The imperfections were obtained by measuring the geometry of two manufactured cylinders. The out-of-roundness of the axially-stiff cylinder was more than 3 times that for the circumferentially-stiff cylinder. The most prominent influence of the out-of-roundness of the axially stiff cylinder was on the transition from buckling to post-buckling. Specifically, after buckling the perfect axially-stiff cylinder developed, simultaneously, a deep dimple in both keel and crown. In contrast, after buckling the imperfect axially-stiff cylinder developed a dimple in the keel, but not in the crown. With a slight increase in end shortening this deformed configuration continued until the crown became unstable and also developed a dimple. Riddick and Hyer showed that the circumferentially-stiff cylinder was unaffected by the measured out-of-roundness of that cylinder.

## 2.2.2 Tailoring by Spatially Varying Fiber Orientations

### Flat Panels

Two of the first to make use of curvilinear fibers to improve the compressive load carrying capability of composite panels with holes were Yau and Chou (1988), who forced the fibers to shape around the hole by inserting metal pins into woven fabric prior to curing. The resulting laminates demonstrated better open-hole strength compared to similar panels with drilled holes.

The use of curvilinear fibers to improve the tensile load carrying capacity of a plate with a central hole has been studied analytically by Hyer and Charette (1991). The fiber orientations were designed to be aligned with the principal stress directions to provide a more effective load path around a hole compared to the straight-fiber counterpart. The resulting laminates outperformed the quasi-isotropic laminates in tension, but did not show any improvements in buckling load. Hyer and Lee (1991) therefore focused on improving the buckling load of panels with a central hole. A sensitivity analysis and a gradient-search technique were used to find the optimum fiber orientations in a number of discrete regions in the plate. Substantial increases in buckling load were achieved, while simultaneously the tensile strength was improved. The most important mechanism behind the increased buckling loads was a redistribution of the loads from the unsupported edge hole to the supported edges. Subsequently Hyer et al. (1994) manufactured two curvilinear panels using a Cincinnati Milacron fiber placement machine, one of which was tested in tension and the other in compression. The buckling load carrying capacity of the manufactured curvilinear panel was slightly higher than the capacity of the straight-fiber panel; the tensile load carrying capability was considerably less. The latter was caused by an adjustment of the curvilinear fiber paths to make them suitable for manufacturing. An investigation of the same panel

configuration by Nagendra et al. (1995) included manufacturing considerations based on advanced fiber placement. The fiber angle variation was defined in terms of uniform rational B-splines (NURBS) to avoid discrete fiber angle changes. Similar improvements in buckling load and tensile strength capability to those demonstrated by Hyer and Lee (1991) were found.

The concept of a continuous, linear fiber angle variation along one direction within a ply to tailor the stiffness of a composite laminate was introduced by Gürdal and Olmedo (1993). The resulting laminates are called *variable-stiffness laminates*. In Gürdal and Olmedo the fiber angle variation is defined using a small number of parameters: the fiber angle at the center of the laminate  $T_0$ , the fiber angle  $T_1$  at a characteristic distance  $d$  from the panel center, and the direction angle  $\phi$  determining the direction of variation. These variables are illustrated in figure 2.8.

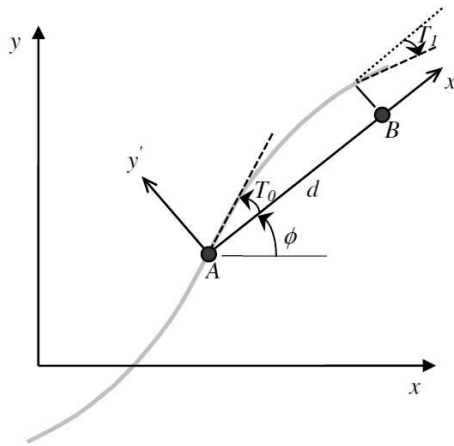


Figure 2.8: The parameters  $T_0$ ,  $T_1$ ,  $d$  and  $\phi$  determining the linear angle variation (Gürdal et al., 2008)

Gürdal and Olmedo (1993) used a closed-form solution to study the in-plane response of panels with a linear angle variation and the Rayleigh-Ritz method was applied to determine the lowest buckling load of these panels subjected to a uniform end displacement. Two cases of stiffness variation were considered: first, a stiffness variation in the direction of the load and second, a stiffness variation in the direction perpendicular to the load (Gürdal et al., 2008; Olmedo and Gürdal, 1993). The former resulted in improvements of up to 19 percent compared to the best constant-stiffness laminate due to the non-uniform distribution of transverse stresses induced by the non-uniform stiffness distribution. Improvements of up to 80 percent were achieved by varying the laminate stiffness in the direction perpendicular to the applied load due to a redistribution of the primary loads from the center section of the panel to the simply supported sides of the panel. This redistribution of loads is obtained by having a higher laminate stiffness at the edges of a panel than at the center, i.e. the fibers at a panel's edges are more aligned with the loading direction than the fibers at a panel's center, as shown in figure 2.9.

Olmedo and Gürdal (1993) also showed that variable-stiffness laminates could have a



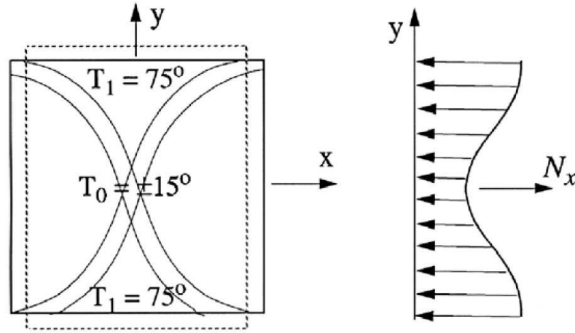


Figure 2.9: Load redistribution due to a fiber angle variation perpendicular to the loading direction (Gürdal et al., 2008)

wide range of different axial stiffness values for a given value of the buckling load, as opposed to constant-stiffness laminates, that have only one corresponding axial stiffness value. This is illustrated in figure 2.10 where the non-dimensional buckling load of variable-stiffness designs with values of  $T_0$  and  $T_1$  ranging from 0 to 90 degrees is plotted versus the non-dimensional axial stiffness of these designs. The bold light gray line represents the constant-stiffness designs.

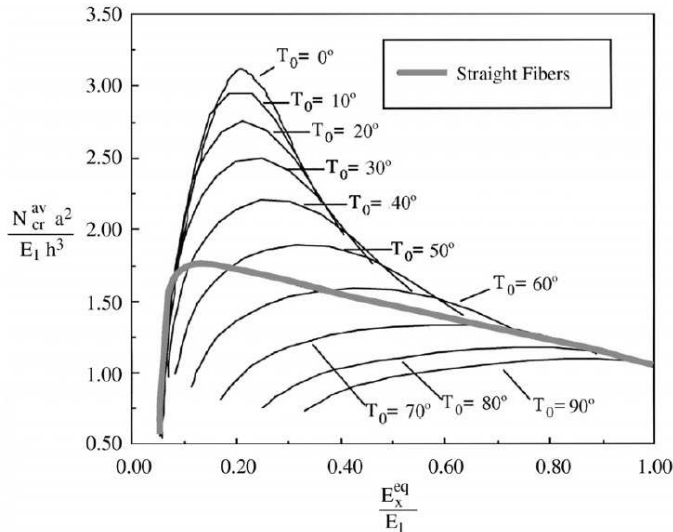


Figure 2.10: Buckling load versus axial stiffness for variable-stiffness designs (Gürdal et al., 2008)

Two methods for constructing a full variable-stiffness ply based on a curvilinear reference path have been proposed by Waldhart et al. (1996). In the *shifted* method a ply is constructed by shifting fiber paths identical to the reference path perpendicular to the direction of angle variation. In the *parallel* method subsequent fiber paths are created by placing

the new paths parallel to the original fiber path. The shifted method proved to be more efficient in redistributing loads than the parallel method and therefore higher improvements in buckling load were obtained with the shifted method. In addition, the curvature constraint imposed by the advanced fiber placement process was more restricting for parallel plies than for shifted plies, this reduces the feasible design space for parallel plies.

The work by Waldhart et al. (1996) led to the design and manufacture of two variable-stiffness panels using a Cincinnati Milacron VIPER advanced fiber placement machine by Tatting and Gürdal (1998). These panels were built to validate the manufacturability of tow steering through the application of curvilinear fiber paths. In one of the panels the course width was kept constant, resulting in a panel with overlapping courses, see figure 1.6. In the other panel the overlaps were eliminated by using the tow cut and restart capability of the fiber placement machine, so that the panel thickness was kept constant. The first type of panels where course width was kept constant, and the second where overlaps were eliminated, will be referred to as *overlap* panels and *tow-drop* panels, respectively.

The overlaps were included in a finite element model by Langley (1999) to assess their influence on the structural response of the variable-stiffness panel, because earlier analytical solutions did not take thickness buildup into account. A study of the in-plane response showed that overlaps act as integral stiffeners and that their influence should not be neglected.

Thermal and compression testing of the two variable-stiffness panels and one straight-fiber baseline panel, designed and manufactured by Tatting and Gürdal (1998), were conducted by Wu et al (2001; 2002). Improper shifting of identical plies during manufacturing caused the variable-stiffness panels to be asymmetric and unbalanced, resulting in a warped geometry after consolidation. The panel edges were forced straight during the compression test, and therefore thermal and mechanical pre-stresses were included in the nonlinear finite element analysis. A good match between the analytical and experimental results was found in the pre-buckling and near post-buckling range, confirming that variable-stiffness laminates can improve the buckling load of composite panels. Wu and Gürdal (2006, 2007) substantially improved the agreement between the predictions and the experimental results in the deep post-buckling regime by extending the finite element model to include the measured geometric imperfections and nonlinear material shear behavior.

After the first variable-stiffness panels were built, Tatting and Gürdal (2001) performed a second design study in which genetic algorithms were used in combination with a Rayleigh-Ritz solver to optimize a 20 ply rectangular variable-stiffness panel under axial compression, subjected to manufacturing constraints. The most promising designs were evaluated using STAGS finite element models that accurately represented the test conditions and geometries to decide upon the final designs for manufacturing and testing. Three configurations were analyzed: a panel without a hole, a panel with a small hole and a panel with a large hole. Improvements of more than 60 percent compared to the optimum constant-stiffness designs were shown with no appreciable increase in weight. The best variable-stiffness design was manufactured using a VIPER fiber placement machine (Tatting and Gürdal, 2002). Again panels with and without overlap were manufactured, in which identical plies were shifted (staggered) with respect to each other to distribute the overlaps and tow-drop areas over the panel, creating smoother load and thickness distributions. The effect of staggering on the thickness distribution can be seen in figure 2.11, where the number of layers is shown for a laminate without staggering, see figure 2.11(a), and for a laminate with staggering applied,

see figure 2.11(b) (Tatting and Gürdal, 2002).

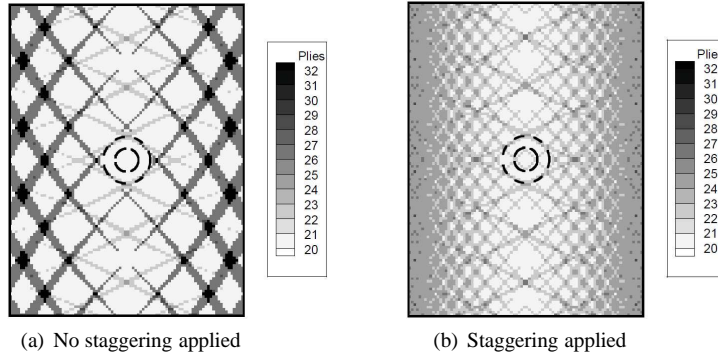


Figure 2.11: The effect of staggering on the thickness distribution of variable-stiffness laminates (Tatting and Gürdal, 2002)

Both the tow-drop and overlap panels were built based on the tow-drop design. An optimization using genetic algorithms together with a STAGS analysis, also performed by Tatting and Gürdal (2003), showed that the buckling load of overlap panels could be increased by another 30 percent if overlaps are taken into account in the optimization.

An experimental program for the rectangular variable-stiffness panels was led by Jegley et al. (2003), who showed that experimental buckling loads are significantly higher than buckling loads predicted using the STAGS finite element models of Tatting and Gürdal (2003). This was confirmed by Lopes et al. (2008) who simulated Jegley's experiments using the ABAQUS finite element code (ABAQUS, Inc., 2005). Lopes predicted the non-linear buckling load and the laminate strength according to the physically-based NASA LaRC04 failure criteria. Residual thermal stresses induced by the curing process were included in the analysis in a follow-up study by Lopes et al. (2007), which resulted in a close agreement between analytical and experimental buckling values. Additionally, Lopes et al. (2007) expanded the first-ply failure model to a continuum progressive-failure model, predicting the onset of damage and final failure within 10 percent of the experimental values.

Jegley et al. (2005) used some of the variable-stiffness panels, designed and manufactured by Tatting and Gürdal (2002), for additional testing. One configuration included a hole in the stiff section of the overlap panel, as opposed to having a hole in the soft section of the panel as it was designed. The optimization of overlap panels performed by Tatting and Gürdal (2003) demonstrated that the mechanism for improving the buckling load carrying capability of overlap panels with central holes could change from reinforcement of the edges, i.e. the dominating mechanism for tow-drop designs, to reinforcement of the panel center, depending on the hole size. In that case thickness buildup in the center of the panel causes the bending stiffness at the hole to increase such that it dominates the stress increase caused by the higher in-plane stiffness. The additional test by Jegley et al. (2005) was used to study this effect experimentally. The buckling response of the tested panel was dominated by the increased stress levels at the center and not by the increased bending stiffness due to the overlaps, such that the buckling load was not improved compared to the straight-fiber panel.

Jegley et al. (2005) also cut a square panel with a central hole from the manufactured variable-stiffness sheet and tested it in shear. The predictions showed a slight improvement in buckling load of the variable-stiffness panels over the straight-fiber panels. A good correlation between the analytical and experimental buckling load was found for the variable-stiffness panels, but not so good for the straight-fiber laminate. The experimental results showed a higher buckling load of the straight-fiber panel. An optimization to maximize the buckling load for shear loaded panels with a hole, carried out by Tatting and Gürdal (2003), showed that if the panels had been optimized for shear instead of in-plane compression, the tow-drop method would have resulted in a slight improvement of the buckling load and the overlap method would have increased the buckling load by more than 200 percent compared to the best straight fiber laminate.

The compression tests of the variable-stiffness panels by Wu et al. (2002) and Jegley et al. (2003) demonstrated that thermally induced stresses had a considerable, positive influence on the buckling load. Abdalla et al. (2009) found that the mechanism responsible for the improvement in buckling load carrying capability was the presence of tensile stresses at the center of the panel, induced by the curing process as a result of the non-uniform distribution of the thermal expansion coefficient across the panel. The tensile pre-stresses relieve some of the mechanical compressive stresses when an external load is applied, resulting in a higher buckling load carrying capacity. Abdalla et al. (2009) also showed that increasing the cure temperature increases the magnitude of the residual tensile stresses so that even larger improvements in buckling load are obtained.

Other efforts to improve the performance of composite panels by changing the internal fiber geometry have been made by Jones and Platts (1996). They applied a Michell structure geometry to reduce the stress concentrations around a pin-loaded hole and showed that considerable improvements were possible compared to panels made of 0/90 woven cloth.

In another study by Tosh and Kelly (2000) and Li et al. (2002a,b) the principal stress vectors or alternatively the principal load paths were used to determine the fiber trajectories in composite panels with the objective to increase the panel strength. The panels were manufactured by placing dry steered tows onto a tacky resin film and inserting them in between unidirectional or fabric plies. Subsequent testing showed that the specific strength of specimens with an open hole tested in tension increased by 62 percent (Tosh and Kelly, 2000), while the bearing strength in bolted joints increased by 169 percent (Li et al., 2002b). Panels with large cutouts that were reinforced by fibers following the maximum and minimum principal stress trajectories carried a shear load that was 37 percent higher compared to the quasi-isotropic baseline at a 3 percent weight penalty (Li et al., 2002a).

A near-field material orthotropy distribution was used by Huang and Haftka (2005); Huang et al. (2003) to maximize the strength of a composite plate with a hole based on the first-ply Tsai-Wu failure criterion. The steered plies were divided into 2 fields: a small concentric field near the hole in which the fiber angle was allowed to vary continuously, and a relatively large field away from the hole where the fiber angle was 0 degrees. The failure loads were maximized by iteratively alternating between a gradient-based search and a genetic algorithm to determine the optimum fiber angles. The optimum fiber angle pattern contained fiber angles that were almost tangent to the hole edge close to the hole and gradually changing fiber directions away from the hole to bridge with the far-field longitudinal fibers, thereby resembling the distribution of the principal stress orientations.

Huang and Haftka (2005) showed that a laminate with 6 identically steered plies doubled the load-carrying capacity of a  $[0, \pm 45]_S$  laminate with a hole. The strength improvement was reduced only slightly by combining  $\pm 45$  plies with two steered plies, while the robustness of the design was improved by the presence of the  $\pm 45$  degree plies.

A series of theoretical studies by Alhajahmad et al (2008a; 2008b; 2008c) focused on tailoring fuselage skin panels for pressure pillowling using curvilinear fibers. Panels were loaded with out-of-plane pressure loads and corresponding in-plane tensile loads to simulate the pressure pillowling problem and, in a second load step, in-plane compression loading was added. First, the panels were optimized for maximum strength based on the Tsai-Wu failure criterion, where the von Kármán plate equations were solved using the Rayleigh-Ritz method (Alhajahmad et al., 2008a). A nonlinear angle variation offered improvements of up to 26 percent for different aspect ratios compared to straight-fiber configurations due to a stress redistribution over the panel. In a follow-up study Alhajahmad et al. (2008c) expanded the work to panels with window cutouts, subject to the same loading conditions. Linear and nonlinear finite element analyses were performed using an ABAQUS-Python script. Considerable improvements in load carrying capacity were achieved compared to straight-fiber laminates with one designed layer, however, no improvements were found compared to a quasi-isotropic laminate. In addition, the buckling loads of the variable-stiffness panels were lower than those of the straight-fiber panels. An optimization of a laminate containing 2 variable-stiffness ply definitions showed that failure load could also be improved compared to the quasi-isotropic laminate, while buckling loads were comparable. Another study by Alhajahmad et al. (2008b) showed that the strength performance of panels subjected to pressure-pillowing loads improved even more by allowing 4 different variable-stiffness plies in the laminate, but in general this improvement was achieved at the expense of buckling load carrying capability. This study also showed that laminates that were optimal for maximum buckling load carrying capability failed at significantly lower loads than quasi-isotropic laminates.

Other examples of theoretical and numerical studies in which composite laminated panels are optimized by tailoring fiber orientations and thickness distributions are given in the work of Pedersen (1989; 1991), Banichuk et al. (1995), Duvaut et al. (2000), Parnas et al. (2003), Setoodeh et al (2004; 2006c; 2009) and Muc and Ulatowska (2010).

## Cylinders

The concept of tailoring material properties by varying fiber orientations with circumferential position in elliptical composite cylinders for the purpose of improving axial buckling load carrying capacity is discussed by Sun and Hyer (2008). The buckling load carrying capacity was improved by making the entire cylinder participate in the buckling deformations. The fiber angle variation with circumferential position was based on a simplified buckling analysis of circular composite cylinders. It was shown that improvements in buckling capacity could be achieved for both small and large cylinders, regardless of the boundary conditions applied. Moreover, material failure characteristics were not compromised by varying fiber orientation with circumferential position.

Elliptical composite cylinders were the subject of study by Khani et al. (2009b). A bi-symmetric linear fiber angle variation was used to study the compliance of elliptical cylinders parametrically under internal pressure and bending about the major axis. The

designs with linear angle variations did not show appreciable improvements over straight-fiber designs under internal pressure or bending, while small improvements were achieved for load cases combining internal pressure and bending.

Possible performance improvements of thin circular cylindrical shells using the variable-stiffness concept have been examined by Tatting (1998). Stress analysis and initial buckling estimates were formulated for a general variable-stiffness cylinder to be used in optimization studies. Two cases of loading and stiffness variation on short cylinders were selected to investigate the possible areas of improvements that the variable-stiffness concept might offer over constant-stiffness structures. In the first case Tatting considered was a cylinder with axial stiffness variation only, subject to constant loads of axial compression, pressure and torsion. The results for these load cases showed little improvement compared to traditional laminates, mainly due to the presence of a weak link area within the stiffness variation that carried the ultimate load. The second design problem involved a cylinder with a stiffness variation in circumferential direction subject to axial compression, pressure, torsion, bending or transverse shear. The most significant improvements in load-carrying capacity were found for cases that involve loads that also vary circumferentially, i.e. bending and shear forces. Tatting (1998) showed that the stiffness variation of the optimal designs contribute to increased performance in two ways: lowering the stresses in the critical areas through redistribution of the stresses; and providing a relatively stiff region that alters the buckling behavior of the structure.

Wu (2008) studied a composite cylindrical shell with circumferentially varying fiber orientations. The shell was intended to represent a fuselage section of an aircraft subjected to bending loads. As such Wu designed the variable-stiffness cylinders to resemble an I-beam, with 10 degree fiber angles in the keel and crown sections to resist bending and 45 degree fiber orientations on the side to resist shear in a  $[\pm 45, \pm \theta]_s$  layup. The change in fiber angle from the crown to the sides was such that the path curvature was constant and the complete ply was constructed according to the shifted ply method defined by Waldhart et al. (1996). Wu (2008) then analyzed a tow-drop and an overlap design for the described fiber angle variation using STAGS finite element models and compared them to an 8-ply quasi-isotropic baseline. The shell with overlaps showed improved buckling load capacity and higher bending stiffness for bending about the horizontal axis. No improvements were found for bending about the vertical axis. The tow-drop shell did not show improved bending stiffness or buckling load carrying capacity in either direction. Wu (2008) therefore evaluated an angle ply with an orientation smaller than 15 degrees at the keel and crown sections to improve the shell structural performance, showing that large increases in bending stiffness were possible for such a configuration.

Two variable-stiffness shells with the fiber angle varying from 10 degrees at the crown to 45 degrees at the side, back to 10 degrees at the keel were manufactured by Wu (2009) using an Ingersoll fiber placement machine. Manufacturability required small adjustments of the nominal circumferential spacing and fiber orientation angles of the curvilinear steered paths to better conform to the desired shell geometry and to minimize gaps in the tow-drop cylinder. The formation of puckers in the steered plies was suppressed by debulking the laminate between plies, reducing lay-down rate and increasing compaction force. Wu (2009) then performed post-fabrication surface surveys on the cured shells' inner and outer surfaces to determine their initial imperfections and thickness variations. The cured cross-sections of both shells vary along the length and are generally elliptical with the major

axis rotated 90 degrees between the shells with and without overlaps. The gaps between adjacent courses where tows were dropped on the tow-drop shell were more prominent than was predicted during the design. Testing of these shells is planned in the near future.

### Miscellaneous Structures

An integrated design and analysis system for use in preliminary through detailed design phases of a fiber-placed structure was developed by Schueler et al. (2004). The Steered Composites Analysis and Design System (SCADS) tool was used to model the tows, courses and plies of a fiber placed part. Analysis methods to quantify gaps, overlaps, and tow level properties were implemented in SCADS and the generation of files for use by finite element analysis packages was enabled. Three methods to define varying fiber orientations within plies were implemented. The first method is called the *band offset* method and is identical to the *parallel* method as introduced by Waldhart et al. (1996). The second method is the *fixed angle ply* method, where the ply consists of courses of which the paths are defined by a vector projected onto the placement surface, preserving tow orientations with respect to the direction vector. The last method introduced by Schueler et al. (2004) is the *laminated family ply* method in which fiber paths are mapped onto a given guiding ply, i.e. one of the two mentioned above, such that the angle between the fiber path and the closest tow in the original ply is constant, e.g. 45 or 90 degrees.

Hale et al. (2004) studied four simple test problems to investigate the possible payoffs of using fiber steering with conceptual design. The weight of these structures was minimized using recursive quadratic programming, while subject to a maximum-strain-first-ply-failure criterion, upper and lower ply thickness bounds and angle bounds. Both the fiber angle and layer thickness were allowed to vary. The steered laminates were then compared to quasi-isotropic laminates. The first test case was a square plate with a central circular hole under various loadings, for which improvements of up to 20 percent were achieved. An intermediate complexity wing subjected to aerodynamic loads was improved by 21 percent when only optimized for strength, while including buckling resulted in a 7 percent improvement. A cantilever rectangular panel under transverse loads was improved by 17 percent and a cantilever cylindrical tube subject to combined compression, torsion and bending was improved by 26 percent. After optimization of these four simple structures proved to be successful Hale et al. (2004) also optimized three representative aircraft structures using the fiber steering conceptual design. These were a representative of a regional jet's primary wing structure, subjected to aerodynamic loads and internal fuel loads at take-off, climb and landing, constrained by limits on the strength and maximum wing tip deflection; an aft pressure bulkhead under cabin pressure subject to strength constraints; and a representative horizontal stabilator of a tactical fighter subject to aerodynamic loads at 2 angle of attack positions with strength and buckling constraints. The weight reductions for these three cases were respectively 17 percent, 4 percent and 30 percent.

Temmen et al. (2006) tailored the fiber orientation within a selected layer of a composite laminate by aligning them as closely as possible to the direction of the principal stresses. The reduction of shear stresses in the structure caused an increase in load-carrying capacity. The developed method was used to optimize a preliminary version of the horizontal tail plane of an Airbus A340-500/600 fuselage structure, resulting in a 60% improvement in tension and a 79% improvement in compression, while the load carrying capacity for bending

decreased by 8%. The developed tool set included an optimization program to calculate the optimum fiber angle distribution and a program to generate the distribution of fiber rovings for manufacturing.

### 2.2.3 Stiffness Tailoring using Lamination Parameters

An alternative method for designing composite laminates with spatially varying stiffness properties is through the use of spatially varying lamination parameters, as opposed to designing fiber orientations and stacking sequences directly. Lamination parameters, first introduced by Tsai and Pagano (1968) and Tsai and Hahn (1980), provide a compact notation for the description of the stiffness properties of a laminate layout configuration. The A, B and D stiffness matrices of any laminate can be described as a linear function in terms of 12 lamination parameters, which can be reduced to 4 lamination parameters for balanced, symmetric laminates. The number of lamination parameters is independent of the number of layers such that the complexity of an optimization problem can be greatly reduced by using lamination parameters instead of optimizing a stacking sequence directly. Moreover, the feasible region of the lamination parameter design space is convex. The optimal stiffness design in terms of spatially varying lamination parameters provides an upper bound for the best design using plies with spatially varying fiber orientations, because lamination parameters represent the most general layup configuration possible. The stacking sequence can be constructed once the optimal lamination parameters are determined, see for example the work of Autio (2000) and Diaconu et al. (2002). The stacking sequence for a given set of lamination parameters is not unique, such that the designer has a range of suitable laminate designs to choose from.

#### Flat and Curved Panels

Some of the first to consider spatially varying lamination parameters for maximizing the stiffness design of laminated plates were Hammer et al. (1997). Two examples of panels subjected to in-plane loads were given for which lamination parameters were allowed to vary from point to point. In a second step the corresponding ply angles and thicknesses were determined.

Spatially varying lamination parameters were used by Setoodeh et al. (2005) for solving the classical minimum compliance design problem, for which optimization was performed with a feasible sequential programming solver. Cases of general, balanced symmetric laminates and balanced symmetric laminates with equal thickness layers were studied. A simplified feasible domain for laminates with equal thickness layers for an increasing number of layers was presented and a restricted problem was proposed that maintained the convexity of the design space for laminates with equal thickness layers. The compliance of the variable-stiffness design was shown to be reduced by 42 percent compared to the best constant stiffness design, both obtained using lamination parameters. Minimum compliance designs for both in-plane and out-of-plane loading were considered in a follow-up study by Setoodeh et al. (2006a). The computation of optimal laminate designs was performed using local rules based on optimality conditions. An investigation of a cantilever beam subjected to a uniform load showed that the variable-stiffness design using lamination parameters was significantly better than the constant-stiffness design using lamination parameter. Compar-



ison with the best configuration that was obtained using fiber angles as design variables showed a small improvement. Similar results were obtained for a simply supported and a clamped square plate subject to out-of-plane pressure. Abdalla et al. (2007) showed that also the fundamental frequency of composite panels can be significantly increased by allowing the lamination parameters to vary spatially.

An efficient design approach for variable-stiffness laminates under compressive loading in which lamination parameters were used as design variables was proposed by IJsselmuiden et al. (2010). Two examples were studied, yielding buckling load improvements of up to 189 percent with respect to quasi-isotropic laminates and up to 129 percent with respect to the best constant-stiffness laminate. A survey of the in-plane load distributions revealed that load redistribution is the primary mechanism responsible for improved buckling performance, confirming earlier findings of Hyer and Charette (1991) and Gürdal and Olmedo (1993). Additionally IJsselmuiden et al. (2010) showed that a variable-stiffness laminate with in-plane stiffness properties equivalent to a quasi-isotropic laminate could be designed to withstand more than twice the compressive load before buckling.

In a follow-up study IJsselmuiden et al. (2009a) used the same approach to study the behavior of a curved shell subject to an out-of-plane pressure load. The use of in-plane and out-of-plane lamination parameters resulted in a redistribution of membrane and bending stiffnesses, leading to smaller rotations about the hinged edges and smaller deflections in the center of the panel. Improvements between 70 and 80 percent were obtained for 3 different side-length-to-thickness ratios, using both in-plane and out-of-plane lamination parameters.

IJsselmuiden et al. (2009b) also combined thickness tailoring and in-plane stiffness tailoring to study the effect of adding thickness on the buckling performance of panels under in-plane compression as opposed to stiffness tailoring where the thickness is kept constant. Improvements in the order of 440 percent compared to quasi-isotropic designs were demonstrated. The thickness distribution forces the buckling modes towards the center of the panel, in addition to redistributing the in-plane loads.

A perturbation approach was used by Rahman (2009) to study the post-buckling behavior of variable-stiffness laminates designed for maximum buckling load under in-plane compression. The optimal designs, which were obtained by IJsselmuiden et al. (2010), typically exhibited two clustered buckling modes. The extent to which the post-buckling stiffness was reduced with respect to the pre-buckling stiffness depended on which of the clustered buckling modes prevailed. In most cases the mode with the lower post-buckling stiffness prevailed for the variable-stiffness panels, representing the lowest post-buckling stiffness, although the post-buckling stiffnesses of the variable-stiffness panels were equivalent or better than the post-buckling stiffness of the quasi-isotropic panel. Rahman (2009) also showed that the limit load and the ultimate load can be influenced by the pre-buckling stiffness, the post-buckling stiffness and the buckling load. In the future the post-buckling behavior could be taken into account in the optimization phase due to the availability of the perturbation method presented by Rahman.

The importance of residual thermal stresses on the buckling performance of variable-stiffness panels was demonstrated by IJsselmuiden et al. (2009c) for panels defined in terms of lamination parameters. Panels with thermal residual stresses corresponding to temperature steps of 0°C, -100°C and -200°C were optimized for buckling performance under in-plane compression. The predicted buckling loads of all variable-stiffness designs were increased when thermal residual stresses were present. An investigation of the three designs

over a range of applied thermal loads showed that designing a panel for a higher curing temperature resulted in a higher buckling load and that the range over which a design exhibits good buckling behavior increased when the panel was designed for higher curing temperatures. The maximum buckling load for a given design occurred at a temperature below the chosen design temperature. The improvements in buckling load were caused by tensile residual stresses that developed in the midsection of the panel due to non-uniform coefficients of expansion, as was also shown by Abdalla for curvilinear panel designs (Abdalla et al., 2009).

Methods that use parametric representation of the stiffness matrices, such as the lamination parameters, as design variables might lead to theoretically optimal designs, but their manufacturability requires another step in the design procedure. This step is the construction of actual stacking sequences that match the stiffness terms defined in the first step. A procedure for retrieving the stacking sequence of a variable-stiffness panel that was optimized in terms of lamination parameters was presented by Setoodeh et al. (2006b). They proposed a curve-fitting approach to match a given lamination parameter distribution in a least-square sense. The fiber paths following Lobatto polynomials were retrieved for a cantilever beam earlier optimized for minimum compliance (Setoodeh et al., 2006a). Setoodeh et al. (2006b) showed that, depending on the allowed fiber path curvature and the total number of plies, the compliance of the approximate fiber angle design could be within 2.5 percent of the compliance of the optimal laminate parameter design.

A continuation of the work by Blom et al. (2010) focused on the manufacturability of the obtained fiber paths if they were to be built by advanced fiber placement. The most important constraint, a limit on the in-plane curvature, was already taken into account while retrieving the fiber angle distribution. An aspect that was not taken into account in the laminate optimization and fiber path retrieval steps was the possibility of thickness buildup when fiber paths are not parallel. Blom et al. (2010) applied a streamline analogy to estimate the thickness buildup for a given fiber angle distribution, since increasing thickness can severely influence the response of a panel. It was shown that certain fiber angle distributions would lead to extremely large thickness buildups, which are undesirable in practical designs and which could not be reduced to a constant-thickness design using the tow cut and restart capability of an AFP machine. Discrete fiber courses were generated for a design for which the predicted maximum thickness was reasonable, to show the feasibility of the proposed method for generating manufacturable designs.

Hierarchical shape functions were used by Klees et al. (2009) to retrieve the fiber angle distributions for the rectangular panels optimized by IJsselmuiden for maximum buckling load (IJsselmuiden et al., 2010). A multi-objective optimization was performed with both maximization of the buckling load and minimization of the maximum fiber path curvature as design objectives. Pareto fronts for different numbers of design variables, i.e. the order of the shape functions and the number of layers, showed that increasing the order of the shape functions is more effective than increasing the number of variable-stiffness plies. Improvements of up to 106 percent in buckling load compared to the quasi-isotropic design were achieved, which is less than the 189 percent that was achieved with the lamination parameter design. The difference in improvement between the varying fiber angle design and the design using lamination parameters was expected, because lamination parameters represent the most general laminate possible.

Three different stacking sequence retrieval methods were used by Van Campen and Gürdal (2009) to find the fiber angle distribution of a balanced, symmetric laminate containing two different variable-stiffness ply definitions to match an optimal lamination parameter distribution. The reduction in buckling load compared to the optimal stiffness design in terms of lamination parameters was small when using the corresponding point method while regularizing the fiber angle variation.

A difficulty with using lamination parameters for the design of composite laminates is the incorporation of strength constraints, because the conventional failure prediction methods need information about the laminate stacking sequence. A conservative failure envelope expressed in terms of laminate strains was derived from the Tsai-Wu stress criterion by IJsselmuiden et al. (2008) and called the strain-equivalent Tsai-Wu criterion. The envelope guaranteed a failure-free region of the lamination parameter space, regardless of the fiber angle orientations present in the laminate. IJsselmuiden et al. (2008) showed that the envelope accurately represented the safety factor of practical laminates under in-plane loading, whereas the criterion might be too conservative for bending dominated problems. A comparison was made between strength-driven and stiffness-driven designs, which demonstrated that differences between the two optimal designs strongly depended on material properties and loading conditions. An increase in safety factor of up to 48 percent was obtained by strength-driven designs compared to stiffness-driven designs.

### Cylinders

The strain-equivalent Tsai-Wu failure criterion was applied in a strength optimization of a long elliptical cylinder using lamination parameters as design variables by Khani et al. (2009a). Approximately 90 percent improvement was found for a cylinder subjected to a combination of internal pressure and bending about the long axis of the ellipse compared to a quasi-isotropic composite cylinder. Khani et al. (2009b) also optimized elliptical cylinders for minimum compliance under combined internal pressure, axial loading, bending about the major axis and torsion by allowing the lamination parameters to vary around the circumference. The results showed that improvements of variable-stiffness designs over constant-stiffness designs rarely exceeded 10 percent for combined load cases, whereas improvements over quasi-isotropic cylinders of 238 percent were achieved for internal pressure and almost 260 percent for pure bending.

## 2.3 Context of Current Work

Numerical studies on composite laminate tailoring demonstrated that spatially varying the stiffness of a laminate has great potential for improving structural performance. Advanced fiber placement technology has made it possible to manufacture laminates with continuously varying fiber orientations in an automated fashion. A number of flat panels with continuously varying fiber orientations were produced to validate the numerical studies. Structural tests of the variable-stiffness panels confirmed that large improvements could be obtained compared to straight-fiber laminates, but also revealed challenges in the design and manufacturing of variable-stiffness panels.

At the time the research work covered by this thesis was started, the only research on variable-stiffness cylinders by varying fiber orientations had been conducted by Tatting (1998). His work is quite thorough, but does not include thickness buildups due to manufacturing using fiber placement in his predictions nor does it include experimental validations.

No work on tailoring of composite conical shells exists to the author's knowledge, although some research has been performed in which the manufacturing process was shown to cause stiffness variations along the surface of a conical shell (Baruch et al., 1994; Khatri and Bardell, 1995), and the influence of these stiffness variations on the structural performance was investigated (Goldfeld and Arbocz, 2004; Goldfeld et al., 2005; Wu and Lee, 2001). When a conical shell is manufactured by filament winding the laminate stiffness varies along the length of the cone, as shown by Baruch et al. (1994). Open conical shell panels that are manufactured by molding prepreg around a mandrel exhibit stiffness variation in circumferential direction, as proven by Khatri and Bardell (1995). Goldfeld and Arbocz (2004) and Wu and Lee (2001) demonstrated that the stiffness variations resulting from one of these manufacturing techniques render the assumption of constant stiffness that is often assumed in the analysis of laminated conical shells invalid, because for most cone geometries and fiber configurations the structural response is significantly different from that of a constant-stiffness shell.

The research described in this thesis is aimed to fill in some of the gaps that currently exist in the field of tailored conical and cylindrical shells, both numerically and experimentally. To this end the shifted ply method, introduced by Waldhart et al. (1996), will be applied to conical and cylindrical shells, because it is a straightforward way of defining variable-stiffness laminates and is readily made suitable for manufacturing with advanced fiber placement. Fiber paths will be formulated for conical and cylindrical shells, and their corresponding in-plane curvature will be derived for evaluation of the manufacturing constraint in terms of maximum curvature (chapter 3). Subsequently, a numerical optimization study of conical shells for maximum fundamental frequency will be performed (chapter 4) and the influence of the curvature constraint on the design will be demonstrated. A second design study will be focused on cylinders in bending, with the objective to select a variable-stiffness design for manufacturing and testing (chapter 5), after which the issues encountered during manufacturing of the selected variable-stiffness shell will be discussed (chapter 6). The results for two experiments that were conducted will be presented to show the validity of the analytical models used to predict the structural behavior of variable-stiffness shells (chapters 7 and 8). Finally, conclusions will be drawn about the contributions of the current work to the field of tailored composite shells and recommendations for future research will be made (chapter 9).

## Chapter 3

# Variable-Stiffness Laminate Definition

The variable-stiffness laminates discussed in this thesis are constructed of plies in which the fiber orientation is varied spatially. Spatial angle variation can be achieved in a wide variety of ways, even if only restricted to continuous fiber paths used in fiber placement. Methods will be given to define fiber paths to construct a full ply on the surface of a conical or cylindrical shell. The fiber orientation for these geometric shapes is defined as varying in only one direction, either axial or circumferential, such that the shifted course method introduced by Olmedo and Gürdal (1993) and defined in subsection 2.2.2 can be used to cover the shell surface. The stacking sequence of the laminate must be recoverable at any location to enable structural analysis, and therefore a description is given on how to track ply properties such as the local fiber orientation angle and the existence of overlaps in the laminate. Furthermore, four specific path definitions will be introduced for the conical and cylindrical shells, i.e. i) a geodesic path, ii) a constant angle path, iii) a path with a linear angle variation; and iv) a path with a constant curvature. Examples will be given for each of the path definitions and their manufacturability.

The generation of fiber paths and the tracking of ply properties will be described for three configurations: i) axial stiffness variation on a conical shell; ii) axial stiffness variation on a cylindrical shell; and iii) circumferential stiffness variation on a cylindrical shell. The circumferential stiffness variation on a conical shell was not included, because the shifted ply method can not be used to construct a ply which has a fiber angle that varies in the circumferential direction due to the variation of the circumferential length of a cone. Therefore a different approach has to be adopted for the construction of a ply and this was beyond the scope of this thesis.

### 3.1 Variable-Stiffness Laminate Construction

Fiber-placed variable-stiffness laminates can be constructed in different ways. The shifted method has first been presented by Olmedo and Gürdal (1993). This method is based on a one-dimensional angle variation, where a reference path is defined by the desired fiber angle

variation and is covered by a course. Subsequent courses are placed by shifting the reference course perpendicular to the direction of variation until the complete surface is covered. The shifted courses are not parallel, except for special cases, such as a constant angle path on a flat plate, resulting in gaps or overlaps between adjacent courses. Two courses with an angle variation as function of the horizontal coordinate are depicted in figure 3.1. They are shifted in the vertical direction. The effective course width,  $w_e$ , which is defined to be the course width in the direction of shift, varies with the fiber angle if the course width  $w$  is kept constant, as can be seen in figure 3.1(a). The amount of shift is chosen to be smaller than the minimum effective course width,  $w_{e,\min}$ , when gaps are undesirable. The gaps that exist in figure 3.1(b) are then avoided and overlaps are formed instead, see figure 3.1(a). In many situations however, overlaps are also undesired. This can be solved by using the tow cut/restart capability of the machine such that a constant thickness ply is created. The tows are cut on both sides of the courses in figure 3.1(c). It is also possible to make the tow cuts on one side of the course.

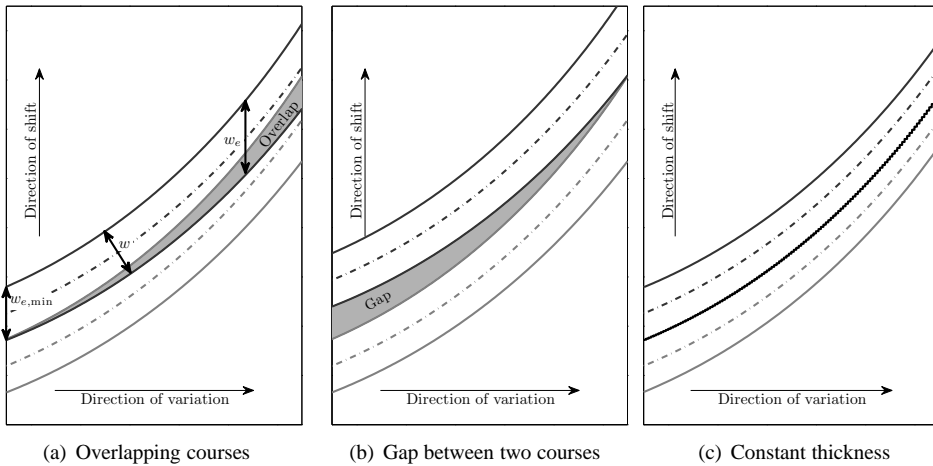


Figure 3.1: Laminate construction by shifting courses

A second method to define a variable-stiffness ply is the parallel method, introduced by Waldhart et al. (1996). With the parallel method one main course is placed on the surface and neighboring courses are placed parallel to the main course until the complete surface is filled. This method has the following disadvantages. First, there is less control over the fiber angle distribution than with the shifted method, because only the fiber angle orientation of the first course is actively controlled. Second, the curvature of a parallel course becomes infinite when the in-plane curvature of the original course is large or when a large surface needs to be filled, such that the placement of additional parallel courses can become impossible. Finally, parallel courses intersect and cause discontinuous angle distributions on surfaces that loop or close into a continuous surface like cylinders, cones or spheres.

The streamline method developed by Blom et al. (2010) is a third method used to construct a ply with spatially varying fiber angles, this can be used to generate fiber courses for a given two-dimensional fiber angle distribution. It is based on a streamline analogy and takes into account desired boundary conditions to predict overlaps or to estimate the amount

of tow cutting required to obtain a constant-thickness ply. The streamline method can be applied to flat plates, singly curved open surfaces and cylinders, but is rather complicated and computationally expensive for one-dimensional angle variations. The shifted method introduced by Olmedo and Gürdal (1993) was used in the current research.

## 3.2 Paths on Conical and Cylindrical Shells

A general representation of a conical shell will be defined first, to make the theoretical path definitions that will be derived as widely applicable as possible. Then equations will be derived that define the in-plane curvature for an arbitrary fiber path on a generic cone surface. Finally, the expressions will be simplified for cylindrical shells.

### 3.2.1 Geometry of a Conical Shell

A three-dimensional representation of the geometry of a conical shell is shown in figure 3.2. The generalized coordinates for a thin conical shell are the longitudinal distance  $x$ , which runs along the surface starting from the small radius of the shell, and the circumferential angle  $\theta$ , which is measured in the indicated direction with  $\theta = 0^\circ$  at the positive  $Z'$ -axis. The basic parameters used to define the shell are the cone angle  $\alpha$  and the small and large

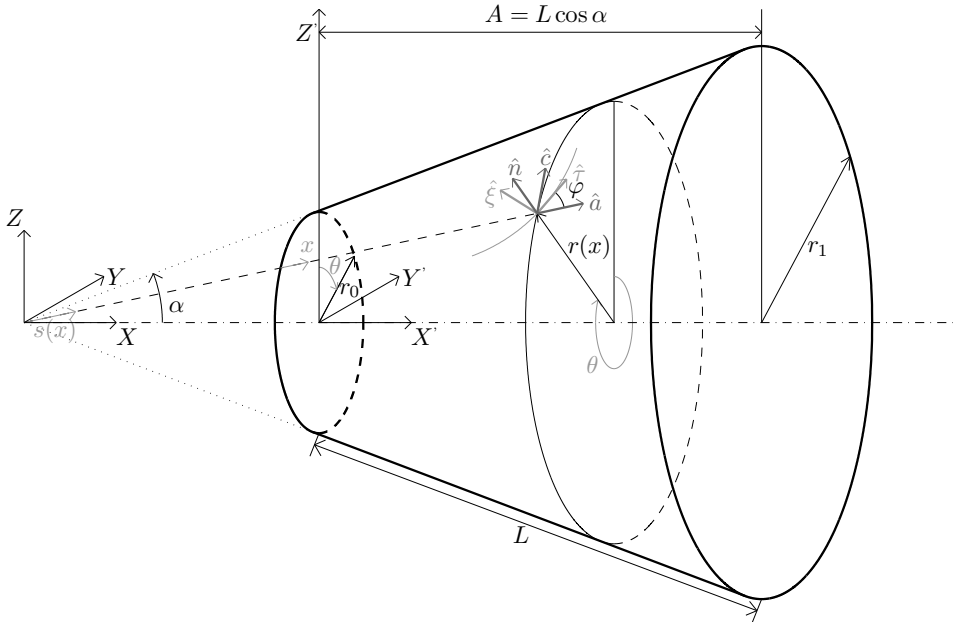


Figure 3.2: Cone geometry

radii at the two ends,  $r_0$  and  $r_1$ , respectively. Alternatively, the axial length  $A$  or the length along the surface  $L$  could be defined, together with the two radii  $r_0$  and  $r_1$ . The cone angle

$\alpha$  can then be expressed in terms of these lengths using the following relations:

$$\tan \alpha = \frac{r_1 - r_0}{A} \quad \text{or} \quad \sin \alpha = \frac{r_1 - r_0}{L} \quad (3.1)$$

The radius  $r(x)$ , which is the perpendicular distance from the axis of revolution to a point on the shell, varies linearly for a conical shell:

$$r(x) = r_0 + x \sin \alpha \quad (3.2)$$

The conical longitudinal surface coordinate  $s(x)$  is defined by measuring the distance from the cone vertex to a point on the surface:

$$s(x) = \frac{r(x)}{\sin \alpha} = x + \frac{r_0}{\sin \alpha} \quad (3.3)$$

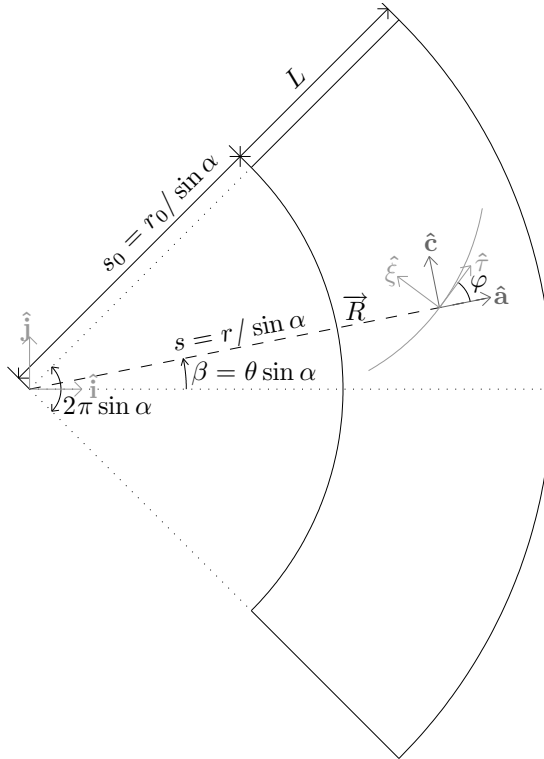


Figure 3.3: Developed cone configuration

The unit vectors for the longitudinal and circumferential surface directions,  $\hat{a}$  and  $\hat{c}$  and the surface normal  $\hat{n}$  will be used in the fiber path definitions, in addition to the rectangular coordinate system  $\{X, Y, Z\}$  shown in figure 3.2. A two-dimensional view and definition of



the cone is used for visualization and derivation purposes. The two-dimensional representation of the three-dimensional cone, see figure 3.3, was obtained by performing an imaginary cut along the longitudinal line at  $\theta = 180^\circ$  and developing the surface. The surface coordinates that correspond to the developed configuration are the radial distance  $s$ , which is the same as the longitudinal surface coordinate  $s$  in the three-dimensional representation, and the circumferential coordinate  $\beta = \theta \sin \alpha$ .

Note that lengths remain the same for both geometrical representations due to the zero Gaussian curvature of a conical surface. This can be seen by the expressions for differential lengths for the unrolled configuration.

$$dx = ds \quad r(x)d\theta = sd\beta \quad (3.4)$$

### 3.2.2 Paths on the Shell Surface

General expressions are required for the orientation and curvature of a fiber path contained on the surface of the conical structure, such that a feasible ply can be constructed by laying down multiple paths. The coordinates  $\{x, \theta\}$  will be used for the derivations below. The fiber orientation angle, expressed as  $\varphi$ , is defined as the angle between the longitudinal surface direction  $\hat{a}$  and the tangent to the path  $\hat{\tau}$ , see figures 3.2 and 3.3. The fiber angle can be a function of either the longitudinal coordinate  $x$  or the circumferential coordinate  $\theta$ . The fiber orientation angle, using geometrical formulas, is expressed as:

$$\tan \varphi = r(x) \frac{d\theta}{dx} \quad (3.5)$$

The path tangent vector in terms of the surface vectors is:

$$\hat{\tau} = \cos \varphi \hat{a} + \sin \varphi \hat{c} \quad (3.6)$$

The curvature of the path can be defined once the tangent vector is known:

$$\vec{\kappa} = \frac{d\hat{\tau}}{dl} = \frac{d\hat{\tau}}{dx} \frac{dx}{dl} \quad (3.7)$$

where  $dl$  represents an infinitesimal arc length along the fiber path. Following the derivations given in appendix A this results in:

$$\begin{aligned} \vec{\kappa} &= \left[ \frac{d\varphi}{dx} \cos \varphi + \frac{\sin \alpha \sin \varphi}{r(x)} \right] \hat{\xi} + \left[ \frac{-\cos \alpha \sin^2 \varphi}{r(x)} \right] \hat{n} & \text{if } \varphi = \varphi(x) \\ &= \left[ \left( \frac{d\varphi}{d\theta} + \sin \alpha \right) \frac{\sin \varphi}{r(x)} \right] \hat{\xi} + \left[ \frac{-\cos \alpha \sin^2 \varphi}{r(x)} \right] \hat{n} & \text{if } \varphi = \varphi(\theta) \end{aligned} \quad (3.8)$$

where  $\hat{\xi}$  represents the in-plane vector normal to the fiber path and  $\hat{n}$  represents the vector normal to the cone surface. Inspecting equation 3.8 for known configurations, such as flat plates ( $\alpha = 90^\circ$ ) and cylinders ( $\alpha = 0^\circ$ ), the first term turns out to be the in-plane component of the curvature. Envisioning the head of a tow-placement machine moving along a surface, this in-plane curvature dictates the amount of steering that is required to follow the given path. Conversely, the second term represents the curvature in the direction normal to the

surface. Again using the tow-steering analogy, this curvature represents the change of the mandrel surface as the conical part is rotated during fabrication. That is, this curvature represents a different degree of freedom of the tow-placement machine than the in-plane steering of the tows. The first term will be referred to as the curvature,  $\kappa$ , during design, since it relates to the curvature constraint discussed in subsection 2.1.2. The value of the curvature depends on the variation of the fiber orientation and on the cone geometry:

$$\begin{aligned}\kappa(x) &= \frac{d\varphi}{dx} \cos \varphi(x) + \frac{\sin \alpha \sin \varphi(x)}{r(x)} & \text{if } \varphi = \varphi(x) \\ \kappa(x, \theta) &= \left( \frac{d\varphi}{d\theta} + \sin \alpha \right) \frac{\sin \varphi(\theta)}{r(x)} & \text{if } \varphi = \varphi(\theta)\end{aligned}\quad (3.9)$$

Equation 3.9 can be simplified when the shell is a cylinder the radius  $R$  is constant and the cone angle is zero, such that it is given by:

$$\begin{aligned}\kappa(x) &= \frac{d\varphi}{dx} \cos \varphi(x) \\ \kappa(\theta) &= \frac{d\varphi}{Rd\theta} \sin \varphi(\theta)\end{aligned}\quad (3.10)$$

### 3.3 Ply Construction and Property Tracing

General expressions for constructing variable-stiffness plies on conical and cylindrical shells are derived in this section. A distinction will be made between fiber paths with axial and circumferential angle variation. The axial angle variation is applicable to both general conical shells and cylinders, while the circumferential angle variation is only derived for cylindrical shells. The determination of the exact stacking sequence of the laminate at a specific location will also be explained.

#### 3.3.1 Axial Angle Variation on Conical Shells

The first step in constructing a variable-stiffness ply is to define a feasible fiber path to be followed by the centerline of the machine head. This fiber path is governed by the fiber orientation angle  $\varphi(x)$  and is defined by the three-dimensional circumferential coordinate  $\theta(x)$ , or alternatively by the two-dimensional circumferential coordinate  $\beta(s)$ , see figure 3.3. These are related by:

$$\begin{aligned}s &= s_0 + x \\ \beta &= \theta \sin \alpha\end{aligned}\quad (3.11)$$

A complete ply can be constructed by laying down multiple courses next to each other. A neighboring course is found by rotating the original course over an offset angle,  $\Delta\theta$ , due to the axisymmetric nature of the cone. This offset angle depends on the number of courses,  $N$ , that is used to build up a ply:

$$\Delta\theta = \frac{2\pi}{N}\quad (3.12)$$

Alternatively, the offset angle can be expressed in the two-dimensional coordinate  $\Delta\beta$ :

$$\Delta\beta = \Delta\theta \sin \alpha = \frac{2\pi \sin \alpha}{N} \quad (3.13)$$

Complete coverage of the cone by one ply was desired for the current research, while a minimum number of courses was used to minimize production time. This implied that at every longitudinal location, the number of courses multiplied by the width of the course in the circumferential direction, which was defined as the effective head width,  $w_e$ , needed to be at least as large as the local circumference. The effective course width differs from the physical width of the course,  $w$ , due the non-zero fiber orientation and the cone angle. The course width can be equal to the head width of the tow-placement machine  $\bar{w}$  or, if tows are dropped, smaller than the machine head width. The analysis needed to find the effective course width will be shown later in this section. The condition for complete coverage of the cone surface is represented by the following equation:

$$Nw_e \geq 2\pi r(x) \quad 0 \leq x \leq L \quad (3.14)$$

The minimum number of courses, which has to be an integer value, is defined by:

$$N_{\min} = \left\lceil \frac{2\pi r(x)}{w_{e,\min}} \right\rceil \quad 0 \leq x \leq L \quad (3.15)$$

where the  $\lceil \cdot \rceil$  represents a function that rounds the real number to the nearest higher integer value.

It is necessary to find the course edges,  $\beta_l$  and  $\beta_r$ , shown in figure 3.4, to calculate the effective course width. The coordinates of the course edges can be found by vector analysis if the course width at one side of the central path is known. The machine head extends perpendicular to the fiber path and therefore the unit in-plane normal vector  $\hat{\xi}$ , see figure 3.3, should be multiplied by the course width at one side of the central path,  $p$  ( $-\frac{\bar{w}}{2} \leq p \leq \frac{\bar{w}}{2}$ ) and added to the vector pointing to the central path (subscript  $c$ ). Both the vector pointing to an arbitrary point on the course and the normal vector at that point can be expressed in rectangular coordinates using the geometry of figure 3.3:

$$\begin{aligned} \vec{R}_c &= s_c \cos \beta_c \hat{i} + s_c \sin \beta_c \hat{j} \\ \hat{\xi} &= -\sin(\beta_c + \varphi_c) \hat{i} + \cos(\beta_c + \varphi_c) \hat{j} \end{aligned} \quad (3.16)$$

The edges (subscript  $e$ ) of a course with a finite width  $p$  can then be found as:

$$\vec{R}_e = [s_c \cos \beta_c - p \sin(\beta_c + \varphi_c)] \hat{i} + [s_c \sin \beta_c + p \cos(\beta_c + \varphi_c)] \hat{j} \quad (3.17)$$

The corresponding edge coordinates  $s_e$  and  $\beta_e$  are:

$$s_e = \sqrt{s_c^2 + p^2 - 2ps_c \sin \varphi_c} \quad (3.18)$$

$$\tan \beta_e = \frac{s_c \sin \beta_c + p \cos(\beta_c + \varphi_c)}{s_c \cos \beta_c - p \sin(\beta_c + \varphi_c)} \quad (3.19)$$

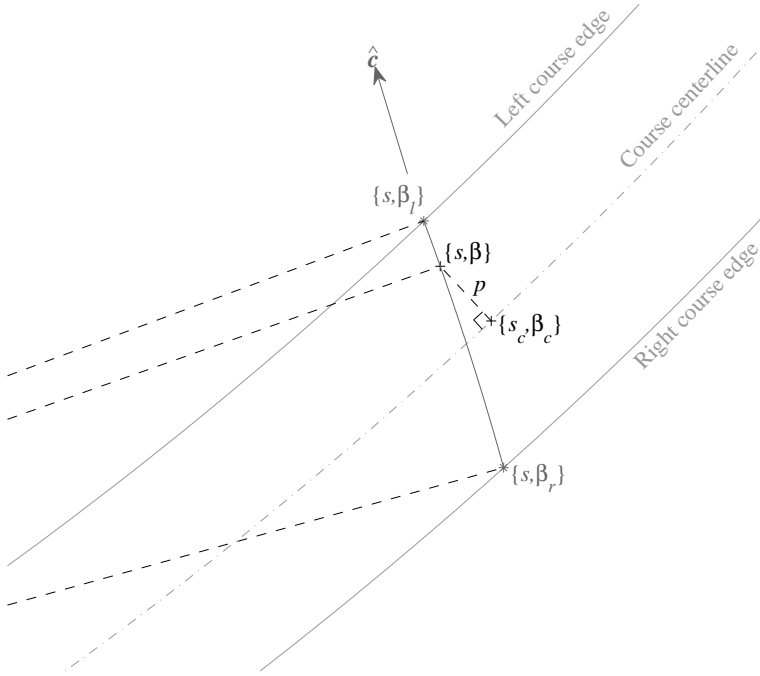


Figure 3.4: Course edges

In these two equations  $s_c$  and  $\beta_c$  represent a point on the centerline, which is defined by the path definition. The edge coordinates  $\beta_l(s)$  and  $\beta_r(s)$  are needed to find the effective course width at an arbitrary location  $s$ . The effective course width is represented by the line that connects  $\{s, \beta_l\}$  and  $\{s, \beta_r\}$  in figure 3.4. The distances between the central path and the course edges for a laminate with a constant course width are given, namely  $p_l = \frac{\bar{w}}{2}$  and  $p_r = -\frac{\bar{w}}{2}$ . The corresponding coordinate on the central path  $s_c$  can be solved for each edge from equation 3.18, which is then substituted in equation 3.19 to find  $\beta_l(s)$  and  $\beta_r(s)$ . The effective course width is related to these edge coordinates by:

$$w_e = s(\beta_l - \beta_r) \quad (3.20)$$

The minimum number of courses required to cover the complete cone surface can be determined using equation 3.15 once the effective course width is calculated for every location along the length of the cone.

Successive courses will overlap when the course width is kept constant and no gaps are allowed between courses, unless the courses are parallel (Tatting and Gürdal, 2002). An alternative is to use the tow cutting and restarting capabilities of the tow-placement machine to achieve a constant thickness ply. Consequently, the course width  $w$ , or actually even  $p_l$  and  $p_r$ , are a function of location. More control over the overlap between courses is also possible by having a course width which is in-between the one needed for constant thickness and the maximum course width. An example of the thickness buildup for a  $\pm\varphi(x)$  overlap

layer with constant course width is shown in figure 3.5.

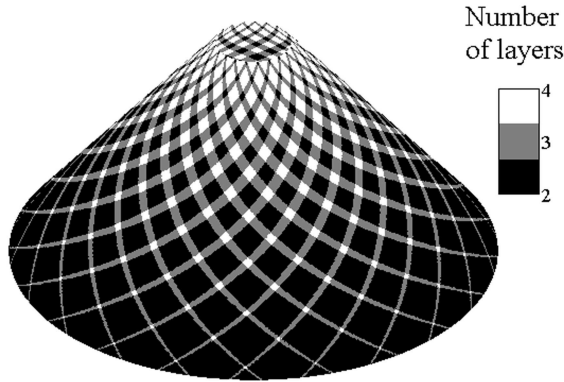


Figure 3.5: Number of layers of an overlap laminate, consisting of two plies with opposite orientations

When calculating laminate properties it is necessary to know the number of layers present and the fiber orientation angle. A formulation that can be used to determine the local fiber orientation per layer is given below, see equations 3.21 through 3.25.

The machine head is perpendicular to the local fiber orientation when a course is laid down. Consequently, every point on a line perpendicular to the fiber direction, e.g.  $\{s, \beta\}$  in figure 3.6, has the same orientation as the point at the centerline of the machine head,  $\{s_c, \beta_c\}$ . Moving away from the course centerline changes the  $\beta$ -coordinate with respect

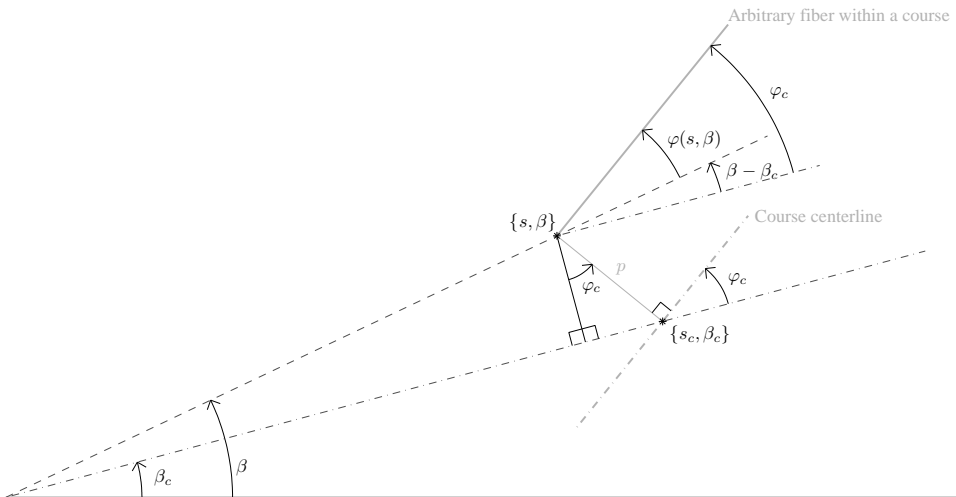


Figure 3.6: Course geometry

to the  $\beta$ -coordinate of the centerline and the longitudinal surface direction  $\hat{a}$  also changes. Therefore, the fiber angle of a point that does not lie on the centerline deviates from  $\varphi(s)$  and needs to be calculated. In other words, the fiber orientation at an arbitrary point is a

function of both  $s$  and  $\beta$ , instead of only a function of  $s$ . The  $s$ -coordinate ( $= s_c$ ) that is crossed by the center of the machine head at the moment that the fiber at  $\{s, \beta\}$  is laid down needs to be determined first before this angle  $\varphi(s, \beta)$  can be found. Simple geometry is used to find the desired equation. Equations 3.21 and 3.22 can be derived from figure 3.6, where  $p$  is defined as the distance to the central path rather than the course width at one side of the central path.

$$s_c \cos \beta_c - p \sin(\beta_c + \varphi_c) = s \cos \beta \quad (3.21)$$

$$s_c \sin \beta_c + p \cos(\beta_c + \varphi_c) = s \sin \beta \quad (3.22)$$

The perpendicular distance  $p$  is also derived from the trigonometric relations in figure 3.6:

$$p = \frac{s \sin(\beta - \beta_c)}{\cos \varphi_c} \quad (3.23)$$

Finally, by combining equation 3.23 with either equation 3.21 or equation 3.22, the relation between  $s$ ,  $\beta$  and  $s_c$  becomes the following:

$$s \cos(\beta_c + \varphi_c - \beta) = s_c \cos \varphi_c \quad (3.24)$$

This equation can be solved for  $s_c$  since both  $\beta$  and  $\varphi$  are functions of  $s$ . The fiber angle at  $\{s, \beta\}$  differs from the fiber angle at the origin as can be seen from figure 3.6. This deviation is caused by the curved surface and results in the following local fiber orientation  $\varphi(s, \beta)$ :

$$\varphi(s, \beta) = \varphi_c + \beta_c - \beta \quad (3.25)$$

Equations 3.23 and 3.24 can also be used to determine the course width at one side of the centerline if the desired course boundaries are known. An example could be a constant thickness ply, where the boundary is chosen to lie exactly in-between the centerlines of two adjacent courses. Then,  $s$  and  $\beta$  are known and  $p$  is the course width at one side of the central path that is needed to obtain the prescribed boundary. In reality the course width is not a continuous function, because a course is built up from individual tows so that the course width has a discrete change when a tow is dropped or restarted. Small triangular holes or overlaps occur, depending on the position of tow cutting chosen by the designer. For simplicity, these deficiencies are not taken into account when ply properties are traced, thereby a smooth boundary is assumed.

A ply is made by offsetting the basic path over an angle  $n\Delta\beta$ , given by equation 3.13, where  $n$  is an integer number between 0 and  $N-1$  identifying each course, and  $\Delta\beta$  is the offset angle between two adjacent courses. The course with  $n=0$  is assumed to be the basic course defined by  $\beta_c(s_c)$ , such that  $\beta_c^n(s_c) = \beta_c^0(s_c) + n\Delta\beta$ . Property tracing as described above is only possible when it is known in which course the specified point  $\{s, \beta\}$  is located. The course identifier  $n$  can be found by:

$$n = \left\lfloor \frac{\beta - \beta_r(s)}{\Delta\beta} \right\rfloor \quad (3.26)$$

where the  $\lfloor \cdot \rfloor$  function rounds the real number to the nearest smaller integer number.

Each point in a constant-thickness ply with tow drops belongs to a unique course, but

in a ply with overlap an arbitrary point could be part of multiple courses and the course numbers of all the courses have to be determined. The order in which courses overlap depends on the order in which the courses are laid down during manufacturing. A regular overlap sequence is assumed, such that the first course identifier is found by equation 3.26, while the presence of any additional courses is found by increasing an integer  $k$ , starting from 1, such that:

$$n_{k+1} = n - k \quad (3.27)$$

provided the following condition is fulfilled:

$$\beta_r \leq \beta - (n - k)\Delta\beta \leq \beta_l \quad (3.28)$$

The procedure for finding the fiber angle can be followed for every layer once the course numbers are identified. Scanning all plies successively and using the order in which the courses are laid down during manufacturing provides the local stacking sequence, so that the local stiffness matrix can be calculated.

### 3.3.2 Axial Angle Variation on Cylindrical Shells

The coordinate transformation from  $\{x, \theta\}$  to  $\{s, \beta\}$  is not valid for a cylindrical shell, because  $\alpha = 0$ . The developed cylinder surface becomes a rectangle and therefore a rectangular coordinate system is used. Furthermore, the radius is constant such that  $r(x)$  becomes  $R$ . Now the vector pointing to an arbitrary point on the fiber path is defined by:

$$\vec{R}_c = x_c \hat{i} + R\theta_c \hat{j} \quad (3.29)$$

and the path normal vector is:

$$\vec{\xi} = -\sin \varphi \hat{i} + \cos \varphi \hat{j} \quad (3.30)$$

such that the vector pointing to the course edge becomes:

$$\vec{R}_e = (x_c - p \sin \varphi_c) \hat{i} + (R\theta_c + p \cos \varphi_c) \hat{j} \quad (3.31)$$

The left and right circumferential coordinates of the course need to be determined at a given  $x$ -location to find the effective head width  $w_e$ , defined by:

$$w_e = R(\theta_l - \theta_r) \quad (3.32)$$

The following example is given to illustrate the procedure:

#### Example

Determine  $w_e$  at  $x = 0$

Given:  $\varphi(x) = \phi$ ,  $p_l = \frac{w}{2}$ ,  $p_r = -\frac{w}{2}$  and  $\theta_0 = 0$

1. Determine  $\theta_l$ :

- (a) Determine  $x_c$  and  $\varphi(x_c)$  for  $x_e = x$  and  $p = \frac{w}{2}$ :

$$x_e = x_c - p \sin \varphi(x_c)$$

gives

$$x_c = x_e + \frac{w}{2} \sin \phi$$

and

$$\varphi(x_c) = \phi$$

- (b) Calculate  $\theta_c$ :

$$\frac{d\theta}{dx} = \frac{\tan \varphi(x)}{R}$$

and

$$\theta_0 = 0$$

give

$$\theta_c = \frac{x_c \tan \phi}{R} = \frac{x + \frac{w}{2} \sin \phi}{R} \tan \phi$$

- (c) Calculate  $\theta_e$ :

$$\theta_e = \theta_c + \frac{p \cos \varphi_c}{R} = \frac{x \tan \phi}{R} + \frac{w}{2R} \sin \phi \tan \phi + \frac{w}{2R} \cos \phi$$

Simplifying this expression results in:

$$\theta_l = \theta_e = \frac{x \tan \phi}{R} + \frac{w}{2R \cos \phi}$$

2. Determine  $\theta_r$  following the same steps as for  $\theta_l$ , now with  $p = -\frac{w}{2}$ :

$$\theta_r = \frac{x \tan \phi}{R} - \frac{w}{2R \cos \phi}$$

3. Calculating the effective head width:

$$w_e = R(\theta_l - \theta_r) = R \left[ \left( \frac{x \tan \phi}{R} + \frac{w}{2R \cos \phi} \right) - \left( \frac{x \tan \phi}{R} - \frac{w}{2R \cos \phi} \right) \right] = \frac{w}{\cos \phi}$$

The example shows that the effective course width for a path with a constant fiber orientation on a cylinder is equal to  $\frac{w}{\cos \phi}$ .

The procedure for calculating the exact fiber angle orientation for an arbitrary point is similar to the one explained above for the conical shell. In this case the arbitrary coordinates



are linked to the coordinates of the central path by the two parts of equation 3.31:

$$\begin{aligned} x &= x_c - p \sin \varphi_c \\ \theta &= \theta_c + \frac{p \cos \varphi_c}{R} \end{aligned} \quad (3.33)$$

Combining the two equations above to exclude  $p$  gives:

$$(x - x_c) \cos \varphi_c = -R(\theta - \theta_c) \sin \varphi_c \quad (3.34)$$

Both  $x$  and  $\theta$  are known and  $\varphi_c$  and  $\theta_c$  are functions of  $x_c$  so that equation 3.34 can be solved for  $x_c$ . Subsequently, the fiber orientation  $\varphi_c$  can be calculated and if the distance to the central path  $p$  is desired, it can be solved from either one of the equations 3.33 by substituting  $x_c$ ,  $\varphi_c$  and  $\theta_c$ .

A ply is generated by offsetting the basic path over an angle  $n\Delta\theta$ ,  $\Delta\theta = \frac{2\pi}{N}$ , where  $n$  is an integer number between 0 and  $N-1$ , identifying each course and  $\Delta\theta$  is the offset angle between two adjacent courses. The course with  $n=0$  is assumed to be the basic course defined by  $\theta_c(x_c)$ , such that  $\theta_c^n(s_c) = \theta_c^0(s_c) + n\Delta\theta$ . The course identifier is found by:

$$n = \left\lfloor \frac{\theta - \theta_r(x)}{\Delta\theta} \right\rfloor \quad (3.35)$$

Overlapping courses are identified by reducing the course number  $n$  by  $k$  starting at  $k=1$  as with the cone, such that:

$$n_{k+1} = n - k \quad (3.36)$$

provided that:

$$\theta_r \leq \theta - (n - k)\Delta\theta \leq \theta_l \quad (3.37)$$

The procedure is repeated for increasing values of  $k$  until the condition in equation 3.37 is no longer satisfied.

### 3.3.3 Circumferential Angle Variation on Cylindrical Shells

The orientation for a fiber path on a cylindrical shell with a circumferentially varying fiber orientation is defined as:

$$\varphi = \varphi(\theta) \quad (3.38)$$

The definition of the circumferential coordinate  $\theta$  and the fiber angle orientation  $\varphi$  are shown in figure 3.7. Again, a rectangular coordinate system is used for the developed cylinder surface so that the vector pointing to the edges is defined by equation 3.31:

$$\vec{R}_e = (x_c - p \sin \varphi_c) \hat{i} + (R\theta_c + p \cos \varphi_c) \hat{j} \quad (3.39)$$

Now the effective course width is defined by:

$$w_e = x_l - x_r \quad (3.40)$$

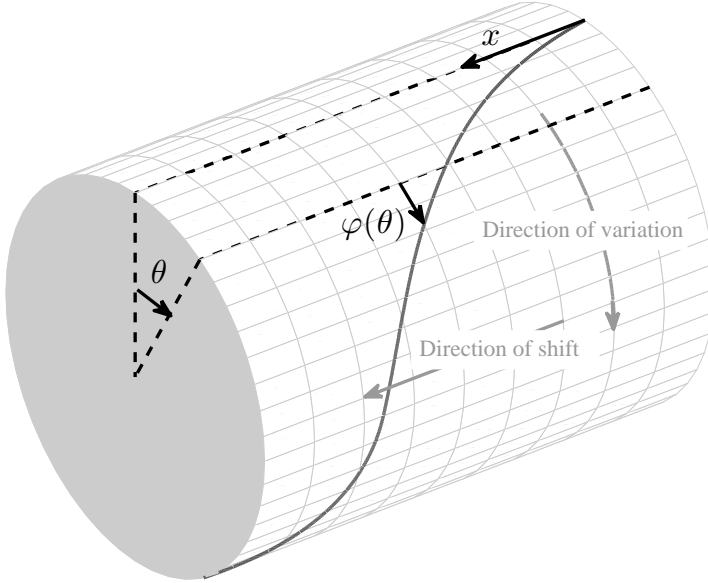


Figure 3.7: Fiber angle definition for circumferential variation on a cylinder

Therefore  $\theta_c$  and  $\varphi_c$  need to be determined first, after which  $x_c$  and finally  $x_e$  can be found for a given head width.

The variation in the circumferential direction has to be periodic over  $2\pi$  to obtain a continuous angle variation. Moreover, the discrete courses also need to be periodic. This is achieved by tailoring the amount of shift along the axial direction to the length at which a fiber path would wrap around the cylinder if the cylinder was sufficiently long, i.e. at  $x = L_{2\pi}$ , shown in figure 3.8. The original path is repeated at the point where the path wraps around the cylinder and thus a discrete number of courses is needed within the distance  $L_{2\pi}$  to produce a regular pattern. The minimum number of courses required for full coverage of the surface is:

$$N_{\min} = \left\lceil \frac{L_{2\pi}}{w_{e,\min}} \right\rceil \quad (3.41)$$

such that the amount of shift becomes:

$$\Delta x = \frac{|L_{2\pi}|}{N} \quad (3.42)$$

The path segments that are present on a short cylinder are based on the original path, even if the cylinder is not long enough for the original path to wrap around, e.g. the black part shown in figure 3.8. Therefore the number of courses still depends on the periodic length.

Equation 3.34 of the axial angle variation can be used to determine the fiber angle:

$$(x - x_c) \cos \varphi_c = -R(\theta - \theta_c) \sin \varphi_c \quad (3.43)$$

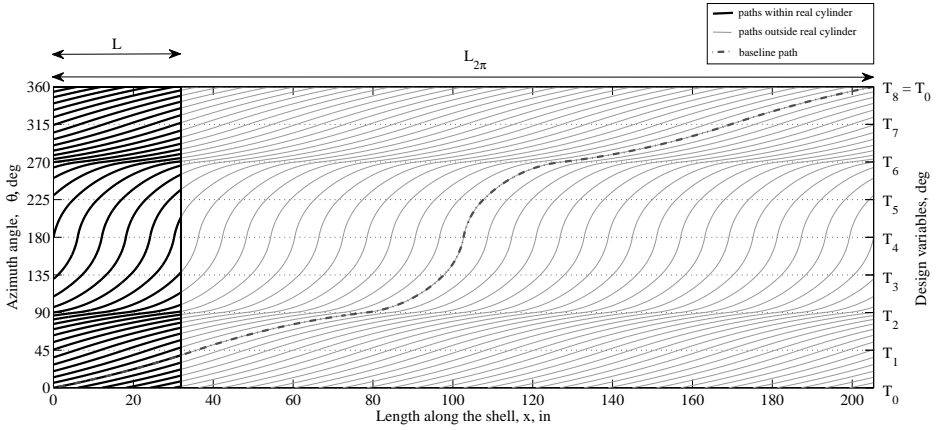


Figure 3.8: Fiber paths on an expanded cylinder

$x$  and  $\theta$  are again given, but now  $x_c$  and  $\varphi_c$  are functions of  $\theta_c$ , so that the equation needs to be solved for  $\theta_c$ . The fiber angle and the distance  $p$  can be found once  $\theta_c$  is known.

Course identification is similar to the previous two cases. The course identifier  $n$  can be found by:

$$n = \left\lfloor \frac{x - x_r(\theta)}{\Delta x} \right\rfloor \quad (3.44)$$

where  $\Delta x$  is given by equation 3.42 and  $x_r$  is the right edge of the course. Overlapping courses are found by increasing  $k$ , such that:

$$n_{k+1} = n - k \quad (3.45)$$

provided that the following condition is met:

$$x_r \leq x - (n - k)\Delta x \leq x_l \quad (3.46)$$

### 3.4 Path Candidates

Four different path definitions are suitable for use in a design environment: i) the geodesic path definition (Goldfeld et al., 2005), which is a path laid down on a surface in a natural manner, i.e. no steering is required; ii) a constant angle path, which is useful from an analytical and practical point of view; three, a linear angle variation which is derived, analogous to the definitions used for flat plates (Tatting and Gürdal, 2002); and four, a path with constant curvature (Tatting and Gürdal, 2003) can be defined, which simplifies evaluation of a curvature constraint that may be imposed because of machine limitations.

### 3.4.1 Geodesic Path

The first path definition, having zero in-plane curvature, is a geodesic path. This path definition serves as a basis for other path definitions, because experience in the field of geodesic paths for use with filament winding is already available.

#### Axial angle variation on conical shells

Equation 3.9  $\left( \kappa(x) = \frac{d\varphi}{dx} \cos \varphi(x) + \frac{\sin \alpha \sin \varphi(x)}{r(x)} \right)$  can be solved by a change of variables,  $u(x) = r(x) \sin \varphi(x)$ , using the fact that  $\kappa = 0$ . Then, by stipulating the fiber angle at the small radius to be  $T_0$ , the fiber angle variation for a geodesic path is:

$$\sin \varphi = \frac{r_0 \sin T_0}{r(x)} = \frac{s_0 \sin T_0}{s} \quad (3.47)$$

The actual path  $\theta(x)$  is found by integrating equation 3.5  $\left( \tan \varphi = r(x) \frac{d\theta}{dx} \right)$ . Alternatively, this equation can be written in the coordinates of the developed cone surface, see figure 3.3:

$$\tan \varphi(s) = s \frac{d\beta}{ds} \quad (3.48)$$

Then, the path of the geodesic is defined by:

$$\beta(s) = (\beta_0 + T_0) - \varphi(s) \quad (3.49)$$

where  $\beta_0$  defines the starting position of the path.

#### Axial angle variation on cylindrical shells

The definition of the in-plane curvature for cylindrical shells with an axial angle variation is defined by the first part of equation 3.10:

$$\kappa(x) = \frac{d\varphi}{dx} \cos \varphi(x) \quad (3.50)$$

The curvature can only be zero if either  $\frac{d\varphi}{dx} = 0$  or if  $\cos \varphi(x) = 0$ . The first condition is fulfilled if  $\varphi = \text{constant}$  and the second if  $\varphi = \pm 90^\circ$ , which leads to the conclusion that the fiber orientation of a geodesic path on a cylinder is constant.

#### Circumferential angle variation on cylindrical shells

The derivation for the axial variation on cylindrical shells has shown that the geodesic path has a constant fiber angle. This can be verified by looking at the equation for the in-plane curvature for a circumferential angle variation on cylindrical shells, the second part of equation 3.10:

$$\kappa(\theta) = \frac{d\varphi}{Rd\theta} \sin \varphi(\theta) \quad (3.51)$$

Indeed  $\frac{d\varphi}{d\theta} = 0$  if  $\varphi = \text{constant}$ , reducing the curvature to zero.

### 3.4.2 Constant Angle Path

An alternative to the geodesic path is a constant angle path, which is often used in theoretical studies because it is easy to analyze, although not always manufacturable. The fiber angle along the entire path is defined to be:

$$\varphi(x) = \phi \quad (3.52)$$

Substituting this relation into equations 3.5 and 3.9, the governing equations for a constant angle path become:

$$\begin{aligned} \frac{d\theta}{dx} &= \frac{\tan \phi}{r(x)} \\ \kappa(x) &= \frac{\sin \alpha \sin \phi}{r(x)} \end{aligned} \quad (3.53)$$

#### Axial angle variation on conical shells

Inspecting equation 3.53 it can be noticed that the largest value of the curvature occurs at the small radius of the cone, which makes it easy to determine the feasibility of a path once the geometry is known. The function defining the path is:

$$\beta(s) = \tan \phi \ln \left( \frac{s}{s_0} \right) + \beta_0 \quad \text{or} \quad s(\beta) = s_0 e^{\frac{\beta - \beta_0}{\tan \phi}} \quad (3.54)$$

#### Cylindrical shells

The path curvature of a constant angle path is zero on a cylindrical shell, as shown in section 3.4.1, and the path itself is defined by:

$$\frac{d\theta}{dx} = \frac{\tan \phi}{R} \quad (3.55)$$

So that:

$$\theta(x) = \tan \phi \left( \frac{x - x_0}{R} \right) + \theta_0 \quad \text{or} \quad x(\theta) = \frac{R(\theta - \theta_0)}{\tan \phi} + x_0 \quad (3.56)$$

### 3.4.3 Path with Linearly Varying Fiber Angles

The linearly varying angle path, in which the fiber angle varies linearly from  $T_0$  to  $T_1$ , is a path definition that has been used for flat plates.

### Axial angle variation on conical shells

The fiber angle on a conical shell is defined to vary linearly along the axial direction from  $T_0$  at the small radius to  $T_1$  at the large radius:

$$\varphi(x) = T_0 + (T_1 - T_0) \frac{x}{L} \quad (3.57)$$

The expressions for the three dimensional path definition and the curvature are:

$$\begin{aligned} \frac{d\theta}{dx} &= \frac{\tan\left(T_0 + (T_1 - T_0) \frac{x}{L}\right)}{r(x)} \\ \kappa(x) &= \frac{T_1 - T_0}{L} \cos \varphi + \frac{\sin \alpha \sin \varphi}{r(x)} \end{aligned} \quad (3.58)$$

Unfortunately, the path definition can not be written as an explicit function of  $x$  and  $\theta$ , so that the coordinates have to be determined numerically by integrating equation 3.58:

$$\begin{aligned} \theta(x) &= \int_0^x \tan\left(T_0 + (T_1 - T_0) \frac{x}{L}\right) \frac{dx}{r(x)} \\ \Rightarrow \beta(s) &= \int_{s_0}^s \tan\left(T_0 + (T_1 - T_0) \frac{s - s_0}{L}\right) \frac{ds}{s} \end{aligned} \quad (3.59)$$

The minimum curvature also has to be found numerically.

### Axial angle variation on cylindrical shells

The equations for the conical shell can be simplified for the cylindrical shell by stating  $\sin \alpha = 0$  and  $r(x) = R$ . The equation for the fiber angle variation is the same as in equation 3.57, while equations 3.58 become:

$$\begin{aligned} \frac{d\theta}{dx} &= \frac{\tan\left(T_0 + (T_1 - T_0) \frac{x}{L}\right)}{R} \\ \kappa(x) &= \frac{T_1 - T_0}{L} \cos \varphi \end{aligned} \quad (3.60)$$

Integration of the first of these equations results in the path definition:

$$\theta = \frac{-L}{R(T_1 - T_0)} \ln(\cos \varphi) + \frac{L}{T_1 - T_0} \ln(\cos T_0) \quad (3.61)$$

where  $\varphi$  is given by equation 3.57.

### Circumferential angle variation on cylindrical shells

The definition for a fiber path that has a linear fiber angle variation in the circumferential direction is:

$$\varphi(\theta) = T_0 + (T_1 - T_0) \frac{\theta - \theta_0}{\theta_1 - \theta_0} \quad (3.62)$$

where  $\theta_0$  and  $\theta_1$  are the circumferential locations at which the linear angle variation respectively starts and ends. Substituting equation 3.62 in equation 3.10 results in the following expression for the in-plane curvature:

$$\kappa(\theta) = \frac{T_1 - T_0}{R(\theta_1 - \theta_0)} \sin \varphi \quad (3.63)$$

The differential equation for the path

$$\frac{d\theta}{dx} = \frac{\tan \varphi}{R} \quad (3.64)$$

can be integrated to obtain  $x$  as a function of  $\theta$ :

$$x = \frac{\theta_1 - \theta_0}{T_1 - T_0} (\ln \sin \varphi - \ln \sin T_0) \quad (3.65)$$

where  $\varphi$  is given by equation 3.62

### 3.4.4 Constant Curvature Path

Finally, a path with constant curvature will be defined, so that the curvature constraint can be readily evaluated.

#### Axial angle variation on conical shells

The angle variation for a constant curvature path is again defined to start from an angle  $T_0$  at  $r_0$  (or  $s_0$ ) and to end at an angle  $T_1$  at  $r_1$  (or  $s_1$ ) and is given by:

$$\begin{aligned} \sin \varphi(x) &= \frac{r_0 \sin T_0}{r(x)} + \frac{\kappa}{\sin \alpha} \left( \frac{r(x)^2 - r_0^2}{2r(x)} \right) \\ &= \frac{s_0 \sin T_0}{s} + \kappa \left( \frac{s^2 - s_0^2}{2s} \right) \end{aligned} \quad (3.66)$$

The derivation of this equation can be found in appendix B. The corresponding value of the curvature is:

$$\kappa = \left( \frac{r_1}{\bar{r}} \sin T_1 - \frac{r_0}{\bar{r}} \sin T_0 \right) \frac{1}{L} \quad \left[ \bar{r} = \frac{r_0 + r_1}{2} \right] \quad (3.67)$$

The path on the shell surface can be found by numerical integration:

$$\beta(s) = \int_{s_0}^s \frac{\tan \varphi(s)}{s} ds \quad (3.68)$$

which can then be transformed back to three-dimensional cone coordinates using  $\beta = \theta \sin \alpha$ .

### Axial angle variation on cylindrical shells

The equation for the fiber angle on a conical shell, equation 3.66, can be simplified for a cylindrical shell and after substituting the expression for the curvature  $\kappa$  from equation 3.67 it can be rewritten as:

$$\sin \varphi(x) = \sin T_0 + (\sin T_1 - \sin T_0) \frac{x}{L} \quad (3.69)$$

The curvature is:

$$\kappa = \frac{\sin T_1 - \sin T_0}{L} \quad (3.70)$$

and the path definition becomes:

$$\theta = -\frac{\cos \varphi - \cos T_0}{\kappa R} \quad (3.71)$$

where  $\varphi$  is defined by equation 3.69.

### Circumferential angle variation on cylindrical shells

The definition for the circumferential angle variation can be derived, similar to the derivations for the axial angle variation on cylindrical shells:

$$\cos \varphi(\theta) = \cos T_0 + (\cos T_1 - \cos T_0) \frac{\theta - \theta_0}{\theta_1 - \theta_0} \quad (3.72)$$

while the curvature is:

$$\kappa = \frac{\cos T_0 - \cos T_1}{R(\theta_1 - \theta_0)} \quad (3.73)$$

The path is defined by:

$$x = \frac{\sin \varphi - \sin T_0}{\kappa} \quad (3.74)$$

where  $\varphi$  is given by equation 3.72.

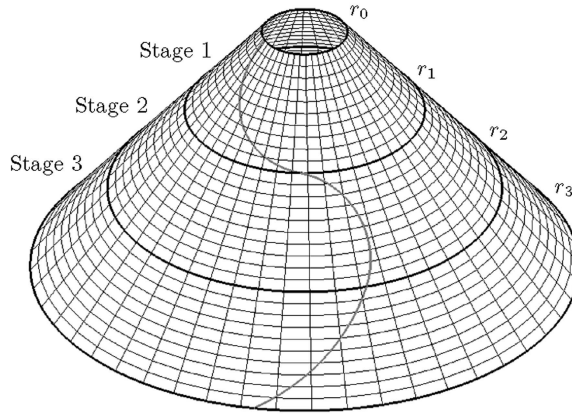
## 3.4.5 Multiple Segment Angle Variation

The path definitions described above can be used in a multiple segment angle variation. The multiple segments enable an expansion of the design space, while keeping the number of design variables manageable. The principles of the multiple segment variation are explained below.

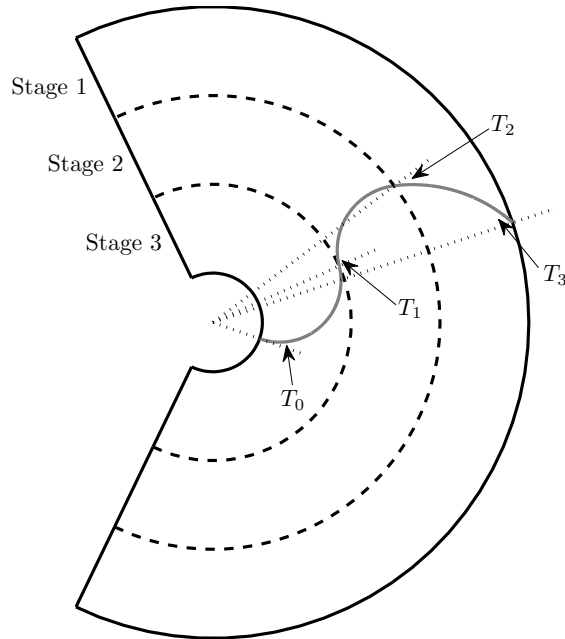
### Axial angle variation on conical and cylindrical shells

The cone or cylinder is divided in multiple parts for the axial angle variations, so that they can be considered separate cones or cylinders with their own angle variation. It is necessary to have continuity at the transition between two segments to ensure manufacturability. The fiber angle must therefore be the same for both segments at this connection. Different segments can have different types of path definitions, i.e. constant, geodesic, linear or constant curvature, as long as the continuity condition at the transition is satisfied. These angles would be the design variables in a design case.





(a) Conical shell with three-stage angle variation

(b) Developed cone representation with  $T_0 = 0^\circ$ ,  $T_1 = 80^\circ$ ,  $T_2 = -30^\circ$  and  $T_3 = -60^\circ$ *Figure 3.9: Multiple-stage angle variations*

An example of a three-stage constant curvature angle variation is shown in figure 3.9, where a conical shell with  $\alpha = 35^\circ$  has different fiber angle variations between  $r_0$  and  $r_1$ , between  $r_1$  and  $r_2$  and between  $r_2$  and  $r_3$ . The starting value of one stage is the same as the ending angle of the previous stage.

The notation for a cone with an arbitrary number of stages  $N_s$  is given below for a

constant curvature path. The fiber angle variation is defined by:

$$\sin \varphi(x) = \frac{r_i \sin T_i}{r(x)} + \frac{\kappa_i}{\sin \alpha} \left( \frac{r(x)^2 - r_i^2}{2r(x)} \right), \quad (3.75)$$

$$i = 0, 1, 2, \dots, N_s - 1$$

where the curvature per stage is:

$$\kappa_i = \left( \frac{r_{i+1}}{\bar{r}} \sin T_{i+1} - \frac{r_i}{\bar{r}} \sin T_i \right) \frac{1}{L_i}, \quad \left[ \bar{r} = \frac{r_i + r_{i+1}}{2} \right] \quad (3.76)$$

In this equation  $L_i$  is the surface length of cone segment  $i$  and is defined by  $L_i = x_{i+1} - x_i$ . The vector with design variables that defines this ply is  $\vec{T}^{(k)} = \{T_0^{(k)}, T_1^{(k)}, \dots, T_{N_s}^{(k)}\}^T$ , where each  $T_i^{(k)}$  represents the fiber angle at the small radius of the  $i+1^{\text{st}}$  cone and the fiber angle at the large radius of the  $i^{\text{th}}$  cone.

### Circumferential angle variation on cylindrical shells

At least two segments are needed for the circumferential angle variation to satisfy the periodicity constraint at  $\theta = 2\pi$ , unless it is a constant angle ply. More segments provide more design freedom and consequently a better chance of improving the design and therefore it is beneficial to use more than 2 segments. Too many segments might increase the design space too much and may result in a slow optimization process, requiring a balance between the amount of design freedom desired and the amount of time needed to optimize the design.

The path definition for the circumferential angle variation in multiple segments is defined similar to the axial angle variation. The constant curvature variation, for example, becomes:

$$\cos \varphi(\theta) = \cos T_i + (\cos T_{i+1} - \cos T_i) \frac{\theta - \theta_i}{\theta_{i+1} - \theta_i} \quad (3.77)$$

In this equation  $T_i$  is the fiber angle at the  $\theta_i$  location around the circumference, where there is a transition between two segments. At the transition the fiber angle is continuous, but the in-plane curvature changes. The in-plane curvature  $\kappa$  within one stage for a cylinder with radius  $R$  is:

$$\kappa_i = \frac{\cos T_i - \cos T_{i+1}}{R(\theta_{i+1} - \theta_i)} \quad (3.78)$$

The curvature for each segment can easily be calculated when the design variables  $T_i$  are known.

## 3.5 Examples of Fiber Paths and Curvature Constraints

A conical shell with a small radius  $r_0 = 0.125$  m, a large radius  $r_1 = 0.8$  m and a cone angle  $\alpha = 40^\circ$  will be used to demonstrate some of the theoretical fiber paths described in the previous section. A minimum turning radius of  $\rho_{\min} = 0.635$  m ( $= 25$  in), or equivalently a maximum curvature of  $\kappa_{\max} = 1.57 \text{ m}^{-1}$  ( $= 0.04 \text{ in}^{-1}$ ) is assumed to incorporate the limitations of a typical fiber placement machine.

**Example 1**

The fiber paths, fiber angle variations and curvature variations for three different fiber paths are shown in figure 3.10. The three courses corresponding to the different path definitions are plotted on the three-dimensional cone surface in figure 3.10(a). The centerline, the left edge and the right edge are shown for each course, where the subscripts  $l$  and  $r$  represent the left and right edges. The displayed constant curvature path, constant angle path, and geodesic path all have the same starting angle  $T_0 = 45^\circ$ , while the constant curvature path also has  $T_1 = 45^\circ$ . The constant angle path can be considered as a special case of the linearly varying angle path with  $T_0 = T_1$ , which is why linear fiber angle variation is not present in this example. The constant angle and constant curvature paths are completely different, even though they have the same starting and ending angles, see figures 3.10(a) and 3.10(b).

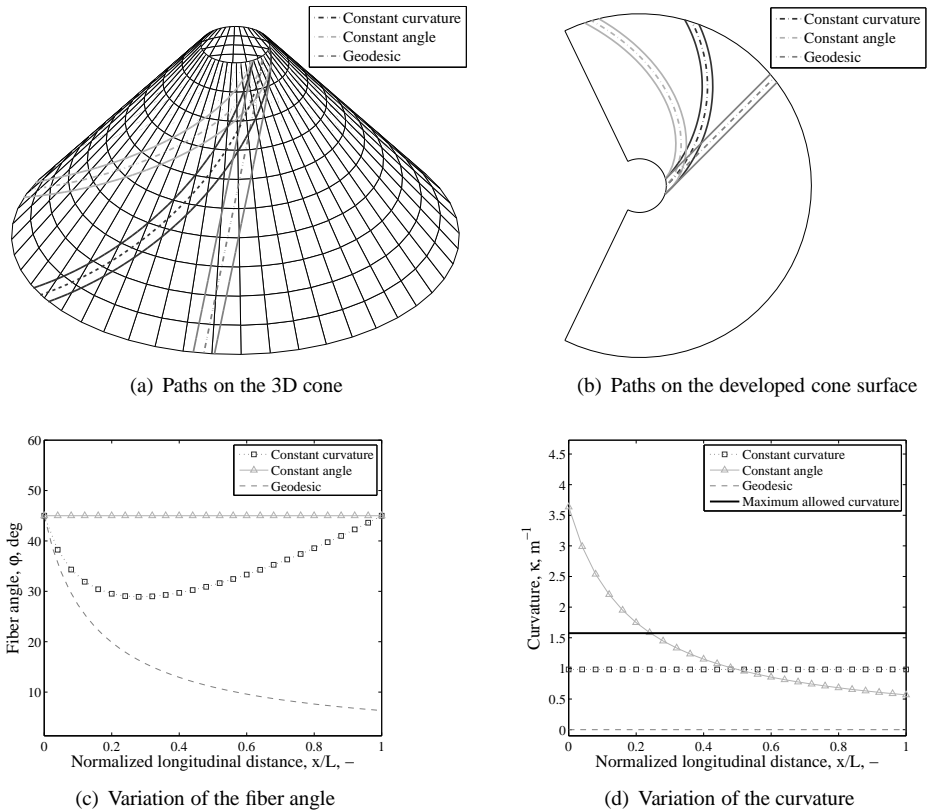


Figure 3.10: Different fiber paths with  $T_0 = 45^\circ$  and  $T_1 = 45^\circ$

The geodesic path is represented by a straight line on the developed cone surface, which deviates considerably from the other two paths. The fiber angle variations are plotted in figure 3.10(c). The fiber orientation of a geodesic path will always go to zero when moving from the small to the large radius of a cone and therefore it will never resemble paths that have a (relatively) large angle at the large radius. The large difference between the constant curvature and constant angle path is caused by the variation of the fiber angle in-between

the small and large radius, see figure 3.10(c).

Manufacturability, which is determined by the maximum curvature of a path, also varies from one path to another. The curvature variation of the three paths is plotted in figure 3.10(d), together with the maximum allowed curvature. The geodesic path can always be manufactured, because it's curvature is zero by definition. Furthermore, the constant curvature path does not violate the maximum curvature constraint for this combination of starting and ending angles. The constant angle path exceeds the maximum allowed curvature, which means that this particular configuration cannot be manufactured using a typical fiber placement machine.

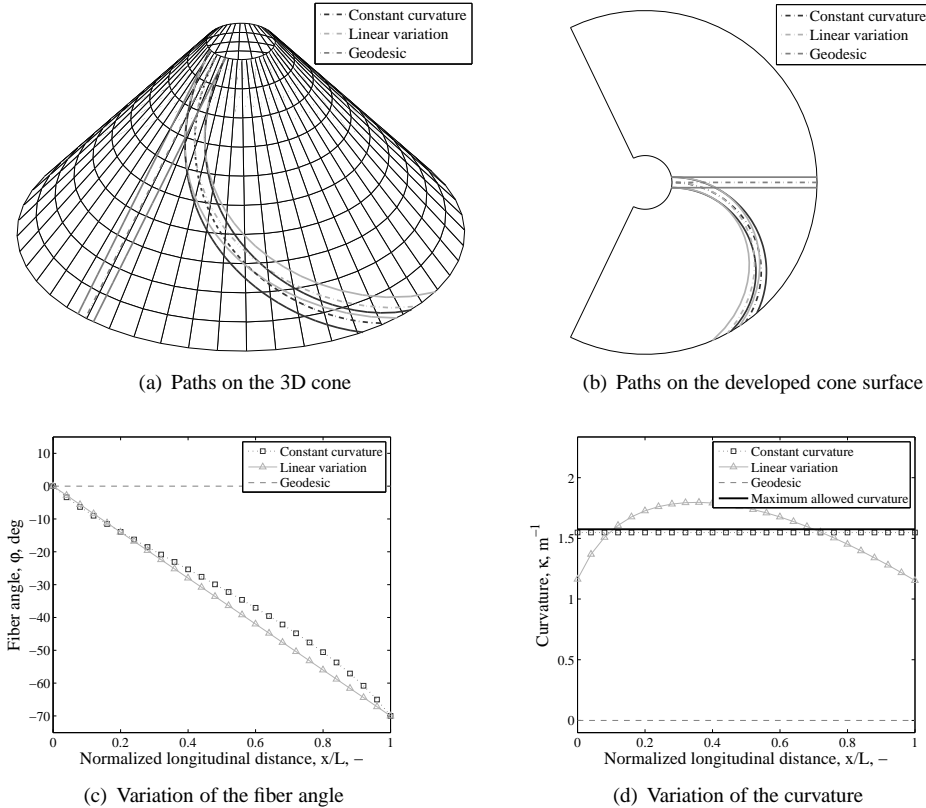


Figure 3.11: Different fiber paths with  $T_0 = 0^\circ$  and  $T_1 = -70^\circ$

## Example 2

Another example of three courses with varying fiber orientations is shown in figure 3.11, the paths in this figure all have a zero starting angle, while the linearly varying angle path and the constant curvature path have  $T_1 = -70^\circ$ . The last two paths are very similar, as can be seen from figures 3.11(a) through 3.11(c). The major difference between the two is again the curvature, shown in figure 3.11(d). The constant curvature path just satisfies the curvature constraint, whereas the linearly varying angle path violates it. The sharp variation

of the curvature along the length implies that linear fiber orientation variation should be implemented with care for conical structures.

### Example 3

A more general overview of feasible combinations of  $T_0$  and  $T_1$  is given in figure 3.12, where a contour plot of the maximum curvature is given as a function of the design variables  $T_0$  and  $T_1$ . The feasible design space consists of the combinations of  $T_0$  and  $T_1$  for which the maximum curvature is less than or equal to the fiber placement machine dependent curvature  $\kappa_{\max} = 1.57 \text{ m}^{-1}$ . The maximum curvature value is indicated by the white markers. The feasible designs for both the linear angle variation and the constant curvature variation are in the middle, while the infeasible designs are on the sides of the design space. The linear angle variation, figure 3.12(a), shows a considerable reduction in design space due to manufacturing limitations for this particular cone configuration. This emphasizes the need to determine the manufacturability of a fiber path before using it in a design such that structural analyses of infeasible designs is avoided. The constant curvature variation, figure 3.12(b), has a considerably larger design space than the linear angle variation, but is still limited by maximum curvature.

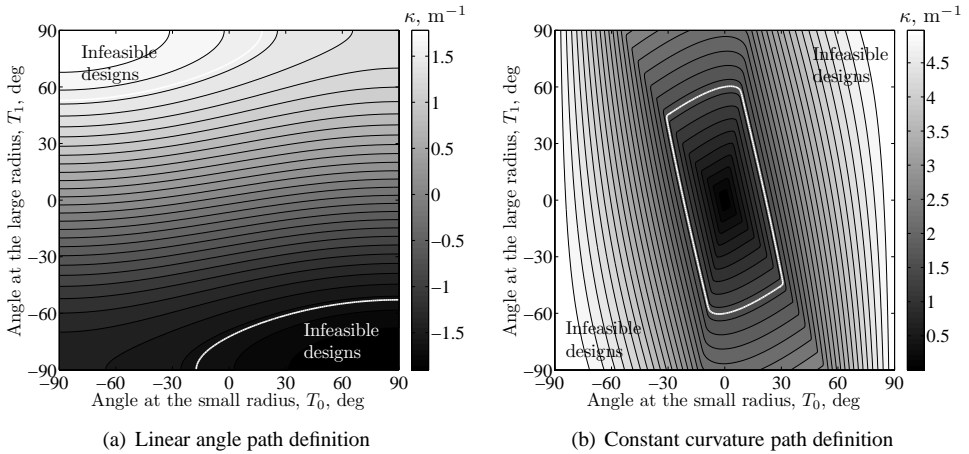


Figure 3.12: Maximum path curvature, maximum allowed curvature  $\kappa_{\max} = 1.57 \text{ m}^{-1}$

## 3.6 Conclusions

A method for tracing local fiber orientations and overlaps on conical and cylindrical shells with a variable-stiffness ply constructed by fiber placement was developed. Four different theoretical path definitions that describe the angle variation in axial or circumferential direction were defined: a geodesic path, a constant angle path, a linearly varying angle path, and a constant curvature path. The latter two path definitions provide an extended design space compared to traditional straight fiber paths, especially when multiple segments are

used, although curvature constraints imposed by the fiber placement process can considerably limit the amount of variation in fiber angle orientation. It is therefore important to investigate the manufacturability of a fiber path before using it in a design. The four path definitions, and the procedure to calculate the stacking sequence locally, provide a firm basis for constructing stiffness models that take into account varying stiffness in the form of varying fiber orientation angles and varying thickness.

The path definitions derived in this chapter will be used to define variable-stiffness plies in the following chapters. The axial angle variations will be employed in chapter 4, where the laminate of conical shells will be optimized for maximum fundamental frequency. The different fiber paths will be compared and the influence of the curvature constraint on the optimum design will be studied. The procedure to calculate the stacking sequence is used to construct finite element models to predict the structural behavior of the variable-stiffness conical and cylindrical shells. The circumferential angle variation will be applied to optimize a cylindrical shell under bending in chapter 5, where the influence of overlaps will also be discussed.

## Chapter 4

# Optimization of the Fundamental Frequency by Axially Varying Stiffness on Conical and Cylindrical Shells

Conical shells and cylinders with various dimensions are optimized for maximum fundamental frequency in this chapter, using the fiber path definitions introduced in chapter 3. A comparison with existing work by Hu and Ou (2001) is made, and the influence of the curvature constraint on the attainable frequency is also evaluated. Conclusions are drawn based on the numerical examples and recommendations for further work are provided.

### 4.1 Introduction

Earlier research on the design of fiber-reinforced conical shells for maximum fundamental frequency was done by Hu and Ou (2001). In their work they study the influence of the fiber orientation on the fundamental frequency of conical shells using sequential linear programming (Schittkowski, 2004). The fundamental frequency is optimized by finding the optimum fiber orientation  $\varphi$  in composite laminates with a  $[\pm\varphi/90_2/0]_{n,s}$  layup, where  $n$  indicates the number of repetitions of the stacking sequence within the brackets and  $s$  indicates a symmetric layup. Hu and Ou (2001) showed that the optimum angle depends on the shell thickness and on the large radius over length ratio. The optimum fiber angle is shown to be insensitive to the boundary conditions.

In the research reported here the variable-stiffness definitions introduced in the previous chapter were used to optimize cones with the same dimensions as those studied by Hu and Ou (2001) for maximum fundamental frequency, where stiffness was only allowed to vary in the axial direction. The manufacturability of the optimum designs obtained by Hu and Ou were judged based on the maximum curvature constraint. Three larger conical shells were optimized in addition to the cone geometries used by Hu and Ou (2001) to show the

merit of stiffness variation for potential aerospace applications.

The geodesic path, the constant angle path, and the constant curvature path derived in section 3.4 were used to construct the variable-stiffness conical shells. The constant angle path, which produces a constant-stiffness laminate, served as a baseline for the variable-stiffness designs. Furthermore, the manufacturing constraints for fiber placement were taken into account during the optimization of the variable-stiffness laminates to ensure that the optimal laminate was manufacturable. The curvature constraint was both applicable to the variable-stiffness paths and the constant-angle path, due to the conical shell geometry. The influence of the manufacturing constraint on the performance and the advantages of a variable-stiffness shell over a conventional constant-stiffness shell is demonstrated below.

## 4.2 Problem Definition and Optimization Procedure

The optimization problem was formulated as the maximization of the fundamental frequency  $f$  for a given number of layers, assuming a given shell geometry. Constraints apply on the value of the curvature  $\kappa$  of the fiber paths since the composite shells were designed to be built using a fiber placement machine. The curvature of a path had to be smaller than the maximum allowed curvature  $\kappa_{\max}$ . Elements of a vector  $\vec{T}^k$  are used to represent a finite number of design variables for each layer  $k$ . These design variables determined the variation of the fiber orientation on the surface of the cone. Maximizing the fundamental eigenvalue  $\lambda$  is equivalent to maximizing the fundamental frequency  $f$  as they are related by:  $\lambda = (2\pi f)^2$ . The design problem was formulated as:

$$\begin{aligned} \text{Maximize} \quad & \lambda(\vec{T}^k) & k = 1, 2, \dots, N \\ \text{Subjected to} \quad & |\kappa(\vec{T}^k)| \leq \kappa_{\max} & x \in [0, L] \end{aligned} \quad (4.1)$$

where  $N$  is the number of layers in the laminate,  $x$  is the longitudinal surface coordinate and  $L$  is the length of the cone along the surface. The fundamental eigenvalue  $\lambda$  was obtained by solving the general eigenvalue problem using the finite element program ABAQUS:  $\vec{K}\vec{\zeta} = \lambda\vec{M}\vec{\zeta}$ . Here  $\vec{K}$  and  $\vec{M}$  are the global stiffness and mass matrices and  $\vec{\zeta}$  is the modal displacement vector.  $\kappa$  is the maximum value of the curvature of a path and  $\kappa_{\max}$  is the inverse of the minimum turning radius. The actual value of the allowed curvature depends on the feed rate used to place the fibers on the surface (Moruzzi et al., 2006) and also varies for different types of fiber placement machines. The implementation of the varying stiffness in ABAQUS will be explained in section 4.3.

The occurrence of multiple eigenvalues caused the objective function,  $\lambda$ , in equation 4.1 to be non-differentiable and therefore a bound formulation, as introduced by Olhoff (1989), was applied to the optimization problem. The bound optimization problem is formulated as:

$$\begin{aligned} \text{Maximize} \quad & \gamma & k = 1, 2, \dots, N \\ \text{Subjected to} \quad & \lambda_i(\vec{T}^k) - \gamma \geq 0 & i = 1, 2, 3, 4 \\ & |\kappa(\vec{T}^k)| \leq \kappa_{\max} & x \in [0, L] \end{aligned} \quad (4.2)$$

An additional variable  $\gamma$  is introduced with the bound formulation, which also becomes the



new objective function. The variable  $\gamma$  represents a lower bound for each of the eigenvalues, resulting in additional constraints in the optimization formulation requiring the variable  $\gamma$  to be smaller than the lowest eigenvalues. The four lowest eigenvalues were taken into account using the bound formulation.

The optimization was performed by sequential quadratic programming, where the constrained nonlinear optimization problem with inequality constraints was solved using a Fortran implementation of Schittkowski's NLPQLP optimizer (Schittkowski, 2004). The partial derivatives of both the objective function and the constraints with respect to the design variables were required for the optimization process, while the derivatives of the new objective function  $\gamma$  with respect to the design variables  $\vec{T}^k$  was zero. The sensitivities of the eigenvalue constraints with respect to the design variables  $\vec{T}^k$  were computed using forward finite differences with a step size of  $0.25^\circ$ , for which the eigenvalues were calculated using finite element analysis. The derivatives of the curvature constraints were calculated analytically. An overview of the optimization routine is shown in figure 4.1.

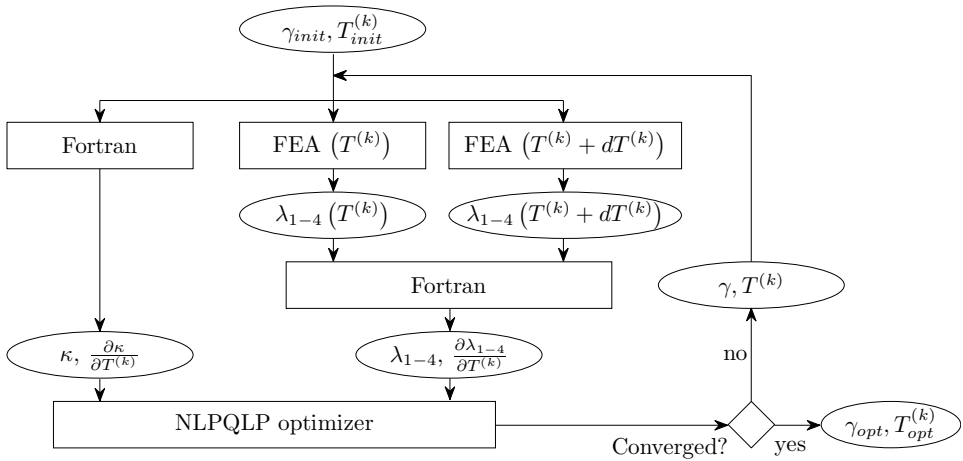


Figure 4.1: Optimization scheme

### 4.3 Finite Element Analysis

The fundamental frequency was calculated using the finite element package ABAQUS (ABAQUS, Inc., 2005). The stiffness variation resulted in unique stiffness properties for each element, which were calculated using the property tracing methods discussed in section 3.3. The stiffness variation was implemented using S4 shell elements in combination with the *UGENS* user subroutine. The S4 shell element is a fully integrated, general-purpose, finite-membrane-strain shell element, with four nodes and four integration points. The *UGENS* subroutine is a user-written FORTRAN subroutine that passes the shell stiffness for each integration point to ABAQUS. The local stacking sequence was calculated based on the position of the element, the material properties and the laminate definition. Then the ABD matrix was calculated using Classical Lamination Theory (Jones, 1999) and the ABD

matrix was provided to the ABAQUS solver. An overview of the analysis sequence is given in figure 4.2.

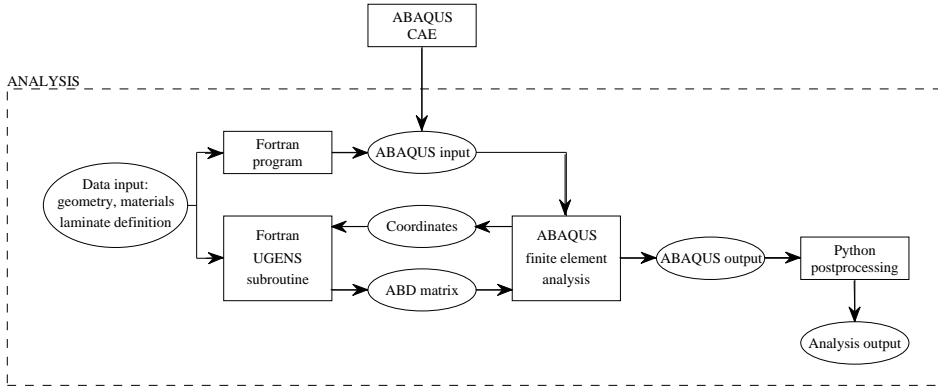


Figure 4.2: Finite element analysis scheme

The computational performance was compared for the approach described above and a method that used direct input of the stacking sequence through a composite shell element, but the latter needs more than twenty times the amount of computation time needed for the USER subroutine method. Hence, the subroutine method became the preferred method for the implementation of variable-stiffness properties.

The local stacking sequence was calculated using the layup that would result from the manufacturing process, which deviated slightly from the ideal variation. This is shown for a circumferential angle variation in figure 4.3. The fiber angles are plotted in a surface contour plot. Ideally, the fiber angle is only a function of the circumferential coordinate, see figure 4.3(a), however, there is some deviation from the ideal fiber angle distribution due to the finite width of the courses, see figure 4.3(b). The latter is modeled by discrete elements in ABAQUS, see figure 4.3(c). A regular analysis can be done within ABAQUS once the stiffness is defined for all the elements.

## 4.4 Numerical Results

Twelve conical shells with different geometries were considered in the design study described in this chapter. The dimensions of these cones are given in table 4.1. Cones 1 through 9 had the same dimensions as those used by Hu and Ou (2001) for the optimization of fundamental frequencies, i.e. the large radius  $r_1$  was 0.10 m and the small radius  $r_0$  was 0.06, 0.08 or 0.10 m, while the axial length of the shell  $A$  was either 0.10, 0.25 or 0.40 m. These cones were used to study the impact of the curvature constraint on the optimum design. They were also optimized using different axial stiffness variations. Three additional cone geometries were defined, which could be used to represent realistic aerospace structures. Cone number 10 represents a cylinder that might be used as a satellite bus, cone number 11 has the dimensions of a typical helicopter tail boom, while cone number 12 has the dimensions of a satellite end cap.

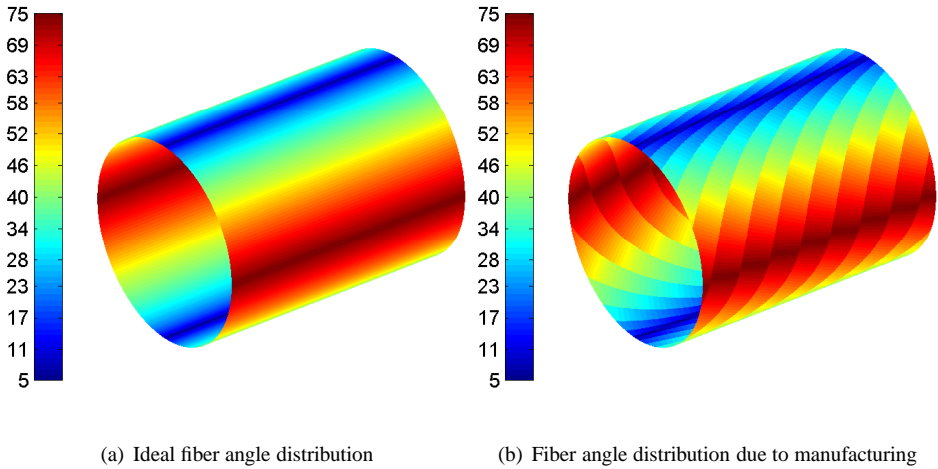


Figure 4.3: Fiber angle distributions within one ply

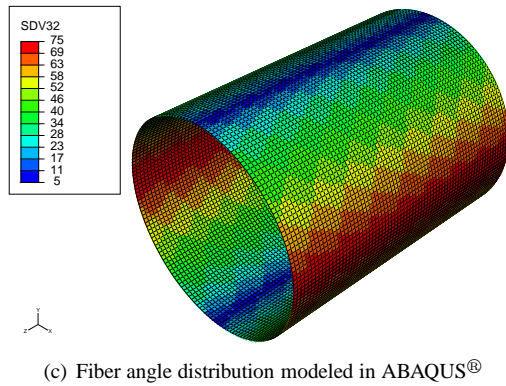


Figure 4.3: Fiber angle distributions within one ply (continued)

The last three structures are often subjected to vibration loads, which might excite the structure with its eigenfrequency, possibly resulting in a structural failure. Maximizing the fundamental frequency of the conical or cylindrical shell structure could be required to avoid the structure to be excited by low frequency vibrations.

The cones were designed with the same Graphite/Epoxy material used by Hu and Ou (2001), the material properties of which are given in table 4.2. A different laminate layup was chosen from that of Hu and Ou, who used a  $[\pm\varphi/90_2/0]_{n,s}$  layup for their optimization, to show the true merits of variable-stiffness designs. The layup used was:  $[\pm\varphi(x)]_{5s}$ , where the  $5s$  notation indicates that the stacking sequence within the brackets is repeated five times and the laminate is symmetric. A  $[\pm\varphi(x)]_{5s}$  laminate thus resulted in 20 layers of material. This layup will be denoted  $[\pm T_0]_{5S}$  for the geodesic and constant angle paths, since the angle variation  $\varphi(x)$  is defined by  $T_0$ . The constant curvature path, which is a function of the two

Table 4.1: Cone geometries

Cone number	Small radius	Large radius	Axial length	Cone angle
	$r_0$ (m)	$r_1$ (m)	$A$ (m)	$\alpha$ ( $^\circ$ )
1*	0.06	0.10	0.10	21.80
2*	0.06	0.10	0.25	9.09
3*	0.06	0.10	0.40	5.71
4*	0.08	0.10	0.10	11.31
5*	0.08	0.10	0.25	4.57
6*	0.08	0.10	0.40	2.86
7*	0.10	0.10	0.10	0.00
8*	0.10	0.10	0.25	0.00
9*	0.10	0.10	0.40	0.00
10	0.30	0.30	0.725	0.00
11	0.30	0.35	1.000	2.86
12	0.125	0.80	0.804	40.00

\* From Hu and Ou (2001)

Table 4.2: Graphite/Epoxy material properties used by Hu and Ou (2001)

$E_{11}$	128 GPa
$E_{22}$	11 GPa
$\nu_{12}$	0.25
$G_{12}$	4.48 GPa
$t_{ply}$	0.125 mm
$\rho$	1,500 kg/m <sup>3</sup>

variables  $T_0$  and  $T_1$ , will be denoted  $[\pm < T_0|T_1 >]_{5s}$ . A multiple-segment constant curvature variation was also used for the optimization. A two-segment variation was selected with  $T_2 = T_0$ , so that only two variables were used. This laminate is denoted  $[\pm < T_0|T_1|T_0 >]_{5s}$ . The design variables,  $T_0$  and  $T_1$ , were allowed to vary between  $-89^\circ$  and  $+89^\circ$  to avoid discontinuities during production. The cones were fully clamped at both ends for the natural frequency analysis.

A mesh study was performed to investigate the influence of the number of elements in the longitudinal and the circumferential direction independently. A mesh with 30 elements in the longitudinal direction and 100 elements in the circumferential direction was selected for all the cone geometries, because it provided accurate results within a reasonable calculation time.

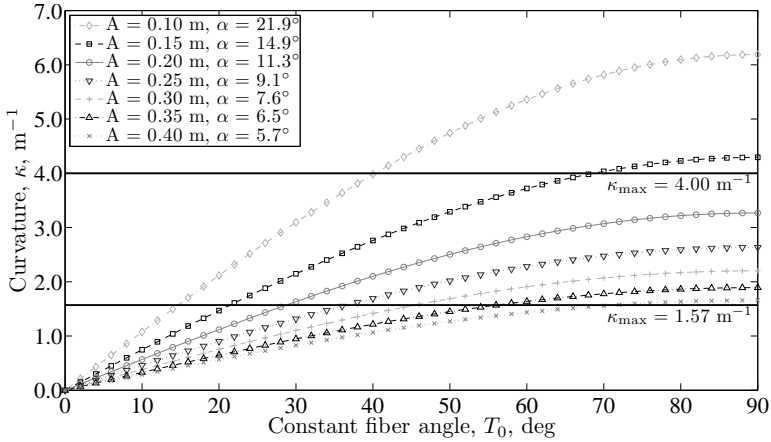
#### 4.4.1 Influence of the Curvature Constraint on Design Feasibility

Some examples will now be given to demonstrate the consequences of the curvature constraint on the feasibility of different fiber orientations for different cone geometries, even though the curvature constraint was automatically taken into account in the optimization process.

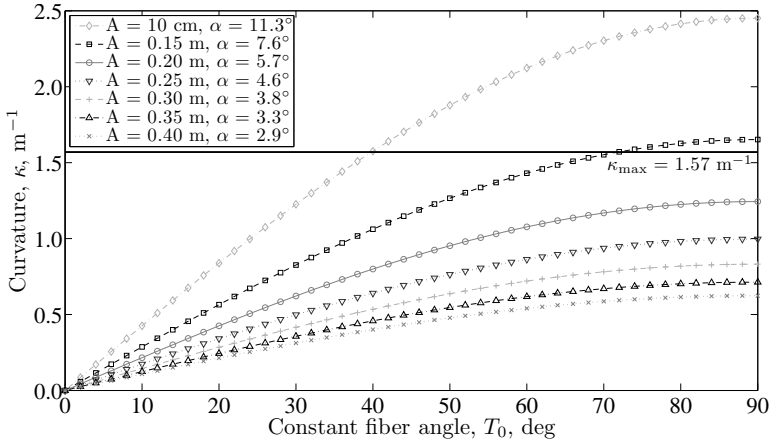
Two different values for the allowed curvature were used to illustrate the consequences of the maximum curvature value on the feasibility of a design. The first maximum curvature

value was  $1.57 \text{ m}^{-1}$ , which corresponds to a minimum turning radius of 0.635 m. This value is the minimum allowed turning radius for a typical fiber placement system. The second maximum curvature value was  $4.00 \text{ m}^{-1}$ , which corresponds to a minimum turning radius of 0.25 m. A reduction in feed rate is required if this turning radius is used, but manufacturability is guaranteed, see Moruzzi et al. (2006).

The maximum curvature values for a constant angle path as a function of the design variable  $T_0$  are shown in figure 4.4 for multiple values of the cone angle  $\alpha$ . The values for



(a)  $r_0 = 0.06 \text{ m}$ ,  $r_1 = 0.10 \text{ m}$



(b)  $r_0 = 0.08 \text{ m}$ ,  $r_1 = 0.10 \text{ m}$

Figure 4.4: Maximum curvature values for constant angle paths

cones that have a small radius  $r_0=0.06 \text{ m}$  and a large radius  $r_1=0.10 \text{ m}$  are shown in figure 4.4(a), while the values for cones that have a small radius  $r_0=0.08 \text{ m}$  and a large radius  $r_1=0.10 \text{ m}$  are shown in figure 4.4(b). The influence of the small radius on the curvature can be seen by comparing figures 4.4(a) and 4.4(b). Note: the scales on the vertical axes are different. The curvatures of the cones with  $r_0=0.06 \text{ m}$  were more than 30 percent higher than the curvatures of the cones with  $r_0=0.08 \text{ m}$  for equal values of the cone angle  $\alpha$ . This

resulted in severe restrictions on the design space for the cones with  $r_0=0.06$  m, whereas few restrictions applied to the cones with  $r_0=0.08$  m. For example, a cone with  $r_0=0.06$  m,  $r_1=0.10$  m and  $\alpha = 21.80^\circ$  could only have a constant fiber orientation between  $0^\circ$  and  $15^\circ$  for a maximum curvature of  $1.57 \text{ m}^{-1}$ , whereas the maximum fiber orientation was  $40^\circ$  if the larger curvature of  $4.00 \text{ m}^{-1}$  is used. The maximum feasible fiber orientations using advanced fiber placement are listed side by side with the optimum fiber angles obtained by Hu and Ou (2001) in table 4.3. Comparison of the maximum feasible fiber angles with the optimum fiber angles obtained by Hu and Ou showed that most of the optimum fiber angles for the cylinder with  $r_0=0.06$  m and  $r_1=0.10$  m could not be manufactured using fiber placement technology if a maximum curvature of  $1.57 \text{ m}^{-1}$  is assumed. Relaxing the curvature constraint to  $4.00 \text{ m}^{-1}$  enables fiber placement of the optimum fiber angles for all cones, except for the one with  $r_0=0.06$  m,  $r_1=0.10$  m, and  $A = 0.10$  m.

Table 4.3: Comparison of maximum feasible fiber orientations using AFP and optimum fiber angles from Hu and Ou (2001)

Axial length A	$r_0=0.06 \text{ m}, r_1=0.10 \text{ m}$			$r_0=0.08 \text{ m}, r_1=0.10 \text{ m}$	
	$\phi_{\max} (^\circ)$		$\phi_{opt}^* (^\circ)$	$\phi_{\max} (^\circ)$	
	$\kappa = 1.57 \text{ m}^{-1}$	$\kappa = 4.00 \text{ m}^{-1}$		$\kappa = 1.57 \text{ m}^{-1}$	$\phi_{opt}^* (^\circ)$
10	15	40	45	40	46
15	22	69	48	72	45
20	29	-	44	-	50
25	37	-	43	-	46
30	45	-	46	-	42
35	56	-	65	-	43
40	72	-	61	-	62

\* values from Hu and Ou (2001), layup  $[\pm\theta, 90_2, 0]_{2s}$

The curvature values for the constant curvature paths are functions of two variables and therefore it is more difficult to compare the feasibility of the design space for many different cone geometries. Here, only two cone geometries are chosen to illustrate the differences in feasibility. The curvature values for different combinations of  $T_0$  and  $T_1$  for a cone with  $r_0 = 0.06$  m,  $r_1 = 0.10$  m and  $\alpha = 21.80^\circ$  are shown in figure 4.5(a). The curvature values for a cylinder with  $r_0 = r_1 = 0.10$  m and an axial length  $A = L = 0.40$  m are shown in figure 4.5(b). White markers indicate the two maximum curvature values,  $\kappa_{\max} = 1.57 \text{ m}^{-1}$  and  $\kappa_{\max} = 4.00 \text{ m}^{-1}$ . The area in between the two markers with the same  $\pm\kappa_{\max}$  is the feasible design space. The feasible design space for the cylinder in figure 4.5(b) is larger than for the cone in figure 4.5(a) due to the larger dimensions of the cone in figure 4.5(a) and the zero cone angle.

#### 4.4.2 Influence of the Curvature Constraint on the Optimum Design

Cone number 1, with a small radius of 0.06 m, a large radius of 0.10 m and a cone angle of 21.80 degrees, was used as an example to illustrate the influence of the curvature constraint on the maximum fundamental frequency, because this cone had large restrictions on fiber orientation due to the curvature constraint. The results of all four path definitions for the two curvature values are given in table 4.4. The percentages in table 4.4 indicate the rel-

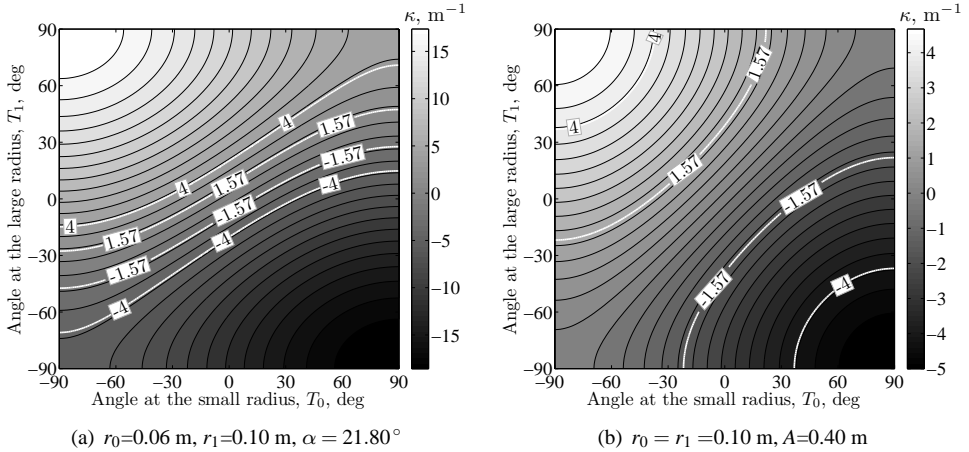


Figure 4.5: Curvature values for constant curvature paths

ative increase in eigenfrequency with respect to the best constant-stiffness design that was obtained with a maximum curvature of  $1.57 \text{ m}^{-1}$ .

Table 4.4: Influence of the curvature constraint on the maximum fundamental frequency of cone number 1,  $r_0 = 0.06$  m,  $r_1 = 0.10$  m,  $\alpha = 21.80^\circ$

$\kappa_{\max} = 1.57 \text{ m}^{-1}$			
Path definition	$T_0$ ( $^\circ$ )	$T_1$ ( $^\circ$ )	$f$ (Hz)
Geodesic*	60.6	-	4374 (+ 32 %)
Constant angle	14.7	-	3292 (+ 0 %)
Constant curvature	49.5	36.2	4447 (+ 35 %)
Constant curvature, two segments	19.8	19.1	3594 (+ 9 %)

$\kappa_{\max} = 4.00 \text{ m}^{-1}$			
Path definition	$T_0$ ( $^\circ$ )	$T_1$ ( $^\circ$ )	$f$ (Hz)
Geodesic*	60.6	-	4374 (+ 32 %)
Constant angle	40.3	-	4488 (+ 36 %)
Constant curvature**	41.4	42.4	4476 (+ 36 %)
Constant curvature, two segments	40.0	42.1	4500 (+ 37 %)

\* The path curvature is always zero

\*\* The curvature constraint was inactive

A comparison of the optimal fundamental frequencies of each path definition for the two different curvature values showed that the value of the maximum curvature had a major influence on the attainable maximum fundamental frequency for the constant angle path and the two-segment constant curvature path. The fundamental frequency for these two paths increased by respectively, 35 and 25 percent when the constraint was relaxed from  $1.57 \text{ m}^{-1}$  to  $4.00 \text{ m}^{-1}$ . The maximum fundamental frequency for the one-segment constant curvature,

path was only slightly influenced by the tighter curvature constraint, while the frequency of the geodesic path was not influenced because of the zero curvature of the path.

The constant curvature path had the highest maximum fundamental frequency of 4447 Hz for a maximum curvature  $\kappa_{\max} = 1.57 \text{ m}^{-1}$ , a 35 percent improvement compared to the best constant-stiffness laminate which had a maximum frequency of 3292 Hz. The curvature constraint of  $1.57 \text{ m}^{-1}$  was active for all configurations. The maximum frequencies of the constant angle path and both constant curvature paths were close when the maximum curvature was relaxed to  $4.00 \text{ m}^{-1}$ , and only the geodesic path, which always has zero curvature, had a slightly lower maximum frequency. The constant angle laminate and the constant curvature laminate with two segments were restricted by the maximum curvature of  $4.00 \text{ m}^{-1}$ . The influence of the curvature constraint on the performance of the conical shell is illustrated by this example, and although for some cones the effect of the curvature constraint was more evident than for others the manufacturability of a cone cannot be ignored during the design.

### 4.4.3 Frequency Results

The optimization results for the rest of the cones of table 4.1 with a curvature constraint of  $4.00 \text{ m}^{-1}$  are given in table 4.5. The last column in table 4.5 gives the percentage increase of the fundamental frequency of the best variable-stiffness laminate, which for all the cases considered was the two-segment constant curvature path design, with respect to the optimum frequency of the constant-stiffness laminate provided in the fifth column. The

Table 4.5: Frequency results, fixed boundaries,  $\kappa_{\max} = 4.00 \text{ m}^{-1}$ ,  $30 \times 100$  finite elements

Cone number	Geodesic		Constant angle		Constant curvature			Constant curvature, two segments			Relative increase (%)
	$T_0$ (°)	$f$ (Hz)	$T_0$ (°)	$f$ (Hz)	$T_0$ (°)	$T_1$ (°)	$f$ (Hz)	$T_0$ (°)	$T_1$ (°)	$f$ (Hz)	
1	60.6	4374	40.3	4488	41.4	42.4	4476	40.0	42.1	4500	0.3
2	60.6	1858	43.8	1837	65.4	28.0	1860	29.0	53.7	1971	7.4
3	89.0	1110	25.6	1123	27.1	25.4	1122	23.3	89.0	1294	15.2
4	47.4	4675	42.4	4705	43.0	42.9	4702	36.8	46.5	4751	1.0
5	35.5	1741	31.0	1748	31.2	31.0	1748	33.0	73.4	1935	10.7
6	39.0	1083	34.5	1082	39.3	30.0	1083	16.8	89.0	1185	9.6
7	42.0	4593	42.0	4593	42.0	42.0	4593	35.5	51.1	4680	1.9
8	37.6	1706	37.6	1706	37.6	37.6	1706	30.0	89.0	1819	6.6
9	40.6	1019	40.6	1019	54.1	28.0	1022	16.4	89.0	1145	12.5
10	32.9	334	32.9	334	33.1	33.1	335	16.6	89.0	393	17.7
11	42.2	227	25.6	227	26.1	25.3	227	15.6	89.0	273	20.4
12	89.0	149	33.9	187	89.0	31.3	186	16.3	88.9	211	12.8

following conclusions can be drawn from the results shown in table 4.5.

1. As stated the variable-stiffness laminate with the optimum two-segment constant curvature variation had a higher fundamental frequency than the optimum constant-stiffness laminate for all cone geometries. The stiffness variation caused a different modal behavior, resulting in a higher fundamental frequency. It is expected that as the number of segments is increased even better designs will be obtained.



2. The geodesic laminates had a lower maximum fundamental frequency than the other path definitions for the cones with larger cone angles, i.e. cones 1, 4 and 12. This can be explained by the fact that if the ratio between the large and the small radius of the cone increases, the fiber orientation angle decreases when moving towards the large radius, i.e.  $\sin \varphi = \frac{r_0 \sin T_0}{r(x)}$ , causing a low stiffness in circumferential direction and consequently causing a lower maximum fundamental frequency.
3. The differences between the geodesic, constant angle and constant curvature cones were relatively small for the cones with small cone angles, i.e. cones 2, 3, 5, 6 and 11. This was due to the similarity of the paths for small cone angles.
4. The geodesic path and the constant angle path were exactly the same for cylinders, i.e. cones 7 through 10, and for these cylinders the best constant curvature path also had zero curvature, which also reduced the constant curvature path to a geodesic path.
5. The improvements of the two-segment constant curvature laminate compared to the constant-stiffness laminate were negligible when the length along the cone surface,  $L$ , was small, i.e. cones 1, 4 and 7. More steering was required to get the desired variation in fiber orientation when the length along the surface was small. The surface length became so small that almost no steering was allowed by the curvature constraint, which especially restricted the angle variation of the two-segment constant curvature variation.
6. The improvements of the variable-stiffness laminates became larger when the overall size of the cone became larger, i.e. cones 10 until 12. This is because curvature no longer restricted the amount of steering of the fiber path that was possible due to the large dimensions of the shell.

## 4.5 Conclusions

The numerical examples discussed above showed that manufacturability can have a large influence on the value of the maximum fundamental frequency of conical and cylindrical composite shells with an axial stiffness variation, and that it is necessary to take the manufacturing constraints into account in the design phase of a variable-stiffness laminate. Furthermore, it was proved that significant improvements in maximizing the fundamental frequency of conical and cylindrical shells can be made by using variable-stiffness laminates, especially for larger cones.

Using multiple-stage angle variations could result in greater improvements, because a multiple-stage variation provides more design freedom when designing composite laminates. In addition to varying only the fiber orientation to change the laminate stiffness, as was done in this chapter, thickness of the laminate could also be varied to change the laminate stiffness locally. Ply repetitions are usually avoided in practical applications and therefore a complete laminate optimization would be the next step for assessing the possible benefits of variable-stiffness composites in the design of conical and cylindrical shells for maximum fundamental frequency. In addition, working with the multiple-segment angle variation could result in larger improvements in structural efficiency if the fiber angle at the

large radius,  $T_2$ , is allowed to differ from the fiber angle at the small radius,  $T_0$ , as opposed to the example shown above.

## Chapter 5

# Optimization of a Cylinder in Bending by Circumferentially Varying Stiffness

### 5.1 Introduction

A cylindrical shell was optimized for buckling under a constant bending moment by varying the fiber angle within a ply as a function of the circumferential coordinate. Tailoring the stiffness in the circumferential direction was expected to lead to improved structural performance, since bending causes loads to vary around the circumference of a cylinder.

Earlier work on circumferential stiffness variation has been done by Tatting (1998) who uses a linear membrane solution to find the optimum fiber angle variation for cylinders with multiple, combined load conditions. He notes that circumferential stiffness variation is most beneficial for load conditions that also contain variation in the circumferential direction. Tatting applied a linear angle variation within segments of the cylinder circumference, in which the design variables could vary in 15 degree increments from one segment to another. Optimization was done using genetic algorithms. Tatting concludes that the stiffness variation of the optimal designs contributes to the increased performance of the cylinder in two ways: i) it lowers the internal loads in the critical areas through redistribution of the stresses; and ii) it provides a relatively stiff region in the cylinder that alters the buckling behavior of the structure.

The difference between the current work and that of Tatting (1998) is that the current design study also included laminates in which courses were allowed to overlap within a single ply, as opposed to laminates with a constant thickness. The exact fiber angle variation based on manufacturing by fiber placement was included explicitly in the finite element implementation. Furthermore, the influence of strength constraints and manufacturing constraints on the optimum buckling moment were investigated in preparation for manufacturing and testing of one of the variable-stiffness designs.

## 5.2 Design and Optimization Formulation

### 5.2.1 Definition of the Optimization Problem

The objective of the design study was to maximize the buckling load of a cylinder with a diameter of 610 mm (24 in) and a length of 813 mm (32 in) in bending by varying the fiber orientation in the circumferential direction, see figure 5.1(a). The design variables were defined by  $T_i^k$ , where  $k$  represents the ply number and  $i$  the location of the design variable  $T$  within that ply, as shown in figure 5.1(b).

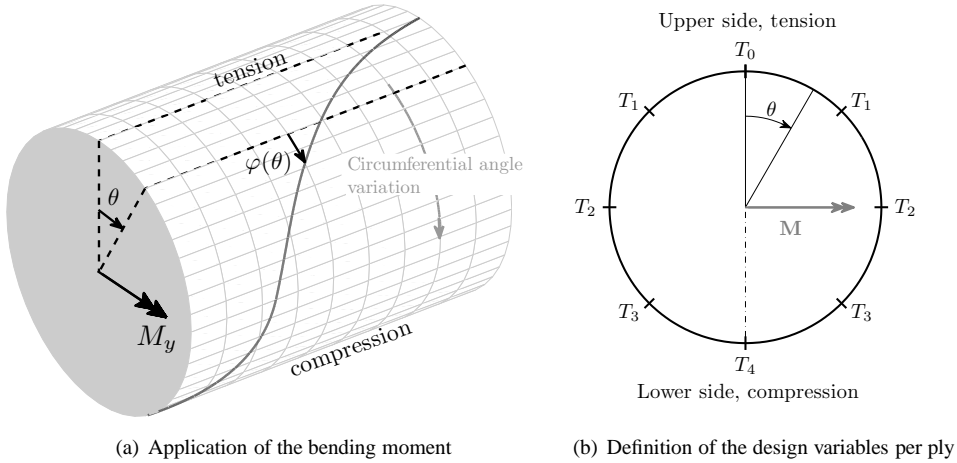


Figure 5.1: Schematic view of loading conditions and design parameters

Three different optimization problems were considered:

1. optimization of the buckling load, with a constraint on the minimum value of the fiber angle:

maximize	$\frac{M_{cr}}{\bar{M}_{cr}}$	for constant-thickness laminates for overlap laminates
subjected to	$T_i^k \geq 1^\circ$	for $i = 0, 1, 2, 3$ and $4$ , and $k = 1, \dots, N_p$ for constant-thickness laminates
	$T_i^k \geq 10^\circ$	for $i = 0, 1, 2, 3$ and $4$ , and $k = 1, \dots, N_p$ for overlap laminates

(5.1)

2. optimization of the buckling load, while taking manufacturing constraints and strength

into account:

$$\begin{array}{lll}
 \text{maximize} & \begin{array}{l} M_{cr} \\ \overline{M}_{cr} \end{array} & \begin{array}{l} \text{for constant-thickness laminates} \\ \text{for overlap laminates} \end{array} \\
 \text{subjected to} & \begin{array}{l} T_i^k \geq 10^\circ \\ |\kappa_i^k| \leq \kappa_{\max} \\ M_f \geq M_{cr} \end{array} & \begin{array}{l} \text{for } i = 0, 1, 2, 3 \text{ and } 4, \text{ and } k = 1, \dots, N_p \\ \text{for } i = 0, 1, 2 \text{ and } 3, \text{ and } k = 1, \dots, N_p \\ \text{in all elements} \end{array}
 \end{array} \quad (5.2)$$

3. optimization of the buckling load, including manufacturing constraints, strength, local and global stiffness constraints:

$$\begin{array}{lll}
 \text{maximize} & M_{cr} & \\
 \text{subjected to} & \begin{array}{l} T_i^k \geq 10^\circ \\ |\kappa_i^k| \leq \kappa_{\max} \\ M_f \geq M_{cr} \\ E_d \geq E_{\min} \\ EI \geq 0.95EI_b \end{array} & \begin{array}{l} \text{for } i = 0, 1, 2, 3 \text{ and } 4, \text{ and } k = 1, \dots, N_p \\ \text{for } i = 0, 1, 2 \text{ and } 3, \text{ and } k = 1, \dots, N_p \\ \text{in all elements} \\ \text{for } d = 0^\circ, 90^\circ, +45^\circ, -45^\circ, \text{ in all elements} \end{array}
 \end{array} \quad (5.3)$$

A distinction was made, in chapter 3, between variable-stiffness laminates that have a constant thickness and those that allow overlap between courses. The optimization results for the first group are presented in section 5.3, the optimization results for the overlap laminates are presented in section 5.4. The structural mass of the constant-thickness laminates was identical to that of the baseline cylinder, allowing a direct comparison of the buckling load  $M_{cr}$ . A new objective function, the specific buckling moment  $\overline{M}_{cr} = \frac{M_{cr}}{m}$ , was introduced for the overlap laminates to account for the structural mass added by allowing courses to overlap within a ply, where  $m$  is the cylinder mass.

Optimization case 1 was focused on maximizing the buckling load under bending with a constraint on the minimum value of the fiber angle. The fiber angle for the constant-thickness laminates was required to be equal or larger than  $1^\circ$ , which arose from the ply definition for circumferential angle variation that was described in section 3.3.3. The fiber path does not continue around the circumference when one of the design variables is  $0^\circ$ , causing numerical problems in the calculation of the ply properties. For this reason the design variables were required to be equal or larger than  $1^\circ$ .

The minimum fiber angle orientation for the overlap laminates was set to  $10^\circ$ , because a minimum fiber angle of  $1^\circ$  could possibly result in a ply thickness of 58 layers locally, see appendix C, producing unrealistic designs. The maximum number of overlaps within one ply was reduced to 6 by setting the minimum fiber angle to  $10^\circ$ , resulting in feasible designs.

The last constraint of this optimization case required the buckling load  $M_{cr}$  to be lower than the bending moment at which material failure occurred,  $M_f$ , to ensure that the cylinder was buckling critical and not strength critical. The strength constraint was implemented using a strain-equivalent Tsai-Wu criterion for each of the elements in the finite element model. The strain-equivalent Tsai-Wu criterion, developed by IJsselmuiden et al. (2008),

makes the stress-based first-ply Tsai-Wu failure criterion independent of the fiber orientations within the laminate. A conservative failure envelope was defined and a failure index was formulated that can be related to the factor of safety. The details of the strain-equivalent Tsai-Wu criterion are given in appendix E. A unit bending moment was applied to the cylinder in the finite element analysis and the safety factor was calculated for each element. The smallest safety factor over all elements then represented the load at which material failure would first occur,  $M_f$ .

The laminate strength of the variable-stiffness laminates was calculated in the same way as that of the traditional  $0^\circ$ ,  $90^\circ$  and  $\pm 45^\circ$  laminates. The strength of the variable-stiffness laminates is likely to be affected by the presence of tow drops and overlaps, which may weaken the laminate locally, and possibly by the curvature of the fibers. These effects were not taken into account during the optimization. Further research is needed to address these issues.

The third optimization case included two stiffness constraints in addition to the manufacturing and strength constraints of optimization case 2. The first stiffness constraint required the equivalent laminate stiffnesses in the  $0^\circ$ ,  $90^\circ$  and  $\pm 45^\circ$  directions to be larger than a minimum value  $E_{\min} = 29$  GPa. The lower limit on the laminate stiffnesses was meant to provide robustness to the laminate in case holes are needed for fasteners and can be regarded as an equivalent to the 10 percent rule that currently exists for traditional laminates. The constraint was calculated at each element because each element had a unique stacking sequence.

The second stiffness constraint that was added was a global stiffness constraint. The bending stiffness of the variable-stiffness cylinder  $EI_v$  was required to be at least 95 percent of the bending stiffness of the baseline cylinder  $EI_b$ .

The third optimization case was not considered for designs with overlap, because the overlapping courses have similar fiber orientations, resulting in a laminate stack that is biased in one direction. Limiting the equivalent in-plane stiffness in the  $0^\circ$ ,  $90^\circ$  and  $\pm 45^\circ$  directions would therefore eliminate too many designs to be interesting.

## 5.2.2 Optimization Using a Surrogate Model

The optimization was performed using the surrogate model optimizer in Design Explorer (Audet et al., 2000; Booker et al., 1999) to minimize the number of finite element (FE) analyses. A general overview of the optimization process is shown in figure 5.2(a). A design of experiments was generated first to sample the design space systematically. Secondly, surrogate Kriging models (Matheron, 1965; Watson, 1984) were constructed to approximate the responses given by the detailed finite element analyses. These models were used to analyze the influence of the design variables on the responses, and to serve as a basis for the optimization. After the design of experiments was performed, the optimizer selected a set of points that served as a starting point for a local poll to refine the surrogate model near these optimum points. Additional points, determined using orthogonal array-based Latin hypercubes, were evaluated using the FE analysis to improve the surrogate model on a global level and to reduce the chances of ending up in a local optimum. The models were updated once the new results were added and a new iteration was started, until one of the termination criteria was met. The optimization algorithm is shown in figure 5.2(b). The termination criteria were defined in terms of a maximum number of iterations, a maximum

number of function evaluations or a maximum number of random grid point searches. After the optimization was finished, convergence of the objective function was examined and if convergence was not reached the optimization was restarted while loosening the termination criterion that caused the optimization to finish.

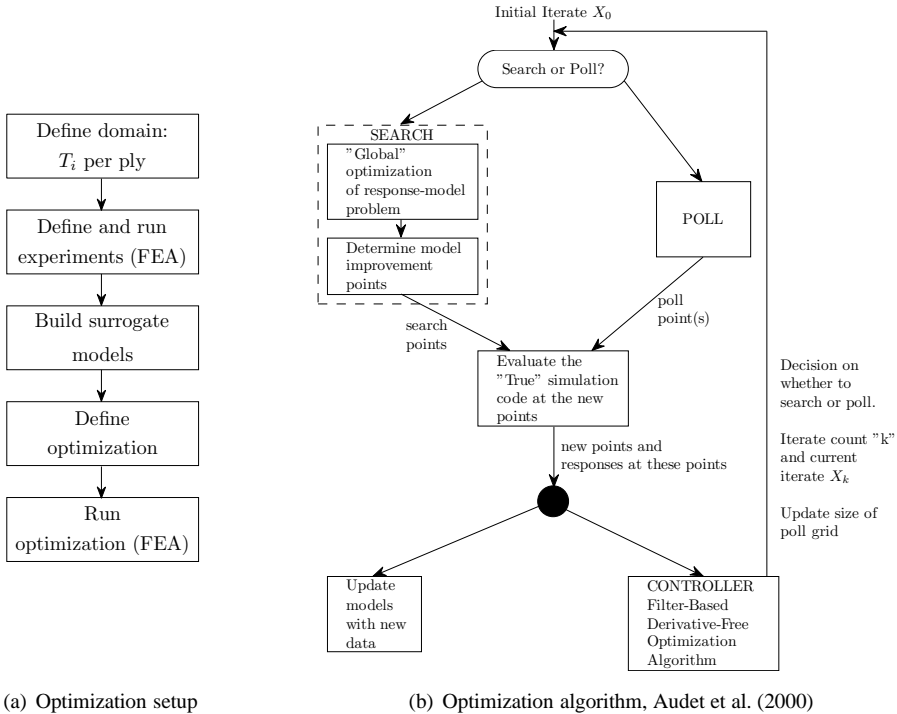


Figure 5.2: Optimization process

The surrogate model optimizer was selected for the design problem under consideration, because derivative information needed for the optimization could be taken from the surrogate models, removing the need to determine the derivatives using finite differences. The structure was optimized for the lowest buckling load and therefore the objective function might not have been completely smooth due to changes of the first buckling mode between different designs. In addition, strength and effective stiffness were determined for each element, after which the most critical value over the entire domain was used to evaluate the constraints. This could also have introduced irregularities in the constraint functions. The surrogate models introduced smoothness and filtered out noise that could be present in the objective and constraint functions.

### 5.2.3 Laminate Design

The laminate was 24 plies thick, symmetric and balanced. Each end of the cylinder was attached to a rigid end plate, such that the edges of the cylinder were clamped to the plate, while the plates were able to move. Opposite and equal bending moments were applied

to the centers of the plates. A linear bifurcation analysis using the finite element program ABAQUS was applied to calculate the buckling moment. The varying stiffness was implemented in the finite element model as described in section 4.3. The finite element model consisted of 71 elements in the axial direction and 170 elements in the circumferential direction, which was sufficient to capture the varying stiffness and the buckling modes.

The material used for the design study was a typical graphite-epoxy AS4/855-2 (Lopes et al., 2007) for which the mechanical and strength properties are given in table 5.1. Part of the optimization was repeated for another graphite-epoxy material system, BMS8-276, to decide on the layup to be manufactured, because BMS8-276 was used for the manufacturing of the variable-stiffness cylinder. The results of that optimization are summarized in subsection 5.3.4.

*Table 5.1: AS4/855-2 Mechanical properties (Lopes et al., 2007)*

$E_1$	129.8 GPa
$E_2$	9.1 GPa
$G_{12}$	5.3 GPa
$\nu_{12}$	0.32
$t_{ply}$	0.183 mm
$\rho$	1589 kg/m <sup>3</sup>
$X_t$	2070 MPa
$X_c$	1160 MPa
$Y_t$	132.7 MPa
$Y_c$	199.8 MPa
$S$	117.1 MPa

A conventional 24-ply laminate consisting of 0, 90 and  $\pm 45$  degree plies was optimized for buckling under bending to serve as a baseline design. The outer plies were defined to be  $\pm 45^\circ$  for robustness against impact. Furthermore the laminate was required to be symmetric and balanced to avoid extension-shear and extension-bending coupling. The laminate was balanced by tying a  $+45^\circ$  ply to a  $-45^\circ$  ply in the laminate definition. The 10 percent rule was also applied. This rule is standard in the aerospace industry and requires a laminate to contain at least 10 percent of each of the four standard orientations:  $0^\circ$ ,  $90^\circ$  and  $\pm 45^\circ$ . Finally, 4 consecutive plies with the same orientation angle were not allowed in the laminate stack.

The variable-stiffness laminates also consisted of 24 plies, of which the outer plies were  $\pm 45^\circ$ . The inner plies were allowed to be either steered, i.e.  $\pm\varphi(\theta)$ , or a combined stack of  $0^\circ$  and  $90^\circ$ , resulting in a hybrid laminate with both straight and steered plies. The combination of  $+\varphi(\theta)$  with  $-\varphi(\theta)$  plies ensured that the laminate was locally balanced. In addition, the laminate was designed to be symmetric. A selection of the available stacking sequences was made to reduce the overall optimization effort. The stacking sequences that were optimized are listed in table 5.2. Straight-fiber laminates with fiber orientations other than  $0^\circ$ ,  $90^\circ$ ,  $+45^\circ$  or  $-45^\circ$  were also optimized. The variable-stiffness laminates are denoted by "VS" in table 5.2. Note that  $\varphi$  represents a ply with varying fiber orientations. The non-traditional, straight-fiber laminates are denoted by "CS" (constant stiffness) and  $\phi$  represents a constant-angle ply with a non-traditional fiber orientation.



Table 5.2: Variable-stiffness laminate definitions

Laminate number	Ply number (half of the symmetric layup)											
	1	2	3	4	5	6	7	8	9	10	11	12
CS-1	+45	-45	$+\phi_1$	$-\phi_1$	$+\phi_2$	$-\phi_2$	$+\phi_3$	$-\phi_3$	$+\phi_4$	$-\phi_4$	$+\phi_5$	$-\phi_5$
CS-2	+45	-45	$+\phi_1$	$-\phi_1$	0	90	$+\phi_3$	$-\phi_3$	0	90	$+\phi_5$	$-\phi_5$
CS-3	+45	-45	0	90	$+\phi_2$	$-\phi_2$	0	90	$+\phi_4$	$-\phi_4$	0	90
VS-1	+45	-45	$+\varphi_1$	$-\varphi_1$	$+\varphi_2$	$-\varphi_2$	$+\varphi_3$	$-\varphi_3$	$+\varphi_4$	$-\varphi_4$	$+\varphi_5$	$-\varphi_5$
VS-2	+45	-45	$+\varphi_1$	$-\varphi_1$	0	90	$+\varphi_3$	$-\varphi_3$	0	90	$+\varphi_5$	$-\varphi_5$
VS-3	+45	-45	0	90	$+\varphi_2$	$-\varphi_2$	0	90	$+\varphi_4$	$-\varphi_4$	0	90
VS-4	+45	-45	$+\varphi_1$	$-\varphi_1$	$+\varphi_2$	$-\varphi_2$	$+\varphi_1$	$-\varphi_1$	$+\varphi_2$	$-\varphi_2$	$+\varphi_1$	$-\varphi_1$
VS-5	+45	-45	$+\varphi_1$	$-\varphi_1$	$+\varphi_1$	$-\varphi_1$	$+\varphi_1$	$-\varphi_1$	$+\varphi_1$	$-\varphi_1$	$+\varphi_1$	$-\varphi_1$

The cylinder was divided into 8 segments around the circumference for the design of a steered ply, thus requiring 8 design variables per ply. The structure was assumed to be symmetric about the longitudinal vertical plane, since the loading condition was also symmetric with respect to this plane, and therefore the 8 design variables could be reduced to 5. These variables are shown in a cross-sectional view of the cylinder in figure 5.1(b). The design variables  $T_0$  and  $T_1$  are located on the tension side of the cylinder,  $T_2$  is located near the neutral axis, while  $T_3$  and  $T_4$  are on the compression side of the cylinder. The path definition that was used in the optimization was the constant curvature path, described in subsection 3.4.4, because evaluation of the curvature constraint for the constant curvature path definition was more straightforward than for the linear angle variation.

## 5.3 Optimization Results for Laminates with a Constant Thickness

### 5.3.1 Optimization Case 1

The results for optimization case 1, which only included minimum fiber angle constraints, are given in table 5.3. The laminate numbers correspond to the constant-stiffness and variable-stiffness laminates listed in table 5.2. The optimum baseline was determined to be a quasi-isotropic layup with a stacking sequence:  $[\pm 45, 0_2, \pm 45, 90, 0, 90, \pm 45, 90]_s$ . The constant-stiffness cylinders with non-traditional fiber orientations had buckling moments comparable to the buckling moment of the baseline cylinder. The ply angles for these laminates are listed in appendix D. A theoretical estimate of the buckling load under pure bending for relatively short cylinders,  $M_{th}$ , is given in the third column of table 5.3. The theoretical buckling load was calculated for the baseline and constant-stiffness cylinders using the following equation (Fuchs et al., 1997; Seide and Weingarten, 1961):

$$M_{th} = 2\pi R \sqrt{E_\theta t D_{11}} \quad (5.4)$$

where  $E_\theta$  is the equivalent laminate stiffness in the circumferential direction of the cylinder,  $t$  is the laminate thickness and  $D_{11}$  is the laminate bending stiffness in the axial direction. A good agreement was found between the buckling moment obtained by the finite element analysis and the theoretical buckling moment.

The improvements in buckling load of the non-conventional constant-stiffness and the

Table 5.3: Optimization results for case 1 with baseline:  $[\pm 45, 0_2, \pm 45, 90, 0, 90, \pm 45, 90]_s$ 

Laminate number	Buckling moment $M_{cr}$ (kNm)	Theoretical buckling moment $M_{th}$ (kNm)	Comparison with baseline $(M_{cr}/M_b) \cdot 100\%$	Material failure moment $M_f$ (kNm)	Comparison with baseline $(M_f/M_{fb}) \cdot 100\%$
Baseline	627	623	100	575	100
CS-1	628	627	100	455	79
CS-2	623	628	99	560	97
CS-3	601	614	96	567	99
VS-1	809	-	129	478	83
VS-2	797	-	127	582	101
VS-3	724	-	115	682	119
VS-4	807	-	129	304	53
VS-5	707	-	113	237	41

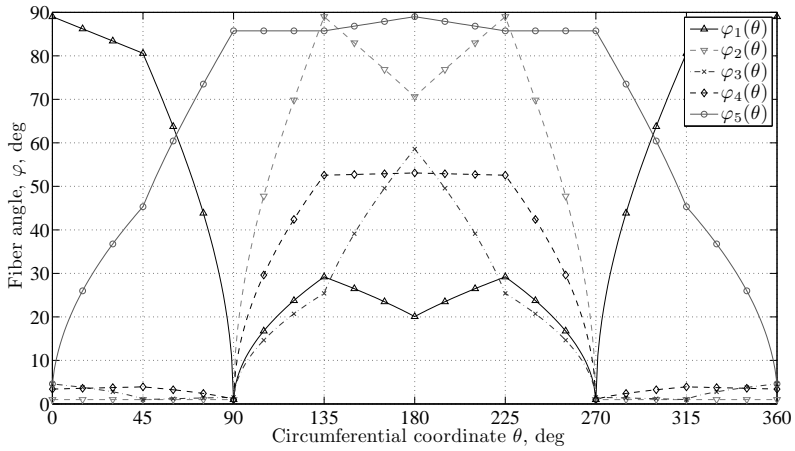
variable-stiffness cylinders compared to the baseline cylinder are given in the fourth column of table 5.3. The largest improvement in buckling load was achieved by cylinder VS-1, the variable-stiffness cylinder with 5 different steered plies, closely followed by VS-4 with two different, repeated steered plies and the hybrid laminate VS-2 which contained  $0^\circ$  and  $90^\circ$  plies in addition to three different steered plies.

Laminate VS-1 is used to illustrate the mechanisms behind the improved buckling load. Subsequently the different variable-stiffness laminates are compared. The optimized design variables for laminate VS-1 with the layup  $[\pm 45, \pm \varphi_1, \pm \varphi_2, \pm \varphi_3, \pm \varphi_4, \pm \varphi_5]_s$  are listed in table 5.4.

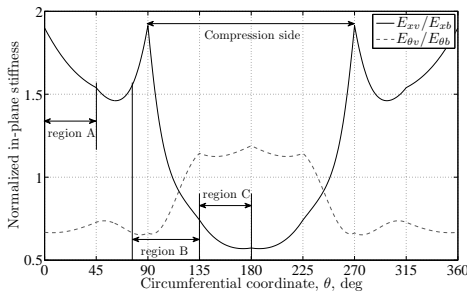
Table 5.4: Design variables for laminate VS-1, case 1

Ply	$T_0$ ( $^\circ$ )	$T_1$ ( $^\circ$ )	$T_2$ ( $^\circ$ )	$T_3$ ( $^\circ$ )	$T_4$ ( $^\circ$ )
$\varphi_1(\theta)$	89.0	80.6	1.0	29.2	20.1
$\varphi_2(\theta)$	1.0	1.0	1.0	89.0	70.6
$\varphi_3(\theta)$	4.6	1.0	1.5	25.4	58.6
$\varphi_4(\theta)$	3.4	3.9	1.0	52.6	53.1
$\varphi_5(\theta)$	4.6	45.3	85.7	85.7	89.0

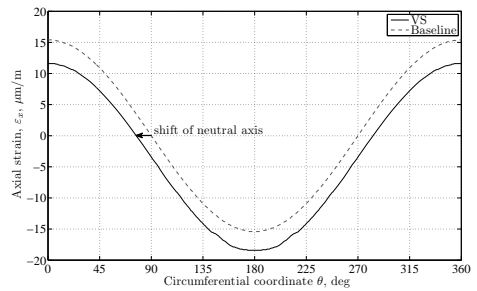
The fiber angle variations that correspond to the design variables of table 5.4 are plotted in figure 5.3(a) and the variations of the axial stiffness  $E_x$  and the circumferential stiffness  $E_\theta$  with the circumferential coordinate are shown in figure 5.3(b), where they are normalized with the in-plane stiffnesses of the baseline laminate (subscript  $b$ ). The axial stiffness of the variable-stiffness cylinder was significantly larger on the tension side and at the neutral axis than the axial stiffness of the baseline cylinder, i.e. at  $0^\circ < \theta < 110^\circ$ , while the stiffness on the compression side was smaller than that of the baseline. Consequently the neutral axis of the cylinder was shifted toward the tension side, from  $\theta = 90^\circ$  to  $\theta = 77^\circ$ . The shift in neutral axis can be seen in the plot of the axial strain distribution, figure 5.3(c). The strain distributions of the variable-stiffness and the baseline cylinder follow elementary beam theory, because the clamped boundary conditions force the cross-section to remain in



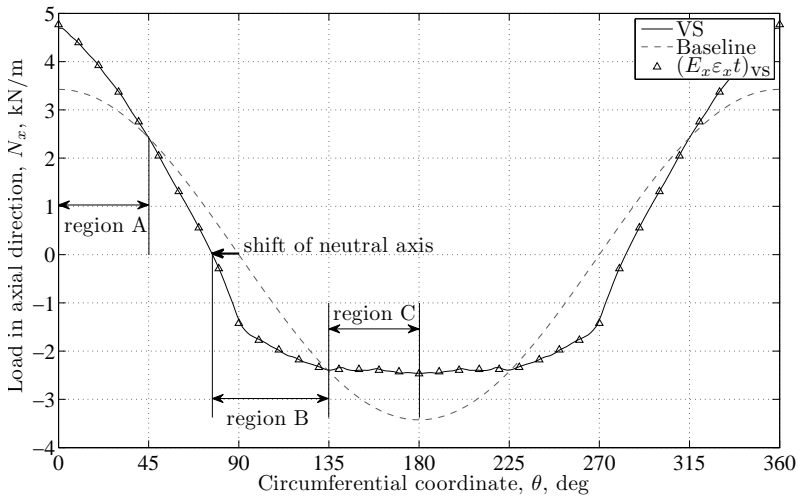
(a) Fiber angle variation per ply



(b) Stiffness variation



(c) Axial strains



(d) Axial loads

Figure 5.3: Results for laminate VS-1, case 1, 1 kNm bending moment

one plane:

$$\varepsilon(\theta) = \frac{M_y z}{\overline{EI}_y} = \frac{M_y(R \cos \theta - z_{NA})}{\overline{EI}_y} \quad (5.5)$$

where  $\overline{EI}_y$  is the average bending stiffness,  $M_y$  is the applied bending moment,  $R$  is the cylinder radius and  $z_{NA}$  is the vertical coordinate of the neutral axis with respect to the geometric center of the cylinder cross-section at  $\theta = 90^\circ = 270^\circ$ . The offset of the vertical coordinate  $z$  caused a vertical shift of the variable-stiffness strain distribution with respect to the baseline strain distribution. The compressive strains of the variable-stiffness cylinder were thus larger than those of the baseline cylinder, while the tensile strains of the variable-stiffness cylinder were smaller.

The distribution of the axial load,  $N_x$ , depended both on the stiffness distribution and on the strain distribution with the circumferential coordinate:

$$\begin{Bmatrix} N_x \\ N_y \\ N_{xy} \end{Bmatrix} = \begin{bmatrix} A_{11} & A_{12} & A_{16} \\ A_{12} & A_{22} & A_{26} \\ A_{16} & A_{26} & A_{66} \end{bmatrix} \begin{Bmatrix} \varepsilon_x^0 \\ \varepsilon_y^0 \\ \gamma_{xy}^0 \end{Bmatrix} + \begin{bmatrix} B_{11} & B_{12} & B_{16} \\ B_{12} & B_{22} & B_{26} \\ B_{16} & B_{26} & B_{66} \end{bmatrix} \begin{Bmatrix} \kappa_x \\ \kappa_y \\ \kappa_{xy} \end{Bmatrix} \quad (5.6)$$

and

$$\begin{Bmatrix} M_x \\ M_y \\ M_{xy} \end{Bmatrix} = \begin{bmatrix} B_{11} & B_{12} & B_{16} \\ B_{12} & B_{22} & B_{26} \\ B_{16} & B_{26} & B_{66} \end{bmatrix} \begin{Bmatrix} \varepsilon_x^0 \\ \varepsilon_y^0 \\ \gamma_{xy}^0 \end{Bmatrix} + \begin{bmatrix} D_{11} & D_{12} & D_{16} \\ D_{12} & D_{22} & D_{26} \\ D_{16} & D_{26} & D_{66} \end{bmatrix} \begin{Bmatrix} \kappa_x \\ \kappa_y \\ \kappa_{xy} \end{Bmatrix} \quad (5.7)$$

where

$$\begin{aligned} A_{ij} &= \sum_{k=1}^N S_{ij}^{(k)} (z_k - z_{k-1}) \\ B_{ij} &= \sum_{k=1}^N S_{ij}^{(k)} (z_k^2 - z_{k-1}^2) \\ D_{ij} &= \sum_{k=1}^N S_{ij}^{(k)} (z_k^3 - z_{k-1}^3) \end{aligned} \quad (5.8)$$

The applied bending moment mainly caused axial loads in the cylinder skin, such that the relation between  $N_x$  and the laminate stiffness could be approximated by:

$$N_x(\theta) \approx E_x(\theta) \varepsilon_x(\theta) t \quad (5.9)$$

where  $E_x$  is the equivalent laminate stiffness in the axial direction, obtained from the inverse of the ABD matrix. The baseline cylinder had a constant stiffness  $E(\theta) = E_b$  and a constant thickness  $t$ , such that the load distribution was scaled with the strain distribution and the shape of the two distributions was the same. The stiffness variation and strain distribution of the variable-stiffness cylinder resulted in an irregular load distribution, as shown in figure 5.3(d). Both the exact load distribution and the approximation to the load distribution for the variable-stiffness cylinder are shown in figure 5.3(d). The load distribution of the variable-stiffness cylinder contained three distinct regions that are discussed here: regions A, B and C, which are indicated in figures 5.3(b) and 5.3(d). The tensile loads carried by the variable-stiffness cylinder in region A were significantly higher than those carried by the baseline cylinder due to the high stiffness in this region, up to 1.8 times the stiffness of the baseline. The shift of the neutral axis resulted in compressive loads in region B for the

variable-stiffness cylinder, while the loads of the baseline cylinder were both tensile and compressive here. The large peak in the axial stiffness at  $\theta = 90^\circ$  made the material in region B even more effective for carrying the compressive loads. The low axial stiffness of the variable-stiffness cylinder in region C resulted in a flattening of the load curve on the compression side of the cylinder, yielding compressive load values almost 30 percent smaller compared to the loads carried by the baseline cylinder.

The buckling modes were also affected by the non-uniform stiffness distribution, in addition to the value of the buckling moment. The first buckling mode of the baseline

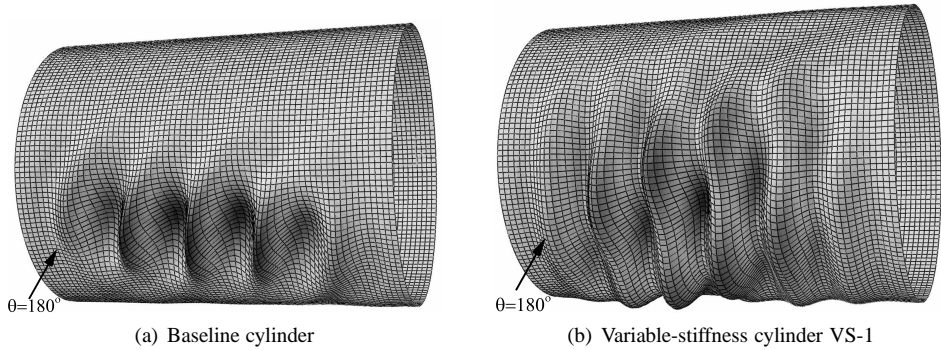


Figure 5.4: First buckling modes of the baseline cylinder and VS-1, optimization case 1

cylinder, shown in figure 5.4(a), consisted of 5 full waves in the axial direction and one local half wave in the circumferential direction. The first buckling mode of the variable-stiffness cylinder, shown in figure 5.4(b) consisted of 6 full waves in the axial direction and 3 local half waves in the circumferential direction. The most striking difference between the two buckling modes was the area that was covered by the buckles, which influenced the value of the buckling load. The buckles of the variable-stiffness cylinder covered a larger section of the cylinder than the buckles of the baseline. This is a direct consequence of the non-uniform stiffness distribution that spread out the compressive load peak over a larger section of the cylinder. A similar effect has been shown by Sun and Hyer (2008) for elliptical cylinders in pure compression where a circumferential stiffness variation was used to make the entire cylinder participate in the buckling deformations.

The load distributions of all the variable-stiffness cylinders and the baseline cylinder are shown in figure 5.5 and the first buckling modes of cylinders VS-2 through VS-5 are given in figures 5.6(a) until 5.6(d). The values of the design variables corresponding to designs VS-2 through VS-5 are listed in appendix D.

The buckling load values of cylinders VS-1, VS-2 and VS-4 were nearly identical, see table 5.3, and the load distributions of these three cylinders were also similar. The load distribution curve of all three cylinders was relatively flat near  $\theta = 180^\circ$ , with slightly larger compressive loads towards the sides of the cylinder, at  $\theta \approx 135 = 225^\circ$  for cylinders VS-1 and VS-2, and at  $\theta \approx 100 = 160^\circ$  for cylinder VS-4. The first buckling mode of cylinders VS-1 and VS-2 both had 3 half waves in the circumferential direction, almost as if two buckling modes were mixed. Cylinder VS-4 contained a local buckling pattern on the sides in addition to the main, diagonal buckling pattern, see figure 5.6(c). These local buckling

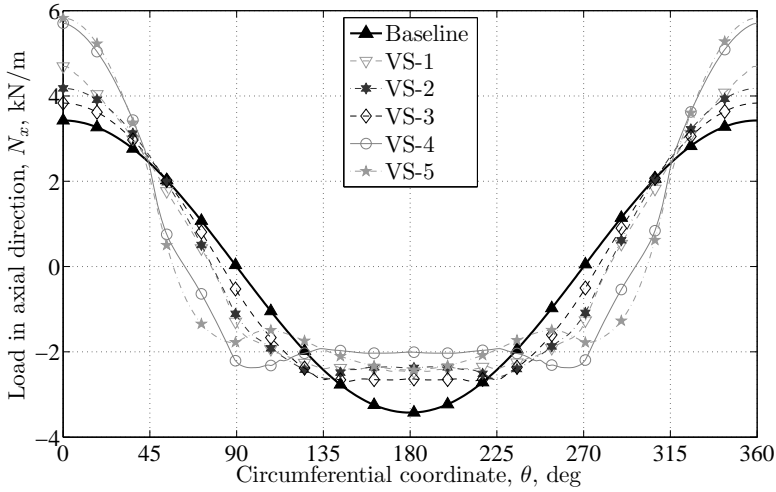


Figure 5.5: Axial load distribution for all variable-stiffness cylinders, optimization case 1

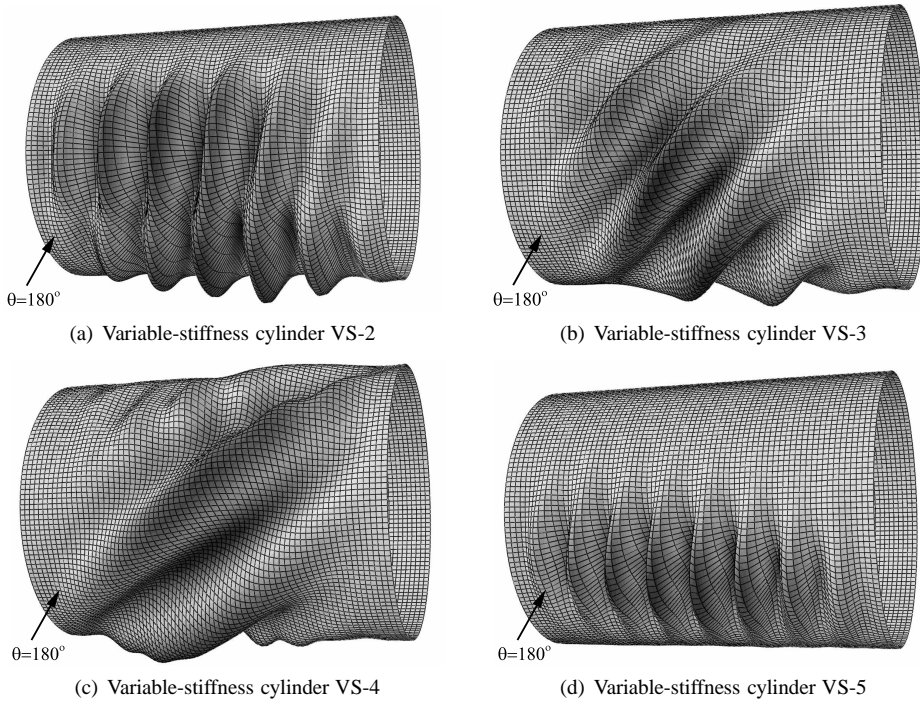


Figure 5.6: First buckling modes of the variable-stiffness cylinders, optimization case 1

deformations were caused by the higher compressive loads at  $\theta \approx 100 = 160^\circ$ . The diagonal pattern of the variable-stiffness cylinders may have been caused by bending-twist coupling due to the presence of non-zero  $D_{16}$  and  $D_{26}$  terms in the laminate stiffness matrix.

The VS-3 cylinder also exhibited a flattening of the load curve on the compression side of the cylinder, but the overall area over which the compressive load was distributed was smaller than for the other cylinders. The first buckling mode of cylinder VS-3, see figure 5.6(b), did not show any mixed modes, because no locally higher loads were present in the load distribution of this cylinder, as was the case for cylinders VS-1, VS-2 and VS-4. The compressive load peak was also higher than that of the other variable-stiffness cylinders and as a consequence the buckling load of cylinder VS-3 was smaller than those of cylinders VS-1, VS-2 and VS-4, i.e. the improvement with respect to the baseline cylinder was 15 percent.

Cylinder VS-5 showed the smallest improvement compared to the baseline cylinder. The first buckling mode of this cylinder, see figure 5.6(d), was confined to a smaller area than for the other variable-stiffness cylinders, which can be explained by looking at the load distribution of cylinder VS-5. The compressive load peak is significantly reduced compared to the baseline cylinder, but the maximum compressive loads were confined to a relatively small region near  $\theta = 180^\circ$ . The difference in buckling load carrying capability may have been caused by large Poisson's ratios present in laminate VS-5. The distributions of the Poisson's ratio of all variable-stiffness cylinders are plotted in figure 5.7, where they are normalized with the Poisson's ratio of the baseline cylinder.

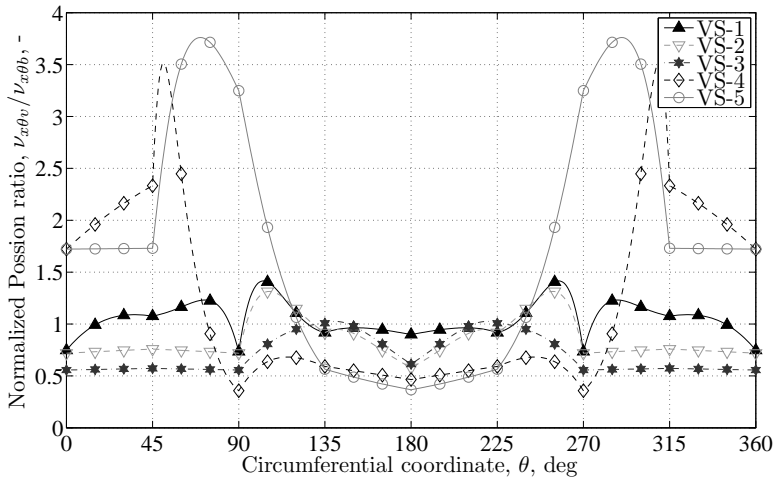


Figure 5.7: Distribution of the Poisson's ratio, optimization case 1

The results presented above were focused on the buckling performance of cylinders with various stiffness distributions. Strength and manufacturability of the obtained designs will be discussed here briefly to show possible shortcomings, although no constraints on strength or manufacturability were included in the optimization.

The bending moment at which material failure would occur for the baseline, the non-traditional constant-stiffness, and the variable-stiffness cylinders are listed in the fifth column of table 5.3, and a comparison with the failure load of the baseline cylinder is given in the last column. The results in table 5.3 show that only cylinders VS-2 and VS-3 performed better than the baseline in terms of strength, and that cylinders VS-4 and VS-5 had only 53 and 41 percent of the baseline strength. This can be explained by looking at the axial and

the circumferential strain distributions of the variable-stiffness cylinders, given in figure 5.8. The shear strains are not shown here, because they are an order of magnitude smaller than the axial and the circumferential strains.

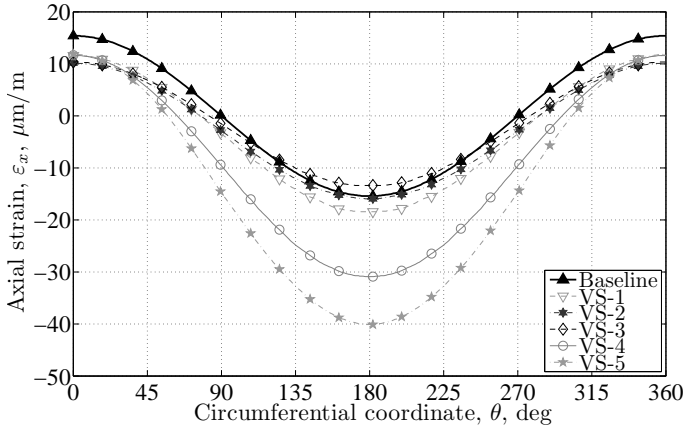
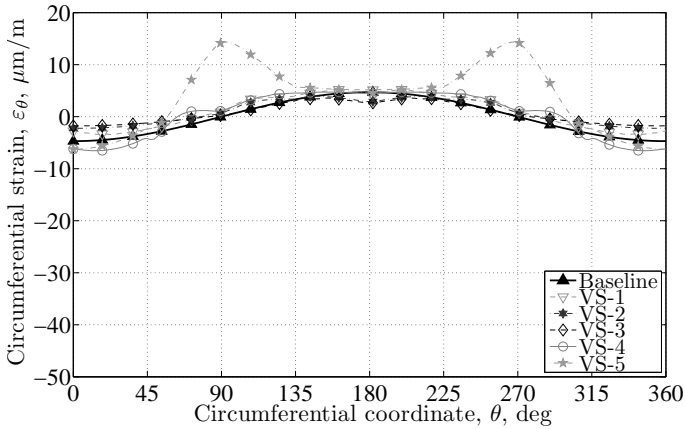
(a) Axial strain,  $\varepsilon_x$ (b) Circumferential strain,  $\varepsilon_\theta$ 

Figure 5.8: Strain distributions for all variable-stiffness cylinders, optimization case 1

All cylinders were critical on the compression side,  $\theta = 180^\circ$ , where the axial strains were the largest. Cylinders VS-1, VS-4 and VS-5 had larger compressive axial strains than the baseline cylinder at this location, while the circumferential strains were the same. These larger axial strains caused the lower material failure loads. Cylinders VS-2 and VS-3 had similar or smaller axial strain values at  $\theta = 180^\circ$ , and smaller strain values in the circumferential direction, leading to higher failure loads compared to the baseline cylinder. The strain distribution in the circumferential direction depended on the strains in the axial direction and on the distribution of the Poisson's ratio around the circumference. The distributions of the Poisson's ratio of all variable-stiffness cylinders are plotted in figure 5.7. The Poisson's ratio of the variable-stiffness cylinders VS-2 and VS-3 near  $\theta = 180^\circ$  was smaller than the Poisson's ratio of the baseline cylinder, such that the induced circumferential strains there



were also smaller.

Based on both strength and buckling values cylinder VS-2, with a 27 percent increase in buckling load and 1 percent increase in material failure load with respect to the baseline, and cylinder VS-3, with a 15 percent increase in buckling load and 19 percent increase in material failure load with respect to the baseline, would be the best candidate designs, because they improve both strength and buckling loads. One drawback of the designs obtained is that all the cylinders would fail due to material failure before they would buckle, assuming that buckling did not occur below the linear bifurcation point. The intension was to manufacture and mechanically test the baseline cylinder and one of the variable-stiffness designs and therefore it was undesirable to have cylinders that were critical for material failure instead of buckling.

Two constraints should be taken into account in the optimization of constant-thickness, variable-stiffness laminates to ensure manufacturability. The first one, the curvature constraint, was violated by all the variable-stiffness cylinders, with the exception of cylinder VS-3. The second constraint is imposed by manufacturing efficiency. The fiber angle variation causes the distance between course centerlines to vary and if a constant-thickness laminate is required the course width also needs to vary to account for these changes. The course width needs to be decreased when the course centerlines converge, while wider courses are needed when the centerlines diverge. The width of a course cannot be reduced beyond one tow, while manufacturing efficiency and laminate quality would probably require a minimum of 5 or 6 tows to be laid down at once. The derivation of the constraint to avoid fiber courses that are too narrow is given in appendix C.

The course centerlines of the 5 steered plies of cylinder VS-1 are shown in figure 5.9 to illustrate the problem of converging centerlines. The fiber paths for both the positive and the negative fiber angle variations are shown for each steered ply. The first steered ply,  $\varphi_1(\theta)$ , shows some convergence of the fiber courses near  $\theta = 90^\circ$  and  $\theta = 270^\circ$ , where the fiber angle is  $1^\circ$ . The path centerlines in plies 2, 3 and 4 are closely spaced between  $\theta = 0^\circ$  and  $\theta = 90^\circ$  and  $\theta = 270^\circ$  and  $\theta = 360^\circ$ , due to the small fiber angles in these regions. Ply 5 shows the least convergence of fiber courses, but even for this ply the course width near  $\theta = 0^\circ$  would be in the order of 5 tows if a maximum course width of 32 tows is assumed.

All variable-stiffness cylinders contain plies with fiber angles of  $1^\circ$  and therefore have the same problems with converging fiber courses, prohibiting manufacturability. The problem of extreme path convergence was solved in the next optimization case by requiring a minimum fiber orientation angle of  $10^\circ$  for the steered plies. In addition, the curvature constraint was implemented to guarantee manufacturability, and a strength constraint was included to ensure the cylinders were buckling critical instead of strength critical.

### 5.3.2 Optimization Case 2

The results for optimization case 2, which also included strength and manufacturability constraints, are given in table 5.5. The design variables corresponding to the designs in table 5.5 are given in appendix D. The baseline laminate was different from the baseline laminate of optimization case 1 due to the strength constraint that was introduced. The new baseline laminate was  $[\pm 45, 0_2, \pm 45, 0_2, 90, \pm 45, 90]_s$ . The buckling loads of all laminates decreased compared to the buckling loads of case 1. The constant-stiffness laminates had slightly higher buckling loads than the baseline laminate, as opposed to optimization case 1,

where the baseline laminate performed better than the constant-stiffness laminates. This is because the strength constraint limited the feasible design space, which was more restrictive for the baseline laminate than for the non-traditional, constant-stiffness laminates. The non-traditional, constant-stiffness laminates allowed designs that were close to the boundary of the feasible design space. This can be seen by looking at the difference between the material failure load  $M_f$  and the buckling load  $M_{cr}$  in table 5.5, where the material failure loads of the constant-stiffness designs are almost equal to the buckling loads. The same trend can be observed for the variable-stiffness laminates.

Table 5.5: Optimization results for case 2 with baseline:  $[\pm 45, 0_2, \pm 45, 0_2, 90, \pm 45, 90]_s$

Laminate number	Buckling moment $M_{cr}$ (kNm)	Comparison with baseline $(M_{cr}/M_b) \cdot 100\%$	Material failure moment $M_f$ (kNm)	Comparison with baseline $(M_f/M_{fb}) \cdot 100\%$
Baseline	598	100	661	100
CS-1	618	103	618	94
CS-2	615	103	616	93
CS-3	600	100	600	91
VS-1	696	116	696	105
VS-2	700	117	700	106
VS-3	678	114	678	103
VS-4	685	115	686	104
VS-5	455	76	455	69

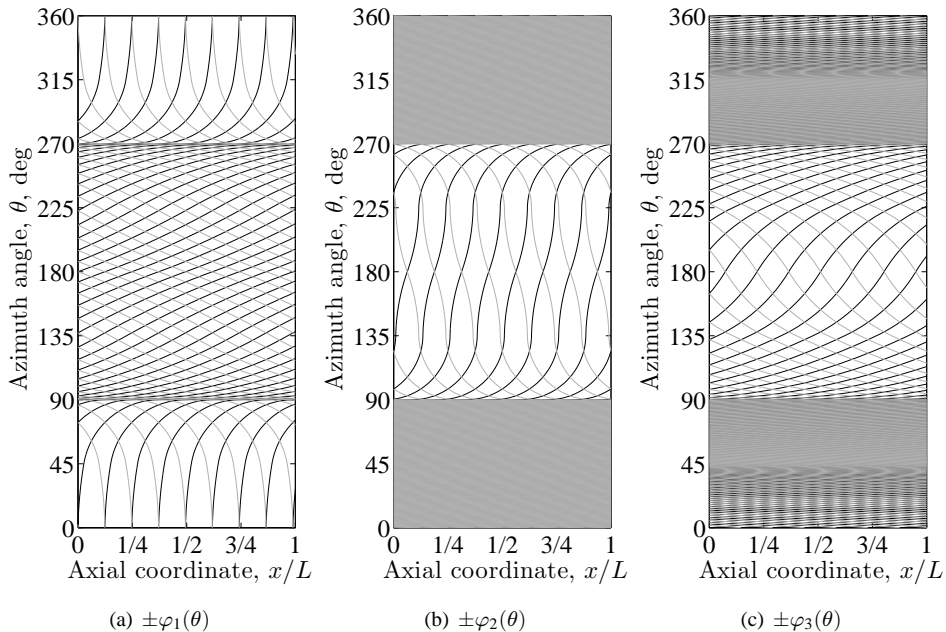


Figure 5.9: Steered fiber paths on a developed surface for laminate VS-1, case 1

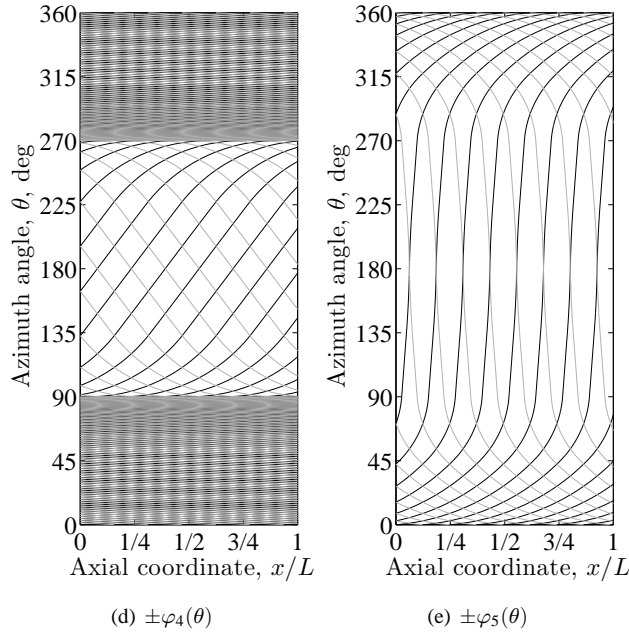


Figure 5.9: Steered fiber paths on a developed surface for laminate VS-1, case 1 (continued)

The material failure loads of the designs obtained in the first optimization case were far below the buckling load for most cases, which was caused by the high strain levels on the compression side of the cylinder. The strength constraint led to higher material failure loads, but at the cost of buckling load carrying capability. Strength improvements were achieved by a reduction of the extreme axial and circumferential strains, shown in figure 5.10. The extreme value of the axial strain on the compression side can be found by substituting  $\theta = 180^\circ$  in equation 5.5:

$$\varepsilon_{x,\min} = \frac{M_y(-R - z_{NA})}{EI} \quad (5.10)$$

The axial compressive strain can be reduced by increasing the overall bending stiffness of the cylinder,  $\overline{EI}$ , or by reducing the shift of the neutral axis, such that  $z_{NA}$  is small. The values of the overall bending stiffness and the location of the neutral axis for the laminate designs of optimization cases 1 and 2 are given in table 5.6. The values of the bending stiffness are normalized with the bending stiffness of the baseline cylinder of optimization case 2 and the location of the neutral axis is normalized with the cylinder radius  $R$ .

The bending stiffness of all cylinders increased and the locations of the neutral axis of the variable-stiffness cylinders shifted toward the compression side. Both changes led to a reduction in axial compressive strain and consequently to a higher material failure load. The distribution of the axial stiffness of the variable-stiffness cylinders for optimization cases 1 and 2 were different, which caused the difference in bending stiffness between the two optimization cases and the different locations of the neutral axis. The axial stiffness distributions for optimization case 1 and 2 are shown in figures 5.11(a) and 5.11(b), normalized with

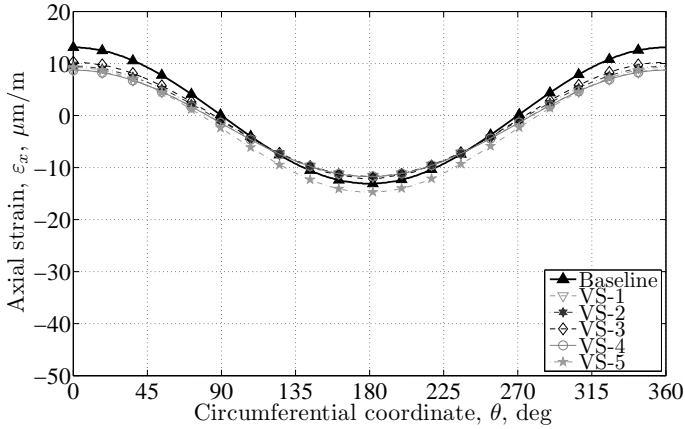
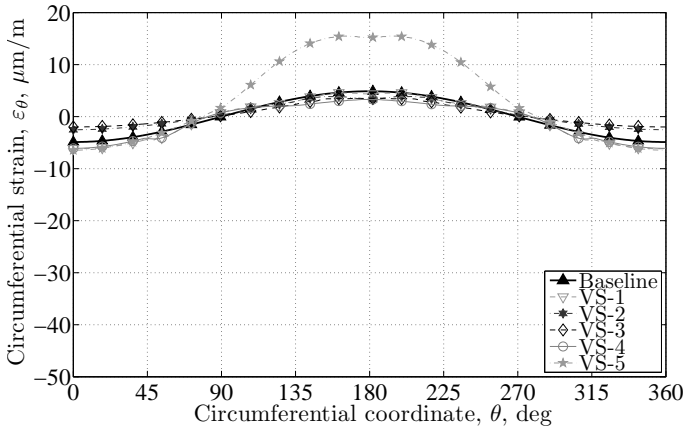
(a) Axial strain,  $\varepsilon_x$ (b) Circumferential strain,  $\varepsilon_\theta$ 

Figure 5.10: Strain distributions for all variable-stiffness cylinders, optimization case 2

the axial stiffness of the baseline cylinder of optimization case 2. The first thing that can be noted about the stiffness distributions of optimization case 2 is that the maximum equivalent laminate stiffness on the tension side was limited by the minimum  $10^\circ$  fiber angle constraint. The maximum axial laminate stiffness that can be achieved with the laminates VS-1, VS-4, and VS-5 corresponds to a layup of  $[\pm 45, (\pm 10)_5]_s$  and is 1.72 times that of the baseline cylinder. The maximum axial laminate stiffness for optimization case 1 was 1.88 times that of the baseline cylinder, which is the stiffness of a  $[\pm 45, (\pm 1)_5]_s$  layup. The maximum axial stiffness value of cylinder VS-2 is 1.5 times that of the baseline cylinder and the maximum stiffness of cylinder VS-3 is 1.37 times that of the baseline cylinder, corresponding with the layups  $[\pm 45, \pm 10, 0, 90, \pm 10, 0, 90, \pm 10]_s$  and  $[\pm 45, 0, 90, \pm 10, 0, 90, \pm 10, 0, 90]_s$ , respectively. The larger bending stiffness of the cylinders could therefore only be achieved if the stiffness on the compression side was increased, in addition to applying the maximum axial stiffness on the tension side. The smaller difference in axial stiffness between the compression side and the tension side also caused the neutral axis to be located closer to

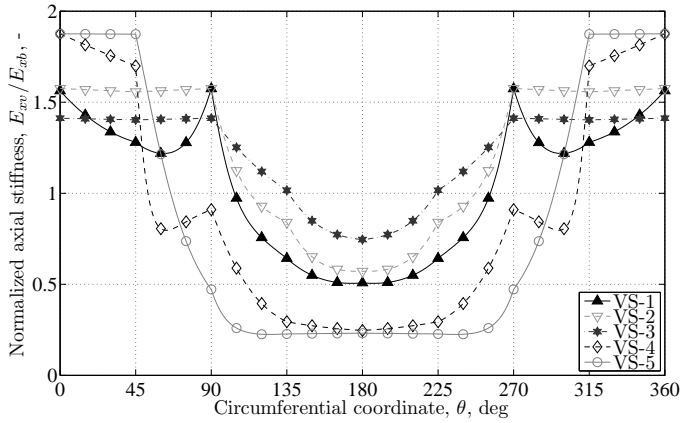
Table 5.6: Changes from optimization case 1 to optimization case 2

Laminate number	Optimization case 1		Optimization case 2	
	Bending stiffness	Location of the neutral axis	Bending stiffness	Location of the neutral axis
	$\frac{EI}{EI_b}$	$\frac{z_{NA}}{R}$	$\frac{EI}{EI_b}$	$\frac{z_{NA}}{R}$
Baseline	0.85	0	1.00	0
CS-1	0.67	0	0.81	0
CS-2	0.81	0	0.89	0
CS-3	0.81	0	0.90	0
VS-1	0.86	0.23	1.26	0.14
VS-2	0.99	0.22	1.22	0.10
VS-3	1.08	0.13	1.16	0.08
VS-4	0.60	0.45	1.10	0.21
VS-5	0.50	0.54	1.26	0.16

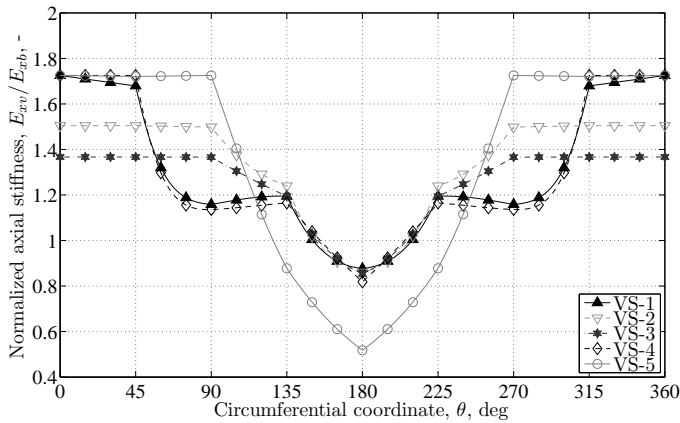
the center of the cross-section, i.e.  $z_{NA}$  is closer to 0. The axial stiffness of cylinders VS-1 and VS-4 were not maximal across the entire tension side to prevent the neutral axis from shifting towards the tension side too much.

The strength and the buckling load of cylinder VS-5 were lower than those of the other cylinders, although cylinder VS-5 had the highest bending stiffness and a location of the neutral axis that was below that of cylinder VS-4, see table 5.6. The difference in strength was caused by the high Poisson's ratio on the compression side of cylinder VS-5, shown in normalized form in figure 5.12. These high Poisson's ratios resulted in large tensile strains in the circumferential direction, figure 5.10(b), causing the low material failure load. Cylinder VS-5 consisted of 5 identically steered plies, such that the Poisson's ratio was directly dependent on the angle variation of that one steered ply definition and could not be tailored by combining plies with different fiber angles. The other laminates contained at least 2 different steered plies, allowing for different combinations of in-plane stiffness and Poisson's ratio.

The changes in stiffness distribution required to achieve the strength increase also influenced the distribution of the axial load around the circumference, and thereby the value of the buckling load and the shape of the first buckling mode. The distribution of the axial loads for the baseline cylinder and the variable-stiffness cylinders are shown in figure 5.13. The loads on the tension side for some of the variable-stiffness cases are reduced by approximately 25 percent when compared to the tensile loads of the cylinders in optimization case 1, shown in figure 5.5. This is caused by the lower axial stiffness on the tension side, and by the change in the location of the neutral axis. The compressive loads are distributed over a smaller portion of the cylinder and the compressive peak load is slightly increased compared to the first optimization case. The strength constraint thus limits the amount of load redistribution, which results in a lower buckling load carrying capability. The load distributions of cylinders VS-1 through VS-4 are similar, resulting in similar first buckling modes, shown in figures 5.14(b) to 5.14(e). The buckling deformations of the baseline cylinder in figure 5.14(a) again covered a smaller portion of the cross-section than the variable-stiffness cylinders, similar to the baseline in optimization case 1. The compressive peak loads of cylinder VS-5 were smaller than the peak loads of the other variable-stiffness cylinders and



(a) Optimization case 1



(b) Optimization case 2

Figure 5.11: Axial stiffness distributions, normalized with the baseline of case 2

the compressive loads were distributed over a larger area. Yet, the buckling load of cylinder VS-5 was smaller compared to the other variable-stiffness cylinders. Again, this might have been caused by the large values of the Poisson's ratio in laminate VS-5, which might induce secondary effects.

### 5.3.3 Optimization Case 3

The results for optimization case 3, which included two stiffness constraints in addition to the minimum fiber angle, strength, and manufacturability constraints taken into account in optimization case 2, are discussed next. The first constraint required the laminate stiffness in the  $0^\circ$ ,  $90^\circ$  and  $\pm 45^\circ$  directions to be larger than the threshold value of 29.0 GPa to provide robustness to the laminate. The constant-stiffness laminates and laminates VS-2 and VS-3 from optimization case 2 complied with the laminate stiffness constraint. Laminates VS-1, VS-4 and VS-5 did not meet the laminate stiffness requirements for the  $90^\circ$  and the  $\pm 45^\circ$

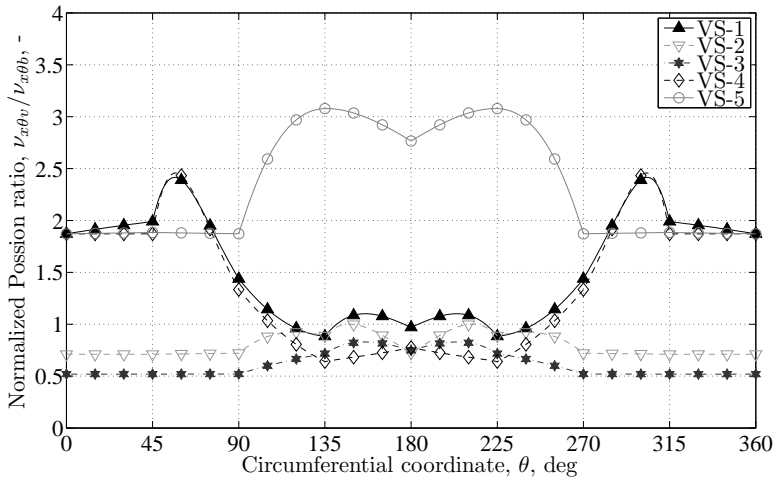


Figure 5.12: Distribution of the Poisson's ratio, optimization case 2

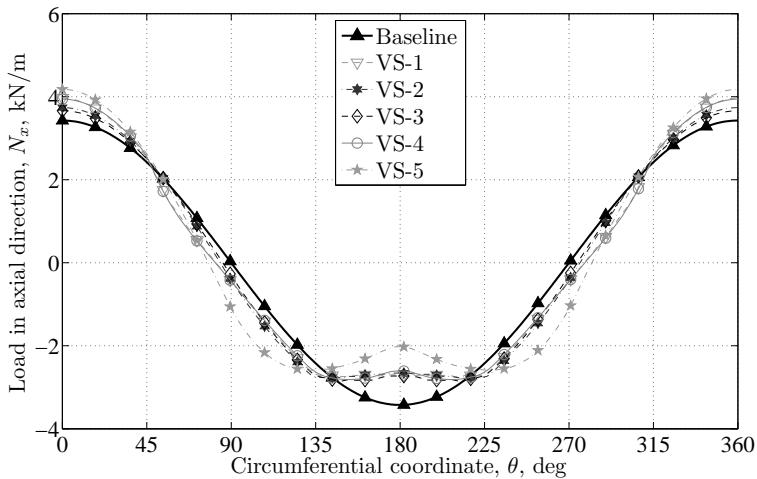
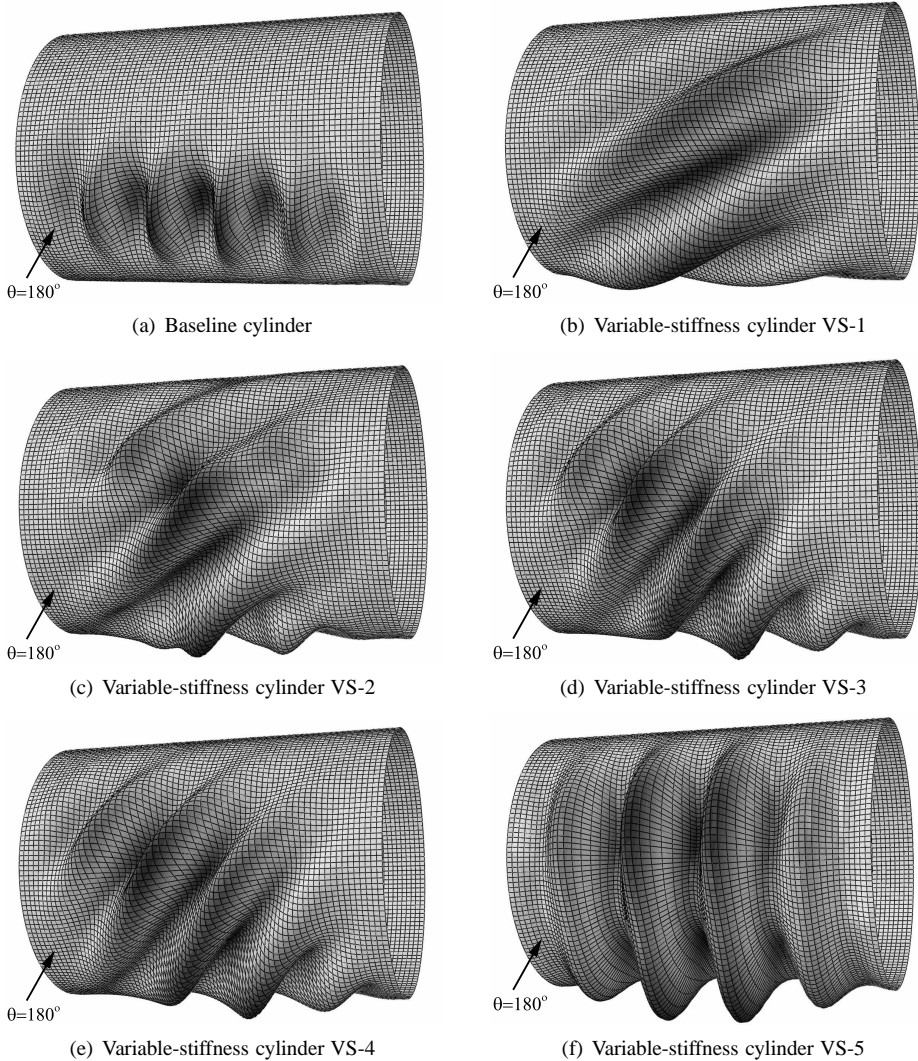


Figure 5.13: Axial load distribution for all variable-stiffness cylinders, optimization case 2

directions. The distributions of the laminate stiffness for the  $90^\circ$  and the  $\pm 45^\circ$  directions with the circumferential coordinate are shown in figure 5.15, where they are normalized with the axial stiffness of the baseline laminate. The results for  $-45^\circ$  are omitted, because they are equal to the  $+45^\circ$  results. The stiffness in the circumferential direction and the  $\pm 45^\circ$  directions were most critical when the stiffness in the axial direction was maximum, i.e. at the tension side of the cylinder, between  $\theta = 270^\circ$  and  $\theta = 90^\circ$ . Laminates VS-1, VS-4 and VS-5 violated the laminate stiffness constraints for the  $90^\circ$  and  $\pm 45^\circ$  directions on the tension side of the cylinder. The maximum value of the axial stiffness of VS-2 and VS-3 was limited due to the presence of the  $0^\circ$  and  $90^\circ$  layers and the minimum required fiber orientation of 10 degrees. The same condition caused the minimum laminate stiffness



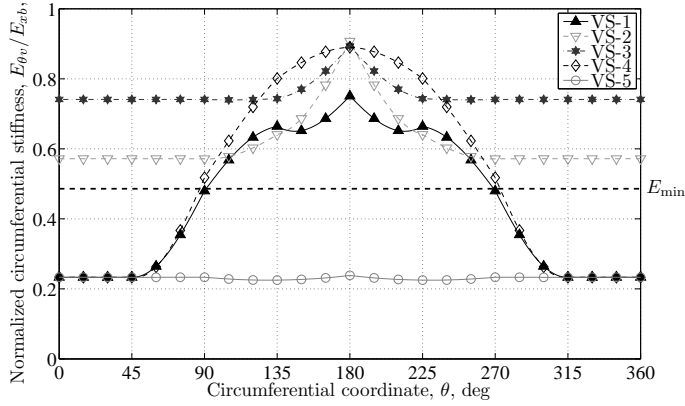
*Figure 5.14: First buckling modes of the baseline and variable-stiffness cylinders, optimization case 2*

requirement for the other directions to be automatically satisfied.

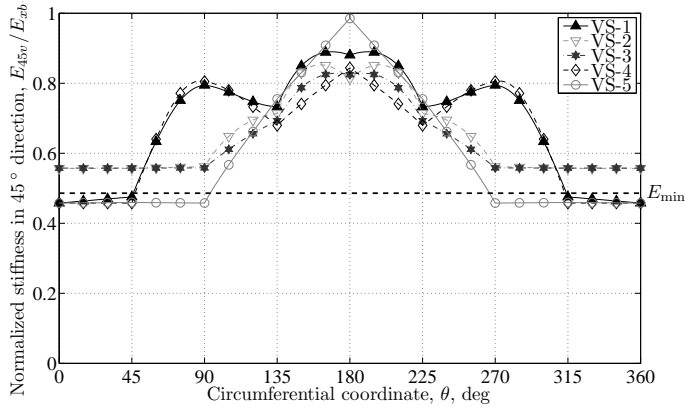
The second stiffness constraint stated that the global bending stiffness could not be more than 5 percent smaller than the bending stiffness of the baseline cylinder. The results in table 5.6 showed that none of the constant-stiffness cylinders met this requirement, while all the variable-stiffness had a higher bending stiffness than the baseline cylinder.

The optimization results for optimization case 3 are listed in table 5.7, while the values of the design variables for these laminates are given in appendix D. The global bending stiffness of the constant-stiffness laminates increased, causing a small decrease in buckling





(a) Stiffness in the 90° direction



(b) Stiffness in the 45° direction

Figure 5.15: Stiffness distributions in different orientations, normalized with the baseline axial stiffness of case 2

Table 5.7: Optimization results for case 3 with baseline:  $[\pm 45, 0_2, \pm 45, 0_2, 90, \pm 45, 90]_s$

Laminate number	Buckling moment $M_{cr}$ (kNm)	Comparison with baseline $(M_{cr}/M_b) \cdot 100\%$	Material failure moment $M_f$ (kNm)	Comparison with baseline $(M_f/M_{fb}) \cdot 100\%$
*Baseline	598	100	661	100
CS-1	611	102	647	98
CS-2	607	102	657	99
CS-3	590	99	662	100
VS-1	687	115	689	104
*VS-2	700	117	700	106
*VS-3	678	114	678	103

\* These results are the same as for optimization case 2

moment carrying capacity and a small increase in strength. Laminates VS-2 and VS-3 from optimization case 2 met both stiffness constraints and therefore the results for optimization case 3 are the same as those reported for optimization case 2. Laminate VS-5 was omitted, because it could never meet the laminate stiffness requirements in all directions simultaneously due to the 5 identical steered plies. The laminate stiffness constraint limited the design space for laminate VS-4 to such an extent that no feasible design could be found. Laminate VS-1 changed such that the laminate stiffnesses on the tension side of the cylinder met the laminate stiffness constraints, see figure 5.16, resulting in a lower axial stiffness in that region. The buckling load carrying capability and the cylinder strength were slightly reduced by the changes in stiffness distribution.

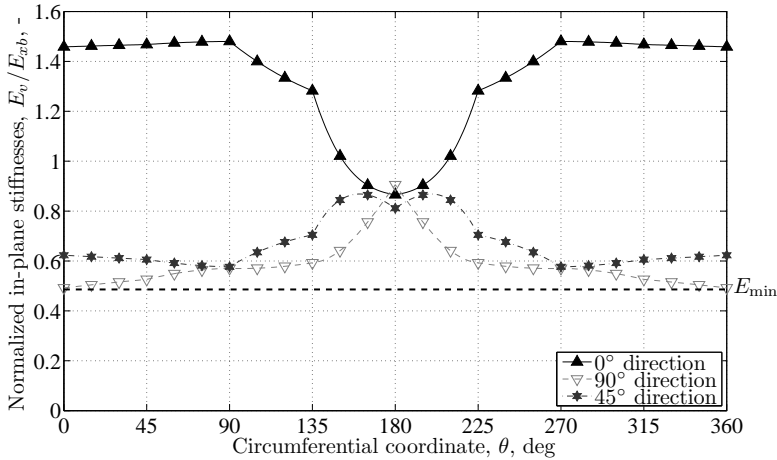


Figure 5.16: Laminate stiffness distributions for cylinder VS-1, case 3

Laminate VS-2 showed the biggest improvement compared to the baseline laminate, after all constraints were taken into account. Laminate VS-2 would therefore be the laminate of choice if this cylinder was manufactured and tested in bending.

The results for cylinder VS-2 were slightly better than those of cylinder VS-1, even though the number of design variables for cylinder VS-1 was larger, i.e. 25 variables for VS-1 versus 15 variables for VS-2. Two things might account for this. First, the design space of laminate VS-2 was not a subspace of the design space of laminate VS-1 due to the presence of the  $0^\circ$  and  $90^\circ$  plies and the fact that a set of balanced plies  $\pm\varphi_i$  in laminate VS-1 could not be split up. Secondly, the optimum solution for laminate VS-1 might be a local optimum. Laminate VS-1 was more likely to converge to a local optimum because the number of design variables was larger.

### 5.3.4 Variable-Stiffness Design for Manufacturing and Testing

Optimization case 3 was repeated for the baseline cylinder and the variable-stiffness cylinders VS-1 and VS-2 with the BMS8-276 graphite-epoxy material system to determine the design for the cylinders to be manufactured and tested. The properties of this material were slightly different from the AS4/855-2 material for which the results were presented in the

previous section. The results for the best baseline cylinder and the two optimum variable-stiffness cylinders are given in table 5.8. The layout of the baseline cylinder was determined to be a quasi-isotropic laminate with the layout:  $[\pm 45, 0_2, 90_2, 0, \pm 45, \pm 45, 90]_s$ .

Table 5.8: Optimization results for the cylinders with BMS8-276 material

Laminate number	Buckling moment $M_{cr}$ (kNm)	Comparison with baseline $(M_{cr}/M_b) \cdot 100\%$	Material failure moment $M_f$ (kNm)
Baseline	678	100	678
VS-1	794	117	794
VS-2	804	119	805

Cylinder VS-2 also gave the best results for the BMS8-276 material system, similar to the AS4/855-2 material, and was selected as the variable-stiffness design to be manufactured and tested. The design will be discussed in more detail below, though the results are similar to the ones presented in section 5.3 for the AS4/855-2 material.

The design variables for the three steered plies in the final variable-stiffness design with a layout of  $[\pm 45, \pm \varphi_1(\theta), 0, 90, \pm \varphi_3(\theta), 0, 90, \pm \varphi_5(\theta)]_s$  are listed in table 5.9 and the fiber paths and the balanced counterparts for these three steered plies are shown in figure 5.17.

Table 5.9: Design variables for the final variable-stiffness cylinder design

Ply	$T_0$ ( $^\circ$ )	$T_1$ ( $^\circ$ )	$T_2$ ( $^\circ$ )	$T_3$ ( $^\circ$ )	$T_4$ ( $^\circ$ )
$\varphi_1(\theta)$	10.0	10.0	10.0	10.0	24.7
$\varphi_3(\theta)$	10.0	10.0	10.6	56.9	61.7
$\varphi_5(\theta)$	10.0	12.0	10.0	34.2	68.9

The variation of the axial stiffness with the circumferential coordinate is shown in figure 5.18(a), where the stiffness of the variable-stiffness cylinder  $E_{xv}$  is normalized with the axial stiffness of the baseline cylinder  $E_{xb}$ . The axial stiffness on the tension side, between  $\theta = 270^\circ$  and  $\theta = 90^\circ$ , was more than 80 percent larger than the stiffness of the baseline cylinder, while the stiffness on the compression side, near  $\theta = 180^\circ$ , was slightly smaller than the stiffness of the baseline cylinder.

The bending moment was applied to the ends of the cylinder through rigid end plates and therefore the distribution of the axial load depended on the distribution of the axial stiffness. The load distributions of the baseline and the variable-stiffness cylinder are shown in figure 5.18(b), where three regions are highlighted.

The high stiffness on the tension side of the variable-stiffness cylinder caused the loads in region A to be up to 13 percent higher than those of the baseline cylinder. Another consequence of the higher stiffness on the tension side is a shift of the neutral axis towards the tension side, i.e. the neutral axis shifted from  $\theta = 90^\circ$  to  $\theta = 81^\circ$ . The shift in neutral axis resulted in all-compressive loads in region B for the variable-stiffness cylinder, whereas the loads carried by the baseline cylinder in this region were smaller or tensile. The low axial stiffness of the variable-stiffness cylinder in region C resulted in a flattening of the load

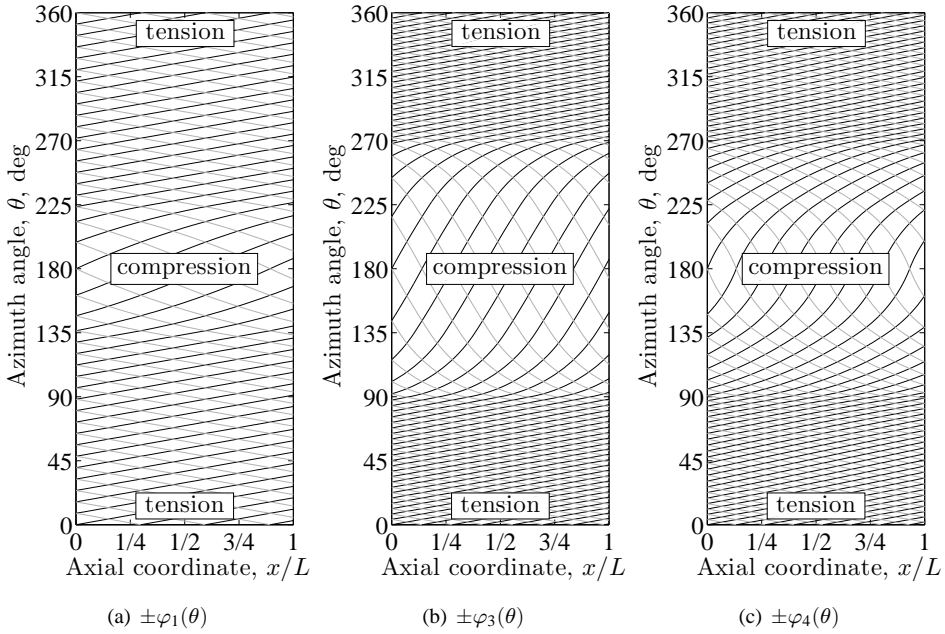


Figure 5.17: Steered fiber paths on a developed surface for the final variable-stiffness cylinder design

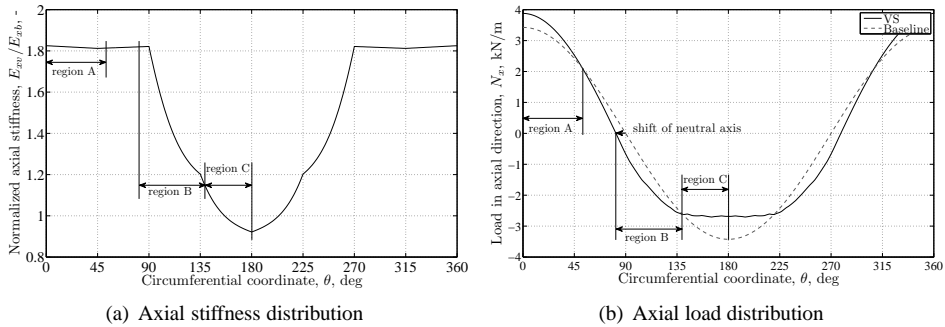


Figure 5.18: Load and stiffness distribution of the variable-stiffness cylinder

curve on the compression side of the cylinder, yielding compressive load values almost 20 percent smaller compared to the baseline cylinder.

The first buckling mode of the baseline cylinder and the variable-stiffness cylinder are shown in figures 5.19(a) and 5.19(b). The region participating in the buckling deformations of the variable-stiffness cylinder was larger than the deformed region of the baseline cylinder, and similar to the designs obtained for the AS4/855-2 material discussed in subsection 5.3.3.

The circumferential stiffness variation resulted in a redistribution of the loads, such that the tension side was more effective in carrying loads, the compressive loads were carried

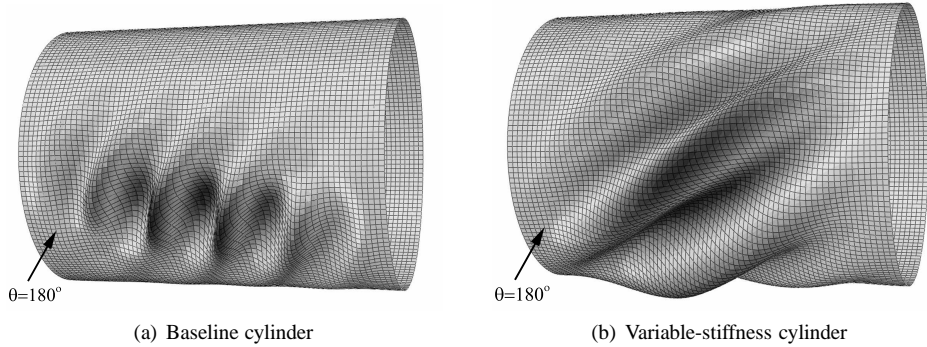


Figure 5.19: First buckling modes of the baseline and the variable-stiffness cylinder

by a larger part of the cylinder and the compressive load peak at  $\theta = 180^\circ$  was significantly reduced. The compressive side of the cylinder was critical for buckling, so redistributing the compressive loads over a larger portion of the cylinder and reducing the compressive peak load near  $\theta = 180^\circ$  permitted a higher bending moment to be carried before buckling occurred.

Two baseline cylinders and one variable-stiffness cylinder were manufactured by Boeing using an Ingersoll fiber placement machine. The details of the manufacturing will be discussed in chapter 6.

## 5.4 Optimization Results for Laminates with Overlaps

The variable-stiffness laminates optimized in section 5.3 were designed to have a constant thickness and thus a constant mass, obtained by using the tow cut and restart capabilities of advanced fiber placement machines to avoid overlapping courses. The variable-stiffness laminates in the current section are allowed to have overlapping courses, resulting in increased structural mass of the variable-stiffness cylinders and additional possibilities for tailoring the laminate stiffness.

### 5.4.1 Optimization Case 1

The results for optimization case 1 are given in table 5.10. The baseline laminate was the same as for the constant-thickness laminate optimization, i.e.  $[\pm 45, 0_2, \pm 45, 90, 0, 90, \pm 45, 90]_s$ . The 24 plies resulted in a mass of 10.9 kg. The variable-stiffness laminates VS<sup>o</sup>-1 through VS<sup>o</sup>-5 refer to the stacking sequences listed for laminates VS-1 through VS-5 in table 5.2, where the superscript *o* denotes overlaps. The buckling moments and structural mass of variable-stiffness cylinders VS<sup>o</sup>-1, VS<sup>o</sup>-4, and VS<sup>o</sup>-5 were within the same range. The specific buckling moments of these cylinders was 4.5 times as large as the specific buckling moment of the baseline cylinder. The buckling moment was 10 times higher than the buckling moment of the baseline at almost 2.5 times the structural mass. The improvements of variable-stiffness cylinders VS<sup>o</sup>-2 and VS<sup>o</sup>-3 were smaller, but still significant. An

Table 5.10: Optimization results for case 1 with overlaps

Laminate number	Buckling moment $M_{cr}$ (kNm)	Mass $m$ (kg)	Spec. buckling moment $\bar{M}_{cr} = M_{cr}/m$ (kNm/kg)	Comparison with baseline $(\bar{M}_{cr}/\bar{M}_b) \cdot 100\%$
Baseline	627	10.9	58	100
VS <sup>o</sup> -1	6860	26.0	264	457
VS <sup>o</sup> -2	3517	19.6	179	311
VS <sup>o</sup> -3	2267	16.9	134	232
VS <sup>o</sup> -4	6746	25.6	264	456
VS <sup>o</sup> -5	6942	26.7	260	451

explanation for the improvements in buckling load carrying capability and a discussion of the differences between the variable-stiffness cylinders are given below.

Variable-stiffness laminate VS<sup>o</sup>-5 is used to illustrate the mechanism for improving the buckling load carrying capability of a composite cylinder by varying the laminate stiffness using curved fiber courses with overlaps. Laminate VS<sup>o</sup>-5 contained 20 steered plies with one variable-stiffness ply definition:  $[\pm 45, (\pm \varphi_1)_5]_s$ . The values of the design variables for the optimum variable-stiffness ply definition are given in table 5.11 and the fiber paths are shown in figure 5.20.

Table 5.11: Design variables for laminate VS<sup>o</sup>-5, case 1

Ply	$T_0$ (°)	$T_1$ (°)	$T_2$ (°)	$T_3$ (°)	$T_4$ (°)
$\varphi_1(\theta)$	10.0	40.2	89.0	10.0	10.0

The influence of the fiber angle variation on the equivalent in-plane laminate stiffness  $E_x$  and the laminate thickness is shown in figure 5.21. The equivalent laminate stiffness and the thickness of the variable-stiffness cylinder (subscript  $v$ ) are normalized with the laminate stiffness and thickness of the baseline cylinder (subscript  $b$ ). The regions with a fiber orientation of  $10^\circ$  had a laminate stiffness more than twice the laminate stiffness of the baseline laminate and a thickness up to 5 times the baseline laminate thickness. The effective course width, the derivation of which was presented in section 3.3, and the amount of overlap are smaller when the fiber orientation angle increases. The fiber angle on the tension side, i.e. near  $\theta = 0^\circ$ , changed to a larger fiber angle at  $\theta = 45^\circ$  and therefore the thickness buildup on the tension side was not as large as on the compression side, even though the fiber orientation  $T_0$  and  $T_4$  were both  $10^\circ$ . The in-plane laminate stiffness of the variable-stiffness cylinder, which was obtained by multiplying the equivalent axial modulus of elasticity with the laminate thickness, is plotted in figure 5.22(a).

The amount of overlap per ply is approximately proportional to  $\sin \varphi_{\max} / \sin \varphi_{\min}$ , where  $\varphi_{\max}$  is the largest fiber angle and  $\varphi_{\min}$  is the smallest fiber angle of a variable-stiffness course. The fact that  $T_3 = T_4 = 10^\circ$  and  $T_2 = 89^\circ$  thus resulted in the maximum attainable laminate thickness on the compression side of the cylinder, given the minimum required

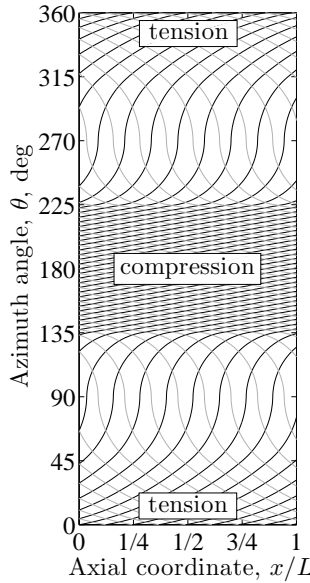


Figure 5.20: Steered fiber paths on a developed surface for laminate VS<sup>o</sup>-5, case 1,  $\pm\varphi_1$

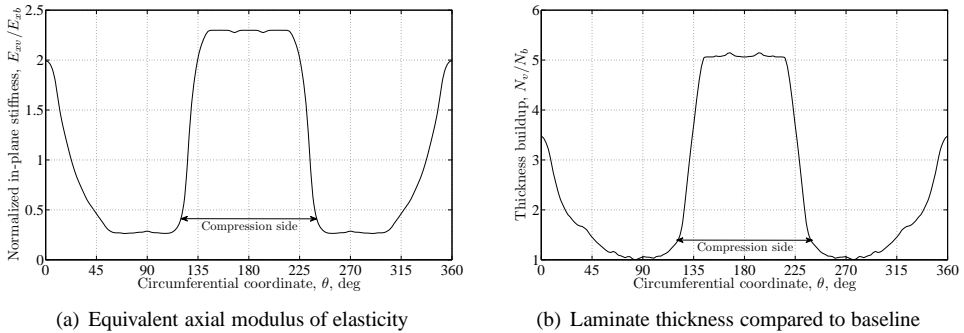


Figure 5.21: In-plane stiffness parameters for variable-stiffness cylinder VS<sup>o</sup>-5, optimization case 1

fiber angle of 10°. The distributions of the laminate bending stiffnesses  $D_{11}$  and  $D_{22}$ , which are proportional to thickness cubed, are plotted in figure 5.22(b), where the bending stiffnesses are normalized with the laminate bending stiffnesses of the baseline laminate. The thickness increase of the laminate on the compression side of the cylinder is reflected by the sharp increase in bending stiffness in that location.

The thickness buildup on the compression side affected the buckling load carrying capability of the variable-stiffness cylinder in a number of ways. The axial loads were redistributed around the circumference due to the non-uniform in-plane axial laminate stiffness. The axial load distributions for the baseline cylinder and variable-stiffness cylinder VS<sup>o</sup>-5 are presented in figure 5.23(a). The high in-plane stiffness on the compression side attracted

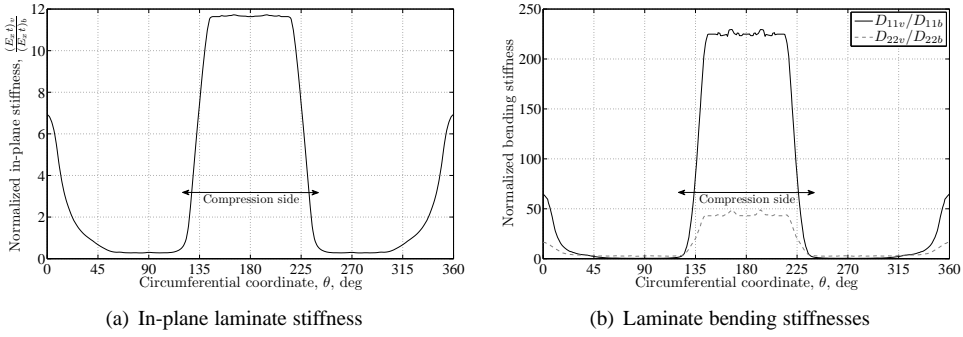


Figure 5.22: Laminate stiffness distributions for variable-stiffness cylinder  $VS^0-5$ , optimization case 1

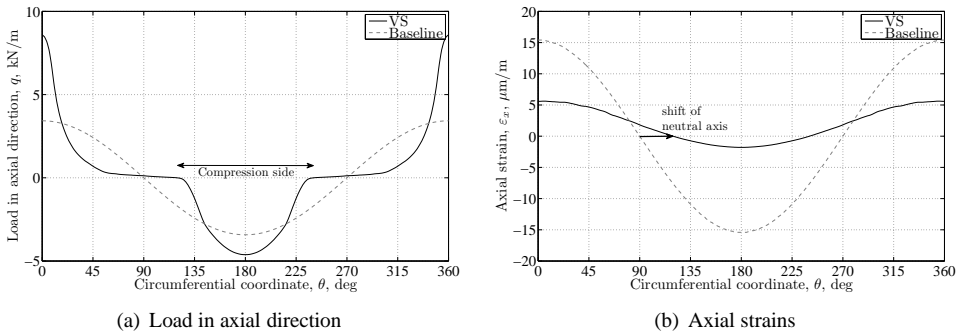


Figure 5.23: Load and strain distributions for variable-stiffness cylinder  $VS^0-5$ , optimization case 1

loads to this region, causing an increase in compressive loads of 35 percent compared to the baseline laminate. The loads on the tension side of the cylinder, i.e. near  $\theta = 0^\circ$ , were carried by a relatively small region with a high in-plane stiffness and therefore the loads were higher than on the compression side. Another factor that contributed to higher load levels on the tension side than on the compression side of the cylinder was the shift of the neutral axis towards the compression side, i.e. from  $\theta = 90^\circ$  to  $\theta \approx 120^\circ$ . The shift in location of the neutral axis can be seen more clearly in the plot of the axial strain distribution, shown in figure 5.23(b). The small fiber angle and the larger thickness at  $\theta = 0^\circ$  prevented the neutral axis from shifting to the compression side too much and increasing the compressive load levels even more.

The higher loads on the compression side of the variable-stiffness cylinder did not result in a lower buckling load, because the increase in bending stiffness was larger than the load increase, see figure 5.22(b). The effect of including overlaps on the load distribution around the circumference of the cylinder was opposite to the effect observed for the variable-stiffness laminates with a constant thickness, presented in section 5.3. The loads were transferred away from the compression side of the cylinder by reducing the in-plane stiffness near  $\theta = 180^\circ$  for laminates with a constant thickness, whereas the in-plane stiff-



ness and thus the load level on the compression side was increased for the laminate with overlaps. The amount of overlap is coupled to the fiber angle variation, such that the largest laminate thickness is obtained if the fiber angle is small. An increase in bending stiffness is thus coupled to an increase in equivalent laminate modulus in the axial direction of the cylinder.

The buckling load carrying capability of a variable-stiffness cylinder could be improved even more if the thickness buildup was independent of the fiber angle variation, such that the laminate modulus of elasticity could be tailored to reduce the loads on the compression side of the cylinder, while the laminate bending stiffness could be increased to improve the resistance against buckling deformations. Uncoupling the laminate thickness from the fiber angle variation complicates the design process and goes beyond the scope of this thesis. Future work might focus on simultaneously designing the in-plane and bending stiffness distribution of composite cylinders, possibly using lamination parameters based on the work on flat panels by IJsselmuiden et al. (2009b).

The results for the other four variable-stiffness laminates are presented below. The values of the design variables for laminates  $VS^o-1$  through  $VS^o-5$  are given in appendix D. The distributions of the in-plane stiffness and bending stiffness in the axial direction of the variable-stiffness cylinders with overlap are shown in figures 5.24(a) and 5.24(b). The stiffness distributions of cylinders  $VS^o-1$ ,  $VS^o-4$  and  $VS^o-5$  were identical on the compression side of the cylinder and differed only slightly on the tension side. These three cylinders had 20 steered plies, which had almost identical fiber angle variations between  $\theta = 90^\circ$  and  $\theta = 270^\circ$ , thus producing near-identical laminate stiffnesses. The near-identical stiffness distribution resulted in a near identical axial load and strain distribution around the circumference, shown in figures 5.24(c) and 5.24(d), and buckling loads that were close together, see table 5.10.

The in-plane stiffness of cylinder  $VS^o-5$  was slightly higher on the tension side than that of cylinders  $VS^o-1$  and  $VS^o-4$ , resulting in a smaller shift of the neutral axis and a slightly lower compressive load. The buckling load of variable-stiffness cylinder  $VS^o-5$  was therefore higher than the buckling load of cylinders  $VS^o-1$  and  $VS^o-4$ , since the laminate bending stiffness on the compression side of the three cylinders was the same. The higher in-plane stiffness on the tension side came at the price of increased mass, and therefore the specific buckling load of cylinder  $VS^o-5$  was lower than those of cylinders  $VS^o-1$  and  $VS^o-4$ .

A parameter study in which the design variables of one ply within laminate  $VS^o-1$ , i.e.  $[\pm 45, \pm \varphi_1, \pm \varphi_2, \pm \varphi_3, \pm \varphi_4, \pm \varphi_5]_s$ , were varied with steps of 5 degrees showed that at least two hundred designs had a specific buckling load within 1 percent of the optimum specific buckling load of cylinder  $VS^o-1$ . All of these laminates had the maximum laminate thickness on the compression side, corresponding to a fiber angle of  $10^\circ$ . The large number of near-optimal designs indicated that the optimal variable-stiffness overlap design was a robust design.

Cylinders  $VS^o-2$  and  $VS^o-3$  were hybrid designs, i.e. they consisted of both variable-stiffness plies and constant-angle plies. The thickness on the compression side of the hybrid cylinders was smaller than for cylinders  $VS^o-1$ ,  $VS^o-4$  and  $VS^o-5$ , because only the variable-stiffness plies had overlaps. As a consequence both the in-plane axial laminate stiffness and the laminate bending stiffness of cylinders  $VS^o-2$  and  $VS^o-3$  were considerably smaller than those of the other three variable-stiffness cylinders. The distribution of the axial loads

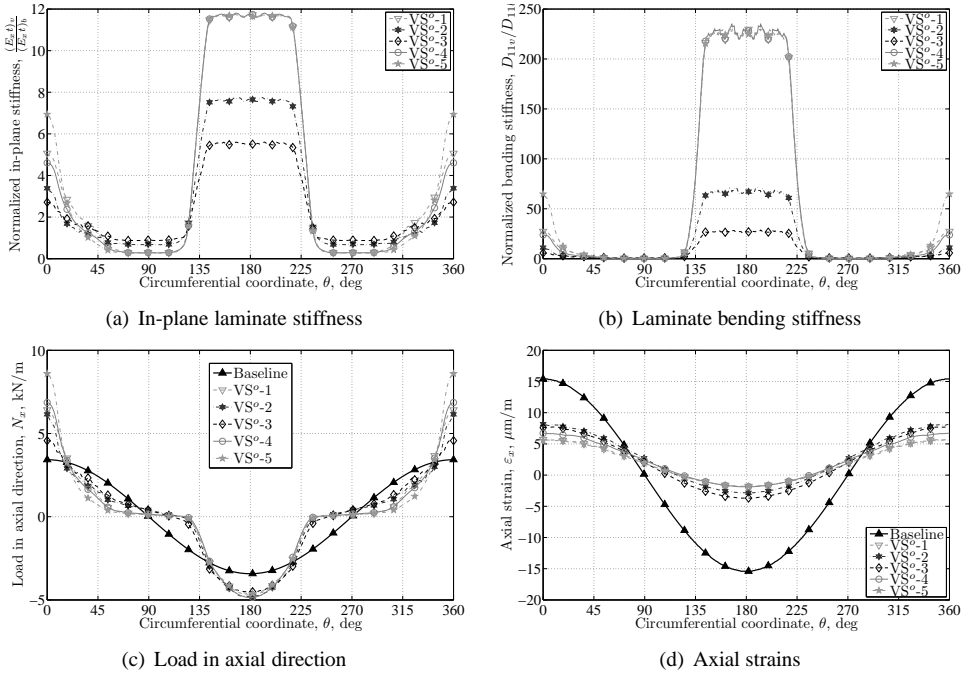


Figure 5.24: Optimization results for all variable-stiffness cylinders with overlap, optimization case 1

around the circumference of cylinders VS<sup>o</sup>-2 and VS<sup>o</sup>-3, see figure 5.24(c), did not differ much from the load distributions of cylinders VS<sup>o</sup>-1, VS<sup>o</sup>-4 and VS<sup>o</sup>-5, and therefore the lower laminate bending stiffnesses on the compression side of the cylinder resulted in a lower buckling load carrying capability. The structural mass also decreased however, such that differences in specific buckling load between the hybrid cylinders and the variable-stiffness cylinders VS<sup>o</sup>-1, VS<sup>o</sup>-4 and VS<sup>o</sup>-5 were smaller than the difference in absolute buckling load.

The first buckling modes of the variable-stiffness cylinders with overlap are shown in figure 5.25. The buckling modes of the variable-stiffness cylinders VS<sup>o</sup>-1, VS<sup>o</sup>-4 and VS<sup>o</sup>-5 were similar, as expected due to the similar stiffness and load distributions. Cylinders VS<sup>o</sup>-2 and VS<sup>o</sup>-3 had a different first buckling mode with more buckles than cylinders VS<sup>o</sup>-1, VS<sup>o</sup>-4 and VS<sup>o</sup>-5, because of the lower laminate bending stiffness.

One comment regarding the results presented above needs to be made before discussing to the results of the second optimization case. Comparing the specific buckling moment of different designs might not correctly reflect the potential benefits of using variable-stiffness laminates with overlaps. The buckling load largely depends on the laminate bending stiffness on the compression side of the cylinder, which increases cubically with a linear increase in thickness. An alternative method of comparison would be to scale the ply thickness of the variable-stiffness laminate with overlaps such that the total structural mass of the variable-stiffness cylinder is identical to that of the baseline cylinder. The finite element results for the ply-thickness-normalized variable-stiffness laminates are given in table 5.12. The de-

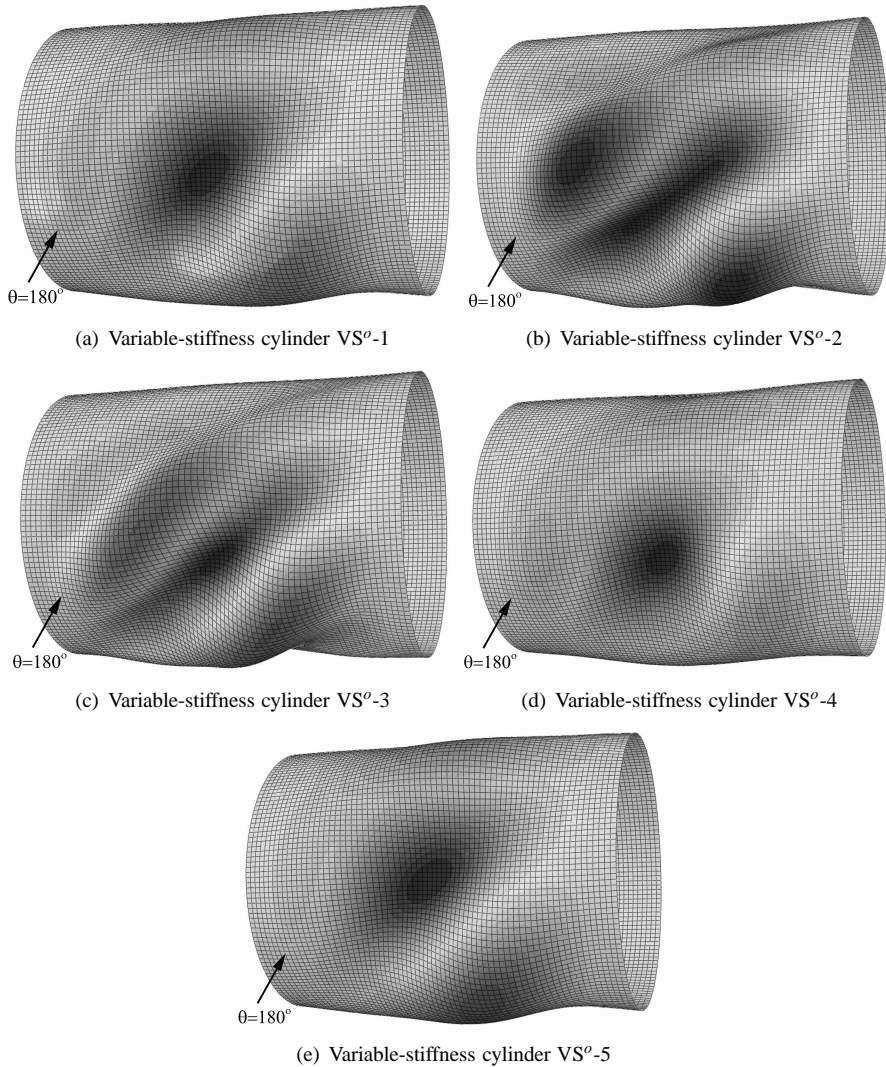


Figure 5.25: First buckling modes of the variable-stiffness cylinders with overlap, optimization case 1

sign variables for designs  $\overline{VS}^o-1$  through  $\overline{VS}^o-5$  are those of laminates  $VS^o-1$  through  $VS^o-5$ . The improvements compared to the baseline cylinder are still considerable, but not as big as those reported in table 5.10. Reduction of the ply thickness might not be feasible in a production environment, but the results in table 5.12 give a better perspective on the potential benefits. A robust stacking sequence optimization is needed to design a variable-stiffness laminate with overlaps with equal or lower structural mass than the baseline. The number of plies then has to be reduced, such that the number of design variables also becomes a variable. This complicates the optimization process to such an extent, that it was not considered

Table 5.12: Optimization results for case 1 with overlaps and normalized ply thickness

Laminate number	Ply thickness $M_{cr}$ (mm)	Buckling moment $t_{ply}$ (kNm)	Mass $m$ (kg)	Spec. buckling moment $\bar{M}_{cr} = M_{cr}/m$ (kNm/kg)	Comparison with baseline $(\bar{M}_{cr}/\bar{M}_b) \cdot 100\%$
Baseline	0.183	627	10.9	58	100
$\overline{VS}^o-1$	0.076	1198	10.9	110	191
$\overline{VS}^o-2$	0.101	1070	10.9	99	171
$\overline{VS}^o-3$	0.117	927	10.9	85	148
$\overline{VS}^o-4$	0.078	1154	10.9	106	184
$\overline{VS}^o-5$	0.074	1210	10.9	112	193

in this dissertation.

### 5.4.2 Optimization Case 2

Optimization case 2 included the curvature constraint for the fiber paths and required the cylinder to buckle before material failure occurred. The optimum designs obtained by the unconstrained optimization violated both constraints, such that the optimum designs of optimization case 2 were different from those of optimization case 1. The differences between the unconstrained and the constrained designs are illustrated below using design  $\overline{VS}^o-5$  as an example. The design variables and result plots of the other variable-stiffness designs are given in appendix D.

The values of the design variables of the unconstrained  $\overline{VS}^o-5$  design (case 1) and the constrained  $\overline{VS}^o-5$  design (case 2) are listed in table 5.13. The unconstrained design  $\overline{VS}^o-5$  violated the curvature constraint in the segments between  $T_1$  and  $T_2$  and between  $T_2$  and  $T_3$  with in-plane curvature values of respectively  $3.2 \text{ m}^{-1}$  and  $4.1 \text{ m}^{-1}$ , where a curvature of  $1.97 \text{ m}^{-1}$  was allowed. These high curvature values were caused by the large fiber angle  $T_2 = 89^\circ$ . The value of  $T_2$  was lower in the unconstrained design and the curvature constraint was met for all segments.

Table 5.13: Design variables for laminate  $\overline{VS}^o-5$ , cases 1 and 2

	Ply	$T_0$ ( $^\circ$ )	$T_1$ ( $^\circ$ )	$T_2$ ( $^\circ$ )	$T_3$ ( $^\circ$ )	$T_4$ ( $^\circ$ )
case 1, unconstrained	$\varphi_1(\theta)$	10.0	40.2	89.0	10.0	10.0
case 2, constrained	$\varphi_1(\theta)$	10.0	11.5	37.2	10.0	10.0

The laminate strength is plotted, in figure 5.26, on a logarithmic scale as a function of the circumferential coordinate for optimization cases 1 and 2. The strength distribution of the constrained baseline is also shown for reference. The laminate strength of the baseline cylinder is lowest on the compression side of the cylinder. The stiffness and strain values on the tension and compression side of the baseline are equal and opposite, but the compression strength of fiber-reinforced composites is lower than the tensile strength and therefore the

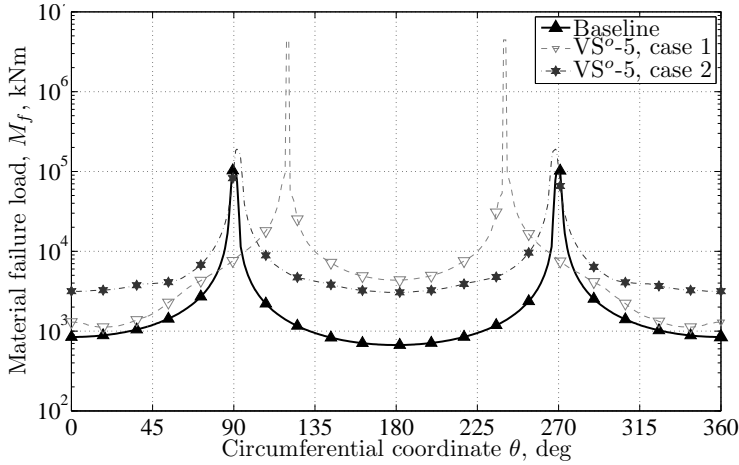


Figure 5.26: Laminate strength distribution for laminate  $VS^o-5$ , cases 1 and 2

compression side is more critical. The unconstrained variable-stiffness cylinder,  $VS^o-5$  case 1, is most critical on the tension side. The high laminate stiffness on the compression side of the variable-stiffness cylinder caused a shift of the neutral axis towards the compression side of the cylinder, such that the compressive strains became smaller than the tensile strains and therefore the tension side of the cylinder became critical for strength. The critical locations in terms of laminate strength are indicated in figure 5.26. The difference between the unconstrained and the constrained variable-stiffness designs is that the constrained design fails almost simultaneously on the compression side and on the tension side. The strength of the variable-stiffness cylinder is higher for optimization case 2 than for optimization case 1, i.e. the lowest strength value of case 2 is higher than that of case 1. The higher strength was achieved by reducing the difference in axial laminate stiffness between the compression side and the tension side, such that the neutral axis did not shift towards the compression side. The axial stiffness distributions and the laminate bending stiffness distributions of the optimum laminates for optimization cases 1 and 2 are shown in figures 5.27(a) and 5.27(b). The axial laminate stiffness and the laminate bending stiffness on the compression side of the cylinder decreased, because the amount of overlap was reduced due to the smaller value of  $T_2$ . The laminate stiffness on the tension side increased to the same level as the compression side, causing the axial loads and strains on the tension side to be similar to those on the compression side, see figures 5.27(c) and 5.27(d).

The increased strength came at the cost of reduced buckling load carrying capability: the specific bending moment dropped from  $\bar{M}_{cr} = 264$  kNm to  $\bar{M}_{cr} = 126$  kNm. The large decrease in buckling load carrying capability was caused by the reduction in laminate thickness and the corresponding reduction in laminate bending stiffness, see figure 5.27(b).

Similar trends as described above were observed for the other variable-stiffness laminates, for which the results are summarized in table 5.14. The values of the design variables and the result graphs are given in appendix D. The ply thickness of the optimum variable-stiffness laminates was again normalized such that the structural mass of the overlap laminates was equal to that of the baseline. These results, denoted by  $\sqrt{VS}^o$ , are also presented in

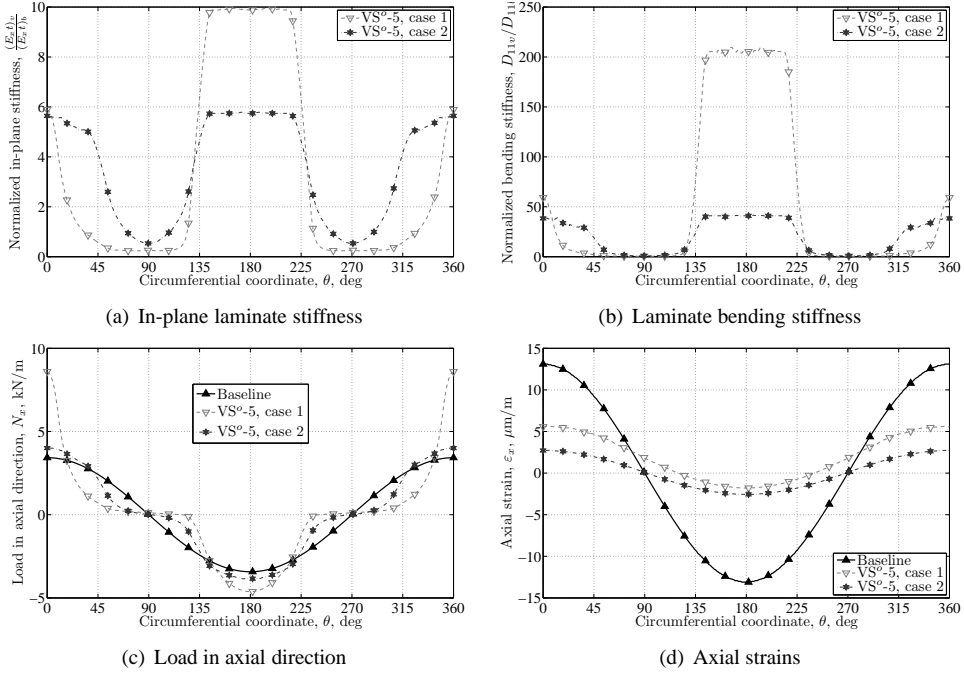


Figure 5.27: Optimization results for variable-stiffness cylinders  $VS^o-5$ , optimization cases 1 and 2

table 5.14.

Table 5.14: Optimization results for case 2 with overlaps

Laminate number	Ply thickness $t_{ply}$ (mm)	Buckling moment $M_{cr}$ (kNm)	Mass $m$ (kg)	Spec. buckling moment $\bar{M}_{cr} = M_{cr}/m$ (kNm/kg)	Comparison with baseline $(\bar{M}_{cr}/\bar{M}_b)$ ·100%	Spec. material failure moment $\bar{M}_f = M_f/m$
Baseline	0.183	598	10.9	55	100	61
* $VS^o-1$	0.183	2974	23.4	127	231	127
* $\bar{VS}^o-1$	0.085	636	10.9	59	106	128
$VS^o-2$	0.183	2650	20.9	127	230	127
$\bar{VS}^o-2$	0.095	710	10.9	65	119	127
$VS^o-3$	0.183	2119	17.4	122	221	122
$\bar{VS}^o-3$	0.114	817	10.9	75	137	123
$VS^o-4$	0.183	2968	23.6	126	228	126
$\bar{VS}^o-4$	0.084	623	10.9	57	104	125
$VS^o-5$	0.183	2974	23.4	127	231	127
$\bar{VS}^o-5$	0.085	636	10.9	59	106	128

\* This design is identical to  $VS^o-5$

The specific buckling moments of the ply-thickness-normalized variable-stiffness de-

signs were smaller than the specific buckling moment of the original designs and although the buckling load carrying capability was still higher than that of the baseline cylinders, the amount of improvement of some of the designs was marginal. Variable-stiffness design  $VS^o-3$  was the best after the ply thickness was adjusted, because the reduction in ply thickness was not as big as that of the other variable-stiffness designs.

The strength of the ply-thickness-normalized variable-stiffness laminates was not affected by the reduction in ply thickness, which implies that the strength of the cylinder is linearly related to the ply thickness and the structural mass. The normalization of the ply thickness for equal structural mass caused a large difference between the specific buckling moment and the material failure moment. This means that optimizing the specific buckling moment of variable-stiffness laminates with overlaps while requiring the material failure moment to be larger than the buckling moment is not appropriate if the ply thickness is reduced later. The original designs were bounded by the strength constraint, which is no longer critical. The ply-thickness-normalized variable-stiffness designs are thus expected to have a higher buckling moment carrying capability if the reduction in ply thickness is taken into account in the constrained optimization, instead of applying the normalization as an afterthought.

Again, a full stacking sequence optimization with a variable number of plies would be recommended for the design of variable-stiffness laminates with overlap which are subjected to a strength constraint and a constraint on the structural mass.

The optimization for variable-stiffness laminate  $VS^o-4$  resulted in a slightly lower buckling load than for variable-stiffness laminate  $VS^o-5$ , while the optimization for laminate  $VS^o-1$  did not reach the optimal values of either  $VS^o-4$  or  $VS^o-5$ . Variable-stiffness design  $VS^o-5$  is a subset of  $VS^o-1$  and therefore the optimum  $VS^o-5$  design is also listed as the optimum  $VS^o-1$  design. A larger number of design variables is normally expected to give better results, but the optimization routine got stuck in local optima. The irregular mass, buckling and strength responses caused these local optima. Global search routines, such as implemented in Design Explorer in addition to the response surface optimizer, are more likely to get stranded if the number of designs is larger.

## 5.5 Conclusions

Variable-stiffness designs were shown to be effective in increasing the structural performance of a fiber-reinforced composite cylinder under bending. Variable-stiffness laminates with a constant thickness improve the buckling load carrying capability by tailoring the in-plane laminate stiffness such that the in-plane loads are redistributed around the circumference of the cylinder. The compressive loads are reduced and spread out over a larger part of the cylinder and the tensile loads, unimportant for buckling, are increased. The redistributed loads caused the first buckling mode to change such that a larger part of the cylinder participated in the buckling deformations.

The unconstrained variable-stiffness designs increased the buckling load carrying capability by up to 29 percent compared to the optimized baseline design. Curvature, strength and stiffness constraints caused a small reduction in buckling load carrying capability of the variable-stiffness designs. These manufacturable and more practical laminates showed improvements of up to 17 percent compared to the optimized baseline consisting of  $0^\circ$ ,  $90^\circ$

and  $\pm 45^\circ$  plies.

The buckling load carrying capability of variable-stiffness designs that included overlapping fiber courses was optimized by increasing the laminate thickness on the compression side of the cylinder. The larger laminate thickness was achieved by having a small fiber orientation on the compression side of the cylinder and a large fiber orientation near the neutral axis. The increased laminate thickness and the small fiber orientation caused a high axial stiffness, resulting in high axial loads on the compression side of the cylinder. The laminate bending stiffness on the compression side increased more than linear with the laminate thickness, however, such that it compensated for the higher axial loads and dominated the response.

The overlap laminates were optimized for specific buckling moment, i.e. the buckling moment normalized with the structural mass, to account for the mass increase due to the overlaps. Laminate bending stiffness and buckling moment do not scale linearly with mass and therefore the laminate thickness of the optimum variable-stiffness designs were scaled such that the mass became identical to the mass of the baseline design. The ply-thickness-normalized cylinders were then analyzed again and the results were compared to the original results. The specific buckling moment of the ply-thickness-normalized variable-stiffness laminates was smaller than that of the original variable-stiffness designs, but still showed improvements of up to 90 percent compared to the baseline design.

Including the curvature and strength constraints had a higher impact on the variable-stiffness designs with overlap than on the ones with a constant thickness. The amount of thickness buildup on the compression side was limited, because the shift of the neutral axis associated with the high axial laminate stiffness on the compression side caused failure on the tension side of the cylinder. The laminate stiffness and thickness on the tension side became similar to those on the compression side. The improvement of the best constrained, ply-thickness-normalized variable-stiffness design compared to the baseline design was 37 percent.

Normalizing the ply thickness did not make sense for the optimum strength-constrained designs, because strength scales linearly with thickness while buckling does not. The strength of the ply-thickness-normalized laminates was therefore higher than the buckling load. A complete stacking sequence optimization with a variable number of plies is recommended for the design of a variable-stiffness laminate with overlaps with an identical or lower mass than the baseline. In practice a composite structure is designed for minimum structural weight with a minimum level of structural performance and not for maximum structural performance for a given weight. This would also require the elimination of plies and a full stacking sequence optimization.



# Chapter 6

## Manufacturing

Two sets of cylinders were built as part of the research project presented in this thesis. The first set, built by Boeing using an Ingersoll AFP system, included three specimens: two reference cylinders and one cylinder with a circumferential angle variation, which had a constant thickness that was achieved by using the tow-cut and restart capability of the fiber placement machine. The laminate of the variable-stiffness cylinder was the optimized laminate determined in section 5.3.4. This set of cylinders was used to verify the computed designs through testing.

The second set, which was built by NLR, the National Aerospace Laboratory of the Netherlands, contained one baseline cylinder and one cylinder with an axial stiffness variation. The shifted method and the parallel method, described in section 3.1, were combined to construct a variable-stiffness laminate with overlaps. These two cylinders were not tested and serve as an example for the construction of a laminate in which the shifted method and the parallel method are combined.

The manufacturing data for the AFP systems was transferred to the machine in terms of path coordinates, direction vectors, surface normal vectors, and tow-mask definition, where the tow-mask definition describes which tows are active and which are not. The manufacturing of both cylinder sets will be discussed below.

### 6.1 Cylinders with Circumferential Stiffness Variation

The cylinders built by Boeing were optimized for maximum load carrying capability under bending as described in subsection 5.3.4. These cylinders were made of 24 plies of BMS8-276 material and the baseline cylinder and the variable-stiffness cylinder had equal mass. The optimum layup of these cylinders was discussed in chapter 5, but will be repeated briefly below.

The baseline cylinder had a quasi-isotropic layup of  $[\pm 45, 0_2, 90_2, 0, \pm 45, \pm 45, 90]_s$ . The variable-stiffness cylinder contained 12 plies with 3 different steered ply definitions and 12 plies with a constant fiber angle. The layup of the variable-stiffness cylinder was  $[\pm 45, \pm \varphi_1(\theta), 0, 90, \pm \varphi_3(\theta), 0, 90, \pm \varphi_5(\theta)]_s$ , where the  $\varphi(\theta)$  represented plies with an 8-segment constant curvature variation in the circumferential direction, see section 5.3.4. The

design variables and the path curvature values for the steered plies are given in table 6.1, where the curvature  $\kappa_{i,j}$  denotes the path curvature in segment  $i$ , between  $T_i$  and  $T_j$ .

Table 6.1: Ply variables and path curvatures of the manufactured variable-stiffness cylinder with layup  $[\pm 45, \pm \varphi_1(\theta), 0, 90, \pm \varphi_3(\theta), 0, 90, \pm \varphi_5(\theta)]_s$

Ply	Design variables					Path curvatures			
	$T_0$ ( $^\circ$ )	$T_1$ ( $^\circ$ )	$T_2$ ( $^\circ$ )	$T_3$ ( $^\circ$ )	$T_4$ ( $^\circ$ )	$\kappa_{0,1}$ ( $\text{m}^{-1}$ )	$\kappa_{1,2}$ ( $\text{m}^{-1}$ )	$\kappa_{2,3}$ ( $\text{m}^{-1}$ )	$\kappa_{3,4}$ ( $\text{m}^{-1}$ )
$\varphi_1(\theta)$	10.0	10.0	10.0	10.0	24.7	0	0	0	0.32
$\varphi_3(\theta)$	10.0	10.0	10.6	56.9	61.7	0	0.01	1.82	0.30
$\varphi_5(\theta)$	10.0	12.0	10.0	34.2	68.9	0.03	-0.03	0.66	1.95

The optimization results provided the general parameters for the layup, but many details needed to be taken into account to produce the desired laminate quality. A number of manufacturing details, such as the curvature constraint, the coverage parameter and the minimum cut length, were discussed in section 2.1. These details will also be discussed briefly below, in addition to other manufacturing issues that were encountered during the manufacturing of the variable-stiffness cylinder, to provide a complete overview of the challenges encountered during the detailed design for manufacturing of variable-stiffness laminates.

### 6.1.1 Curvature Constraint

The one manufacturing constraint that was taken into account during the optimization of the cylinders was the curvature constraint. The curvature constraint was set to  $1.97 \text{ m}^{-1}$ , which corresponded to a minimum in-plane turning radius of the central path of 508 mm (20 in). The turning radius was chosen to be smaller than the typical value of the minimum turning radius used in the aerospace industry for a 32 tow course with 3.175 mm wide tows, which is 635 mm (25 in). This was because the dimensions of the test specimen were quite small, which could have limited the design space too much if the larger value of the turning radius was used, i.e. if the maximum curvature was set to  $1.57 \text{ m}^{-1}$ . The curvature values listed in table 6.1 all satisfied the curvature constraint of  $1.97 \text{ m}^{-1}$ , while the curvatures  $\kappa_{2,3}$  in ply 3 and  $\kappa_{3,4}$  in ply 5 were larger than  $1.57 \text{ m}^{-1}$ , indicating that the fibers are most severely curved in these two segments.

The curvature constraint should prevent severe local wrinkling of tows on the inside of a turn, called puckering. Some puckering still occurred, especially in the segments with large curvature values, but intermediate debulking of the laminate was used to suppress the puckers, such that the final product had a smooth surface. An example of the puckers that were observed during manufacturing is shown in figure 6.1(a). It can be seen in this picture that the puckers mainly occurred in locations where underlying plies had course boundaries. The occurrence of puckers at underlying course boundaries may be caused by reduced tackiness at these locations. A picture of the finished product is shown in figure 6.1(b). The white lines on the cylinder served as a reference for the fiber angle distribution, i.e. lines were drawn at  $\theta = 0^\circ$ ,  $\theta = 90^\circ$ ,  $\theta = 180^\circ$ , and  $\theta = 270^\circ$ .

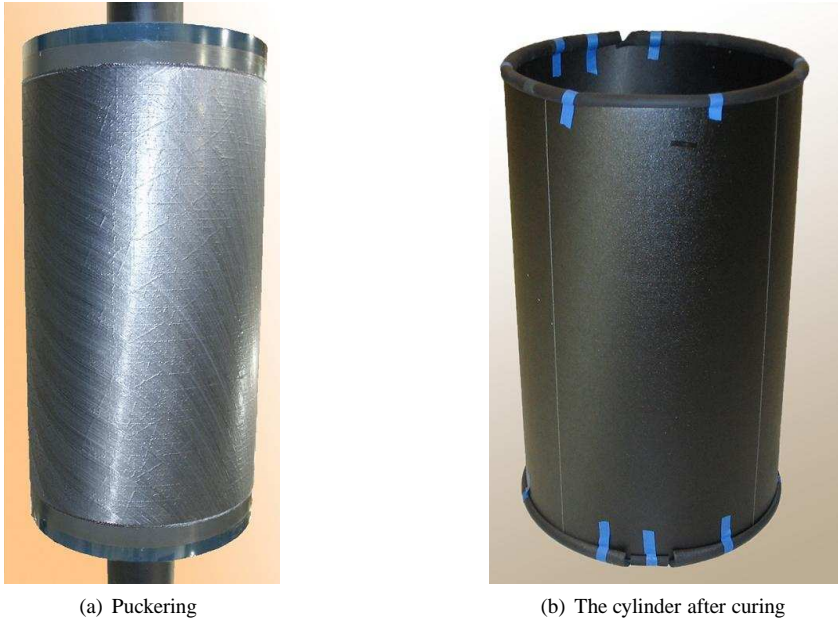


Figure 6.1: Cylinder with a stiffness variation in the circumferential direction during lay down and after curing (photos: Boeing)

### 6.1.2 Compaction Pressure

The quality of a fiber-placed laminate depends on the amount of compaction applied during laydown of the fibers. The pressure is delivered by the compaction roller which has some flexibility to conform to the surface. The compaction roller might not be able to deform enough to supply sufficient compaction at the course edges if the surface is too curved. This is most evident for 0 degree courses on a cylinder, i.e. courses that are aligned with the axial direction. An example is shown in figure 6.2 where a gap between the roller and the surface can be seen.

The compaction roller available on the Ingersoll fiber placement machine was not flexible enough for the given cylinder geometry, which would have resulted in insufficient compaction of the tows on the outsides of the course if the design had not been adjusted. The compaction problem was solved by only placing the inner tows which had sufficient compaction. The number of tows that could be placed was calculated based on the geometry depicted in figure 6.3. The maximum conformance  $c$  for the edge of a 4 inch wide roller was 3 mm (0.12 inch). The following geometric relationships hold:

$$\begin{aligned} R - R \cos \gamma &= c \\ R \sin \gamma &= \frac{w_p}{2} \end{aligned} \quad (6.1)$$

where  $w_p$  is the course width measured tangent to the surface and perpendicular to the axial

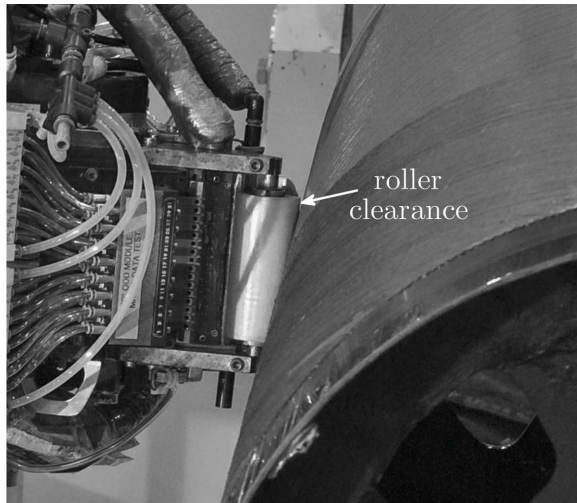


Figure 6.2: Gap between the roller and the cylinder surface, causing insufficient compaction (photo: Boeing)

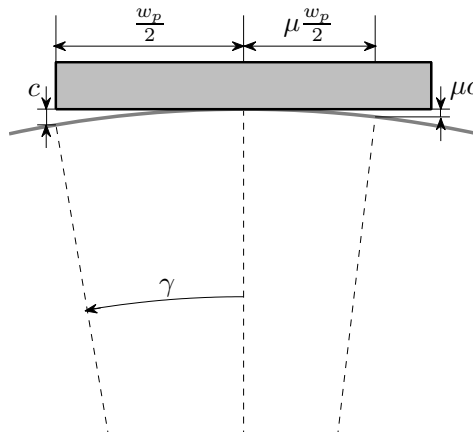


Figure 6.3: Geometry for the compaction pressure constraint

direction and  $R$  is the cylinder radius. Combining these two equations gives:

$$R^2 = \left(\frac{w_p}{2}\right)^2 + (R-c)^2 \quad (6.2)$$

which can be simplified to:

$$0 = \left(\frac{w_p}{2}\right)^2 - 2Rc + c^2 \quad (6.3)$$

The course width perpendicular to the axial direction is  $w_p = w \cos \varphi$ , where  $w$  is the course width. Equation 6.3 can not be satisfied if the full head width of 102 mm is placed at a fiber angle of 0 degrees. The course width thus needs to be adjusted. A point at a distance  $\mu \frac{w_p}{2}$

from the course centerline is chosen to determine the maximum course width that can be placed on the cylinder surface with sufficient compaction pressure.  $\mu$  has a value between 0 and 1. The roller is not expected to deform as much as  $c$  at the location  $\mu \frac{w_p}{2}$  and therefore  $c$  is also scaled by  $\mu$ , assuming a linear deformation of the roller. Equation 6.3 becomes:

$$\frac{\mu^2 w_p^2}{4} = 2\mu Rc - \mu^2 c^2 \quad (6.4)$$

This equation can first be divided by  $\mu$ , assuming  $\mu \neq 0$  and then it can be solved for  $\mu$ :

$$\mu = \frac{2Rc}{\frac{w_p^2}{4} + c^2}, \quad \text{if } \mu > 1 \text{ then } \mu \equiv 1 \quad (6.5)$$

The allowed course width can also be calculated as a function of the fiber orientation, since the perpendicular course width varies as a function of the fiber orientation as  $w_p = w \cos \varphi$ .

$$\mu = \frac{2Rc}{\frac{w^2 \cos^2 \varphi}{4} + c^2}, \quad \text{if } \mu > 1 \text{ then } \mu \equiv 1 \quad (6.6)$$

The maximum number of tows can be derived from  $\mu$ . The allowed number of tows is given by equation 6.7, assuming the number of tows on the left side of the centerline and on the right side of the centerline are the same.

$$N_{t,\max} = \left\lfloor \frac{32\mu}{2} \right\rfloor \quad (6.7)$$

where the  $\lfloor \cdot \rfloor$  function rounds the real number to the nearest smaller integer number. The maximum number of tows  $N_{t,\max}$  are plotted as a function of the fiber angle orientation for a 304.8 mm (12 in) radius cylinder in figure 6.4. The continuous value of  $32\mu$  is also plotted. The compaction pressure does not have any effect on the maximum allowed course width for fiber angles larger than  $31^\circ$ , where  $N_{t,\max}$  is 32. The course width for the  $0^\circ$  plies had to be adjusted from 32 tows to 22 tows to ensure sufficient compaction pressure. The maximum course width for steered ply  $\varphi_1$  was adjusted to 26 tows, the maximum course width for a fiber angle of  $24.7^\circ$ . The course width for the other variable-stiffness plies did not have to be adjusted, because the course width at smaller fiber angles was already reduced to avoid overlapping courses.

### 6.1.3 Coverage Parameter and Parallel Courses

The coverage parameter determines where tows are terminated and restarted with respect to the boundary of a neighboring course. Cutting and restarting tows create either small triangular gaps or small overlaps or a combination of gaps and overlaps. A coverage of 0 percent indicates that a tow is cut as soon as one edge reaches the boundary of the adjacent course. This results in a small triangular area without fibers. At 100 percent coverage the tow is cut only when the second tow edge crosses the boundary, creating a small triangular overlap area. Coverage values between 0 and 100 percent represent the intermediate cases.

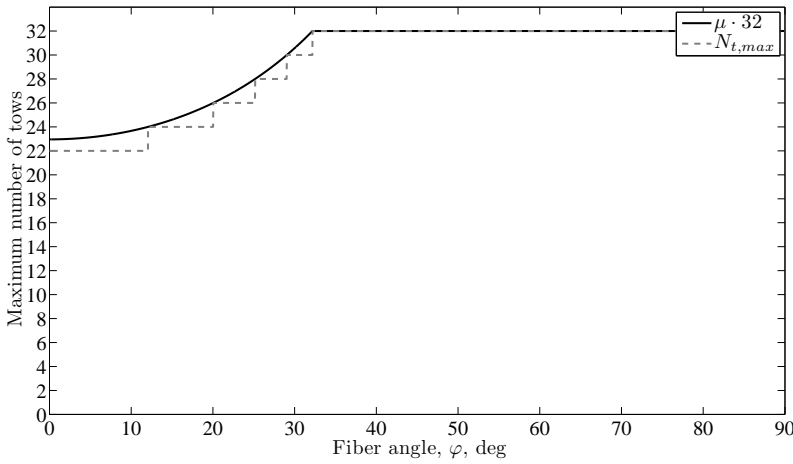


Figure 6.4: Maximum number of tows allowed for sufficient compaction

A coverage parameter of 0 has been demonstrated to be undesirable by Blom et al. (2009), because the resin-rich tow-drop areas act as stress raisers, while 100 percent coverage might result in an uneven surface. No test data is publicly available for either of these cases and therefore a coverage parameter close to 50 percent was used in the design. Furthermore the boundary between two courses was chosen to lie exactly between the centerlines of two adjacent courses to minimize the deviation of the fiber angle from the ideal fiber angle. The result can be seen in figure 6.5, where the white marked tows belong to one course and partially overlap the black marked tows, belonging to the adjacent course.

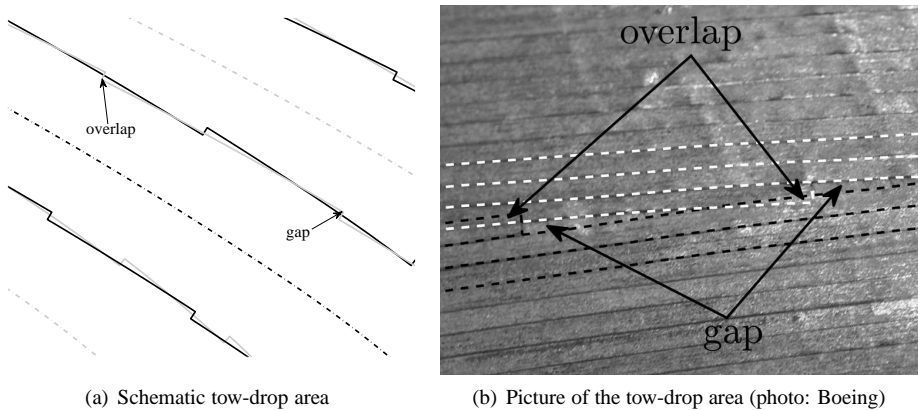


Figure 6.5: Gaps and overlaps between tows for 40-60 % coverage parameter

Adjustment of the coverage parameter alone is not always sufficient to eliminate large gaps or overlaps between adjacent courses. The first steered ply of the optimum variable-stiffness laminate, for example, had a large area where the fiber orientation angle was a

constant  $10^\circ$ , which resulted in long stretches of parallel courses. In general, these parallel courses do not line up exactly, causing either a long slit or a long line with overlapping tows between courses. A schematic view of this is shown in figure 6.6. The parts of the

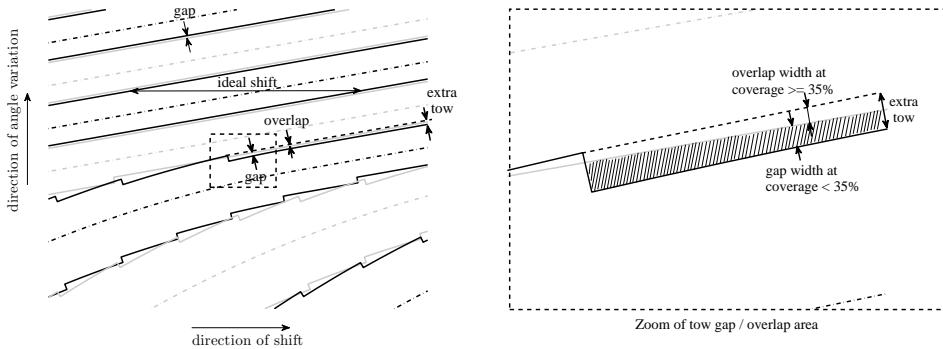


Figure 6.6: Long gaps or overlaps due to parallel courses

laminate that have parallel courses can be designed such that the courses exactly line up and a good laminate quality is obtained. This is achieved by applying the proper amount of shift between courses. The amount of shift was adjusted by changing the number of courses, such that periodicity was maintained, see equations 3.41 and 3.42 in chapter 3. The result of this design adjustment is shown in figure 6.7. It can also be concluded, based on this picture, that the accuracy with which the courses are laid down was excellent, since there were no gaps or overlaps between parallel courses, as it was designed.

Variable-stiffness plies  $\varphi_1$  and  $\varphi_2$  both contained a large region where the fiber angle was constant at  $10^\circ$ . These courses were only 6 or 7 tows wide to avoid overlaps, but contained no tow-drops or tow-adds. Multiple narrow parallel courses could therefore be combined into one wider course to reduce the total number of courses and to speed up the production process. A condition is that no tow-drops or tow-adds are present in-between the courses that are combined, because that would mean that the courses are not exactly parallel.

An NDI scan of the manufactured cylinders was made to look at possible defects introduced by the stiffness variation. The NDI scan of the variable-stiffness cylinder, in which the location of the tow cuts can be seen, is shown in figure 6.8. On one side of the cylinder the courses are steered more, requiring more tow drops to maintain a constant thickness, i.e. the areas on the left and the right in figure 6.8. The other side of the cylinder contains mainly parallel courses, showing less irregularities, i.e. the middle of figure 6.8. The circumferential irregularities in the middle of figure 6.8, i.e. the dark horizontal lines, also indicate defects which may be due to a thermal mismatch between the part and the tool. The laminate in-between  $\theta = 270^\circ$  and  $\theta = 90^\circ$  is biased in the axial direction and therefore has a relatively large coefficient of thermal expansion in the circumferential direction. A detailed finite element analysis of the cylinder and the tool during curing, including thermal and chemical shrinkage and tool-part interaction, could provide more insight in the origin of the defects.

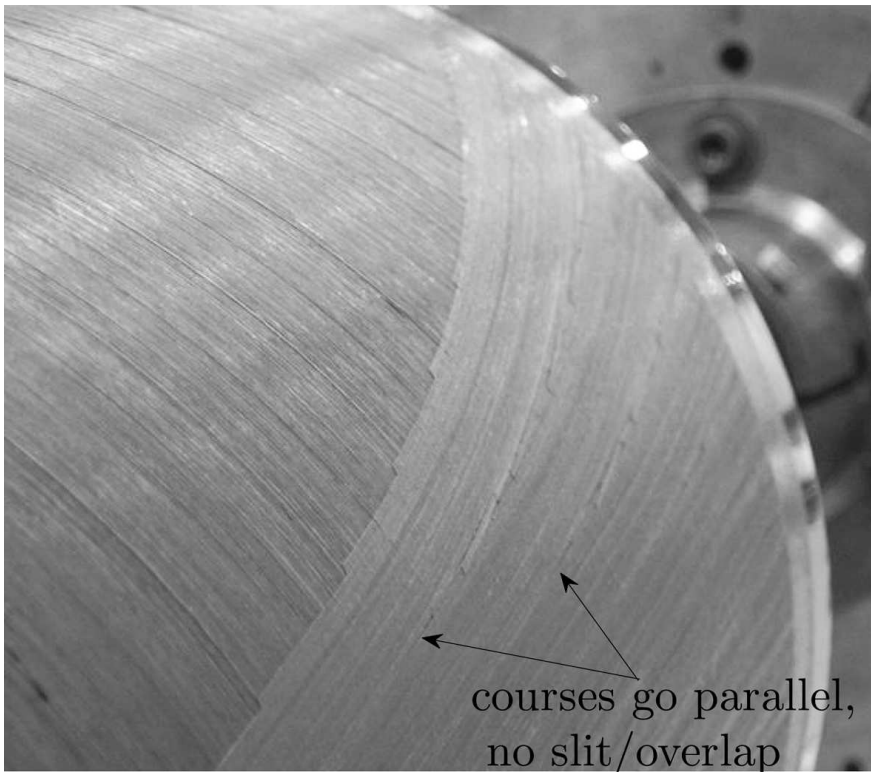


Figure 6.7: Parallel courses without a long gap or overlap (photo: Boeing)

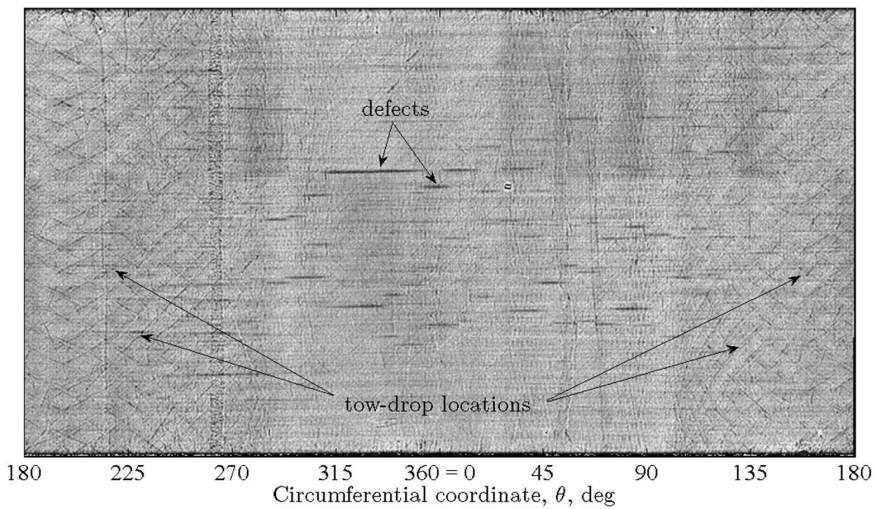


Figure 6.8: NDI of the variable-stiffness cylinder



### 6.1.4 Minimum Cut Length and Fiber Straightening

The ability of the fiber placement machine to cut and restart tows was used to eliminate overlaps between adjacent courses and to create constant-thickness plies. The curved courses sometimes required the start and termination of a tow within a course, so that attention had to be paid to the minimum cut length. The minimum cut length is the minimum tow length that needs to be laid down before a tow can be cut after it has been started.

A tow is moved forward by pinching rollers when it is (re)started and continues until it reaches the surface, where it is pulled forward by the friction between the compression roller and the tool surface. There is no control over the tow if the desired length to be put down is smaller than the distance between the cutter and the contact point, in which case the fiber placement software prevents the placement of the tow. The minimum cut length thus depends on the distance between the cutters and the contact point between the compaction roller and the tool surface. This distance is indicated by the dotted line in figure 6.9. The

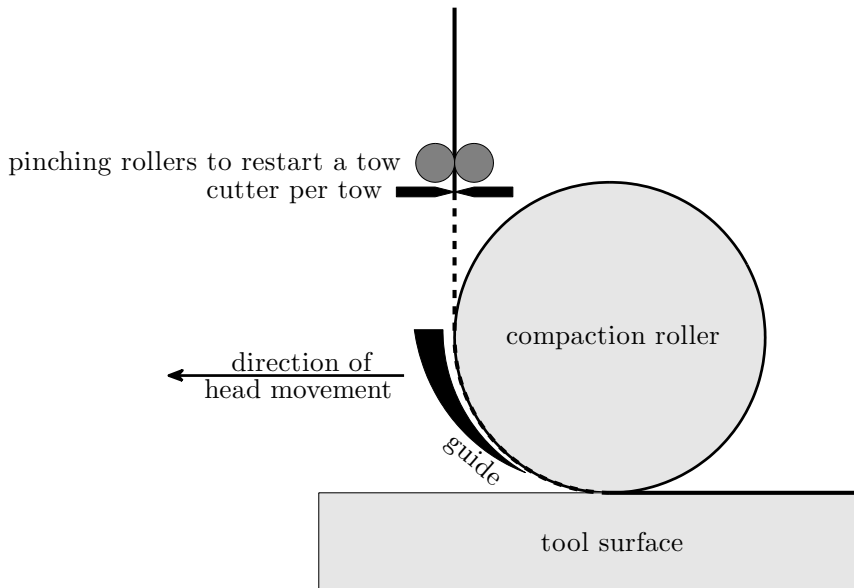


Figure 6.9: Schematic view of fiber placement head

minimum cut length for the Ingersoll machine, used for the production of the variable-stiffness cylinder, was 107 mm (4.2 inches). Small adjustments of the coverage parameter were made to meet the required minimum length of 107 mm in the case of minimum cut length violations. The minimum cut length requirement could not always be met at the part edges, as shown in figure 6.10, and the gaps were filled in by hand. Most of these areas were trimmed from the final part.

The minimum cut length also played a role when a steered fiber path was placed on the surface and the outermost tows on the side with the largest turning radius, i.e. the tows on the outside of the turn, were cut. There was very little control over the direction of a tow by the guiding rollers once a tow was cut, such that the cut tow followed the geodesic path

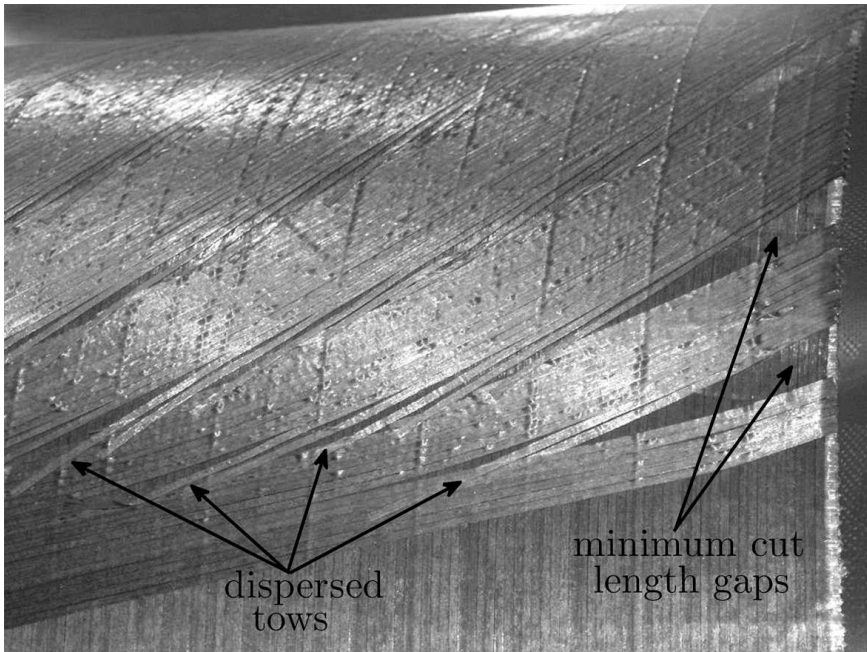


Figure 6.10: Tow drop areas at part edges and fiber straightening (photo: Boeing)

instead of the curved path, called fiber straightening. Fiber straightening is shown in figures 6.10 and 6.11. The length  $l$  in figure 6.11 over which the tow deviated from the designed path was 104 mm (4.1 in), which was almost equal to the minimum cut length of 107 mm. The amount of deviation  $\delta$  can be related to the path turning radius  $\rho$  and the length over which the tow deviates  $l$  using the definitions for a geodesic path and a constant curvature path:

$$\delta = \sqrt{\rho^2 + l^2} - \rho \quad (6.8)$$

Substituting the value of the turning radius of that course segment,  $\rho = 549$  mm (21.6 in), and the deviation length,  $l = 104$  mm (4.1 in), in equation 6.8 results in a deviation of 9.8 mm (0.38 in), which matched well with the measured deviation of 9.7 mm (0.38 in). The amount of deviation can thus be calculated based on the curvature of the course and the minimum cut length.

Fiber straightening does not occur when the tow is cut on the inside of the turn, because then the neighboring tow forces it to follow the curve. No design adjustments were made to prevent the fiber straightening, because it was not anticipated. The straight tows in the manufactured variable-stiffness cylinder were aligned with the curved tows by hand to obtain the intended configuration.

The deviation from the intended path due to fiber straightening is smaller when a larger turning radius is used. The deviations on a larger cylinder with a similar fiber angle variation as manufactured would not be as large as on the test cylinder that was manufactured, because a smaller turning radius would be required to obtain the same fiber angle variation.

Fiber straightening can be avoided in future designs by designing the steered courses

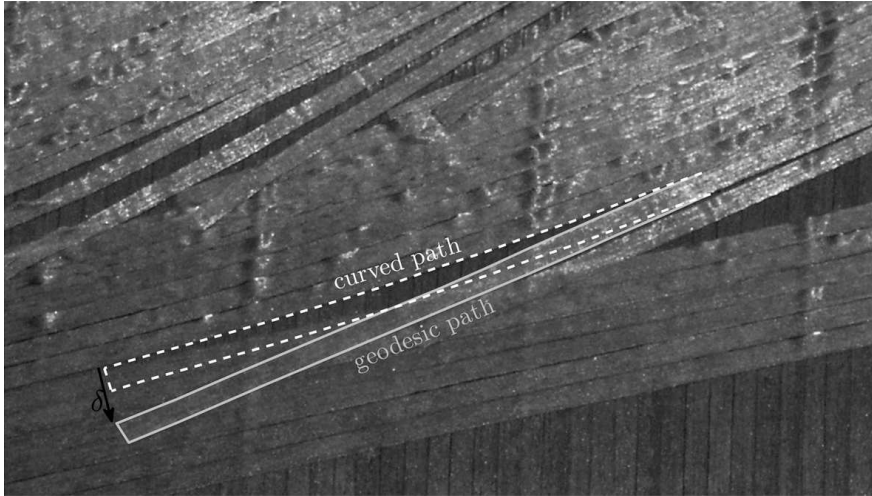


Figure 6.11: Fiber straightening (photo: Boeing)

such that no tows are cut on the outside of a turn. One method to avoid tow cuts on the outside of a turn is to reverse the direction of lay down. Reversing the direction of lay down converts tow-drops into tow-adds, which solves the fiber straightening problem, because adding tows on the outside of a turn is not a problem. Fiber straightening can not be avoided if the course contains tows on the outside of the turn that are first added and then cut, because the tow-adds will be converted into tow-cuts and the problem persists. Other adjustments in the design are then required.

Furthermore, the number of tow cuts and adds could be reduced by placing a number of courses parallel, as if a wider course was placed on the surface. The shifted method would be combined with the parallel method to construct a variable-stiffness laminate, similar to the construction of the cylinder with the axial stiffness variation, which will be described in section 6.2, except that overlaps would be avoided. Wider courses cause larger deviations from the intended fiber angle distribution, see section 3.3.3 for the formulas and figure 4.3 for an example, but since the deviation of the fiber angle can be taken into account in the finite element analysis, the influence of this deviation on the structural performance can be evaluated. For example, the variation of the buckling moment of the optimized cylinder as a function of the maximum course width is shown in figure 6.12, where the value of the buckling moment is normalized with the buckling moment of a cylinder with a perfect circumferential variation. The buckling load was calculated using finite elements and the exact modeling of the fiber angle orientation based on fiber placement and a given maximum course width. The manufactured cylinder, which had a maximum course width of 102 mm (4 in), showed less than 0.1 percent reduction in buckling load compared to the ideal layup. A maximum course width of 305 mm (12 in) would result in less than 2 percent reduction in buckling load, while the number of tow drop boundaries would be three times less than in the current design.

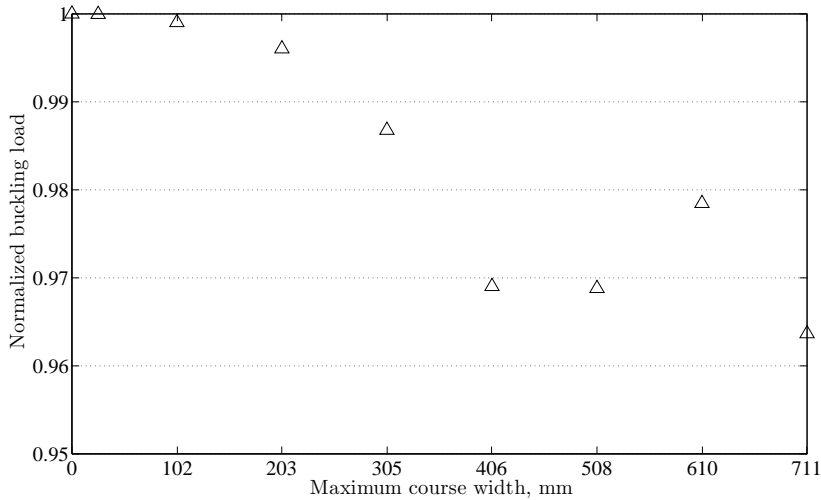


Figure 6.12: Buckling load variation as a function of the maximum course width

## 6.2 Cylinder with Axial Stiffness Variation

A second set contained of cylinders was built by the NLR, the National Aerospace Laboratory of the Netherlands, using an Automated Dynamics work cell. This set contained one baseline cylinder and one cylinder with an axial stiffness variation. The shifted method and the parallel method, described in section 3.1, were combined to construct a variable-stiffness laminate with overlaps. These two cylinders were not tested and serve as an example for the construction of a laminate in which the shifted method and the parallel method are combined.

The diameter of the cylinders manufactured by the NLR was 600 mm and the length was 725 mm. Both the reference cylinder and the variable-stiffness cylinder consisted of 8 plies with a ply thickness of 0.181 mm and were made of unidirectional AS4/8552 carbon-epoxy prepreg.

Two different configurations were built: a baseline cylinder, which had a quasi-isotropic layup of  $[\pm 45, 0, 90]_s$ , and a variable-stiffness cylinder, which had a stiffness variation in the axial direction and overlapping courses. The variable-stiffness cylinder had a layup of  $[\pm 45, \pm \varphi(x)]_s$ , where  $\varphi(x)$  represented a ply with fiber angles that varied in the axial direction. The fiber angle was varied according to a two-segment constant curvature variation  $T_0 = 60^\circ$ ,  $T_1 = 15^\circ$ ,  $T_2 = 60^\circ$  and  $L_0 = L_1 = \frac{L}{2}$ .

These two cylinders were manufactured using an automated fiber placement work cell by Automated Dynamics (ADC). This machine placed 4 tows with a total width of 12.7 mm (0.5 in) at a time and did not have the capability to cut the tows individually. It was thus decided to allow overlaps of the courses, resulting in a thickness buildup towards the edges. Typical AFP machines are able to deliver more than 4 tows per course and therefore a scheme was implemented to combine parallel courses with shifted courses, such that a machine head with a larger number of tows could be simulated. The variable-stiffness cylinder

was fabricated by placing 5 courses in parallel, forming 20 parallel tows, to simulate a total course width of 63.5 mm (2.5 in). Subsequently another 63.5 mm wide course was placed on the surface, where it was shifted in the circumferential direction with respect to the first course. The spacing between courses was such that all courses were equally spaced and gaps were avoided. As an example four 20-tow wide courses, consisting of 5 parallel 4-tow wide courses, are shown in figure 6.13. A picture of the steered courses during manufacturing is given in figure 6.14.

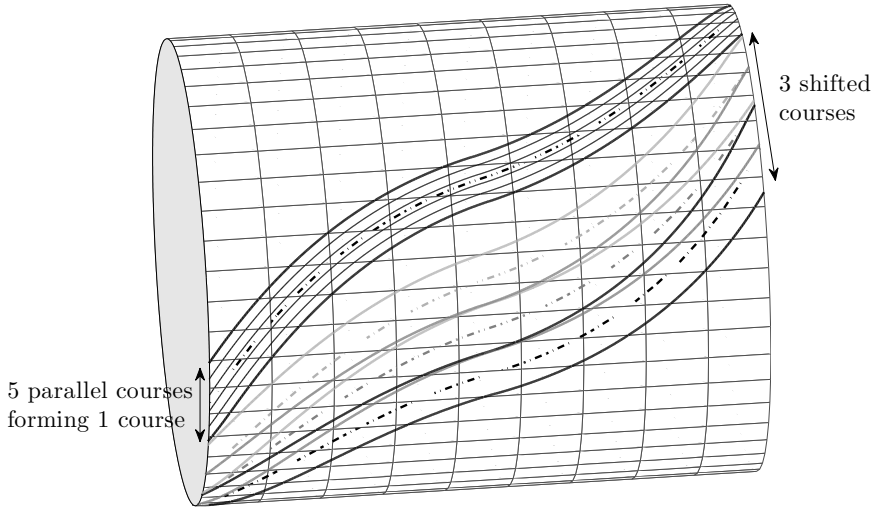


Figure 6.13: Shifted and parallel courses combined in one laminate

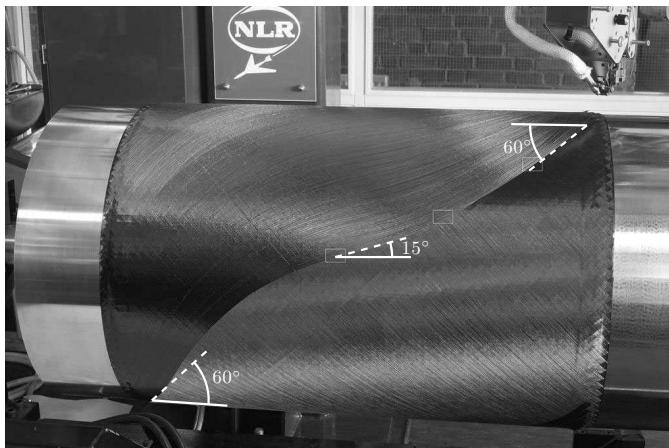
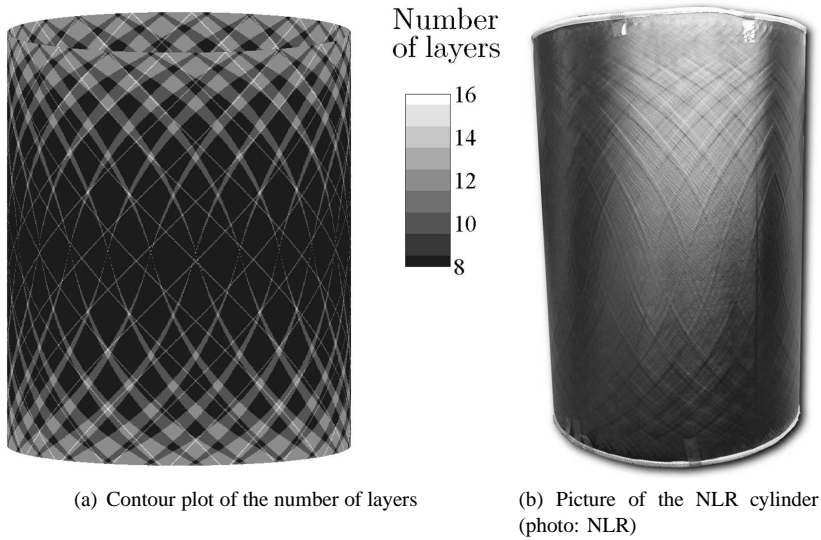


Figure 6.14: Axial stiffness variation

The resulting thickness distribution is shown in figure 6.15. A contour plot of the number of layers resulting from the simulation is shown in figure 6.15(a), while figure 6.15(b) is a picture of the actual cylinder where the overlaps are clearly visible. The picture shows the

cylinder before it was trimmed to the final dimension, which is why it looks thinner than the simulation. The mass of the variable-stiffness cylinder was increased from 3.11 kg to 3.52 kg compared to the baseline cylinder. The technique of combining the parallel method with the shifted method to create a variable-stiffness laminate and its usefulness was discussed in subsection 6.1.4.



*Figure 6.15: Overlaps on the NLR cylinder*

### 6.3 Conclusions

Cylindrical shells with varying fiber orientations were manufactured using advanced fiber placement technology. The small dimensions of the cylinder required a small turning radius, causing puckers to form during lay-down which were not visible in the end product. A larger turning radius can be used on a cylinder with larger dimensions to obtain the same stiffness variation, resulting in less puckering. In the constant-thickness test cylinder the amount of small triangular gaps and overlaps was minimized by using a 50 percent coverage parameter, while long gaps between parallel courses were avoided by adjusting the shift between courses. The minimum cut length requirement was taken into account during the design, preventing any deficiencies in placing tows on the surface. Cutting tows on the outside of a steered course caused the tows to straighten, because the outer tows were not restrained and thus followed a geodesic path. Fiber straightening can be avoided in future designs by not allowing tows to be cut on the outside of a turn. Furthermore, increasing the maximum course width by combining the shifted method with the parallel method would result in less tow drop areas.

# Chapter 7

## Modal Test

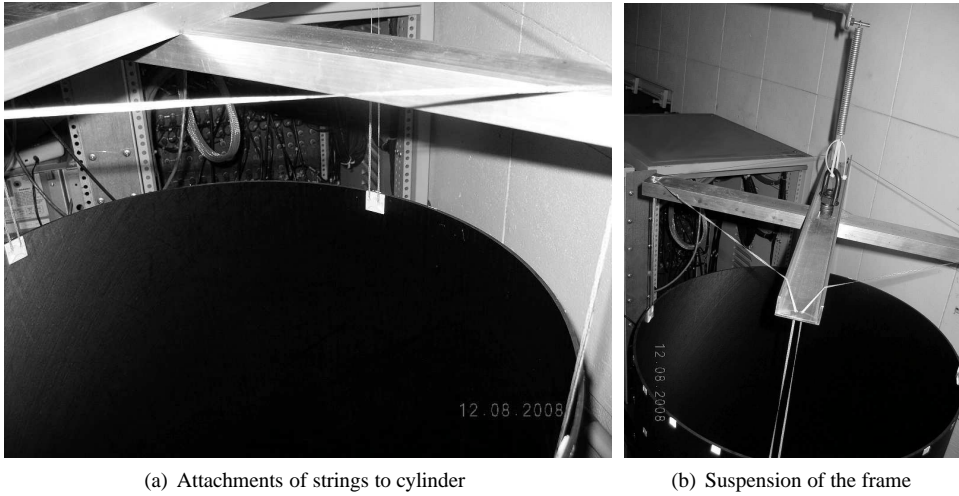
Three carbon fiber-reinforced cylinders were manufactured by the Boeing Company using fiber placement based on the optimizations given in section 5.3.4. Two of these cylinders, also referred to as baseline cylinders, had an identical, quasi-isotropic layup, while the third cylinder had a circumferentially varying laminate stiffness. A modal test of one of the baseline cylinders and the variable-stiffness cylinder was performed at the dynamic test laboratory of the Boeing Company in Seattle, WA. Both these tests, baseline and variable-stiffness, served as a means to determine the accuracy of the finite element models in capturing mass and stiffness distributions, and to study the influence of the stiffness distribution on the modal response. A description of the test configuration will be given in this chapter, followed by a comparison of the experimental and analytical eigenfrequencies and eigenmodes. Then the baseline and the variable-stiffness cylinder will be compared and the physical responses of the cylinder in terms of frequency response functions and power spectral densities will be compared to the finite element prediction. Finally, conclusions will be drawn about the accuracy of the finite element model with respect to the experimental results.

### 7.1 Description of Specimens

The specimens that were tested were the cylinder with a circumferential stiffness variation and one of the two manufactured baseline cylinders described in subsection 5.3.4. They were manufactured by the Boeing Company, see section 6.1. Both cylinders consisted of 24 plies of carbon-fiber reinforced epoxy, had an inner diameter of 609 mm and a test length of 990 mm.

### 7.2 Test Configuration

The boundary conditions of the cylinder for the modal test were free-free. One of the cylinder edges was attached to an aluminum cross through four wires that were spaced at 90 degree intervals, such that the cylinder was hanging vertically. At the center section the aluminum cross was suspended by a spring to the ceiling, as shown in figure 7.1. This way

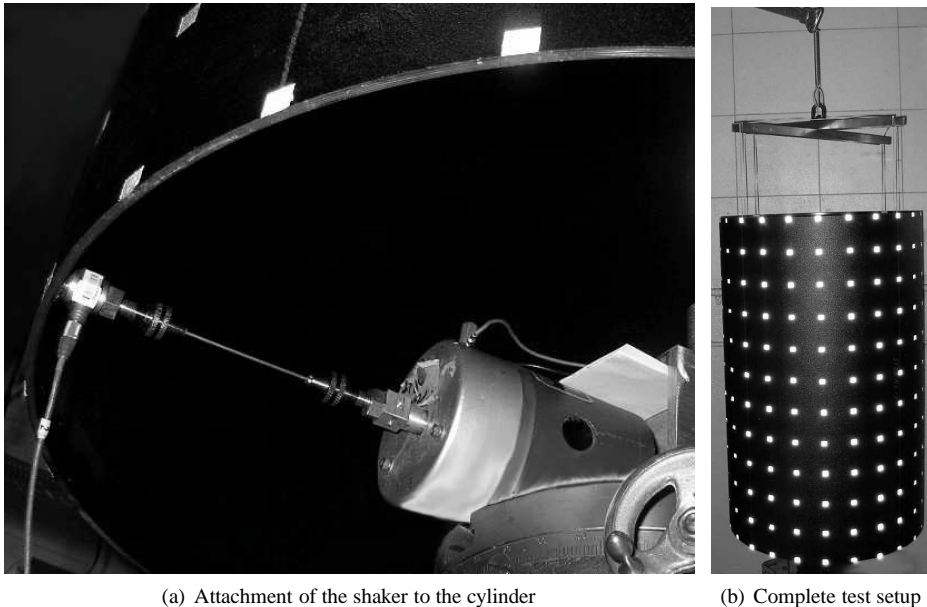


(a) Attachments of strings to cylinder

(b) Suspension of the frame

*Figure 7.1: Suspension of the structure*

the axial degrees of freedom at the boundaries were affected as little as possible, while the cylinder was free to move horizontally. The test setup closely approached free-free boundary conditions. A load cell was bonded to a point on the inside of the cylinder at the lower edge and attached to an electrodynamic shaker as shown in figure 7.2(a). The shaker was used to excite the cylinder with random vibrations in the frequency range from 0 up to 1250



(a) Attachment of the shaker to the cylinder

(b) Complete test setup

*Figure 7.2: Modal test configuration*



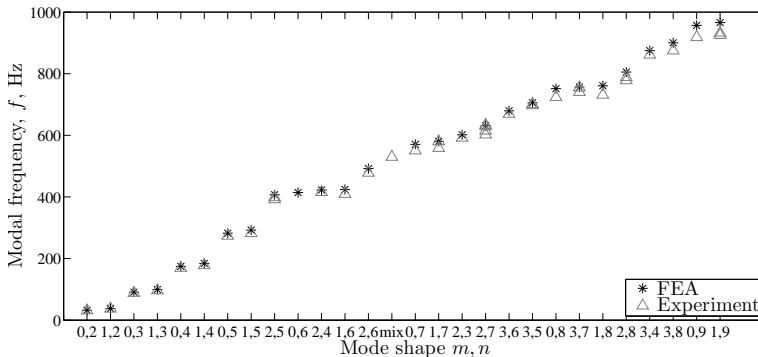
Hz. Deformations were measured at discrete points on the cylinder surface using a laser vibrometer, and to improve the quality of the measurements highly reflecting tape was used, see figure 7.2(b). The grid of both cylinders consisted of 12 points in the axial direction, with a circumferential spacing of 15 degrees. The baseline cylinder was measured over 180 degrees of the circumference, while the variable-stiffness cylinder was measured over the full circumference. The responses were measured until the cylinder was fully damped. Each point was excited and measured over the full frequency range ten times to filter out noise. This cycle was repeated for all points in the measurement grid.

### 7.3 Comparison of Modal Frequencies and Mode Shapes

The experimental and analytical results for the mode shapes and modal frequencies will be compared in this section. The analytical results were obtained with the finite element program ABAQUS. The Lanczos eigensolver (ABAQUS, Inc., 2005) was used to calculate the eigenfrequencies and eigenmodes of the cylinders, which had free-free boundary conditions. The model consisted of 78 shell elements in the axial direction and 156 shell elements in the circumferential direction. The stacking sequence was calculated for each element of the variable-stiffness cylinder using a Fortran program to account for the circumferential stiffness variation.

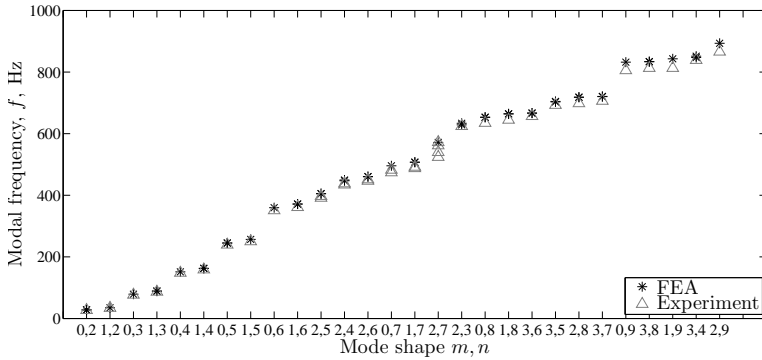
The shape of the eigenmodes and the modal frequency values provide information about the mass and stiffness properties a structure. The quality of the analytical model to predict these properties can be assessed by comparing the experimental and analytical modes and frequencies. The measured and predicted modal frequencies are plotted versus the mode shape in figure 7.3. The results for the baseline cylinder are given in figure 7.3(a) and the results for the variable-stiffness cylinder are given in figure 7.3(b).

The modes are described by their number of half waves in axial direction  $m$  and their number of full waves in circumferential direction  $n$ . Overall the analytical results corresponded well with the experimental results. In the analysis of the baseline cylinder there



(a) Frequencies and modes of the baseline cylinder

Figure 7.3: Comparison of the modal frequencies and modes between the experiment and the finite element analysis



(b) Frequencies and modes of the variable-stiffness cylinder

Figure 7.3: Comparison of the modal frequencies and modes between the experiment and the finite element analysis (continued)

was always one duplicate mode with exactly the same modal frequency, however, in the experiment the frequency of the duplicate mode was slightly different, see for example modes (2,5) and (1,7), and for mode (2,7) more than one duplicate mode was observed. This could be due to imperfections present in the test article, which were not included in the finite element model and therefore did not show up in the simulation. Up to 500 Hz the analytical results matched the experimental results within 5 percent. At higher frequencies the difference varied between 5 and 12 percent. The varying stiffness of the variable-stiffness cylinder already caused slightly different frequencies for duplicate modes in the finite element simulations. However, also for this cylinder no more than two duplicate modes were found in the analysis, yet the experiment showed more than two duplicate modes for the (2,7) mode. With the exception of the (2,7) mode, the predictions for the frequencies of the variable-stiffness cylinder were always within 5 percent of the measured frequencies.

A comparison between the calculated modal frequencies of the baseline cylinder and the

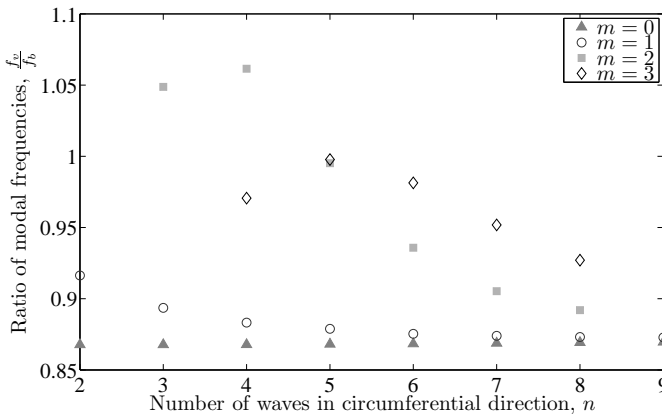


Figure 7.4: Comparison of the modal frequency per mode

variable-stiffness cylinder is shown in figure 7.4. The variable-stiffness cylinder had a lower frequency than the baseline cylinder, except for the modeshapes with  $m = 2$  and  $n = 3, 4$ . This can be explained by looking at the laminate bending stiffnesses of both cylinders, see figure 7.5.  $D_{11}$  is the laminate bending stiffness in the axial direction of the cylinder, while  $D_{22}$  is the laminate bending stiffness in the circumferential direction of the cylinder, as defined by the classical lamination theory (Jones, 1999). Since the laminate stiffness varied as a function of the circumference for the variable-stiffness cylinder (subscript  $v$ ), the values of the axial bending stiffness  $D_{11v}$  and the circumferential bending stiffness  $D_{22v}$  are given as a function of the circumferential coordinate  $\theta$ , normalized by the bending stiffnesses of the baseline cylinder (subscript  $b$ ),  $D_{11b}$  and  $D_{22b}$  respectively. Most mode shapes

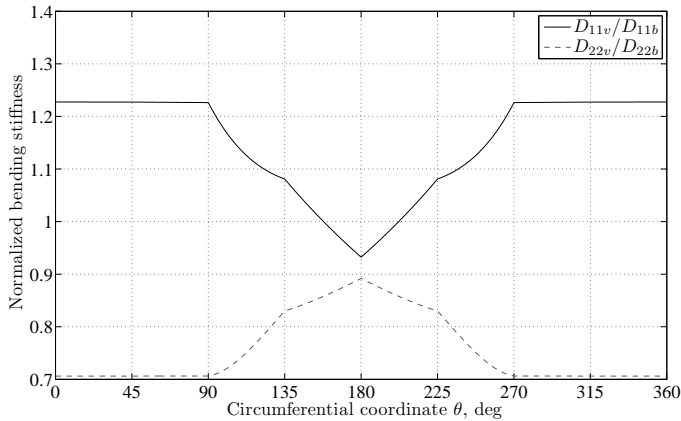


Figure 7.5: Bending stiffnesses of the variable-stiffness cylinder

had a larger number of full waves in the circumferential direction ( $n$ ) than number of half waves in the axial direction ( $m$ ), and therefore the bending stiffness in the circumferential direction ( $D_{22}$ ) was the most important stiffness term for the given cylinder geometry. The  $D_{22}$  bending stiffness of the variable-stiffness cylinder was always smaller than that of the baseline cylinder, i.e.  $\frac{D_{22v}}{D_{22b}} < 1$  in figure 7.5, which resulted in a smaller resistance against the formation of waves in the circumferential direction and therefore in a lower modal frequency. When the number of waves in the axial direction was increased, the value of the bending stiffness in axial direction  $D_{11}$  became more important. The axial bending stiffness of the variable-stiffness cylinder was larger than that of the baseline cylinder for most of the circumference, i.e.  $\frac{D_{11v}}{D_{11b}} > 1$  in figure 7.5, and this had a positive influence on the modal frequency. In the case of the mode shapes (2,3) and (2,4) the axial bending stiffness dominated and the natural frequency of the variable-stiffness cylinder became higher than that of the baseline cylinder. Furthermore, as the number of waves in circumferential direction increased the ratio between the frequencies tended to converge to one value, approximately 0.87, this was also the case for higher numbers of axial half waves.

A comparison of the mode shapes of the baseline cylinder and the variable-stiffness cylinder showed few differences in the low frequency modes. A smaller amplitude on the bottom side of the variable-stiffness cylinder than on the top side was found for the first

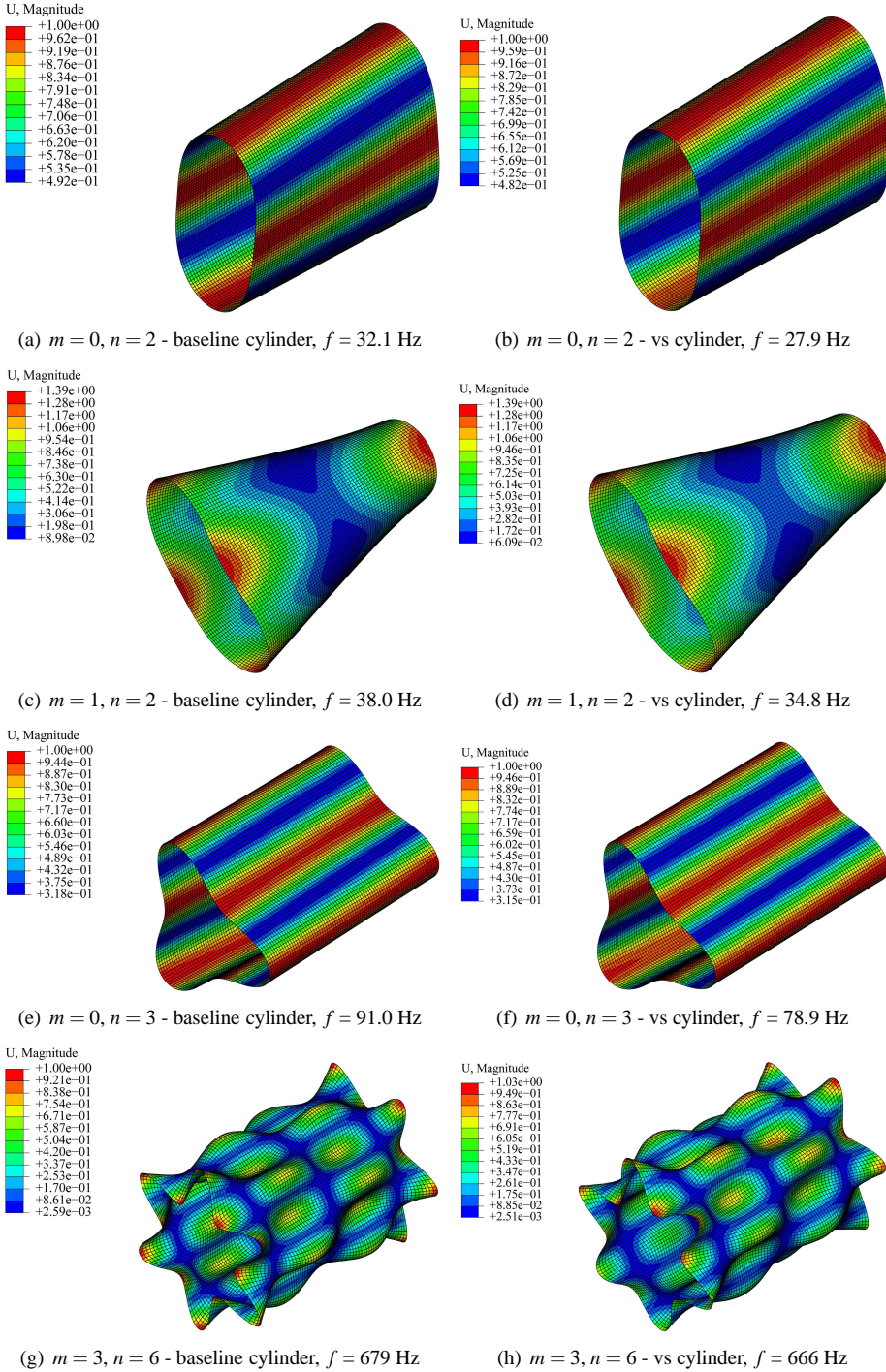


Figure 7.6: Eigenmodes for the baseline cylinder and the variable-stiffness (vs) cylinder

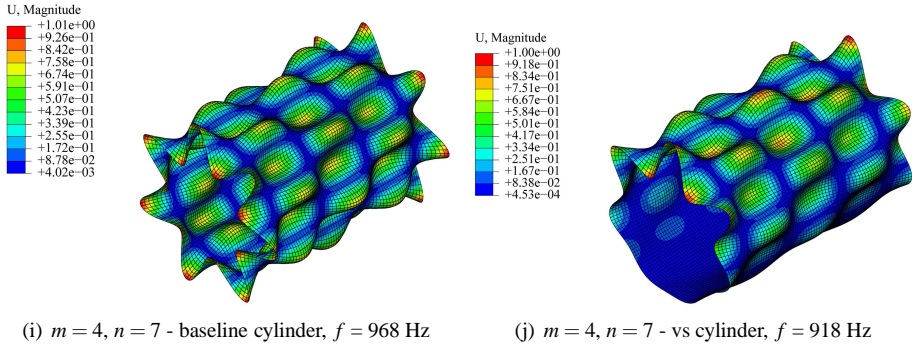


Figure 7.6: Eigenmodes for the baseline cylinder and the variable-stiffness cylinder (continued)

mode (0,2), see figure 7.6(b), with no difference in amplitude for the baseline cylinder, see figure 7.6(a). This was to be expected because the baseline cylinder had a constant stiffness, while the stiffness varied in the circumferential direction for the variable-stiffness cylinder. Looking at figures 7.6(c) to 7.6(f) the varying amplitude is not readily noticeable, however, for higher modes, such as the (3,6) and the (4,7) mode, the stiffness variation has a bigger influence on the deformation amplitudes around the circumference of the cylinder, as can be seen in figures 7.6(g) until 7.6(j). The laminate bending stiffness becomes more important as the wavelength of the modal waves gets smaller and thus the varying stiffness results in a larger difference in mode shape amplitude.

An interesting mode to compare would be the pure bending mode, as the cylinders were optimized for increasing the buckling bending moment. However, the ratio between the cylinder radius and the cylinder length was small and therefore the natural modes for the cylinders considered here were shell type modes and not beam type modes. The pure bending mode for the baseline cylinder occurred at a frequency of approximately 1900 Hz according to the finite element prediction, and the bending mode of the variable-stiffness cylinder was above 2500 Hz and since the reliability of the finite element results at these high frequencies was unknown it was not possible to draw any conclusions regarding the bending behavior.

## 7.4 Comparison of Physical Response

The modal response of both cylinders was simulated with a steady state dynamic analysis in ABAQUS. The previously calculated eigenfrequencies and eigenmodes were used in the dynamic analysis, while the damping factors required for the simulation were calculated using the experimental data. The modal response is characterized by two different functions: the frequency response function and the power spectral density. The frequency response function normalizes the amplitude of the response with the amplitude of the forcing function such that the influence of the excitation force is eliminated. The frequency response function

$H(f)$  is defined by:

$$|H(f)| = \left| \frac{V(f)}{F(f)} \right| \tag{7.1}$$

where  $V$  is the measured velocity, while  $F$  is the forcing function. A plot of the frequency response function versus frequency provides information about the mass, stiffness and damping of a structure. If the system is undamped, the amplitude of the response is infinite when the forcing frequency approaches the modal frequency of the structure. Structural damping reduces the magnitude of the vibration to a finite value, while the location of the peak depends on the resonance frequency values which depend on the mass and stiffness distribution in the system. The frequency response functions of three distinct points on the variable-stiffness cylinder are given in figure 7.7. The locations of the points 24, 114, and 253 for which the frequency response functions were given are shown in figure 7.7(d). Point 24 represents the location of the shaker, while the other two points are spread out over the cylinder. Since these three points are representative of the other points shown in figure 7.7(d), the results for the other points are omitted. The results for the baseline cylinder were similar to those of the variable-stiffness cylinder, and therefore not given here, see appendix F for these results.

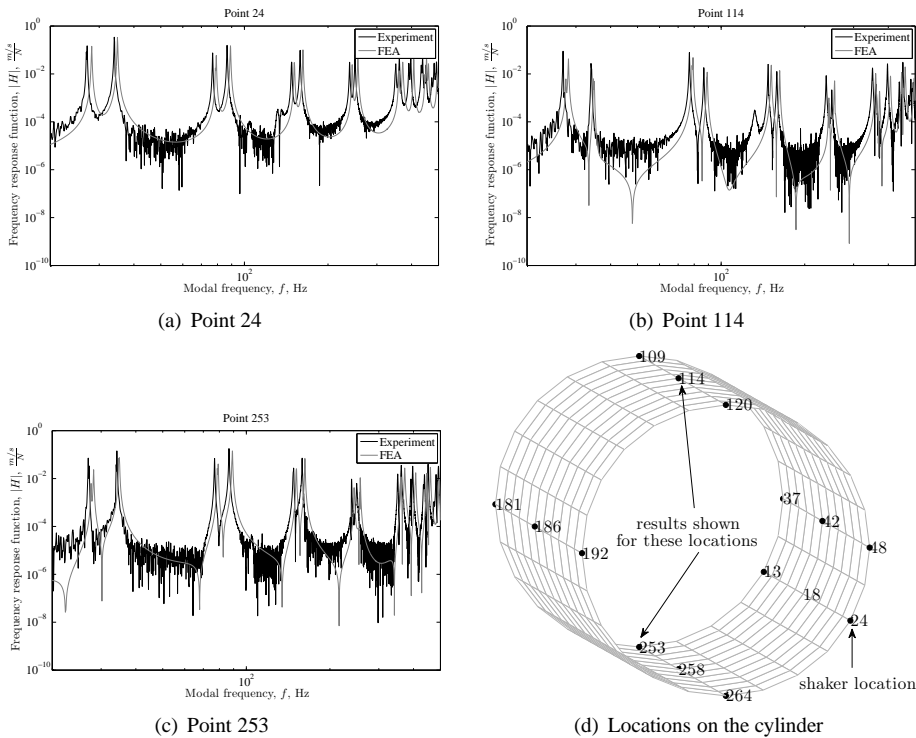


Figure 7.7: Frequency response function of the steered cylinder

A good correlation was found for all three points, see figures 7.7(a), 7.7(b), and 7.7(c), when the location and the magnitude of the response peaks of the measured data were com-

pared with those of the finite element prediction. The locations of the peaks depend on the mass and stiffness distribution within the cylinder, and thus the good correlation indicated that the finite element model correctly captured these distributions. Since the damping factors were unknown in advance, the measured damping factors were used as input in the finite element model, the magnitude depending on the mode shape. This explained why the amplitudes of the response peaks also showed a good correlation with the experimental results. The frequency response functions predicted by the finite element analysis (FEA) did not show any noise, whereas the measured responses did. The valleys seen in the plot of the finite element response functions of points 114, figure 7.8(b), and 253, figure 7.8(c), were due to a change in sign of the response, which was not shown because the absolute value of the response was plotted. These valleys were absent in the measured response due to the noise present in the data.

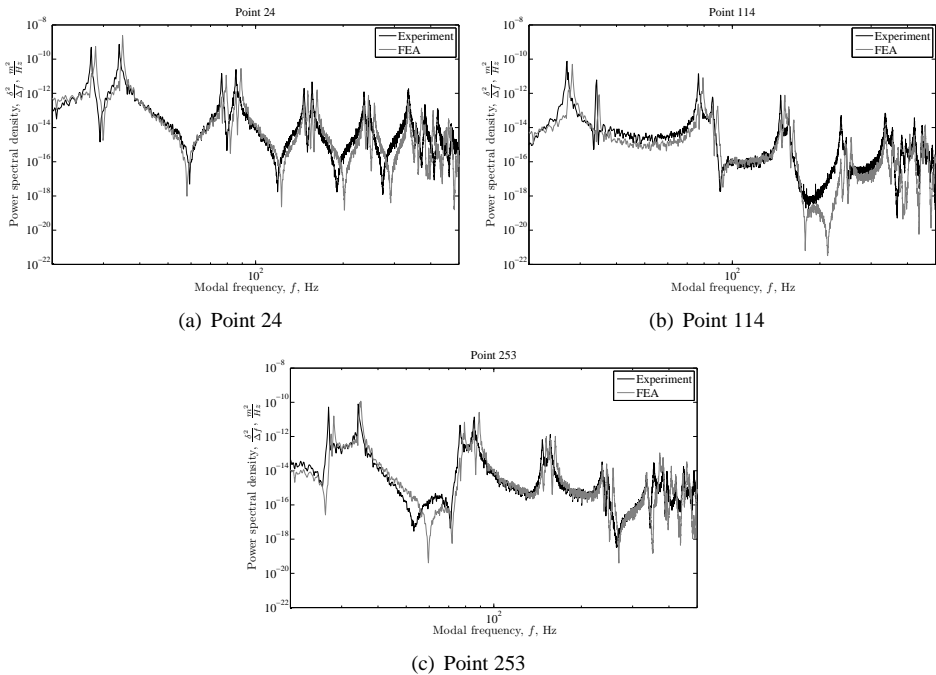


Figure 7.8: Power spectral density for displacement of the variable-stiffness cylinder

The second type of modal response, the power spectral density (PSD) describes how the variance of a signal is distributed with frequency. The PSDs of the three points are given for displacement in figure 7.8. The PSD for displacement is defined by:

$$PSD = \frac{\delta^2}{\Delta f} \quad (7.2)$$

in which  $\delta$  is the radial displacement at a given point and  $\Delta f$  is the frequency step between subsequent data points. Alternatively, the PSD can be expressed in terms of velocity or acceleration, see appendix F for these plots. As with the frequency response function, the

PSD depends on the mass and stiffness distribution. The PSD results of the finite element analysis again showed a good correspondence with the experimental results, both in location and in amplitude of the response peaks, indicating that the mass, damping and stiffness properties of the cylinder were properly captured in the finite element model. Note: the valleys present in the response were caused by dips in the forcing function, shown in figure 7.9, because the response was not normalized with the excitation force.

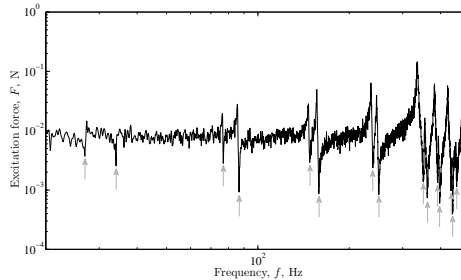


Figure 7.9: Forcing function over the frequency spectrum

## 7.5 Conclusions

A modal test was carried out on two fiber-reinforced composite cylinders. One of the cylinders contained plies with continuously varying fiber orientations, the other had a conventional layup with 0, 90 and  $\pm 45$  degree plies. A finite element model was used to predict the modal behavior of the cylinders.

The analytically predicted mode shapes and modal frequencies showed a good agreement with the experimental results, both for the baseline and for the variable-stiffness cylinder. The modal frequencies of the baseline cylinder were higher than those of the variable-stiffness cylinder due to the higher laminate bending stiffness in the circumferential direction, which plays an important role in the formation of waves in the circumferential direction. The larger axial stiffness of the variable-stiffness cylinder became apparent for modes with an increasing number of axial half waves and the modal frequency of the variable-stiffness cylinder approached or even exceeded the modal frequency of the baseline cylinder. The modal response simulations executed in ABAQUS matched the experimental results both for location and amplitude of the response. Although only 2 cylinders were tested, the presented results indicated that the finite element model for the variable-stiffness cylinder provides a good representation of the cylinder in terms of mass and stiffness distributions.

The fact that the analytical results have captured the modal constituent frequencies and physical responses for a wide frequency range are fundamental to expect reasonable static and dynamics analysis results associated with the cylinders.



# Chapter 8

## Bending Test

A first assessment of the accuracy of the finite element model for variable-stiffness cylinders was made based on a modal test, as described in chapter 7. The test showed a good agreement between the analytical and the experimental results. The experimental results of a bending test of the cylinders manufactured by Boeing, see section 6.1, will be presented in this chapter to make a second assessment of the analytical tools for variable-stiffness cylinders. Two baseline cylinders and one variable-stiffness cylinder were tested. The variable-stiffness cylinder was tested in two configurations, first loaded in the orientation for which it was designed and then loaded in the opposite direction, which was obtained by mounting the cylinder upside down in the test rig. These two orientations are referred to as the preferred and the reversed orientation, respectively.

First, the test fixture design, data acquisition and test procedure will be discussed. Subsequently, the finite element model used to predict the experimental results will be discussed. The finite element model was adjusted based on the experimental results for the baseline cylinder to account for the test conditions. This model was then used to predict the experimental results of the variable-stiffness cylinder. The experimental results are compared to the analytical results and a comparison is made between the variable-stiffness cylinder and the baseline cylinder, both are presented in section 8.5. The chapter concludes with a summary of the test results and an outlook for future work.

### 8.1 Test Setup

#### 8.1.1 Design of the Test Fixture

The objective of the test setup design was to apply pure bending to the baseline and variable-stiffness cylinders, introduced in chapter 5, and to compare the experimental results with the analytical data. In the past two different setups were used to apply a pure bending moment to a cylindrical shell. In the setup of Davis (1982); Peterson (1956); Peterson and Anderson (1966) and Anderson (1971) the cylinders are cantilevered from a strong back and bending is applied by rotating a plate on the other end of the cylinder using an hydraulic lever, while axial movement is allowed by rolled supports at the actuation end. The second setup, that of Fuchs et al. (1997), is a 4-point bending setup, where the test article is mounted in the

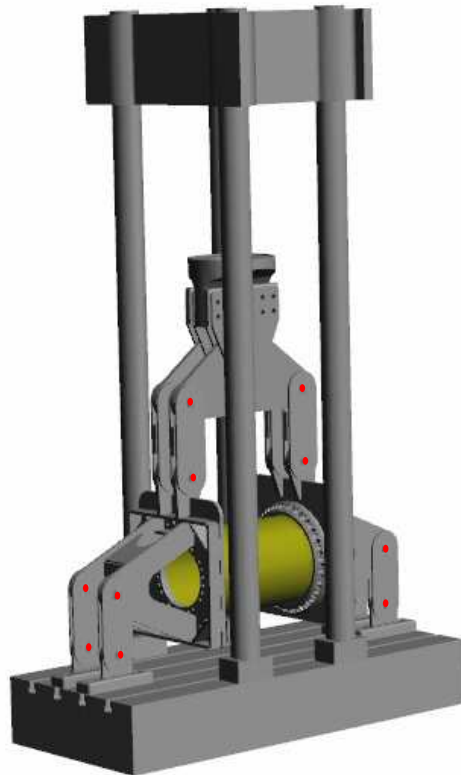
area without shear loads such that it is loaded in pure bending. Two hydraulic actuators are used to apply the shear force on the far ends of the setup, while the cylinder is kept in place by the two middle supports. The middle supports are connected in order to carry undesired axial forces.

Although Peterson's setup (1956; 1966) is better in terms of minimizing undesired loads, a configuration close to Fuchs et al.'s setup was favored for this research, because of the availability of a 3.5 MN MTS machine and consequently the lower costs associated with using this design. The design described in this chapter follows the same principles as Fuchs et al. (1997), though the way the specimens were clamped and the actuation of the test setup were different. The loads in the current setup were significantly higher than in the setup of Fuchs et al. (1997) and therefore bolts were used to clamp the specimen instead of potting compound. The MTS machine was used to actuate the setup in the middle, as opposed to the two hydraulic actuators at the far ends of the test setup that were used by Fuchs et al. (1997). A more detailed description of the test setup is given below.

A 3,560 kN MTS test bench, model 311.51S, was used for actuation. The fixture for the bending test was designed exclusively for this test. A picture and a model of the test fixture



(a) Picture



(b) Model

*Figure 8.1: MTS Test bench with the bending fixture*

are shown in figure 8.1. The bending loads were applied symmetrically to the cylinder by allowing the moment arms to rotate, with the rotation of the moment arms controlled by the vertical motion of the machine head. The test fixture was loaded in tension, causing a bending moment such that the upper side of the cylinder was in tension and the lower side of the cylinder was in compression. The kinematics of the fixture might introduce undesirable forces and moments, although the fixture is expected to introduce pure bending. The magnitude of the undesired forces was minimized by the presence of hinges between the different components of the test fixture, indicated in red in figure 8.1(b). A small axial force developed once the end-plates started rotating. Considering the stiffness of the barrel, the rotation of the end-plates was such that the strains caused by the compressive load were less than 0.25 percent of the maximum bending strain and therefore negligible, as shown by a simple model of the test mechanism, see appendix G.

The boundary conditions of the cylinder were designed to approach, as closely as possible, the clamped end conditions as applied in the finite element analysis. A fully bonded connection between the cylinder and the steel end-rings was rejected because the expected tensile loads were too high and a bolted connection with steel end reinforcements of the cylinder was preferred. The cylinder ends were attached to steel outer rings and segmented steel inner rings using 28 steel bolts with a 16 mm diameter. The rings are shown in figure 8.2. The inner ring was segmented to allow the cylinder to be clamped between the inner and outer ring. The amount of clamping was increased by filling the gaps between the rings and the cylinder with paste adhesive. The rings were bolted to rigid end-plates which were integrated with the moment arms.

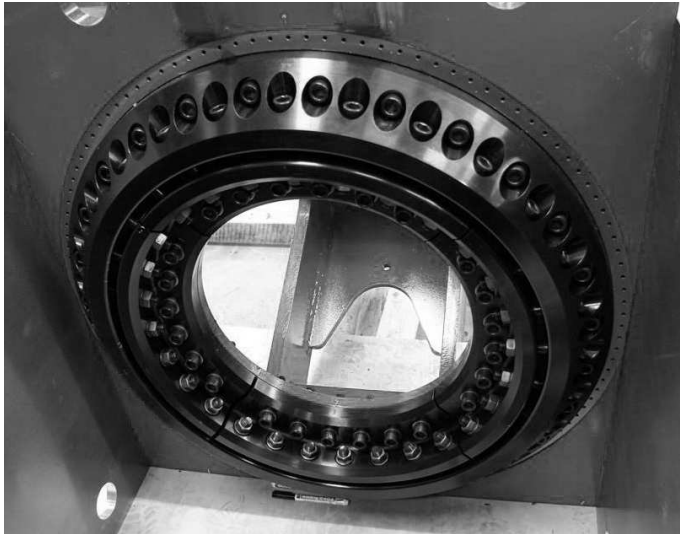


Figure 8.2: Picture of the steel end-rings

### 8.1.2 Test specimens, Preparation and Installation of the Test Article

The test specimens that were tested were 609 mm (24 inches) diameter, 990 mm (39 inches) long cylinders made of uni-directional BMS8-276 carbon-epoxy tape. The laminates consisted of 24 plies. Two baseline cylinders and one variable-stiffness cylinder were tested, the design of which was described in subsection 5.3.4. A description of these specimens and how they will be referred to in the remainder of this chapter is given in table 8.1.

Table 8.1: Bending test specimens

Specimen name	Layup	Test configuration	Subscript used in results
baseline 1	$[\pm 45, 0_2, 90_2, 0, \pm 45, \pm 45, 90]_s$	N.A.	1
baseline 2	$[\pm 45, 0_2, 90_2, 0, \pm 45, \pm 45, 90]_s$	N.A.	2, b
variable-stiffness	$[\pm 45, \pm \varphi_1(\theta), 0, 90, \pm \varphi_3(\theta), 0, 90, \pm \varphi_5(\theta)]_s$	preferred	p
variable-stiffness	$[\pm 45, \pm \varphi_1(\theta), 0, 90, \pm \varphi_3(\theta), 0, 90, \pm \varphi_5(\theta)]_s$	reversed	r

The specimens were manufactured by Boeing using advanced fiber placement technology, see section 6.1. After the prepreg material was laid up on a mandrel, it was cured in an autoclave, removed from the mandrel and trimmed close to the final length of 990 mm. Steel tabs were bonded onto the inner and outer surface on both ends of the cylinder with Hysol 9394EA paste adhesive to increase the bearing capability of the cylinder at the connection with the loading frame. The dimensions of the steel end tabs are specified in figure 8.3. Sizing of the tabs was based on the expected load carrying capability of the laminate in bearing, the maximum amount of load transfer through the adhesive layer between the tabs and the cylinder, and the relative stiffnesses of the composite cylinder and the steel tabs. The tensile loads applied to the variable-stiffness cylinder were the most critical, because the loads carried on the tension side of this cylinder were expected to be higher than those carried by the baseline cylinder, as explained in chapter 5. The higher stiffness of the laminate in this location also caused a higher ratio of the bearing loads to be carried by the laminate than by the steel tabs.

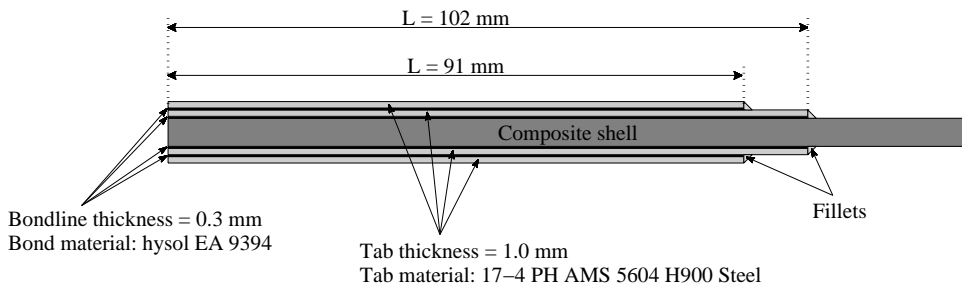


Figure 8.3: Dimensions of the end tabs

The tabs and cylinder surface were sanded such that the cylinder ends were perpendicular to the axis of revolution. The test fixture was set upright with the inner and outer rings installed and the cylinder was centered between the inner and outer rings. Once the cylinder

was fixed in place, 6 and 10 mm diameter holes were drilled successively and concentrically with the end-rings. The cylinder was removed and the holes were drilled to their final diameter of 16 mm on an industrial drilling machine. A picture of the cylinder with end tabs and bolt holes is shown in figure 8.4. The cylinder surface was then cleaned and strain gauges



*Figure 8.4: Cylinder layout before application of the speckle pattern*

were bonded at specified locations on the inner and outer surfaces, as shown in figure 8.4. Subsequently, the outer surface was spray painted white and covered with a black speckle pattern for the digital image correlation (DIC) used during the test. The distribution of the strain gauges and the use of digital image correlation will be discussed in section 8.2.

Adhesive paste was applied between the rings and the cylinder to improve the clamping between the end-rings and the cylinder. The adhesive between the end-rings and the tabs was not intended to transfer shear loads since the connection between the tabs and the cylinder was sized on load transfer through the bolts alone and therefore wax was applied to the rings and the tabs to prevent the adhesive from sticking to the surface. Finally the bolts were inserted in the ring, the cylinder and the inner ring and tightened. The end-plates were held in position using two aluminum plates during the final assembly process such that the end-plates were kept parallel and 990 mm apart. A picture of the aluminum plates attached to the structure is shown in figure 8.5.

## **8.2 Data Acquisition and Instrumentation**

The maximum load that could be applied to the cylinders was limited by the strength of the bolted connection which was most critical on the tension side of the variable-stiffness cylinder. Unfortunately, the cylinders were built before the detailed design of the test fixture was done, resulting in cylinders that were expected to be too stiff to be buckled in the test section before bearing failure occurred on the tension side of the cylinder. It was thus decided to save the cylinders and not to load the cylinders beyond the load that would cause bearing failure. This would allow for a second test run that might include damage or cutouts in the test section to weaken the structure.

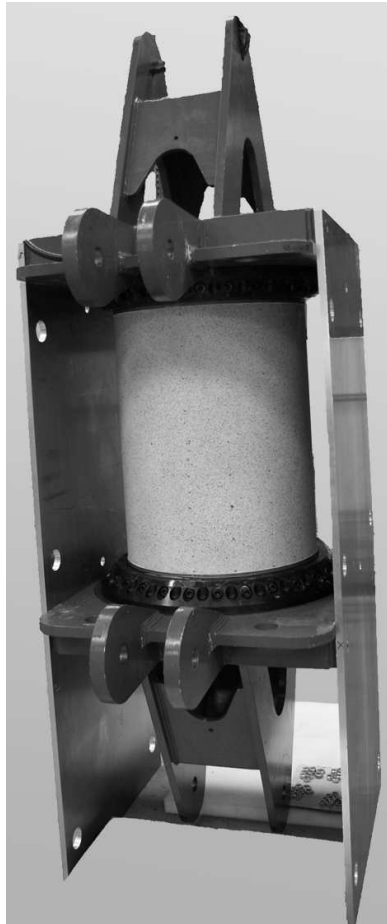


*Figure 8.5: Connection between the two support structures*

The most important sources of information for the comparison of experimental data with analytical data in the pre-buckling load regime are measurements of strains and deformations. If a cylinder is loaded until buckling, measured geometric imperfections of the cylindrical shell can be applied to the finite element model to predict the buckling load more accurately, as imperfections can have a large influence on the buckling behavior of a cylindrical shell.

A buckling analysis including geometric imperfections was not initially carried out, because it was decided not to load the cylinders to buckling, however, geometric imperfections were measured so that they could be used in future analyses, and so that they could be included in the imperfection data bank for thin walled shells (de Vries, 2009). It will become apparent later in this chapter that the geometric imperfection data was not collected in vain and that imperfections play an important role in the mechanical behavior of thin-walled cylindrical shells in compression.

### 8.2.1 Geometric Imperfection Data

Geometric imperfections of the cylinder were measured twice: i) before the cylinder was mounted in the test setup, but after the tabs were applied and the holes were drilled, and ii) while the cylinder was mounted in the test setup. The data was obtained using a VIC3D stereo digital image correlation (DIC) system with two digital cameras. Cameras with 50 mm lenses were used to measure the cylinders outside the test setup and cameras with 8 mm lenses were used to measure the imperfections while the cylinders were assembled in the test setup. To facilitate obtaining this data the specimen were first painted white and then a black speckle pattern was applied, using acrylic paint. The use of a stereo camera system allows for three dimensional correlation, providing information on the initial geometry and on the deformation of the object. Multiple pictures were taken around the circumference of the cylinder to cover the full surface. The separate images were then combined into one data file covering the whole cylinder during post-processing. Pictures of the camera setup and image recording software are shown in figure 8.6. The procedure to calculate the geometric imperfections and the results are presented in subsection 8.5.2.

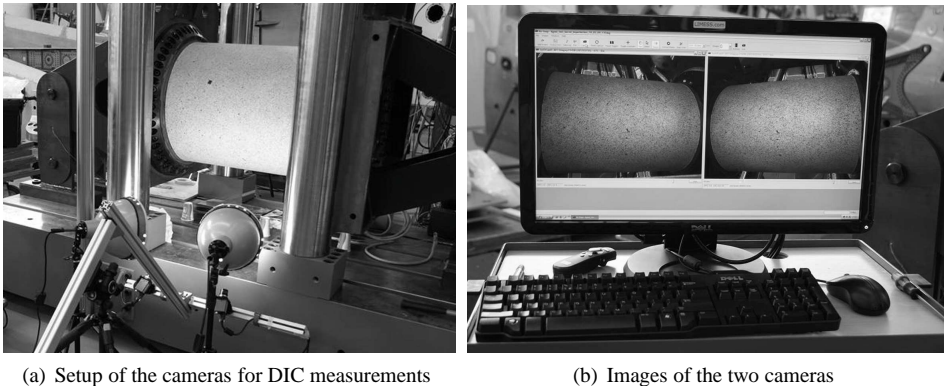


Figure 8.6: Digital image correlation (DIC)

### 8.2.2 Determining the Applied Bending Moment

The bending moment applied to the cylinder could not be measured directly and therefore it was derived from the actuation force and the known weight and configuration of the test fixture. First the assembly without the lower struts, as shown in figure 8.7, was installed in the MTS machine. The machine force indicator (indicating a force  $P$ ) was then set to zero, thus excluding the weight of the supporting structure as shown in figure 8.7. Subsequently the lower struts and lugs were assembled and fixed to the test bed. The bending moment applied to the structure was then calculated by multiplying the reaction force at each end  $P/2$  with the moment arm  $d = 711$  mm and adding the moment caused by the weight of the support structure and rings  $M_s$  which was calculated using the commercially available design software CATIA of Dassault Systems (shaded light gray in figure 8.7):

$$M = \frac{Pd}{2} + M_s \quad (8.1)$$

The weight of the lower struts and lugs was not included in  $M_s$ , since the center of gravity was in line with the reaction force.

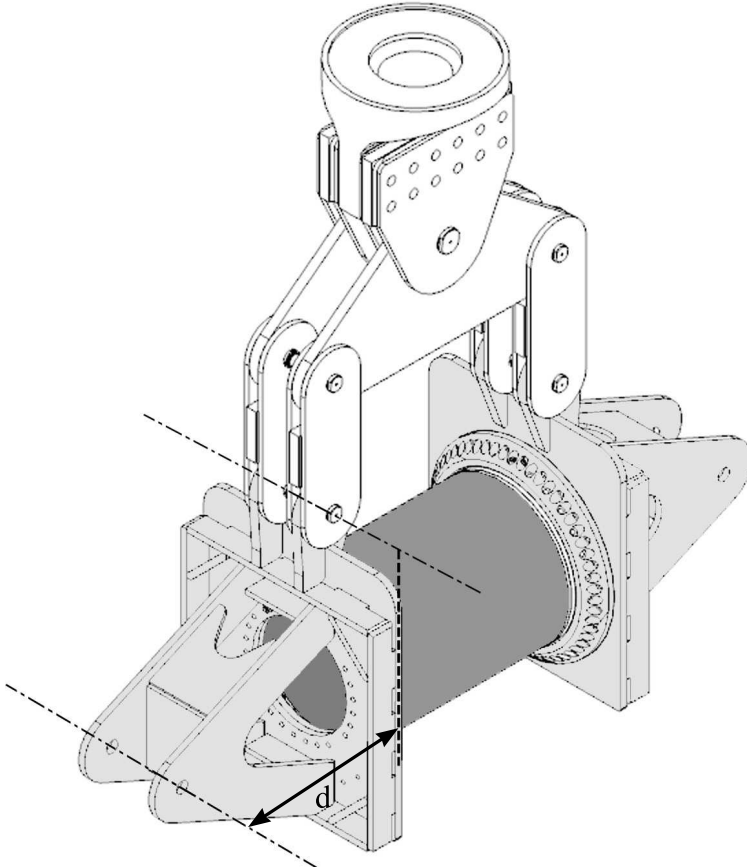


Figure 8.7: Schematic for the determination of the bending moment

### 8.2.3 Displacements

The global displacement of the machine head was measured using the internal mechanism of the MTS test bench. The displacement of the cylinder and rotations of the test equipment were measured using linear variable differential transformers (LVDT's) and lasers. The location of the LVDTs and lasers are shown in a schematic side view of the cylinder and part of the supporting structure in figure 8.8. The rotations of the plates about the horizontal and vertical axes were calculated by measuring the displacements of the end-plates at three distinct locations in a right angle triangular setup. Here the horizontal rotation will be referred to as the end rotation of the cylinder. This information was also used to check the symmetry in the loading conditions. The placement of 2 of the LVDT's on the end-plate is shown in figure 8.9(a). The third LVDT is at the same vertical level as the lower LVDT and placed on the far end of the plate.



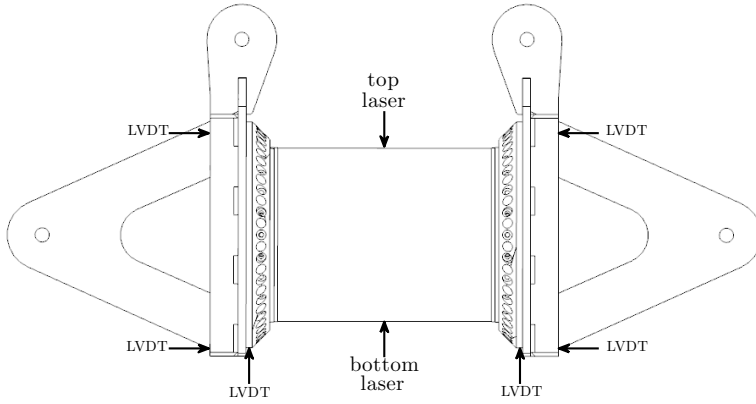


Figure 8.8: Location of LVDTs and lasers



(a) Placement of the LVDT's used to calculate the

(b) Placement of the LVDT to measure the vertical displacement

Figure 8.9: Displacement measurements using LVDT's

The vertical deflections at the top and the bottom of the cylinder were measured halfway the length at  $x/L = 0.5$  using lasers. The vertical displacement of the end-rings was measured as a reference, see figure 8.9(b). The displacement field could also be calculated using the 3D digital image correlation system.

### 8.2.4 Strain measurements

Strains were measured using general purpose strain axial strain gauges and rosettes at the locations shown in figure 8.10. The uniaxial strain gauges used were type KFG-5-350-C1-11 gauges, the rosettes were type KFG-5-350-D17-11, both manufactured by Kyowa. Since this test was a static test of short duration there was no need to use strain gauges with a matching coefficient of thermal expansion. The circumferential location  $\theta = 0^\circ$  corresponded to the tension side of the cylinder in the test setup described, while  $\theta = 180^\circ$  was the compression side. These locations were considered the most interesting to collect data, because they exhibit the largest strains under bending. Thirteen strain gauges were placed along the axial direction at these two locations such that the influence of the boundary conditions on the mechanical behavior of the cylinder could be evaluated. Furthermore a pattern of 20 strain gauges was placed around the circumference halfway along the length of the cylinder, because this is where the boundaries had the least influence. Thirteen back-to-back strain gauges were also placed between  $\theta = 0^\circ$  and  $\theta = 180^\circ$ . One quarter of the cylinder was covered with a grid of 57 strain gauges to capture the variation in the strain field. The remaining strain gauges were spread out over the cylinder so that the symmetry of the mechanical behavior could be checked. Only 19 strain gauges were used in the region between  $\theta = 180^\circ$  and  $\theta = 360^\circ$ , because this side of the cylinder was monitored using the 3D digital image correlation system, which provided a full view of the strain field.

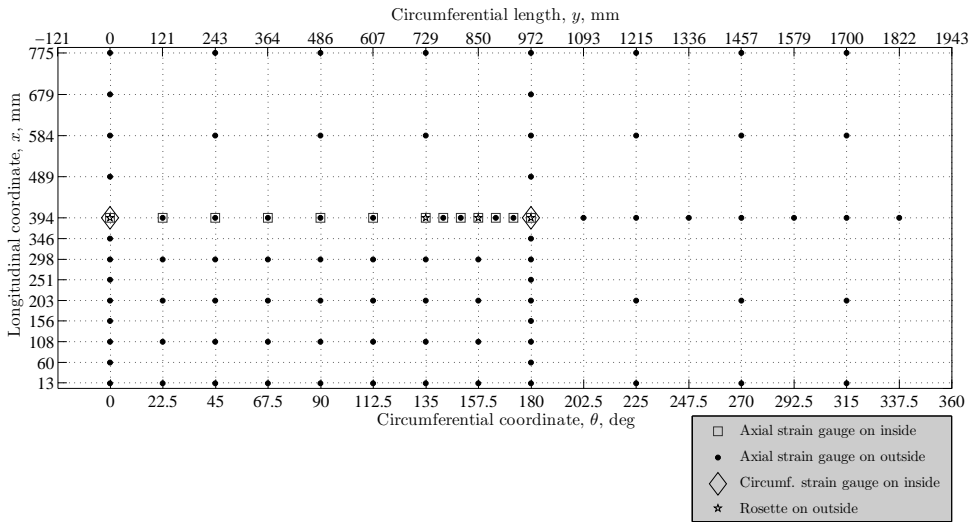


Figure 8.10: Location of strain gauges

### 8.3 Test Procedure

The geometric imperfections of the cylinders were measured using the digital image correlation system before they were assembled in the test fixture. After assembly in the test fixture a negative load was applied to compensate for the weight of the test fixture, such

that the total moment applied to the cylinder, given by equation 8.1, was zero. Then the geometric imperfections were measured again using the DIC system. Subsequently wires were connected to the strain gauges and the instrumentation was set up. The cylinder was then loaded in steps of 10 kN, corresponding to steps of 3.5 kNm bending moment, up to 40 percent of the maximum design load of 415 kNm. Loading the structure to a significant load level served to settle the cylinder and the test fixture. After gradually unloading the structure, the load was again applied in steps of 10 kN, now up to a maximum moment of 415 kNm. The load was then reduced to zero in steps of 10 kN in some tests and 20 kN in others. Strain and displacement data were collected at each load increment, and pictures were made using the DIC system. Multiple test runs were performed where the DIC was first used to monitor the compression side of the cylinder, while the tension side of the cylinder was monitored in a subsequent run. The test of the variable-stiffness cylinder in the reversed orientation was controlled by a prescribed displacement of the machine head of 0.05 mm per step, corresponding to load steps of approximately 5 kNm bending moment.

The maximum load that could be applied to the cylinders was limited by the strength of the bolted connection which was most critical on the tension side of the variable-stiffness cylinder. Unfortunately, the cylinders were built before the detailed design of the test fixture was made, this gave cylinders that were expected to be too stiff to be buckled in the test section before bearing failure would occur on the tension side of the cylinder. It was thus decided to save the cylinders and not to load the cylinders beyond the load that was expected to cause bearing failure. This would allow for a second test run that might include damage or cutouts in the test section to weaken the structure. The maximum design load based on the maximum bearing strength capacity was 415 kNm, approximately 65 percent of the calculated nonlinear buckling load of the baseline cylinder, or 55 percent of the buckling load of the variable-stiffness cylinder, the effect of geometric imperfections not included. The test fixture was sized according to the maximum load of 415 kNm.

## 8.4 Finite Element Predictions

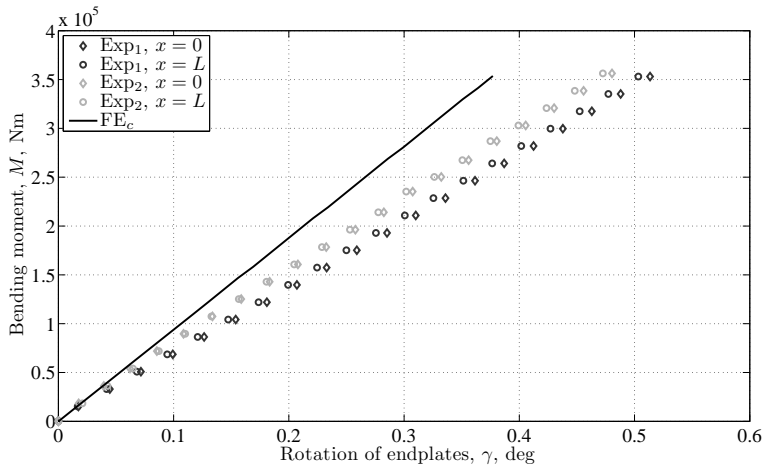
The finite element model described in chapter 5 was used to predict the mechanical response of the cylinders before the actual testing was performed. After the test of the first baseline cylinder it became clear that the finite element model did not properly reflect the boundary conditions that were present in the actual test setup. Therefore the boundary conditions were adjusted in the finite element model such that a good correlation was found with the experimental data of the baseline cylinder. Subsequently this model was used to predict the mechanical behavior of the variable-stiffness cylinder. Finally, geometric imperfections were included in the model to assess the influence of geometric imperfections on the buckling load of the cylinders.

### 8.4.1 Simple Linear and Nonlinear Finite Element Models

Initially, selection of the best laminate for loading under bending was based on a linear analysis of a cylinder with perfectly clamped ends, see chapter 5. It is often accepted in practice to use linear analyses during the design stages of a structure to make a quick assessment of the structural performance, even though actual test conditions are not accurately repre-

sented by the model. The main objective of such a study is to compare the performance of different structural concepts under similar conditions. However, when analytical and experimental results are to be compared, a more realistic representation of the cylinder behavior is required. Thus geometric nonlinearity was introduced into the model. The clamped boundary conditions were maintained in the finite element model, since the interface between the cylinder and the support structure in the test setup were designed to be stiff. Further, the simplified model of the test mechanism, described in appendix G, indicated that the test mechanism induced small undesirable loads and therefore the test mechanism was not modeled in ABAQUS.

The first tests of the baseline cylinder showed a considerable difference between the analytical and experimental results, as can be seen from figure 8.11, where the mechanical



(a) Global response

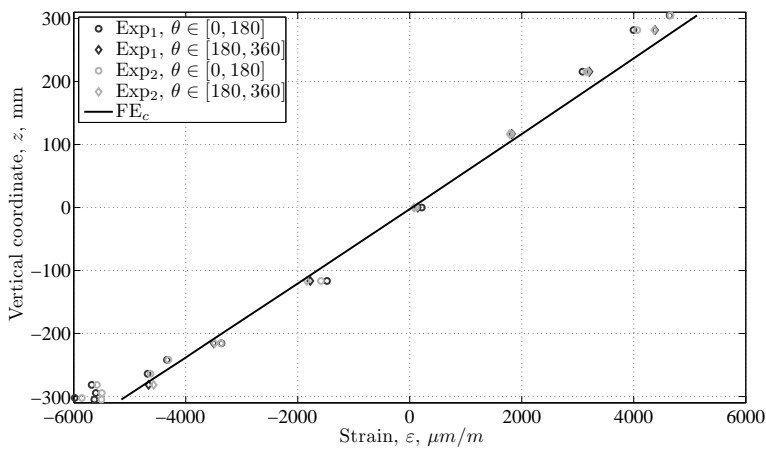
(b) Strain distribution at  $M=356$  kNm

Figure 8.11: Comparison baseline test and FE model with clamped boundary conditions

response of the baseline cylinder for the experiment (Exp<sub>1</sub>) and the nonlinear finite element (FE<sub>c</sub>) results are displayed. The global response is given in the form of a moment-rotation curve in figure 8.11(a). The two dark gray data series for the experimental results represent the rotations at both ends of the cylinder, dedicated  $x = 0$  and  $x = L$ , as shown in figure 8.12. The deviation of the experimental results from the analytical results was approximately 35

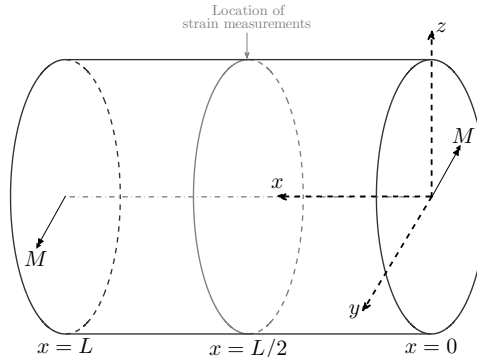


Figure 8.12: Definition of directions

percent, where the experimental response was more compliant than the analytical response. The difference in end rotations was expected to be caused by a difference in boundary conditions between the finite element model and the test, because a modal test of the cylinders (see chapter 7) showed a good agreement between the experimental and analytical data, suggesting that the stiffness modeling was accurate.

The measured distribution of the axial strain with the vertical coordinate  $z$  halfway along the length of the cylinder, i.e. at  $x = L/2$ , supported this hypothesis. The distribution of the axial strain with the vertical coordinate  $z$  should have been linear if the boundary conditions were clamped:

$$\varepsilon = \frac{Mz}{EI} \quad (8.2)$$

where  $M_y$  is the applied bending moment and  $EI$  is the bending stiffness of the cylinder. The vertical coordinate  $z$  is shown in figure 8.12. The strain distribution according to the finite element prediction in figure 8.11(b) was indeed a straight line. The experimental strain distribution, however, showed smaller strain values on the tension side and larger strain values on the compression side, indicating that the cylinder cross-section did not remain in one plane.

This observation was supported by data from the digital image correlation measurements, described in appendix H. The rotations of the end-plates that were measured by the LVDTs were larger than the rotations of the cylinder ends that were measured by the DIC system, an indication of flexibility in the interface between the cylinder and the support structure. Furthermore, the rotations on the compression side as measured by the DIC system were larger than the rotations on the tension side, which was in line with the strain distribution of figure 8.11(b).

An inspection of the load transfer mechanisms on the tension and compression side of the cylinder provided an explanation: on the tension side loads were transferred through

the bolts and through shear at the cylinder-ring interfaces, whereas on the compression side loads were also transferred through direct contact between the end-plate and the cylinder. The latter load transfer mechanism was more efficient and therefore the compression side of the cylinder was loaded higher than the tension side, causing larger strains on the compression side than on the tension side.

Based on the observations described above it was decided to increase the torque of the shear bolts connecting the cylinder to the end-rings and that of the tension bolts connecting the end-rings to the backplate to improve the load transfer from the support structure to the cylinder. The torque of the shear bolts was increased from 70 Nm to 100 Nm ( $\approx 37$  kN pretension), and simultaneously the torque of the tension bolts was increased from 90 Nm to 120 Nm ( $\approx 44$  kN pretension). The cylinder was retested twice under these conditions and the response was compared with the initial test condition. A considerable increase in global stiffness was observed after adjustment of the bolt torque. In response to this, the torque of the tension bolts was again increased, to 200 Nm ( $\approx 74$  kN pretension), and the cylinder was retested, without any obvious changes showing in the response. Finally, the torque of the shear bolts was increased to 125 Nm ( $\approx 46$  kN pretension). The last adjustment only caused marginal changes and therefore this condition was accepted as the best possible clamping condition. The experimental results for these conditions are shown as Exp<sub>2</sub> in figure 8.11, alongside the original experimental results, designated Exp<sub>1</sub>. The difference between the analytical and experimental global stiffness response of the cylinders decreased from 35 to 25 percent by increasing the pretension of the bolts. The experimental strain distribution also approached the analytical results better after the experimental boundary conditions were adjusted, especially on the compression side of the cylinder. Two mechanisms could have played a role in this improvement. i) increased load transfer by shear between the cylinder and the end-rings. Increasing the pretension of the bolts caused the normal pressure on the cylinder and ring surfaces to increase, resulting in higher friction forces. The improvement in load transfer through friction was most important for the tension side of the cylinder, although indirectly the strain distribution on the compression side was also influenced. Since more load can be transferred on the tension side, the loads on the compression side will be reduced, and the strains on the compression side will be lower. ii) decreased rotation of the cylinder around the circumferential direction, due to the increased clamping. This had more influence on the compression side than on the tension side, as out-of-plane rotations were more likely in compression than in tension.

#### **8.4.2 Finite Element Model with Flexible Boundary Conditions and Test Mechanism**

In the previous subsection the boundary conditions were shown to play an important role in the mechanical response of the cylinder. Increasing the pretension of the bolts increased the stiffness of the interface between the cylinder and the test fixture and improved the response of the cylinder, however, large differences between the predicted and measured responses still existed.

The large differences between the analytical response and the experimental response required an adjustment of the boundary conditions in the finite element model and thus linear springs were inserted between the cylinder ends and the rigid end-plates. These springs were rigid in the plane of the cross-section and flexible in the direction of the cylinder

axis, i.e. no in-plane deformation of the cross-section was allowed. In addition to the axial springs, rotational springs with flexibility around the circumference were included, while rotations in the radial and axial directions were restricted. In the finite element model these springs were attached to every boundary node around the circumference, 192 per edge. The springs are shown in figure 8.13. The stiffness of the rotational springs was equal for all

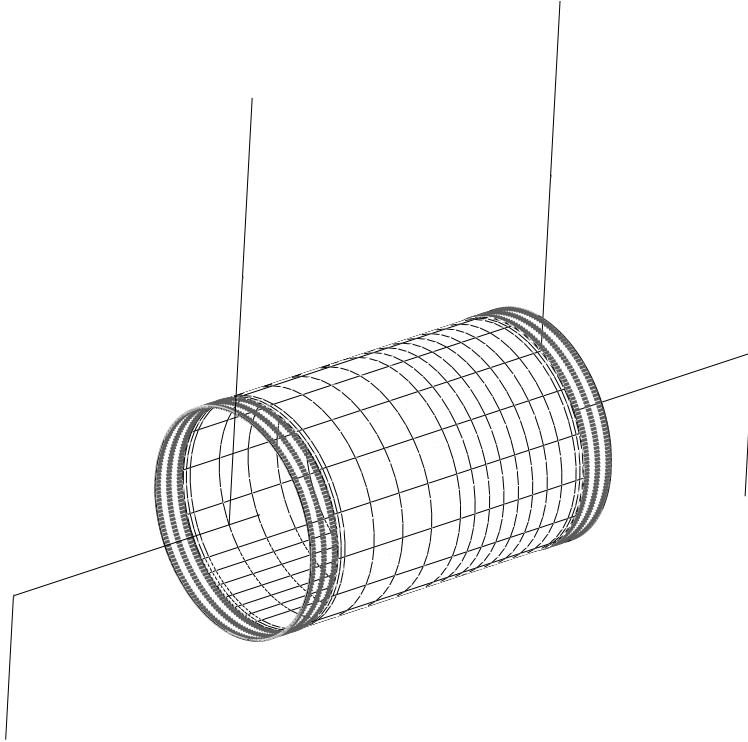


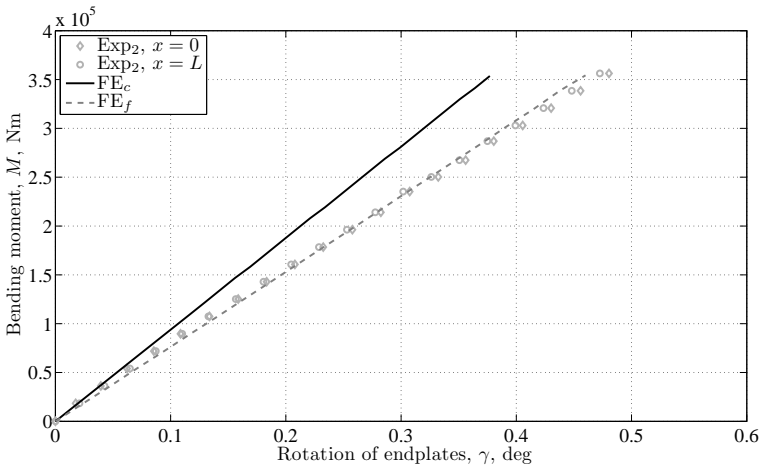
*Figure 8.13: Finite element model including springs and test mechanism*

springs and independent of any degree of freedom, whereas the stiffness of the longitudinal springs depended on the sign of the spring deformation: in tension the spring stiffness was  $k^+ = 1.72 \cdot 10^7 \text{Nm}^{-1}$  and in compression the spring stiffness was  $k^- = 1.19 \cdot 10^8 \text{Nm}^{-1}$ . These values were obtained with a least-squares fit of the test data using a simple spring model in Microsoft Excel. A description of the Excel model is given in appendix I. The compressive stiffness corresponded to the laminate stiffness of the cylinder and tab sections that were clamped between the end-rings, confirming that the load was transferred through direct contact with the backplate. The load transfer on the tension side was less efficient than on the compression side, resulting in a significantly lower stiffness of the interface. A possible improvement of the interface model could be obtained by designing and testing a small, representative assembly of the actual interface, i.e. a piece of composite laminate attached to a backplate through two L-profiles using bolts and adhesive. Note: working to this level of detail was judged unnecessary for the current research.

The change in boundary conditions caused larger rotations and a shift in neutral axis,

possibly causing changes in the behavior of the test mechanism in the finite element model. A simplified representation of the test mechanism was therefore added to the finite element model. The parts representing the test structure are rigid bodies, connected by hinges, with a rigid connection to the end-plate. A complete model of the test fixture in ABAQUS was used to confirm that the test fixture parts could be assumed to be rigid. A picture of this model is shown in figure 8.13.

The experimental results (Exp<sub>2</sub>) and the results of a geometrically nonlinear finite element analysis including the boundary conditions and test mechanism as described above (FE<sub>f</sub>) are plotted in figure 8.14, together with the prediction of the original nonlinear finite element model (FE<sub>c</sub>). The first series of test results are left out for clarity. Note: from figure



(a) Global response

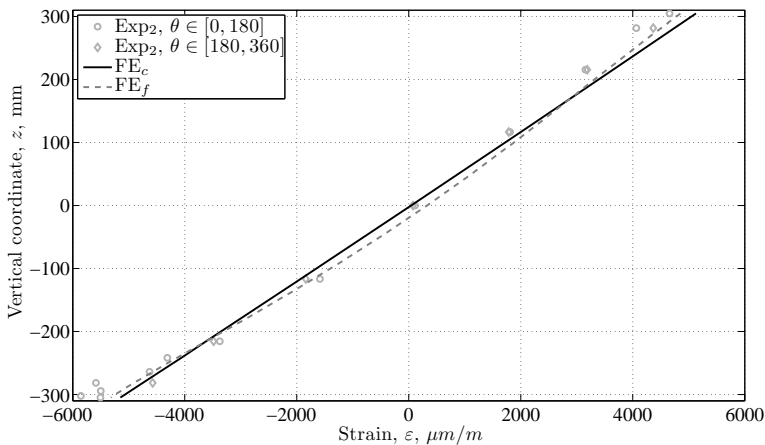
(b) Strain distribution at  $M=356$  kNm

Figure 8.14: Comparison baseline test and FE models with different boundary conditions



8.14(a) it can now be seen that the moment-rotation curves of the experiment and the analysis show a good agreement. The strain distribution, shown in figure 8.14(b), also agrees better with the test results, although the strains on the compression side are still somewhat higher in the experiment than in the analysis.

### 8.4.3 Riks Analysis: Finite Element Model Including Imperfections

One aspect that was not taken into account in the previous model, and that could have a large influence on the experimental buckling load of thin-walled cylindrical shells in compression was the presence of geometrical imperfections. The first ones to recognize the impact of geometric imperfections on the buckling load of thin-walled shells were Koiter (1963), Budiansky and Hutchinson (1964) and Arbocz and Babcock (1969). Following their work, many other researchers have contributed to this field of research, see the work of Singer et al. (1998) for an overview of the work on geometric imperfections. Geometric imperfections of cylindrical shells are expressed in terms of a deviation of the cylinder shape in radial direction when compared to the perfect cylinder, i.e.:

$$w = r - R \quad (8.3)$$

where  $w$  is the imperfection,  $r$  is the local radius and  $R$  is the perfect cylinder radius. The measured imperfections, which will be discussed in the results section, were included in the finite element model by specifying the value of  $w$  on each node. The ABAQUS *\*Imperfection* data card was used for this purpose. Subsequently a Riks analysis was performed to predict the mechanical behavior and the collapse load of the cylinder (ABAQUS, Inc., 2005; Crisfield, 1981; Powell and Simons, 1981; Riks, 1979).

The Riks analysis is a load-deflection analysis in which the load magnitude is treated as an additional unknown: it solves loads and displacements simultaneously, see figure 8.15. The arc length along the static equilibrium path in load-displacement space is used to measure the progress of the solution. In this the Riks analysis differs from most solution procedures in which commonly the progress of the solution is measured either by a

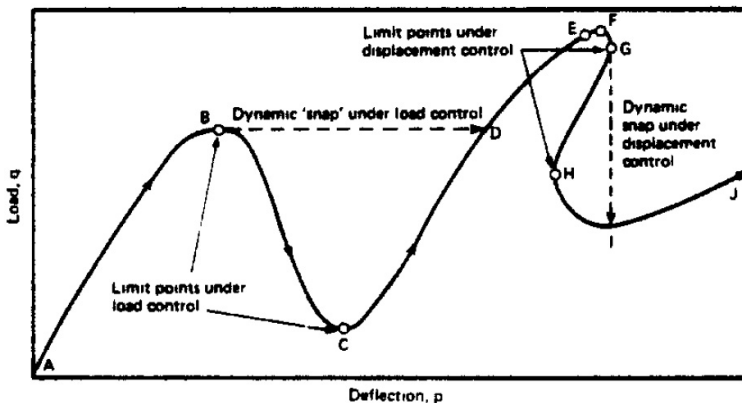


Figure 8.15: Example load path that can be traced with the Riks analysis, (Crisfield, 1981)

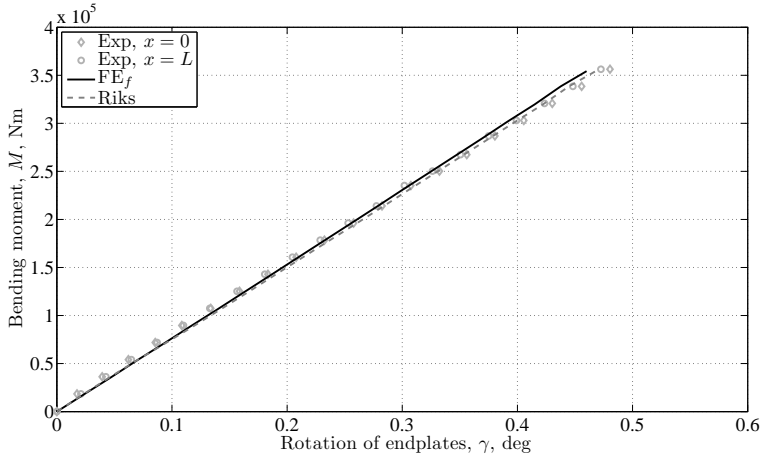
load increment or a displacement increment. The arc length procedure of the Riks analysis makes it possible to predict the unstable behavior and nonlinear collapse of a structure. An example load path is given in figure 8.15. Most analyses that are load controlled cannot go beyond limit point B, while displacement controlled analyses will fail at limit point G. In addition, even these limit points may not be reached due to a convergence failure of the iterative solution procedures, possibly as a consequence of a round-off error (Crisfield, 1981). Therefore it was more reliable to use the Riks analysis to go beyond the first limit point to determine the collapse load of the experimental cylinders than to use a nonlinear static analysis. In the future it might be interesting to compare the results of the Riks analysis with those generated with other nonlinear methods, for example the Newton Raphson method with artificial damping, or explicit methods.

The moment-rotation curves for the nonlinear static analysis without imperfections and the Riks analysis with imperfections are given in figure 8.16(a). Including imperfections had little influence on the shape of the load-deflection curve, but a large influence on the predicted collapse/buckling load. The collapse load predicted by the Riks analysis was 488 kNm, whereas the model without imperfections predicted a buckling load of 570 kNm. The inclusion of imperfections in the analysis also improved the agreement between the analytical strain distribution and the experimental strain distribution on the compression side, as shown in figure 8.16(b). The sudden change in strain at  $z \approx -300$  mm was caused by local changes in curvature of the laminate. Initially local curvatures of the laminate were present, because the laminate was neither perfectly straight in length direction, nor perfectly round in circumferential direction. The local curvature of the laminate will be reduced if a tensile load is applied, while the laminate curvature will increase under a compressive load. The strain gauges were applied to the outside of the laminate and therefore their values were influenced by these local curvature changes. A more extensive discussion on the influence of geometric imperfections on measured strain values will be given in subsection 8.5.3.

## 8.5 Test Results

The test results for 3 test configurations are presented and compared in this section. The first test configuration was the bending test of the baseline cylinder. Two of these cylinders were tested, baseline cylinder 1 and baseline cylinder 2 and, since the mechanical responses of the cylinders were comparable, they will be referred to collectively as the *baseline* cylinder results. The second test configuration was the bending test of the variable-stiffness cylinder in the orientation for which it was optimized. The cylinder had a high axial laminate stiffness at  $\theta = 0^\circ$  and a low laminate stiffness at  $\theta = 180^\circ$ , which are the respective tension and compression side of the cylinder in this configuration. In the third test configuration the variable-stiffness cylinder was rotated  $180^\circ$  about the longitudinal axis, such that the loading on the cylinder was reversed compared to configuration 2. Consequently, the low-stiffness part of the cylinder in configuration 3 was in tension and the high-stiffness part of the cylinder was in compression. In the remainder of this chapter the second configuration will be referred to as the variable-stiffness cylinder in the *preferred* orientation, while the third configuration will be referred to as the variable-stiffness cylinder in the *reversed* orientation, i.e. subjected to a *reversed* bending load.

The baseline results were based on the test with the best clamping conditions. The



(a) Global response

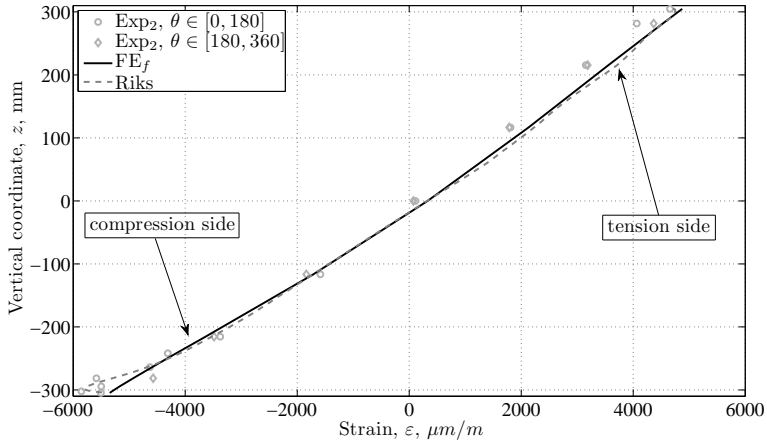
(b) Strain distribution at  $M=356$  kNm

Figure 8.16: Comparison baseline test and FE predictions with and without imperfections

maximum load applied with these conditions was 356 kNm. The maximum load that was applied to the variable-stiffness cylinder in the preferred orientation was 413 kNm. The variable-stiffness cylinder was only loaded up to 302 kNm in the reversed orientation to prevent premature failure of the cylinder.

The experimental results were compared to the results of the finite element predictions using the Riks analysis, including the flexible boundary conditions and the test mechanism. The spring stiffnesses of the springs on the compression side of the variable-stiffness cylinder were adjusted to match the stiffness of the laminate locally. The spring stiffnesses of the springs on the tension side of the cylinder were kept unchanged because these values were assumed to depend on the load transfer through bearing and friction and were therefore,

considered to be independent of the laminate stiffness.

### 8.5.1 Global Response

The global response of a cylinder loaded in bending is characterized by the moment-rotation curve. The moment-rotation curves for the baseline (subscript  $b$ ) and the variable-stiffness cylinder in the preferred orientation (subscript  $p$ ) and reversed orientation (subscript  $r$ ) are given in figure 8.17. The experimental results are denoted "Exp" and the finite element predictions are denoted "Riks".

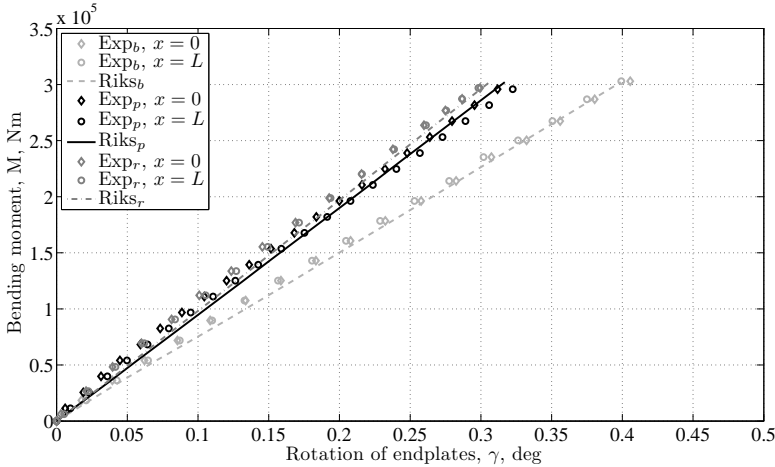


Figure 8.17: Moment-rotation curves

A good agreement between the experimental results and the analytical prediction was found for all configurations. The global stiffness of the variable-stiffness cylinder was larger than that of the baseline cylinder, because  $3/4$  of the variable-stiffness cylinder had a higher laminate stiffness than the baseline cylinder, as was shown in figure 8.18. At higher loads, the analytical response of the variable-stiffness cylinder in the preferred orientation started to deviate more from the experimental results than the results of the other two configurations. This may be due to the load transfer mechanism on the tension side of the cylinder, which consisted of bolt bearing and shear through the adhesive layer. The loads that were transferred on the tension side of the variable-stiffness cylinder in the preferred orientation were higher than for the other two configurations, which may trigger nonlinear behavior in the adhesive. Since the boundary conditions were modeled using linear springs, this behavior was not captured by the finite element model. As mentioned earlier, a detail-level test of the interface could result in a more accurate model of the boundary conditions.

The initial bending stiffness of the variable-stiffness cylinder was equal for both cylinder orientations, but a small difference arose at higher loads: the response was less stiff when the cylinder was loaded in the preferred orientation than when it was mounted in the reversed orientation. This difference was attributed to the influence of the boundary conditions, because the measured end rotation included both the deformation of the cylinder and the deformation of the cylinder-structure interface. The interface on the tension side

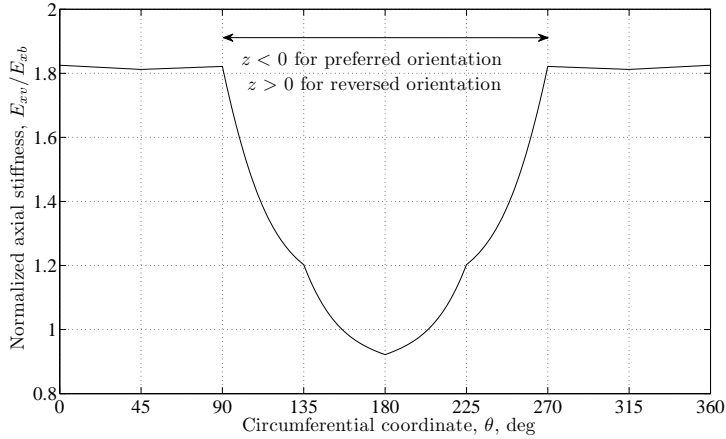


Figure 8.18: In-plane stiffness of the variable-stiffness cylinder

was a factor 7 more flexible than the interface on the compression side and therefore the deformation of the interface on the tension side dominated the amount of end rotation. The stiff part of the laminate ( $\theta = 0^\circ$ ) in the preferred orientation was loaded in tension, requiring high loads to be transferred through the cylinder-structure interface. The tension side of the cylinder carried smaller loads when the cylinder was oriented in the reversed orientation and therefore smaller tensile loads needed to be transferred by the cylinder-structure interface of the variable-stiffness cylinder in this orientation. The spring stiffness of the interface between the cylinder and the end-plates was smaller on the tension side than on the compression side, as explained in subsection 8.4.2. As a consequence, the deformations of the interface on the tension side, and thus the overall end rotations, were smaller for the reversed cylinder orientation than for the preferred orientation.

### 8.5.2 Geometric Imperfections

The measured geometric imperfections are discussed in this section, this is because the other results such as strain data and cylinder buckling predictions are influenced by the geometric imperfections of a cylinder. Geometric imperfections are usually expressed in terms of a deviation from the perfect cylinder radius. A positive imperfection value signifies a radius that is larger than the perfect radius and a negative imperfection value indicates a radius that is smaller. Mathematically the imperfection  $w$  is given by Eq. 8.3.

The geometric imperfections of baseline cylinder 2 and the variable-stiffness cylinder were measured using the digital image correlation system. The data was collected by taking pictures at different locations around the circumference with a stereo camera system and by assembling them into one data set covering the full cylinder using VIC3D software. A best-cylinder-fit option was available in the VIC3D software, but this could only be applied to a subset of the data, covering only a quarter of the cylinder and not to the assembled data set. Therefore an extra post-processing step was necessary to align the coordinate system of the DIC data with the actual cylinder axis. This was done by minimizing the distance of each

point to the ideal cylinder in a least-squares manner, where the location and orientation of the axis and the *perfect* cylinder radius  $R$  were variables. Mathematically this can be expressed as:

$$S = \sum_{i=1}^N d_i^2 = \sum_{i=1}^N (r_i - R)^2 \quad (8.4)$$

where  $d_i$  is the distance between data point  $i$  and the perfect cylinder,  $r_i$  is the distance from the data point to the perfect cylinder axis, and  $N$  is the total number of data points. The geometric imperfection values  $w$  can now be calculated for all data points:

$$w_i = R_i - R \quad (8.5)$$

The spacing of the DIC data was irregular due to the 3-dimensional nature of the cylinder and due to overlaps in the data, however, ABAQUS required regularly spaced data. To account for this the biharmonic spline interpolation method by Sandwell (1987), as implemented in the *griddata* function of Matlab, was used to map the measured imperfection data on the ABAQUS nodes.

The geometric imperfections for the baseline cylinder are depicted as contour plot on the expanded cylinder surface in figure 8.19. The maximum imperfection was 1.5 mm,

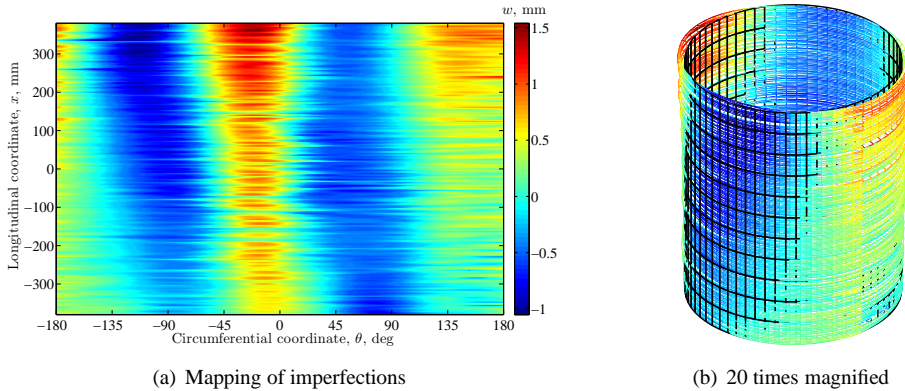


Figure 8.19: Geometric imperfections,  $w$ , of the baseline cylinder

approximately 35 percent of the wall thickness. The shape of the imperfect cylinder was oval with little lengthwise variation. Looking at the lengthwise imperfection at a local level, however, many little variations in radius could be observed, which can be seen as local waviness in the laminate. These small imperfection variations may have been caused by the bagging process.

The imperfection distribution of the variable-stiffness cylinder is given in figure 8.20. A comparison of the shape and magnitude of the imperfection distribution with those of the baseline cylinder in figure 8.19 showed that the absolute values of the imperfections were in the same range and that the shape was very similar. The global imperfection shape was therefore expected to be tool related. Unfortunately, the cylinders were not marked such that the part orientations could be traced back to the tool orientation. The shapes of the imperfection distribution might match if the x-direction of the baseline cylinder plot was reversed

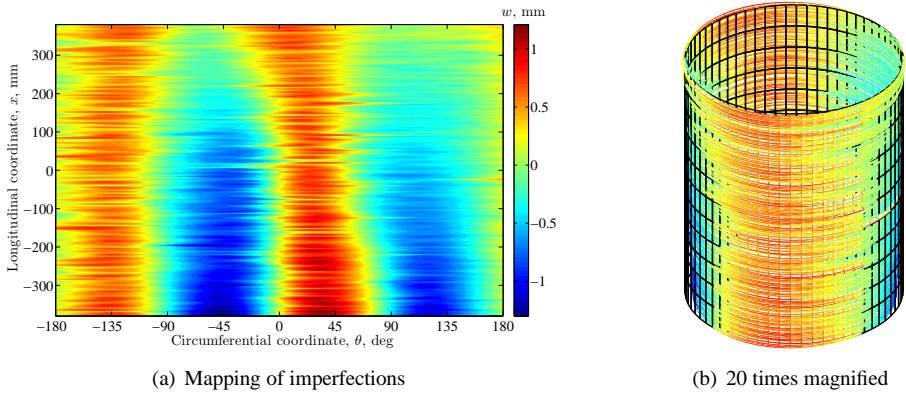


Figure 8.20: Geometric imperfections,  $w$ , of the variable-stiffness cylinder

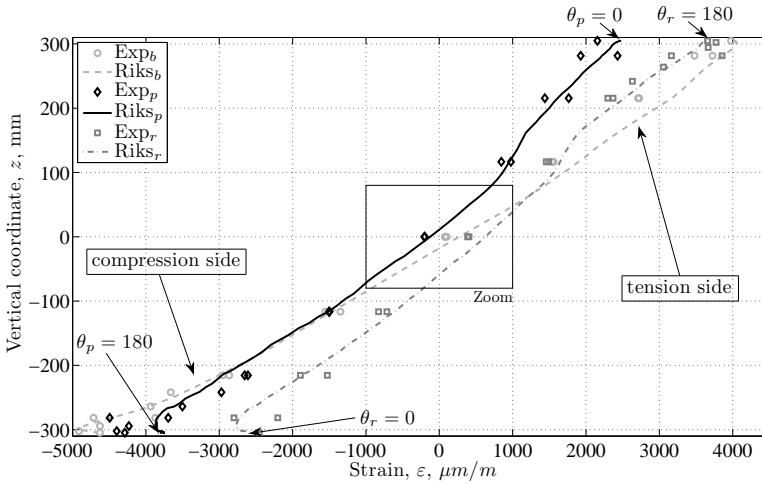
and if the pattern was shifted 90 degrees in the positive  $\theta$ -direction. It would be interesting either to measure the mandrel or to build and measure more cylinders manufactured on the same mandrel to check if the imperfections are indeed tool related.

The magnitude of the imperfections of the variable-stiffness cylinder were surprisingly in the same range as those of the baseline cylinder, although the varying fiber orientations, and consequently the varying coefficients of thermal expansion, were expected to have caused larger imperfections. The constraints on the laminate stiffness that were applied in the design, see chapter 5, excluded extreme stiffness variations and thereby also limited the variation in coefficients of thermal expansion. This could explain why the shape and magnitude of the variable-stiffness cylinder were similar to those of the baseline cylinder for which the imperfections were measured. A detailed finite element analysis of the part during curing including cool-down effects such as thermal expansion, chemical shrinkage and tool-part interaction might shed more light on the effect of varying fiber orientations on the final part shape. Furthermore, the imperfections were measured after the steel tabs were bonded to the surface and after the holes at the cylinder ends were drilled. These operations could also have influenced the final shape of the parts.

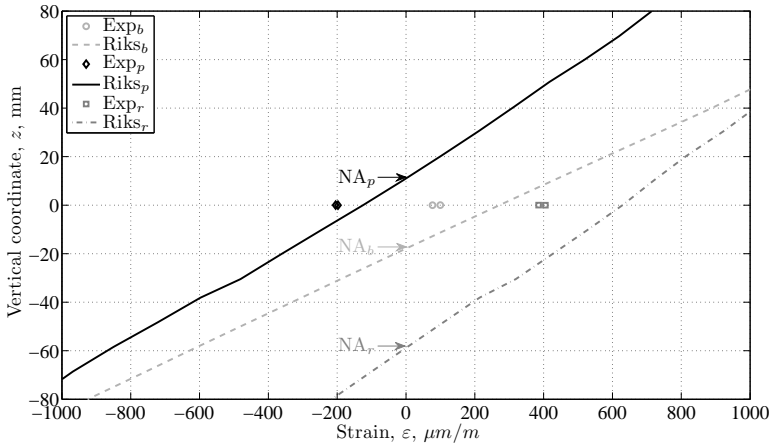
### 8.5.3 Strain Gauge Results

Each cylinder was populated with 113 strain gauges, mostly on the outer surface of the cylinder, see figure 8.10. An overview of the data that was collected by these strain gauges is given below.

The axial strains measured by the series of strain gauges halfway the length of the cylinder ( $x = 394$  mm in figure 8.10) are plotted as a function of the vertical coordinate  $z$  in figure 8.21. The strains predicted by the finite element model are also plotted in figure 8.21. The distribution is given for a bending moment of 302 kNm, which was the maximum load to which the variable-stiffness cylinder was loaded in the reversed orientation. The baseline results are shown by the light gray circles and the dotted line, the black diamonds and the continuous line represent the variable-stiffness cylinder in the preferred orientation and the dark gray squares and the dash-dot line give the results for the variable-stiffness cylinder



(a) Full cross-section



(b) Zoom around neutral axis

Figure 8.21: Axial strain distribution with  $z$ -coordinate of the cylinder at 302 kNm compared to the Riks analysis

in the reversed orientation. Again a good agreement between the experimental and analytical results of the Riks analysis was found. The baseline strain distribution showed a small shift of the neutral axis in negative  $z$ -direction, caused by the stiffer boundary conditions on the compression side. These same boundary conditions caused a small difference in the maximum tensile and compressive strain values of the baseline cylinder, which would have been the same for perfectly clamped boundary conditions. The neutral axis of the variable-stiffness cylinder in the preferred orientation was shifted in the positive direction, this was because the laminate stiffness on the tension side was almost twice as stiff as the laminate stiffness on the compression side. The difference in stiffness also resulted in much lower strains on the tension side than on the compression side, despite the fact that higher loads



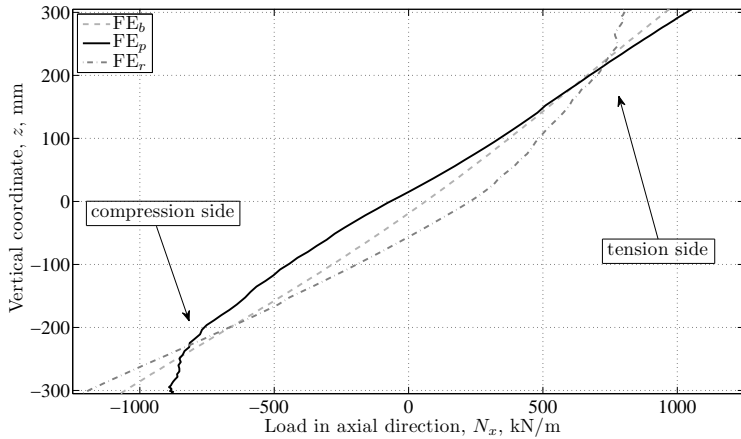
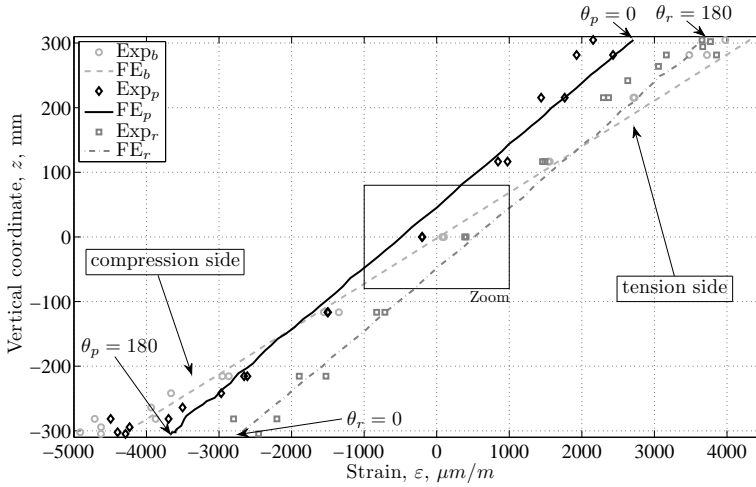


Figure 8.22: Distribution of axial loads with  $z$ -coordinate of the cylinder at 302 kNm

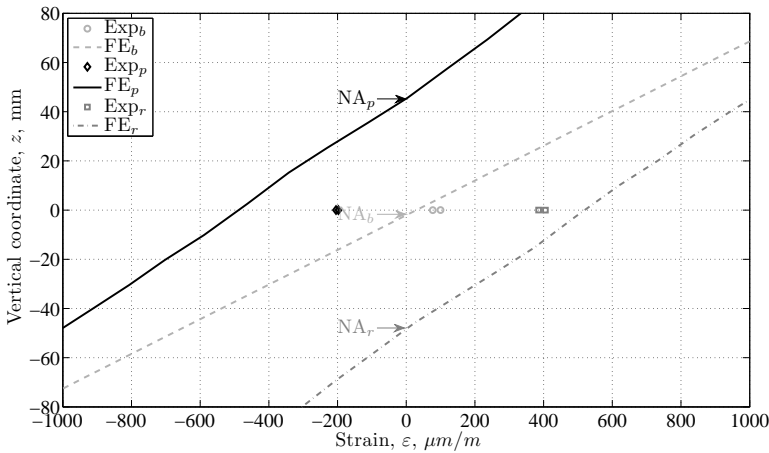
were carried on the tension side, see figure 8.22. The high-stiffness part of the laminate became the compression side when the orientation of the variable-stiffness cylinder was reversed, while the low-stiffness part of the laminate became the tension side. The higher stiffness of the laminate and the boundary conditions on the compression side were mutually reinforced, such that the neutral axis shifted below that of the baseline cylinder.

The shift in neutral axis also influenced the extreme strain values, and reversing the cylinder orientation did not result in a reversal of the strains. The influence of the boundary conditions becomes more apparent when the strain distribution of the Riks analysis is compared to that of a nonlinear finite element analysis with clamped boundary conditions without any imperfections, as shown in figure 8.23. The axisymmetric and clamped boundary conditions resulted in a reversal of the strains in the variable-stiffness cylinder when the cylinder orientation was reversed. The  $\theta = 0^\circ$  and  $\theta = 180^\circ$  locations were marked for both variable-stiffness cylinder orientations in figure 8.23(a). The strain for the reversed orientation at  $\theta = 0^\circ$  was exactly the negative of the strain at  $\theta = 0^\circ$  in the preferred orientation. The same was true for the  $\theta = 180^\circ$  location. The locations of the neutral axes in figure 8.23(b) were also reversed. The shift of the neutral axis of the baseline cylinder was negligible and the neutral axis of the variable-stiffness cylinder in the preferred orientation in positive  $z$  direction was equal to the shift of the reversed orientation in negative  $z$  direction. Reviewing the strain results of the experiment and the Riks analysis of figure 8.21 shows that at  $\theta = 0^\circ$  the tensile strain of the variable-stiffness cylinder in the preferred orientation was smaller than the compressive strain at  $\theta = 0^\circ$  in the reversed orientation. This was caused by the shift of the neutral axis due to the non-symmetric boundary conditions. The same phenomenon can be observed at  $\theta = 180^\circ$ .

The strain values of the baseline cylinder at both the extreme tension side ( $z > 200$  mm) and the extreme compression side ( $z < 200$  mm) exceeded the strain values of the variable-stiffness cylinder in either orientation. Strength constraints in the aerospace industry are often based on maximum strain values, which means that the variable-stiffness cylinder would have an advantage over the baseline cylinder, because the strain values were smaller



(a) Full cross-section



(b) Zoom around neutral axis

Figure 8.23: Axial strain distribution with  $z$ -coordinate of the cylinder at 302 kNm compared to the nonlinear FEA with clamped boundary conditions

at equal load levels. The strains of the variable-stiffness cylinder between  $\theta = 135^\circ$  and  $\theta = 225^\circ$  were smaller than the strains of the baseline cylinder, even though the stiffness of the baseline cylinder at this location was larger. This is because the stiffer side of the cylinder carried higher loads and reduced the load on the other side of the cylinder, as can be seen in figure 8.22. The tension side ( $z > 200$  mm) of the variable-stiffness cylinder in the preferred orientation carried higher loads than the baseline and also the area close to the neutral axis ( $-220$  mm  $< z < 20$  mm) was more effective at carrying compressive loads, so that the compression side ( $z < -220$  mm) carried significantly lower loads. The idea behind the improved performance was the same as predicted by the linear finite element

model with clamped boundary conditions, despite the differences caused by the flexible boundary conditions. The loads carried on the compression side of the variable-stiffness cylinder in the preferred orientation were lower than those of the baseline cylinder, which resulted in an ability to carry a higher bending moment before buckling occurred. The effect for the variable-stiffness cylinder in the reversed orientation was just the opposite: higher loads were carried on the compression side, thereby reducing the buckling load compared to the baseline cylinder. The presentation and the discussion of the numerical results for the buckling loads will be dealt with at the end of this section.

Two series of strain gauges were placed along the length of the cylinder at  $\theta = 0^\circ$  and  $\theta = 180^\circ$  to investigate at what distance from the boundary the edge effects were dissipated. These locations were selected because here the highest strains were expected to occur during the test. The strain distribution along the length is plotted in figure 8.24 for the baseline cylinder and the results for the variable-stiffness cylinder in the preferred orientation are shown in figure 8.25.

The strains predicted by the nonlinear finite element model without imperfections (FE<sub>f</sub>) and the strains predicted by the Riks analysis including imperfections (Riks) are also plotted in figures 8.24 and 8.25. The variation in the Riks analysis was caused by local waviness of the laminate, which could be observed in the geometric imperfection data of figures 8.19 and 8.20.

A schematic picture of a piece of laminate cross-section with imperfections and strain gauges SG1, SG2 and SG3 is given in figure 8.26. The black lines indicate the original cross-section, while the gray dashed lines show the deformed laminate under a tensile load. The laminate curvature is decreased locally under influence of the tensile load, and depending on the location of the strain gauge this has a large or a small influence on the measured strain value. For example, the measured strain in strain gauge 1 (SG1) is larger than the midplane strain, because the laminate curvature is reduced. In strain gauge 2 the strain will be close to the midplane strain, because there is hardly any change in curvature. At strain gauge 3 the curvature changes such that the measured strain is smaller than the midplane strain. Thus, strain gauges 1 and 3 will indicate different strain values, even though they are both on the top side of the laminate, because locally the laminate curvatures are different and under loading the change of curvature is also different. A similar mechanism takes place under compression, except that the absolute value of the curvature is increased instead of decreased, as opposed to a laminate under tension. These kinds of variation are seen in the strain distributions of figures 8.24 and 8.25.

The graphs of the Riks analyses in figures 8.24 and 8.25 were not smooth, because the data was extracted from the ABAQUS model at discrete node locations. The experimental data for both configurations matched the Riks analysis results better than the finite elements results without imperfections. The rate of change in strain values could be large and thus a small positioning error of a strain gauge in the experiment could have caused a substantial difference between the experimental and the predicted values. It was not possible to determine at which point the boundary effects were dissipated, due to the fluctuation in strain values. The finite element result of the variable-stiffness cylinder without imperfections already showed an oscillating strain variation along the entire length of the cylinder, which can be explained by the presence of the discrete fiber courses that were created by the fiber placement process. A discrete change in fiber orientation is present at the transition from one fiber course to another, see figure 4.3(b), causing a local change in laminate stiffness

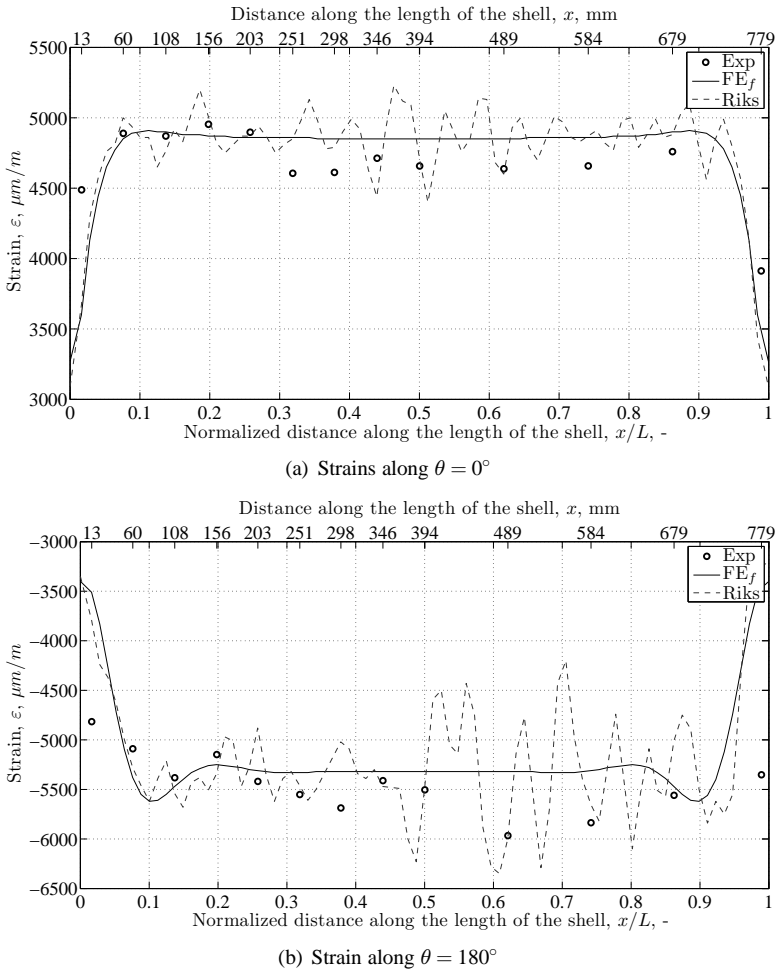
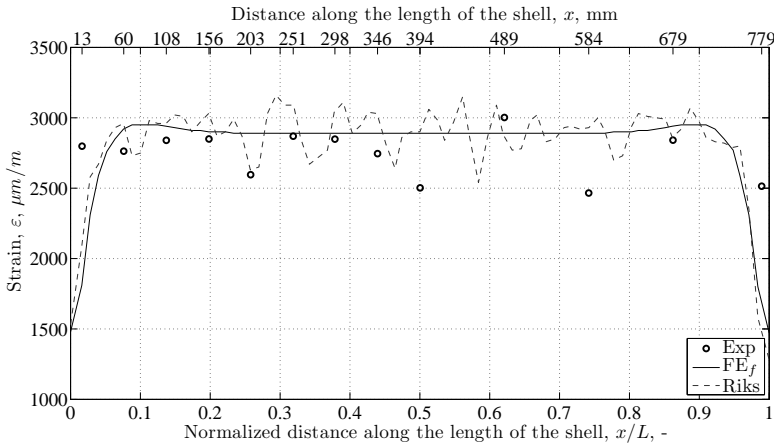


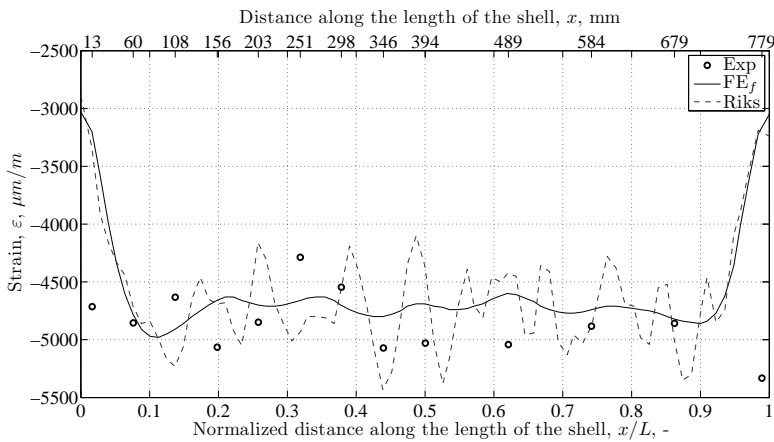
Figure 8.24: Strains along the length of the baseline cylinder at 352 kNm

and consequently a variation in strain.

There were several other locations around the circumference of the cylinder besides the  $\theta = 0^\circ$  and  $\theta = 180^\circ$  locations where more than one strain gauge was present along the length of the cylinder. To illustrate this the strains at different locations along the length are plotted for four locations around the circumference in figure 8.27. The finite element strains shown in these figures were measured halfway the length of the cylinder, i.e. at  $x = 394$  mm. An examination of figure 8.27(a) shows that the values of the strain gauges at the ends of the cylinder, at  $x = 13$  mm and  $x = 775$  mm, deviate most from the other strain values, however, even when the boundary gauges are not taken into consideration, the fluctuation in strain values is 300 microstrains at the maximum load level. The same kind of observations can be made for figure 8.27(b): at  $\theta = 45^\circ$  and  $x = 13$  mm the strain gauge shows a large deviation from the other values with a fluctuation of 350 microstrains at the maximum load.



(a) Strains along  $\theta = 0^\circ$



(b) Strain along  $\theta = 180^\circ$

Figure 8.25: Strains along the length of the variable-stiffness cylinder in the preferred orientation at 352 kNm

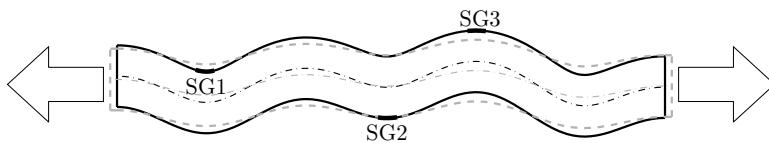


Figure 8.26: Schematic picture to illustrate the influence of imperfections on measured strain values

There was no obvious difference between the strain value at the boundary in figure 8.27(c), possibly because the location was close to the neutral axis and the loads were relatively low, but the data was even more scattered than in the first two result plots. Finally, the

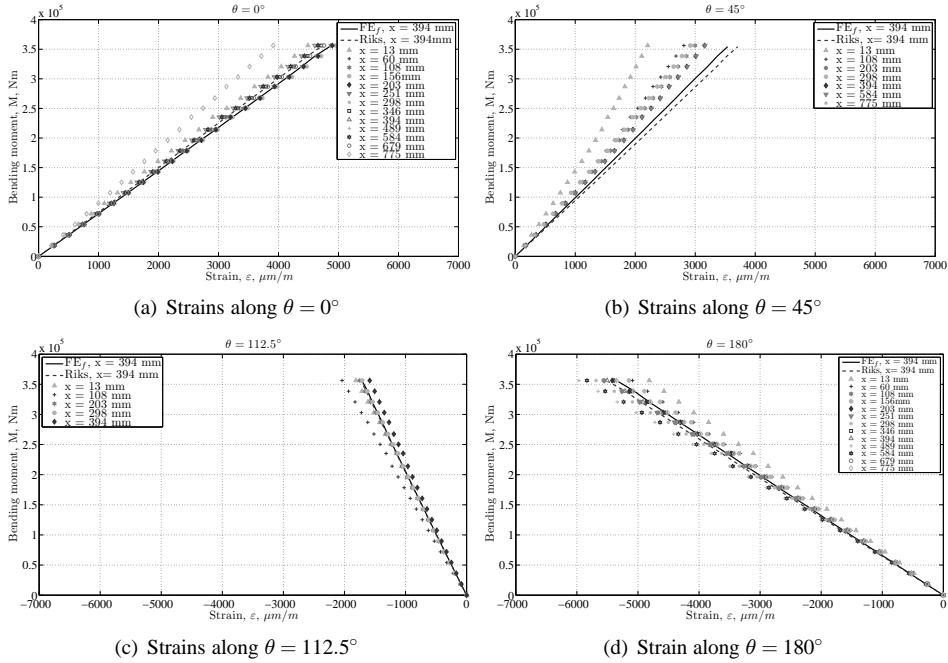


Figure 8.27: Strains at different locations along the length of the baseline cylinder

strain data on the compression side is shown in figure 8.27(d) and again the strain gauges at  $x = 13$  mm and  $x = 60$  mm deviated significantly from the other values, although there is a variation of up to 800 microstrains if these two data points are excluded. The results for other locations around the circumference of the baseline cylinder are omitted here, because they show similar trends to those discussed above, but they are given in appendix J, together with the results for the other two cylinder configurations.

Strain gauges were placed both on the outside and inside of the laminate between  $\theta = 0^\circ$  and  $\theta = 180^\circ$  halfway the length of the cylinder, at  $x = 394$  mm, as shown in figure 8.10. The purpose of these back-to-back strain gauges was to provide information about changes in curvature of the laminate so that out-of-plane deformations could be tracked. The out-of-plane curvature  $\kappa$  is defined by:

$$\kappa = \frac{\varepsilon_o - \varepsilon_i}{t} \quad (8.6)$$

where  $\varepsilon$  refers to the axial strain, the subscript  $o$  denotes the outer surface of the laminate and the subscript  $i$  denotes the inner surface of the laminate. The variable  $t$  is the laminate thickness. Based on the finite element analyses without imperfections the difference between the strains on the outside of the laminate and on the inside of the laminate at the maximum load of 352 kNm will not exceed 100 microstrains at any of the back-to-back strain gauge locations, as shown in figure 8.28(a). Unfortunately, the fluctuation of the strain values was large due to the presence of imperfections, such that a small positioning error could result in a large deviations from the predicted value. It was not possible to derive valid curvature data from the back-to-back strain gauge data, because deviations could occur both on the inside

and the outside of the laminate. The back-to-back strain data are plotted in figure 8.28, for both the experiment and the analysis, to illustrate this. The finite element results without imperfections are shown in figure 8.28(a) and the finite element results obtained using the Riks analysis including imperfections is shown in figure 8.28(b). The triangles represent the experimental strain data of the strain gauges on the outside of the cylinder and the squares represent the strains measured by the strain gauges on the inside of the cylinder. Some data points between  $\theta = 135^\circ$  and  $\theta = 180^\circ$  have been omitted to avoid cluttering of the results.

The main difference between figures 8.28(a) and 8.28(b) is that the differences between the strains on the inside and on the outside of the laminate are smaller for the finite element analysis without imperfections than for the Riks analysis. Overall the experimental data matches the Riks analysis predictions better, but the data never matches at the inside and outside simultaneously, and therefore this data cannot be used to calculate the laminate curvature. Note: the back-to-back strains for the baseline cylinder and for the variable-stiffness cylinder in the reversed orientation are given in figure J.4 in appendix J.

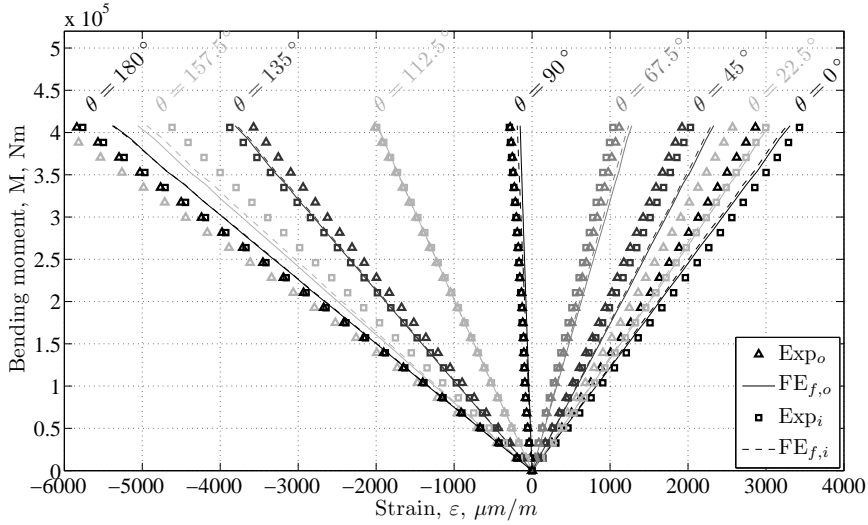
### 8.5.4 Digital Image Correlation Results

The disadvantage of measuring strains with strain gauges, as described above, is that strain gauges only provide point data. This makes it difficult to form a complete picture of the strain field based on strain gauge data. A digital image correlation (DIC) system can provide this kind of information by extracting the deformation field from the digital images and subsequently calculating the strain field. The strains measured by the DIC system were compared to the strains of two neighboring strain gauges which were located at the same circumferential coordinate to serve as a reference for the accuracy of the DIC system. The data points were picked as close to the symmetry plane as possible to minimize the effect of the boundary conditions. These values are listed for the circumferential locations  $\theta = 0^\circ$ ,  $\theta = 180^\circ$ ,  $\theta = 225^\circ$ ,  $\theta = 270^\circ$  and  $\theta = 315^\circ$  in table 8.2 and show a good agreement between the two measurement methods.

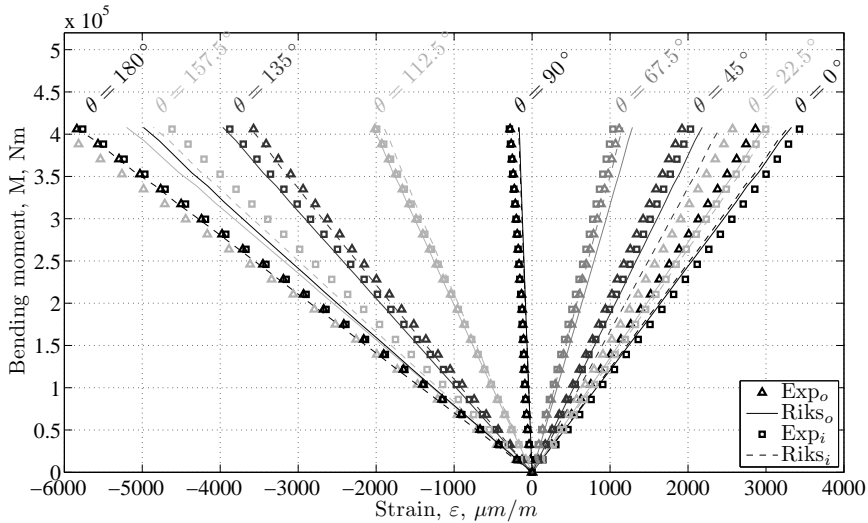
*Table 8.2: Comparison of strains measured with strain gauges and DIC at maximum load*

$\theta = 180^\circ$		$\theta = 225^\circ$		$\theta = 270^\circ$		$\theta = 315^\circ$		$\theta = 0^\circ$	
$x$	$\epsilon$	$x$	$\epsilon$	$x$	$\epsilon$	$x$	$\epsilon$	$x$	$\epsilon$
mm	$\mu\text{m/m}$	mm	$\mu\text{m/m}$	mm	$\mu\text{m/m}$	mm	$\mu\text{m/m}$	mm	$\mu\text{m/m}$
394	-6409	394	-4349	394	100	394	3677	394	5329
489	-6490	584	-4252	584	55	584	3759	489	5326
DIC	-6477	DIC	-4323	DIC	52	DIC	3822	DIC	5258

The DIC results for the compression side of the baseline cylinder and the variable-stiffness (VS) cylinder in the preferred orientation are plotted in figure 8.29. The longitudinal strains are superimposed on a picture of the speckled cylinder surface. The areas with wires were omitted from the analyzed area because correlation across wires gives unreliable results. The figures show an area that covers a section of approximately 110 degrees of the cylinder. The wires on the lower side of the figure were located on the  $\theta = 180^\circ$  line of the cylinder, which was the compression side. The wires on the top of the figure were located at  $\theta = 270^\circ$ , close to the neutral axis. Strain concentrations can be observed at the boundaries of both cylinders and these are most pronounced close to the  $\theta = 180^\circ$  location, whereas the



(a) FE analysis without imperfections



(b) Riks analysis with imperfections

Figure 8.28: Back-to-back strains on the variable-stiffness cylinder in preferred orientation

strain field at the center of the cylinder is undisturbed. It was not possible to draw any conclusions about the dispersion of the edge effects based on the data from the strain gauges, while the boundary effects are clearly visible using the DIC system. Comparing the strain distribution of the baseline cylinder with that of the variable-stiffness cylinder confirmed the findings discussed in the previous section, namely that overall the strains in the variable-stiffness cylinder were lower and that the neutral axis ( $\varepsilon = 0$ ) was shifted upward because of the stiffness variation.



The results for the reversed orientation of the variable-stiffness cylinder did not contain any new features and so are omitted here, appendix J for a complete overview of the results.

The strains predicted by the Riks analysis on the compression side of the baseline cylinder are shown in figure 8.30. Part of the contour is shown in white to indicate that this area was outside the field of view of the DIC measurements. The red squares indicate the location of strain gauges. The strain gauge at the bottom of the figure was located at  $\theta = 180^\circ$  and the top strain gauge was located at the neutral axis at  $\theta = 270^\circ$ . These locations correspond to the wire locations shown in figure 8.29. A comparison of the strain field of the DIC measurements of figure 8.29(g) with the strains predicted by the ABAQUS model showed good agreement. Irregular strain patterns can be seen in both the measured and the analytical results, these were caused by geometric imperfections. These variations in strain were also seen in the strain gauge data. The boundary condition effects were not captured by the finite element model.

Another remarkable feature in the DIC results of the baseline cylinder in figure 8.29 is the apparent stress concentration at the location circled in red. At lower load levels this stress concentration could be distinguished more clearly. This deviation of the expected strain distribution can be explained by looking at the NDI scan that was made of the cylinder before it was tested. The NDI scan is given in figure 8.31. Dark areas indicate flaws in the structure. Several flaws can be noted: At  $\theta \approx 150^\circ$  and  $\theta \approx 325^\circ$  longitudinal surface wrinkles were present which were created during the curing process and caused by insufficient debulking during lay-down of the plies. A horizontal flaw was present at  $x \approx 108$  mm between  $\theta = 45^\circ$  and  $\theta = 67.5^\circ$ , which was due to a repair in one of the 90 degree layers after some of the tows were damaged during production. Finally, two more defects were present at  $\theta \approx 270^\circ$  and  $\theta \approx 280^\circ$ . The one at  $\theta \approx 280^\circ$ , indicated by an arrow, most likely caused the strain anomalies in the DIC results, while the other defect was so close to the neutral axis that it had little effect on the strain distribution. The other defects were not in the field of view of the DIC system and not close enough to any of the strain gauges to be noticed in the measured data.

The strains on the tension side of the cylinder are shown in figure 8.32. The wires located on the top of the figures indicate the  $\theta = 0^\circ$  location, while the two other lines of wires are located at  $\theta = 315^\circ$  and at the neutral axis,  $\theta = 270^\circ$ . Boundary condition effects can again be observed, but this time the higher strain regions are more concentrated. Some of these sites are indicated by arrows in the baseline figures and by the light blue spots in figure 8.32(d). The green spots in figures 8.32(f) and 8.32(h) also indicate strain concentrations. These strain concentrations were caused by the load introduced through the bolted connection. This phenomenon was not observed on the compression side, because in compression the load was transferred by direct contact with the end-plate, which is a more uniform type of load transfer. The stress concentration at  $\theta = 0^\circ$  was most prominent, because this was where the highest loads were transferred. The strains at the left boundary were higher than the strains on the right boundary in the strain distribution of the baseline cylinder, see figures 8.32(a), 8.32(c), 8.32(e) and 8.32(g). This asymmetry was caused by a small misalignment of the test setup in the machine. The fixture was aligned with the machine at installation, but between installation and tests the hydraulic pressure was taken off, which allowed the fixture to slide downward and to sag to one side. Although this was corrected before the test was started, some asymmetry was still present. Sagging of the test fixture was prevented for subsequent tests by maintaining a minimum level of hydraulic

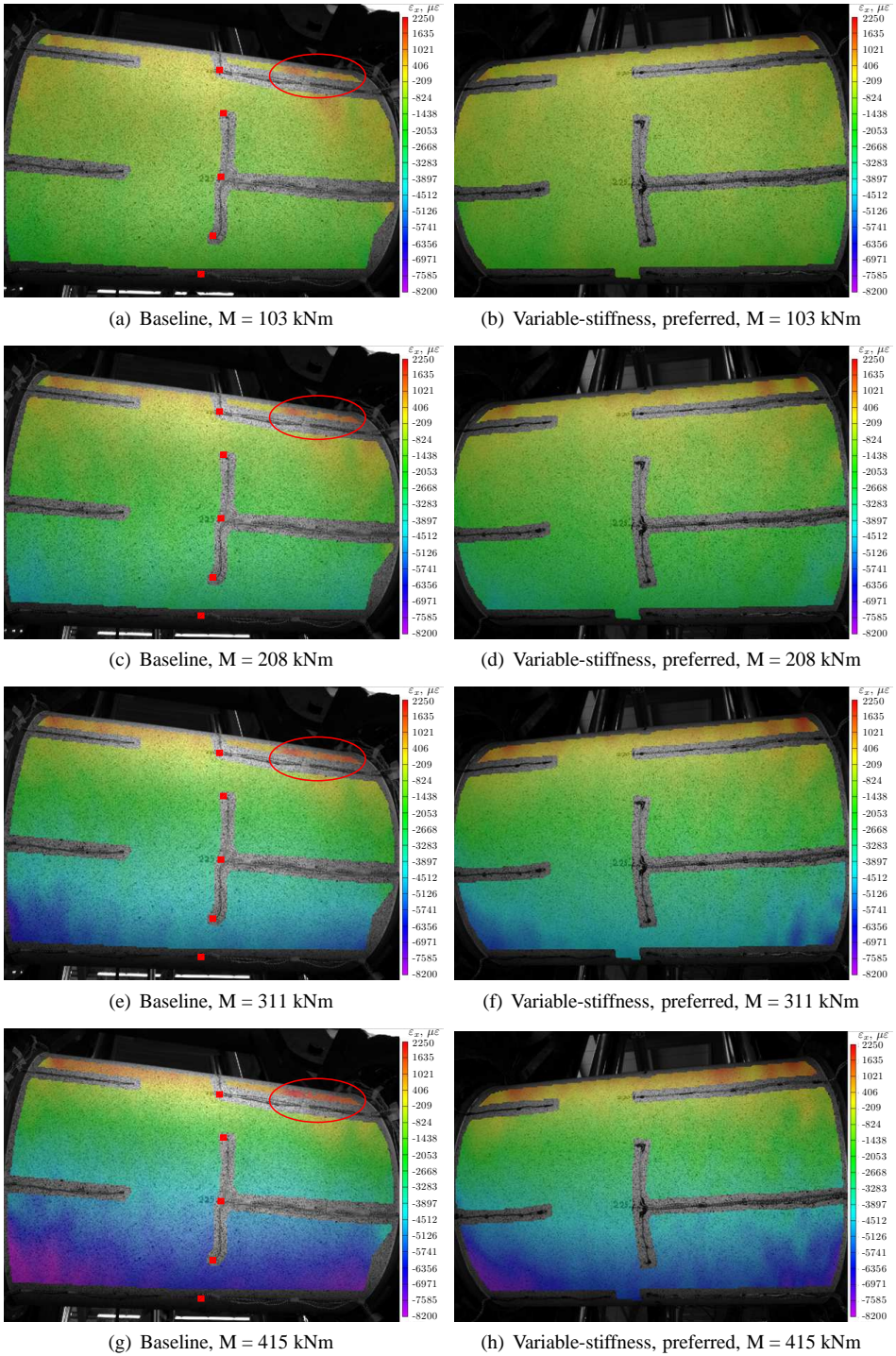


Figure 8.29: Strains on the compression side of the baseline and VS cylinder

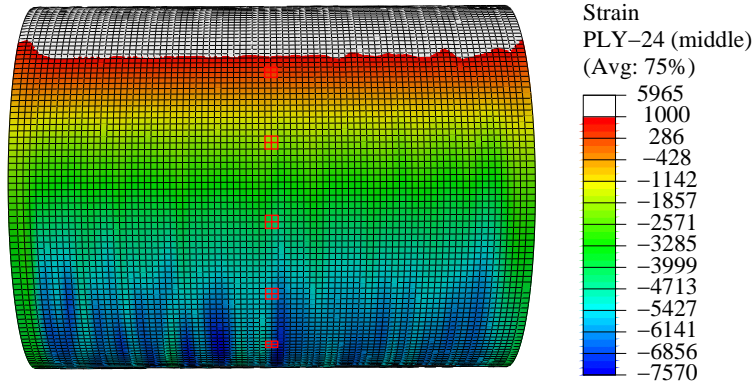


Figure 8.30: Predicted strains on the compression side of the baseline cylinder at  $M = 415$  kNm

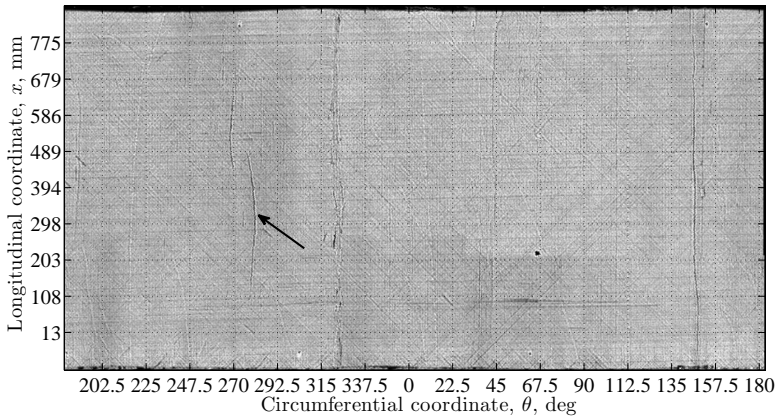


Figure 8.31: NDI scan of the cylinder before testing

pressure after installation.

### 8.5.5 Deflection and Ovalization

The vertical displacements of the cylinder and the support structure were measured at four different locations, as indicated in figure 8.8. The displacements at  $x = 0$  and  $x = L$  were measured by LVDT's that were in contact with the bottom of the outer support rings. Lasers were set to point to the top and the bottom of the cylinder halfway the length of the cylinder, at  $x = L/2$ . The purpose of these measurements was to obtain information about the deflection of the cylinder and to study possible ovalization of the cylinder. The measured displacements for all three cylinder configurations are plotted in figure 8.33. The initial displacements in all three tests were between 0.2 mm and 0.5 mm, probably caused by slack in the test mechanism. The displacements of the baseline cylinder were larger than those of the variable-stiffness cylinder, which is in agreement with the earlier observation that the



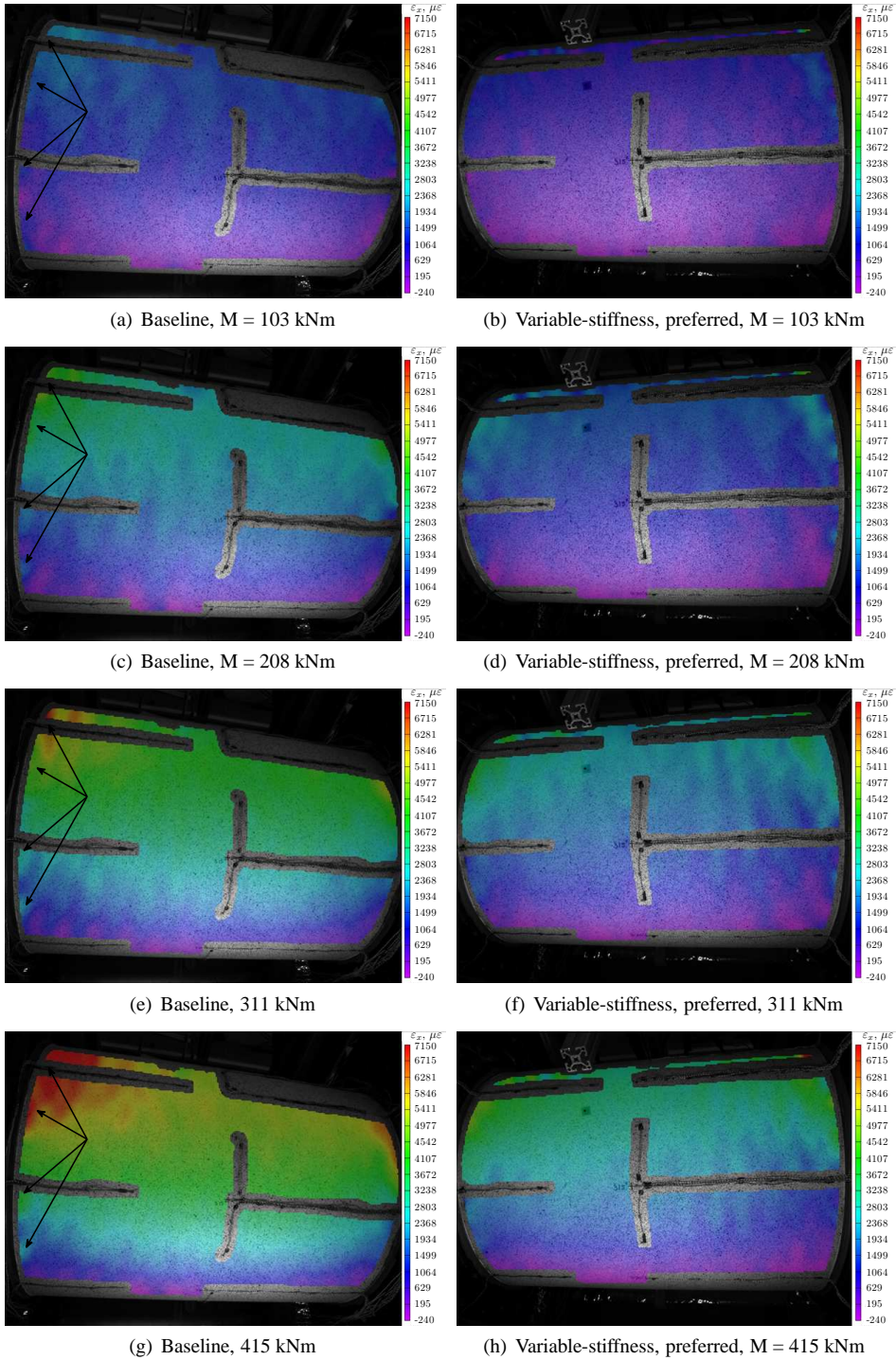


Figure 8.32: Strains on the tension side of the baseline and VS cylinder

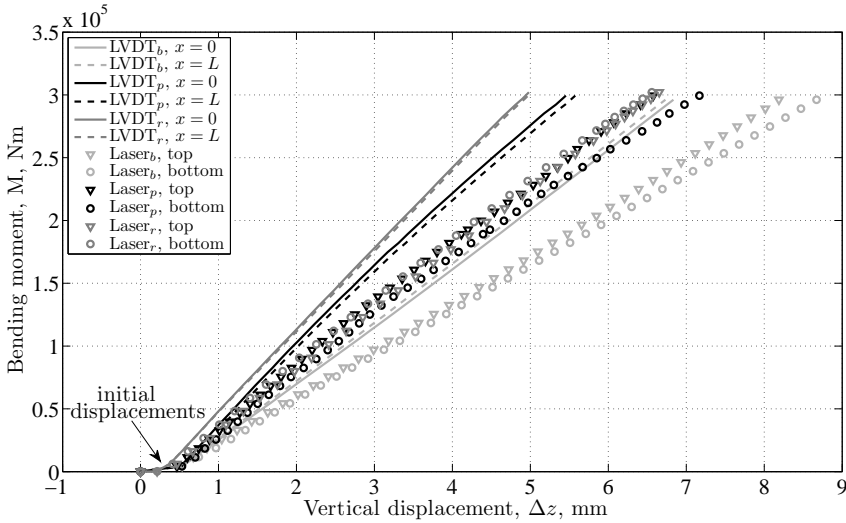


Figure 8.33: Vertical displacements of the cylinder

global stiffness of the baseline was smaller than that of the variable-stiffness cylinder. The stiffness of the variable-stiffness cylinder in the reversed orientation was larger than in the preferred orientation, which also agreed with the moment-rotation results.

The cylinder deflection was determined by calculating the difference in displacement between the cylinder edges and the midplane. The displacement at the midplane was taken as the average of the displacement on the top of the cylinder and the displacement on the bottom of the cylinder, while the displacements on the side were averaged, resulting in the following definition for the cylinder deflection  $\delta$ :

$$\delta = \frac{\Delta z_{top} + \Delta z_{bottom}}{2} - \frac{\Delta z(x=0) + \Delta z(x=L)}{2} \quad (8.7)$$

The deflections of the three cylinder configurations are plotted in figure 8.34. Unfortunately the graphs started out irregular, because the initial displacements of the LVDT's and lasers did not straighten out simultaneously. In addition, the deflection of the variable-stiffness cylinder in the preferred orientation was not smooth, because there were irregularities in the measurements taken by the bottom laser. Possibly the laser was aimed too closely to the center strain gauge, such that it hit the edge of the strain gauge. The surface could also be more irregular close to the strain gauge due to any adhesive that remained on the surface after the strain gauge was bonded to the cylinder. A small difference in slope between the baseline and the variable-stiffness results can be observed if the irregularities are disregarded, again indicating that the bending stiffness of the variable-stiffness cylinder was larger than that of the baseline cylinder.

Bending of cylindrical shells results in ovalization of the cross-section, known as the Brazier effect (Brazier, 1926). The ovalization of a cylinder depends on its laminate stiffness and the Poisson's ratio and therefore it would be interesting to make a comparison between the baseline and the variable-stiffness cylinder. The displacements on the top of the bottom

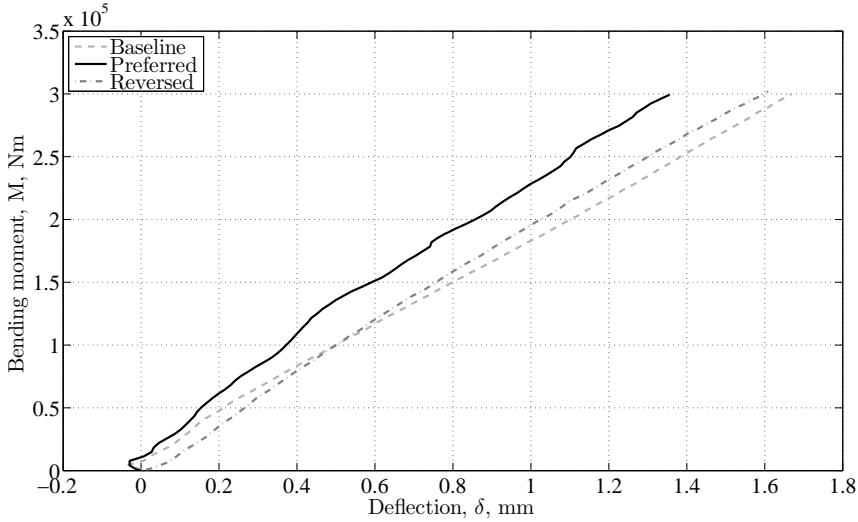


Figure 8.34: Deflection of the cylinders

of the cylinder were measured and the ovalization  $\Omega$  was defined as:

$$\Omega = \Delta z_{bottom} - \Delta z_{top} \quad (8.8)$$

where  $\Omega$  is positive when the cross-section becomes more flat.

Ovalization is given as a function of the bending moment in figure 8.35. Again there was an initial error in the experimental results and large irregularities occurred at increasing values of the bending moment. The variable-stiffness cylinder in the reversed orientation even showed a negative ovalization, which was not possible under the current loading. Furthermore, neither of the other two experiments showed good agreement with the finite element predictions. This can be explained by the sensitivity of the measurements to surface roughness. A picture of the cylinder surface after curing is shown in figure 8.36. The cylinder was painted white after curing and black speckles were applied, making the surface smoother. The variation in surface level of the painted surface was estimated to be around 0.2 mm, which was determined by comparing the cylinder surface with a surface roughness table. Hence, the uncertainty in the displacement measurement could be up to 0.2 mm, because the position of the laser beam on the cylinder surface could shift during the test. The uncertainty was doubled to 0.4 mm by subtracting the top displacement from the bottom displacement. This number is in the same order of magnitude as the expected ovalization and therefore these measurements could not be used to provide reliable ovalization information. In the future better measurements might be taken by measuring the displacements on the inside of the cylinder, as this is the tool side and unpainted, and therefore the inner surface is much smoother than the outer surface. Alternatively, the ovalization could be measured using a DIC system, but at least two camera sets would be required to allow the top side and the bottom side of the cylinder to be observed simultaneously. In this case a segment of more than  $180^\circ$  could be covered and the relative displacement of the top and

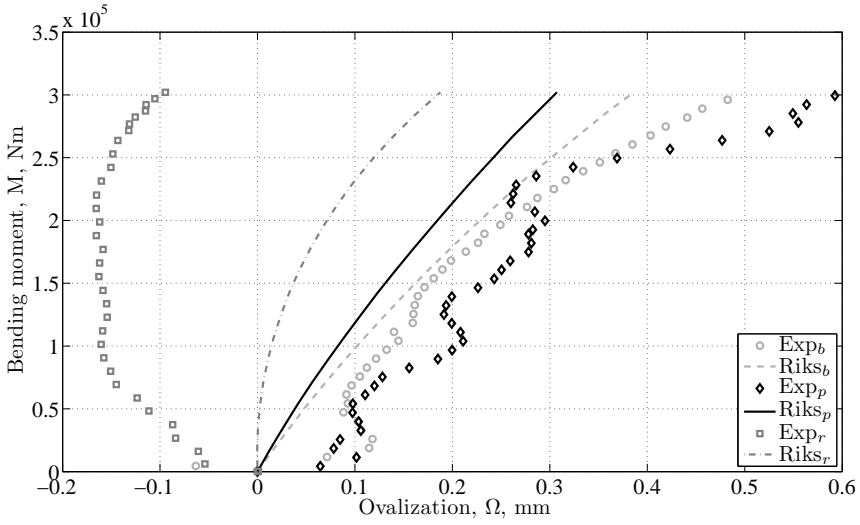


Figure 8.35: Ovalization of the cylinders

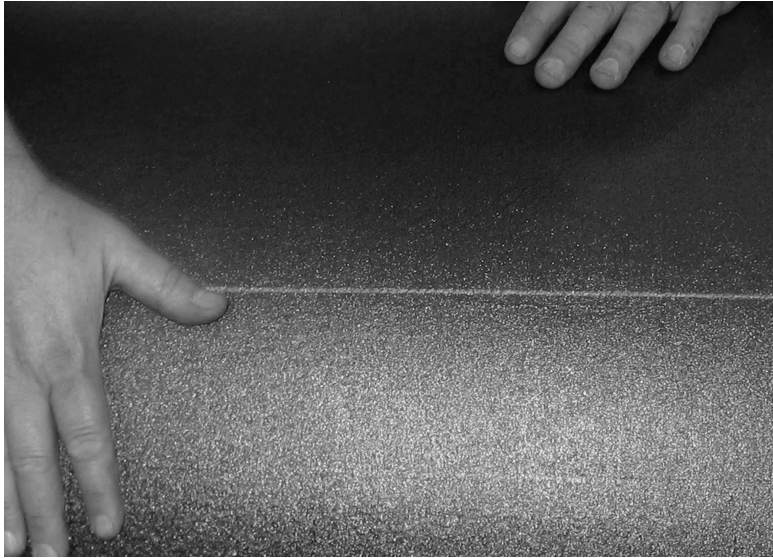


Figure 8.36: Surface roughness of the fiber-placed cylinder

bottom of the cylinder could be extracted from the DIC results. If four sets of cameras were used, the full cylinder surface could be covered by the DIC, making it possible to visualize the ovalization for the whole cylinder.

### 8.5.6 Comparison of the Buckling Load Predicted by the Different Finite Element Models

The different finite element models that were used to predict the buckling load of the cylinders were discussed in section 8.4. It was concluded from that discussion that the boundary conditions and geometric imperfections played an important role in the correct prediction of mechanical responses and the buckling load. The buckling loads for the three cylinder configurations as predicted by the four finite element models are reported in table 8.3.

Table 8.3: Features of the different FE models and the predicted buckling moments

FE Model number	Boundary conditions	Finite element model			Predicted buckling moment		
		Analysis type	Mechanism included	Imperfections included	Baseline $M_{cr}$ kNm	VS <sub>p</sub> $M_{cr}$ kNm	VS <sub>r</sub> $M_{cr}$ kNm
1	clamped	linear static	no	no	678	804	477
2	clamped	ngeom static	no	no	647	763	470
3	flexible	ngeom static	yes	no	570	671	430
4	flexible	static Riks	yes	yes	488	589	409

A comparison of the predictions for the variable-stiffness cylinder in the preferred orientation with the baseline cylinder showed that the buckling load of the variable-stiffness cylinder was about 18 percent higher than that of the baseline cylinder, regardless of which model was used. The general mechanism of redistributing loads within the cylinder was not changed, although the boundary conditions did affect the load introduction. Therefore the buckling load of the variable-stiffness cylinder in the preferred orientation was still higher than that of the baseline cylinder and the buckling load of the variable-stiffness cylinder in the reversed orientation was still lower than that of the baseline. The decrease in buckling load for the preferred orientation of the variable-stiffness cylinder from model 1 to model 4 was 27 percent, which was similar to the baseline cylinder. The reduction for the variable-stiffness cylinder in the reversed orientation was only 16 percent. The reduction in buckling load from model 3 to model 4 was much smaller for the reversed configuration of the variable-stiffness cylinder than for the other baseline cylinder and the variable-stiffness cylinder in the preferred configuration. The only change from model 3 to model 4 was the inclusion of geometric imperfections in the model. The geometric imperfections of the variable-stiffness cylinder in the preferred and reversed direction were the same and thus it can be concluded that the location of the imperfections in relation to the loading direction were also important, because cylinder buckling is governed by imperfections on the compression side, whereas it is insensitive to imperfections on the tension side. The imperfections between  $\theta = 90^\circ$  and  $\theta = 270^\circ$  were important for the reversed cylinder configuration, whereas the imperfections between  $\theta = 270^\circ = -90^\circ$  and  $\theta = 90^\circ$  dominated the buckling behavior for the preferred configuration.

## 8.6 Discussion and Outlook

A fixture was designed to test a cylinder with a diameter of 609 mm and a length of 990 mm in pure bending. Strains and displacements were measured using strain gauges, digital image correlation, LVDT's and lasers. Three carbon fiber-reinforced cylinders were tested:



two with a baseline laminate and one with circumferentially varying laminate stiffness. The variable-stiffness cylinder was tested in two configurations: i) it was tested in the orientation for which it was optimized, called the preferred configuration, and ii) it was tested while rotated  $180^\circ$  about the longitudinal axis, such that the loading on the cylinder was reversed, this was called the reversed configuration. This resulted in three test configurations: the baseline, the variable-stiffness in the preferred orientation and the variable-stiffness in the reversed orientation.

A comparison of the experimental response of the baseline cylinders with the finite element predictions revealed that the experimental boundary conditions were more flexible than originally modeled in the finite element model. The introduction of flexible boundary conditions in the finite element model resulted in good agreement between the experimental and the analytical results. A final improvement of the finite element predictions was achieved by including geometric imperfections in the model and by performing a Riks analysis. The latter model was used to make a prediction for the variable-stiffness test results.

A comparison of the experimental results with the finite element predictions of the Riks analysis in general showed a good agreement for all three configurations. The match of the end rotations and strains was equally good for the variable-stiffness cylinder and the baseline cylinder. The variable-stiffness cylinder was stiffer than the baseline cylinder when comparing the global behavior in terms of end rotations, which was to be expected because of the larger laminate stiffness of the variable-stiffness cylinder. The variable-stiffness cylinder response was stiffer in the reversed orientation than in the preferred orientation due to the boundary condition effects. The most important observation resulted from the strain distribution with the vertical coordinate of the cylinder: at equal load level the maximum compressive strains of the variable-stiffness cylinder in the preferred orientation were about 10 percent lower than those of the baseline cylinder; the tensile strains were 35 percent smaller. This difference in extreme strain values is a large improvement in performance when strain-based strength criteria are applied. In addition, the circumferential stiffness variation resulted in a redistribution of the loads, such that the tension side was more effective in carrying loads, the compressive loads were carried by a larger part of the cylinder and the compressive load peak at  $\theta = 180^\circ$  was significantly reduced compared to the baseline cylinder. The buckling load of the cylinder was increased by 18 percent as a result of this load redistribution. This improvement was maintained even when realistic boundary conditions and geometric imperfections were included.

In the future it would be interesting to include cutouts or damage in a second baseline cylinder and in the variable-stiffness cylinder to reduce the critical load and to make failure of the variable-stiffness cylinder possible. The compression side of the cylinder would be the preferred location for the introduction of a defect, because normally the compression side of a cylinder in bending is the most critical part of the structure. Moreover, the load redistribution mechanism of the variable-stiffness cylinder should result in a higher load-carrying capability when compared to the baseline cylinder, even when cutouts or damage are introduced on the compression side.



# Chapter 9

## Conclusions and Recommendations

This thesis covers the design, analysis and optimization of fiber-placed, variable-stiffness composite conical and cylindrical shells, and the manufacturing and testing of a baseline and a variable-stiffness composite cylinder. The lessons learned and the future challenges associated with each of the aspects listed above will be discussed in this chapter.

### 9.1 Design

Variable-stiffness plies for conical and cylindrical shells were designed according to the shifted course principle first introduced for flat panels by Waldhart et al. (1996). The fiber orientation was defined to vary in either the axial direction or in the circumferential direction of the shell. A limited number of design variables was used to define a reference path to be covered with a fiber course using advanced fiber placement. A full ply was then constructed by shifting subsequent courses, identical to the reference course, perpendicular to the direction of stiffness variation. Additional factors taken into account with respect to the design of flat panels were the changing circumferential length of conical shells and the requirement for continuity of fiber paths around the circumference for conical and cylindrical shells. The combination of changing circumferential lengths and the need for continuity around the circumference prohibited the use of the shifted course method for the design of conical shells with a circumferential stiffness variation. Therefore only an axial stiffness variation was considered for conical shells. Variable-stiffness plies for cylinders could have an axial or a circumferential stiffness variation.

Future work might be aimed at developing a different design method for variable-stiffness plies which can deal with circumferential fiber angle variations for conical shells. Further work is also needed for the design of variable-stiffness laminates for doubly-curved, non-developable surfaces. The use of the shifted course method for the definition of variable-stiffness laminates on simple surfaces is preferred though, because a reasonable amount of stiffness variation can be achieved using a relatively small number of design variables, a desirable feature for optimization. A two-dimensional stiffness variation on a cylindrical

shell could also be obtained by combining plies with an axial stiffness variation and plies with a cylindrical stiffness variation within one laminate. Manufacturing constraints such as in-plane path curvature and the amount of thickness buildup are easily evaluated for plies constructed using the shifted course method, while it is more complicated to evaluate the manufacturing constraints if all fiber paths are unique.

Four path definitions were proposed for the construction of variable-stiffness plies on conical and cylindrical shells: a geodesic path, a constant angle path, a piecewise linearly varying angle path and a piecewise constant curvature path. The geodesic path and the constant angle path are identical for cylindrical shells, but differ for conical shells. Non-geodesic fiber paths are subjected to in-plane curvature constraints imposed by the advanced fiber-placement process. It was shown that the curvature constraint is most restrictive if the length over which the fiber angle is varied is small, i.e. the multiple-segment linear angle and constant curvature variations were more restricted than the single-segment fiber angle variations for a given geometry. Constant angle paths on conical shell surfaces were also shown to be limited by the curvature constraint. Early evaluation of the in-plane curvature of a fiber path was proven to be essential to ensure manufacturability using the current fiber placement technology.

## 9.2 Finite Element Analysis

The variable-stiffness cones and cylinders were analyzed using the commercially available finite element program ABAQUS (ABAQUS, Inc., 2005). The variable-stiffness properties were implemented using a UGENS user subroutine written in Fortran, which determined the stacking sequence at four integration points per element, based on the laminate definition and the exact placement of fiber courses using fiber placement. The subroutine method was preferred over writing the laminate stacking sequence for each element to the ABAQUS input file, because direct input required 20 times more time for pre-processing compared to using the UGENS subroutine. The downside to using the UGENS subroutine is the need for a post-processing step using a python script to extract strain and stress values per ply.

The computational time for directly using the ABAQUS input file can be reduced if multiple elements with identical stacking sequences are assembled in one element set. The fiber placement process however causes local fiber angles to vary slightly with position within a course, resulting in a unique stacking sequence for each element. Ignoring the small deviations of the fiber angles, i.e. using a fiber angle distribution which is a function of only one coordinate such as shown in figure 4.3(a) as opposed to the exact fiber angles as shown in figure 4.3(b), would allow for combining multiple elements in one element set. The simplification of the local stacking sequence causes a negligible error in the finite element results compared to using the exact fiber angles. The difference in buckling load for a cylindrical shell in bending between the simple and exact method can be seen in figure 6.12, where the simple method is represented by a zero course width and the exact method is represented by the 102 mm (4 in) course width. Combining multiple elements within one element set ignoring the exact stacking sequence is therefore recommended to speed up the finite element analysis, especially for optimization.

A continuous course boundary for the fiber courses was assumed during the determination of the local stacking sequence, even if tows were terminated or started to obtain

a constant thickness laminate. Ignoring the presence of small triangular gaps and overlaps due to cutting and restarting tows might adversely affect the strength and stiffness properties of the laminate. The curvature of the tows could also cause a reduction in laminate strength. These effects were not taken account in the research reported on in this thesis. An earlier study on the effect of tow drops by Blom et al. (2009) has shown that local resin-rich areas act as stress concentrations. A more extensive study on the effects of fiber the small gaps and overlaps caused by cutting and restarting tows within a laminate is recommended such that the effects be taken into account in the future. It would also be interesting to investigate how the other parameters such as path curvature and the value of the coverage parameter affect the laminate strength and stiffness.

### 9.3 Optimization Methods

Two different optimization methods were used for the research presented in this dissertation. The first optimization routine was a FORTRAN implementation of an NLPQLP solver (Schittkowski, 2004), suitable for solving constrained nonlinear optimization problems. This routine requires continuously differentiable objective and constraint functions. The derivatives of the objective function were determined using forward finite differences, which was computationally expensive due to the extra finite element analyses needed, i.e. one additional computation for each design variable. Another disadvantage of using an NLPQLP solver is the chance of converging to a local minimum. Therefore the optimization had to be repeated using different initial values for the design variables. The optimization routine was applied to a problem with 2 design variables, but would be computationally too expensive if more design variables were used. NLPQLP is also not viable if one of the objective or constraint functions is discontinuous or has discontinuous derivatives, and thus NLPQLP could not be used to take into account the changing mass for overlap designs. Overlap designs contain plies with a discrete number of fiber courses per ply. Changing a design variable might cause a change in the number of fiber courses and the amount of overlap between courses, which would then result in a discrete jump in structural mass.

A response surface optimizer with global search capability was used for the optimization of the variable-stiffness cylinders in bending. Small irregularities in the response were eliminated using surrogate models. The surrogate models were also used to calculate the derivatives of the response and objective functions, saving the computational effort of additional finite element analyses required to determine the derivatives through finite differences. The initial experiment and the global search routines increased the chance of finding the global optimum, compared to the NLPQLP method. The surrogate models for the constant-thickness laminates correlated well with the finite element predictions, but showed larger deviations when overlaps were allowed, because the buckling load and strength responses were more irregular. The optimization for the variable-stiffness cylinders with overlaps converged to local optima, especially when the number of design variables was large and the optimization was constrained.

The response surface optimization was considered to be an appropriate method for the optimization problem under consideration, even though it converged to a local optimum for a larger number of design variables. NLPQLP was not appropriate because of the need for derivative information and the dependence on the choice of the initial design variables.

Genetic algorithms, not discussed here, could be an alternative optimization method if a different, faster analysis method was used instead of a finite element analysis.

## 9.4 Optimization Results

Numerical examples of variable-stiffness conical shells optimized for maximum fundamental frequency showed that axially varying the laminate stiffness could lead to an increased fundamental frequency of conical and cylindrical shells compared to laminates with a constant stiffness. Multiple-segment angle variations showed the most improvement, especially for larger structures where the curvature constraint was less restrictive than for smaller structures. The fiber angle in the multiple-segment stiffness variation was varied from  $T_0$  at the small radius to  $T_1$  halfway the length of the cone and back to  $T_0$  at the large radius. Larger improvements are expected if the fiber angle at the large radius is allowed to vary independently from the fiber angle at the small radius due to the increased design freedom.

The axial stiffness variation was only used to optimize conical and cylindrical shells for maximum fundamental frequency in this thesis. Optimization of the axial laminate stiffness of conical shells for other load cases, such as axial compression, would be needed to expand the knowledge and understanding of variable-stiffness composites. Tatting (1998) has shown that axially varying the stiffness of cylinders loaded in compression does not have a large effect on the structural performance. Conical shells, however, have an axially varying geometric stiffness, which might require a varying laminate stiffness to achieve maximum structural performance. A follow-up study for other load cases is therefore recommended.

A circumferential stiffness variation proved to be beneficial for the structural performance of composite cylinders loaded in bending. Variable-stiffness laminates with a constant thickness improved the buckling load carrying capability by redistributing the axial loads around the circumference. The tension side of the cylinder became more effective for carrying loads, the load peak on the compression side was reduced and the compressive load was distributed over a larger area. This load redistribution was caused by the high axial stiffness on the tension side and the lower axial stiffness on the compression side of the cylinder. Reducing the compressive peak load and changing the buckling deformations resulted in a higher bending moment carrying capability. The optimum stiffness distribution also caused a reduction in extreme strain values up to 10 percent compared to the baseline cylinder, which is an advantage because in a design environment strength is typically judged based on strains.

The stiffness distribution that resulted from the optimization was not as expected. The intuitive design was one that resembled an I-beam stiffness distribution, with an axially stiff tension and compression side with softer side laminates, similar to the design described and manufactured by Wu (2008). Optimization tools are therefore essential for the design of variable-stiffness composites. Design studies of variable-stiffness composite structures subjected to relatively simple load cases are needed to gain confidence in the optimization tools and to create insight into the behavior of variable-stiffness composites, before they can be used to design structures for complex, combined load cases.

The unconstrained optimization of the constant-thickness, variable-stiffness laminates resulted in improvements in buckling load carrying capability up to 30 percent at equal mass compared to the optimized conventional design. Improvements up to 18 percent were

achieved for the constrained optimization. Constraints on the in-plane path curvature were included to guarantee manufacturability, and a minimum fiber angle orientation of 10 degrees was implemented to ensure a minimum course width of 6 tows. An equivalent of the 10 percent rule was implemented to increase the robustness and practicality of the design. The most restrictive constraint was the requirement that the cylinder had to buckle before material failure was allowed to occur. The strength constraint is expected to be less restrictive if a thinner laminate is optimized, because a thinner laminate is more susceptible to buckling and therefore the improvements might be greater if the laminate is thinner.

The improvements in buckling load carrying capability of variable-stiffness composite cylinders with overlaps were due to the increased laminate thickness on the compression side of the cylinder. The thickness buildup, which was coupled to the fiber angle variation, occurred at small fiber angles. The small fiber angles and large laminate thickness resulted in a high axial stiffness, attracting loads, which was contradictory to the trend observed for the variable-stiffness laminates with a constant thickness. The buckling load carrying capability was increased because the increase in laminate bending stiffness was larger than the increase in axial load. Ideally the thickness buildup should be made independent of the fiber angle orientation, such that the out-of-plane stiffness on the compression side of the cylinder can be increased while the in-plane-stiffness can be kept as low as possible.

The variable-stiffness laminates with overlap were compared on the basis of specific buckling moment, i.e. the buckling moment normalized with the cylinder's mass. The buckling moment does not scale linearly with the laminate thickness though, which might cause a misleading representation of the improvements. A scaling of the ply thickness was applied to obtain a cylinder with a mass that was equal to that of the baseline cylinder to provide a better measure of comparison. The ply-thickness-normalized variable-stiffness laminates with overlap showed an improvement of 90 percent in buckling load carrying capability compared to the baseline laminate without any constraints applied and assuming that the ply thickness could be scaled arbitrarily.

The optimization of the variable-stiffness cylinder with overlaps that includes the manufacturing and strength constraints is not appropriate if the ply thickness is scaled afterwards, because the buckling moment does not scale linearly with laminate thickness, while strength does. Changing the laminate thickness thus changes the difference between the buckling moment and the material failure moment. Again, a full-scale laminate optimization is needed if the cylinder has to be designed such that it buckles before it fails due to material failure.

The design objective in aerospace companies is usually to minimize the structural mass for a given level of performance instead of to increase structural performance for a given mass. Reducing the structural mass requires removal of plies, even more so for the laminates with course overlaps, because the structural mass increases if the number of plies is kept constant, which is highly undesirable. A full scale laminate optimization with a variable number of plies and thus a variable number of design variables was beyond the scope of this thesis, but is highly recommended to show how much of the increased structural performance can be translated to weight savings. Future work on the optimization of variable-stiffness composites might also include multiple or combined load cases, cutouts or damage, and different design objectives. Furthermore, it would be interesting to see how small deviations in thickness, fiber orientation, boundary conditions or material properties affect the structural behavior of the optimized structures.

## 9.5 Manufacturing using Advanced Fiber Placement

The baseline and the variable-stiffness composite cylinders were manufactured using an Ingersoll advanced fiber placement machine which could place up to 32 3.175 mm (1/8 inch) wide tows. The compaction roller was unable to conform to the cylinder surface at small fiber orientation angles, because of the relatively small cylinder diameter. The course width was adjusted to ensure sufficient compaction. A more deformable or a segmented roller could also be used to resolve this issue.

The minimum turning radius of 508 mm (20 inch) caused some puckering during placement of the tows which was suppressed by intermediate debulking of the laminate. The final product did not exhibit any flaws due to puckering of tows as could be seen on the NDI scan. The regions where tows were cut and restarted were visible on the NDI scan.

The minimum cut length was taken into account in the detailed design of the variable-stiffness laminate. Problems were avoided by making small adjustments to the coverage parameter. Minimum cut length violations only occurred at the boundaries of the cylinder, which were trimmed after curing.

Steering a fiber course while cutting tows on the outside of the turn caused the outer tows to straighten. This was caused by a lack of guidance of the tows towards the part surface after the tows were cut, such that the tows were inclined to follow a geodesic path instead of the curved path over a length equal to the minimum cut length. Fiber straightening can be avoided by adjusting the laminate design to only allow tow cuts on the inside of a turn or by combining the shifted and parallel ply construction methods to avoid cutting in general. The feasibility of combining the shifted course method and the parallel course method in one ply was demonstrated with the production of a variable-stiffness cylinder with axial stiffness variation and overlaps. A redesign of the fiber placement machine to reduce the minimum cut length or to extend guidance of the tows closer to the surface would also help to remove the problem of fiber straightening. Furthermore, it would be interesting to investigate at what turning radius the deviation of the fiber angle would be acceptable, so that this can be taken into account in the design.

Part of the current variable-stiffness plies had a constant fiber angle orientation, which would allow for the combination of multiple narrow courses into one. Production rate is an important parameter in a production environment and the production rate can be increased by reducing the number of courses.

## 9.6 Experimental Validation

A modal test of the baseline and the variable-stiffness composite cylinder was performed and the results were compared to the ABAQUS finite element predictions. The analytically predicted and experimental modal frequencies matched within 5 percent up to a frequency of 1000 Hz. The modal response simulations also showed a good agreement with the experimental results both for location and amplitude of the response. The modal frequencies of the baseline cylinder were higher than those of the variable-stiffness cylinder due to the higher laminate bending stiffness in the circumferential direction, which plays an important role in the formation of waves in the circumferential direction. The larger axial stiffness of the variable-stiffness cylinder became apparent for modes with an increasing number of



axial half waves and the modal frequency of the variable-stiffness cylinder approached or even exceeded the modal frequency of the baseline cylinder. Although only 2 cylinders were tested, the presented results indicate that the finite element model for the variable-stiffness cylinder provides a good representation of the cylinder in terms of mass and stiffness distributions.

The second experiment performed was a bending test of the cylinders. The cylinder response was predicted using a nonlinear finite element analysis in ABAQUS. The boundary conditions in the finite element model were adjusted based on the bending test of the baseline cylinder to reflect the test conditions correctly. The flexibility of the interface between the cylinder and test fixture was modeled using springs, which resulted in a good agreement of the predicted and the measured global response of the cylinders. A more detailed cylinder-fixture interface model could be developed by characterizing the interface through a component test.

Geometric imperfections of the cylinders were measured outside the test setup using a 3D digital image correlation (DIC) system. These geometric imperfections were included in the finite element model. The imperfections were also measured while the cylinder was assembled in the test fixture. The post-processing of these data was unsuccessful because the cameras had to be repositioned to capture the full cylinder surface and the images could not be stitched together. Ideally, the imperfections of the assembled cylinder should be used in the finite element model, because this geometry influences the structural behavior, and the difference in geometry introduced during assembly should be included as mechanical pre-stresses in the model. The difference in imperfections of the cylinders measured outside the fixture and assembled in the fixture were assumed to be small due to the high stiffness of the cylinders, and therefore the finite element predictions were assumed to be unaffected by the difference.

Other imperfections, such as variations in laminate thickness, material properties, and local disturbances in the load introduction, can also influence the buckling behavior of unstiffened shells (Degenhardt et al., 2010). It would be interesting to include these effects in the finite element model to see how they affect the structural behavior of the variable-stiffness cylinder.

The geometric imperfections of the baseline cylinder and the variable-stiffness cylinder were similar in shape and magnitude. The variable-stiffness cylinder was expected to have larger imperfections due to thermal residual stresses caused by non-uniform coefficients of thermal expansion during cool-down of the cylinder after curing. A thermal analysis including chemical shrinkage, tool-part interaction and thermal shrinkage during cool-down to simulate the curing process could provide more information about geometric imperfections introduced by the curing process and about thermal residual stresses. The similarity of the geometric imperfections of both cylinders could be caused by an imperfectly shaped mandrel. This could be examined by measuring the mandrel or by manufacturing more specimen on the same mandrel, while marking the position of the part with respect to the mandrel.

Strains were measured using strain gauges and the DIC system. The measured strains showed a good agreement with the predicted strains. The DIC data was useful, because it provided a view of the strain field instead of local strain data as collected by the strain gauges. One DIC system covered approximately a quarter of the cylinder surface, such that different sides of the cylinder had to be measured in different test runs. A possible

improvement compared to the current setup would be to use 4 DIC systems simultaneously, such that the complete cylinder surface could be measured at once. This would also improve the geometric imperfection measurements of the cylinder in the test setup and it would enable calculation of complete cylinder deformations such as ovalization.

The current cylinders were not loaded until failure, because the cylinders were expected to fail in bearing at the cylinder-fixture interface before they would buckle. The bearing failure predictions were based on the predicted load level in tension for the variable-stiffness cylinder and an estimated bearing strength of the variable-stiffness laminate in this location. It was decided not to load the cylinders to failure to avoid bearing failure. A future test of the cylinders with damage or a cutout on the compression side is planned to lower the failure load such that the cylinders will fail in the test section and not at the interface. The test data can then be compared to strength and progressive failure simulations. Thinner laminates are recommended for future variable-stiffness composite structure tests to avoid the possibility of failure at the structure-fixture interface.

The global response and the strain distributions of the baseline and the variable-stiffness cylinder were correctly predicted by the finite element model. The strain distributions showed that the maximum tensile and compressive strains of the variable-stiffness cylinder were lower than those of the baseline cylinder at identical load levels, which is advantageous if strain-based strength criteria are used as a measure of performance.

The values of the buckling moment of the baseline and the variable-stiffness cylinder were negatively affected by the flexible boundary conditions, inclusion of the geometric imperfections and the nonlinear analysis, compared to the initially predicted values. The relative improvement of the variable-stiffness cylinder compared to the baseline cylinder was not affected by the different conditions used in the finite element model and remained in the order of 18 percent at equal mass.

## 9.7 Remaining Challenges

The research on variable-stiffness laminates discussed in this thesis covers only a small part of the work that needs to be done before variable-stiffness composite laminates can be applied to real aerospace structures. One of the big hurdles for the application of any new material system or structural concept is certification. Certification of composite laminates is currently based on allowables databases, generated through extensive test programs. A different approach would be needed for the certification of variable-stiffness laminates, because it is impossible to build a database that covers all possible stacking sequences that could be generated within one variable-stiffness laminate. Strength properties could, for example, be based on general laminate parameters, such as equivalent stiffness values, lamination parameters or components of the ABD matrices. In addition, the effect of factors such as path curvature, tow width and coverage parameter could be taken into account. Certification through analysis, substantiated by test results, would be critical for the certification of variable-stiffness laminates because of the prohibitive amount of testing involved in building an allowables database that covers all possible cases. Certification of structures containing variable-stiffness composite laminates might, as a consequence, require more component-level tests.

An other aspect that requires investigation before variable-stiffness composites can be

applied to real-life aerospace structures is damage modeling of variable-stiffness composites under quasi-static and impact loading. Reliably modeling the initiation and progression of damage in traditional fiber-reinforced composite laminates already forms a challenge to the engineering community and the curved fibers, tow drops, and overlaps of variable-stiffness laminates add even more to the models' complexity. Reliable damage models will also aid in determining the damage tolerance and reparability of variable-stiffness laminates.

Shorter-term applications of variable-stiffness laminates might be found in spacecraft, where structures are more often driven by stiffness requirements than by strength requirements. It was shown in this thesis that stiffness and mass properties of variable-stiffness laminates can be accurately predicted. In addition, variable-stiffness laminates might be used to tailor the coefficient of thermal expansion in space structure to smoothen the transition between different structural parts and thereby minimize thermally induced stresses.

## 9.8 Final Conclusions

The contributions to the state-of-the-art in the field of fiber-placed, variable-stiffness composites of the research presented in this thesis are summarized below.

The application of variable-stiffness composite laminates was expanded from flat panels to conical and cylindrical shells. Mathematical expressions were derived to define fiber paths with varying fiber angles to generate variable-stiffness laminates using advanced fiber placement, and to determine the laminate stacking sequence as function of location.

For the first time composite conical and cylindrical shells were optimized for maximum fundamental frequency by actively tailoring the laminate stiffness as function of the in-plane coordinates. The fundamental frequency of conical and cylindrical shells increased up to 30 percent using laminates with a stiffness variation in the axial direction compared to a constant-stiffness laminate, while having equal mass. Allowing more variation of the fiber orientation angle is expected to yield even higher improvements.

A laminate stiffness variation in the circumferential direction of a cylindrical shell was shown to be beneficial for the structural performance of the cylinder loaded in bending. The optimization results confirmed the findings of Tatting (1998), namely, that a circumferential stiffness variation can alter the internal load distribution around the circumference such that the loads are carried more effectively, i.e. compressive loads are relieved and buckling patterns can be altered, leading to a higher buckling load carrying capability. New in this work compared to that of Tatting (1998), but similar to the work on flat panels, is the inclusion of features introduced by the fiber placement process and design method, for example, the deviation of the fiber orientation within a course, the possibility of overlaps, and the introduction of a minimum fiber orientation to avoid excessive tow cutting or extreme amounts of overlaps.

The optimization of a 24-ply, 609 mm diameter variable-stiffness composite cylinder subjected to bending showed an 18 percent improvement in buckling load carrying capability compared to an optimized baseline laminate consisting of 0, 90, and  $\pm 45^\circ$  plies with equal mass. Manufacturing constraints, a strength constraint, and stiffness constraints were included in the optimization. Strain levels within the variable-stiffness laminate were also reduced compared to those of the baseline laminate, indicating an improvement in strength. The higher buckling load carrying capability and the lower strain levels show that there is

potential for weight reduction using variable-stiffness laminates.

Variable-stiffness laminates with overlaps increased the buckling load of a cylinder loaded in bending by an increase in thickness on the compression side of the cylinder. The laminate thickness increased with smaller fiber angles, coupling the in-plane and out-of-plane laminate stiffnesses. The high in-plane laminate stiffness attracted loads to the compression side, but due to the larger increase in bending stiffness the buckling load carrying capability of the variable-stiffness cylinder was increased. Ideally, the amount of overlap would be uncoupled from the fiber orientation, such that the out-of-plane laminate stiffness can be tailored independently from the in-plane laminate stiffness. This would require a different design method for variable-stiffness laminates.

The manufacturing of the variable-stiffness composite cylinder revealed that cutting tows on the outside of a curved course can result in straightened tows. This problem could be resolved by changing the detailed design for manufacturing or by adjusting the fiber placement machine.

A modal test of a variable-stiffness cylinder showed good agreements between the experimental and analytical results, which indicated that the mass and stiffness distribution of the variable-stiffness composite was correctly modeled using finite elements. This was the first modal test of a fiber-placed, variable-stiffness composite structure.

Finally, a structural bending test was performed to verify the structural behavior of the variable-stiffness cylinder under bending in the form of a strain survey. Two cylinders with a baseline laminate were also tested to serve as a reference. The experimental results showed a good agreement with the finite element model. This model differed from the initial finite element model used for optimization, because it included flexible boundary conditions, geometric imperfections, and a nonlinear pre-buckling analysis, as opposed to a linear bifurcation analysis with clamped boundary conditions. The improvement in buckling load carrying capability of the variable-stiffness cylinder compared to that of the baseline was not affected by the different model and remained in the order of 18 percent. The test results confirmed the favorable strain distribution of the variable-stiffness cylinder compared to that of the baseline. The bending test was the first experimental verification of a fiber-placed, variable-stiffness composite cylinder.

## Appendix A

# Derivation of the Curvature Vector

The curvature vector is defined by:

$$\vec{\kappa} = \frac{d\hat{\tau}}{dl} = \frac{d\hat{\tau}}{dx} \frac{dx}{dl}. \quad (\text{A.1})$$

Starting from equation 3.6 and using the chain rule, the expression for  $\frac{d\hat{\tau}}{dx}$  can be expressed as follows:

$$\frac{d\hat{\tau}}{dx} = -\sin\varphi \frac{d\varphi}{dx} \hat{a} + \cos\varphi \frac{d\hat{a}}{dx} + \cos\varphi \frac{d\varphi}{dx} \hat{c} + \sin\varphi \frac{d\hat{c}}{dx} \quad (\text{A.2})$$

The derivatives of the vectors  $\hat{a}$  and  $\hat{c}$  with respect to  $x$  are found by using the following transformations, where  $\hat{i}$ ,  $\hat{j}$  and  $\hat{k}$  are the unit vectors along the  $X$ ,  $Y$  and  $Z$  axis respectively:

$$\begin{Bmatrix} \hat{a} \\ \hat{c} \\ \hat{n} \end{Bmatrix} = \begin{bmatrix} \cos\alpha & \sin\alpha \sin\theta & \sin\alpha \cos\theta \\ 0 & \cos\theta & -\sin\theta \\ -\sin\alpha & \cos\alpha \sin\theta & \cos\alpha \cos\theta \end{bmatrix} \begin{Bmatrix} \hat{i} \\ \hat{j} \\ \hat{k} \end{Bmatrix} = [T] \begin{Bmatrix} \hat{i} \\ \hat{j} \\ \hat{k} \end{Bmatrix} \quad (\text{A.3})$$

Then:

$$\frac{d}{dx} \begin{Bmatrix} \hat{a} \\ \hat{c} \\ \hat{n} \end{Bmatrix} = \frac{d}{dx} [T] \begin{Bmatrix} \hat{i} \\ \hat{j} \\ \hat{k} \end{Bmatrix} = \frac{d}{dx} [T] [T]^{-1} \begin{Bmatrix} \hat{a} \\ \hat{c} \\ \hat{n} \end{Bmatrix} \quad (\text{A.4})$$

So that

$$\begin{aligned} \frac{d\hat{a}}{dx} &= \sin\alpha \frac{d\theta}{dx} \hat{c} \\ \frac{d\hat{c}}{dx} &= -\sin\alpha \frac{d\theta}{dx} \hat{a} - \cos\alpha \frac{d\theta}{dx} \hat{n} \end{aligned} \quad (\text{A.5})$$

Substituting this in equation A.2 results in:

$$\frac{d\hat{\tau}}{dx} = -\left(\frac{d\varphi}{dx} + \sin\alpha \frac{d\theta}{dx}\right) \sin\varphi \hat{a} + \left(\frac{d\varphi}{dx} + \sin\alpha \frac{d\theta}{dx}\right) \cos\varphi \hat{c} - \cos\alpha \sin\varphi \frac{d\theta}{dx} \hat{n} \quad (\text{A.6})$$

Combining this equation with  $\frac{dx}{dl} = \cos \varphi$  results in the following expression for equation A.1:

$$\vec{\kappa} = -\left(\frac{d\varphi}{dx} + \sin \alpha \frac{d\theta}{dx}\right) \sin \varphi \cos \varphi \hat{a} + \left(\frac{d\varphi}{dx} + \sin \alpha \frac{d\theta}{dx}\right) \cos \varphi^2 \hat{c} - \cos \alpha \sin \varphi \cos \varphi \frac{d\theta}{dx} \hat{n} \quad (\text{A.7})$$

This equation can be simplified by expressing it in the surface coordinates  $\hat{\xi}$  and  $\hat{\tau}$  and  $\hat{n}$ , which are the in-plane path normal and tangent and out-of-plane normal vectors, respectively. The corresponding coordinate transformation is given by:

$$\begin{Bmatrix} \hat{a} \\ \hat{c} \\ \hat{n} \end{Bmatrix} = \begin{bmatrix} \cos \varphi & -\sin \varphi & 0 \\ \sin \varphi & \cos \varphi & 0 \\ 0 & 0 & 1 \end{bmatrix} \begin{Bmatrix} \hat{\tau} \\ \hat{\xi} \\ \hat{n} \end{Bmatrix} \quad (\text{A.8})$$

such that:

$$\vec{\kappa} = \left[ \frac{d\varphi}{dx} \cos \varphi + \frac{\sin \alpha \sin \varphi}{r(x)} \right] \hat{\xi} + \left[ \frac{-\cos \alpha \sin^2 \varphi}{r(x)} \right] \hat{n} \quad (\text{A.9})$$

If the fiber orientation is defined as a function of the circumferential coordinate  $\theta$  the above equation can be rewritten as a function of  $\theta$  by using equation 3.5:

$$\frac{d\varphi}{dx} \cos \varphi = \frac{d\varphi}{d\theta} \frac{d\theta}{dx} \cos \varphi = \frac{d\varphi}{d\theta} \frac{\tan \varphi}{r(x)} \cos \varphi = \frac{d\varphi}{d\theta} \frac{\sin \varphi}{r(x)} \quad (\text{A.10})$$

Then the curvature vector becomes:

$$\vec{\kappa} = \left[ \left( \frac{d\varphi}{d\theta} + \sin \alpha \right) \frac{\sin \varphi}{r(x)} \right] \hat{\xi} + \left[ \frac{-\cos \alpha \sin^2 \varphi}{r(x)} \right] \hat{n} \quad (\text{A.11})$$

## Appendix B

# Derivation of the Constant Curvature Path for Conical Shells

First, the curvature equation is given by:

$$\kappa(x) = \frac{d\varphi}{dx} \cos \varphi(x) + \frac{\sin \alpha \sin \varphi(x)}{r(x)} \quad (\text{B.1})$$

Substitution of the intermediate variable  $u = r(x) \sin \varphi(x)$  results in the following differential equation, which can also be expressed in terms of radial coordinates to aid in integration:

$$\begin{aligned} \frac{du}{dx} &= \sin \alpha \sin \varphi + r(x) \cos \varphi \frac{d\varphi}{dx} = \kappa(x)r(x) \\ &\quad \downarrow \\ \frac{du}{dr} &= \frac{du}{dx} \frac{dx}{dr} = \frac{\kappa(r)r}{\sin \alpha} \end{aligned} \quad (\text{B.2})$$

Assuming an unknown constant value of the curvature, integration is performed for  $u$  resulting in:

$$u(r) = \frac{\kappa r^2}{2 \sin \alpha} + C \quad (\text{B.3})$$

Performing back-substitution, the equation for the orientation angle becomes:

$$\sin \varphi(x) = \frac{\kappa}{\sin \alpha} \left( \frac{r(x)^2}{2} + C \right) / r(x) \quad (\text{B.4})$$

The unknown constant  $C$  is found by stipulating the orientation angle at the small radius  $T_0$ , while the constant curvature value remains unevaluated at this time. This results in the following equation for a constant curvature path:

$$\sin \varphi(x) = \frac{r_0 \sin T_0}{r(x)} + \frac{\kappa}{\sin \alpha} \left( \frac{r(x)^2 - r_0^2}{2r(x)} \right) = \frac{s_0 \sin T_0}{s} + \kappa \left( \frac{s^2 - s_0^2}{2s} \right) \quad (\text{B.5})$$

Dividing the latter of (B.1) by  $\cos \varphi$ , substituting for  $\tan \varphi$  in terms of  $\frac{d\theta}{dx}$ , and subsequently replacing  $\{x, \theta\}$  with the variables  $\{s, \beta\}$ , the equation for the path definition can be expressed as:

$$\frac{d\varphi}{dx} + \sin \alpha \frac{d\theta}{dx} = \frac{\kappa}{\cos \varphi} \quad \text{or} \quad d\varphi + d\beta = \frac{\kappa ds}{\cos \varphi} \quad (\text{B.6})$$

This last equation is the analog of (3.49), using the two-dimensional configuration variables  $s$  and  $\beta$ . It is evident that the introduction of a non-zero curvature renders the equation difficult to integrate. Instead, a useful path in the two-dimensional configuration will be assumed and the derivations will proceed in the other direction toward the curvature equation. The geodesic path satisfies a linear relationship as given by  $y^* = x^* \tan T_0$ . This equation is used as a basis for the constant curvature paths. A constant curvature path on the three-dimensional structure is assumed to translate directly into a similar arc in the flattened configuration. This assumption is based on the fact that the lengths remain the same in both configurations, as seen in the equations of (3.4). A curve of constant curvature  $\kappa$ , based on the rotated rectangular coordinates of the unrolled configuration, is expressed as

$$(x^* - x_c^*)^2 + (y^* - y_c^*)^2 = \rho^2 \quad \text{or} \quad y^* \cos T_0 - x^* \sin T_0 = \frac{\kappa}{2}(x^{*2} + y^{*2}) \quad (\text{B.7})$$

The first equation is derived from figure B.1. The point  $\{x_c^*, y_c^*\}$  in this equation represents the center of rotation of the circular arc that describes the fiber path. The equation for this curve is then translated into polar coordinates for the unrolled system, and expressed in a suitable form:

$$\cos T_0 \sin(\beta - \beta_0) - (\sin T_0 - \kappa s_0) \cos(\beta - \beta_0) = -\frac{s_0 \sin T_0}{s} + \kappa \left( \frac{s^2 + s_0^2}{2s} \right) = f \quad (\text{B.8})$$

Note that the left hand side only depends on  $\beta$ , while the right side is solely a function of  $s$ . This function will be referred to as  $f$ . Taking derivatives with respect to  $s$ , substituting for the orientation angle using (3.5), and simplifying the result yields:

$$[(\cos T_0) \cos(\beta - \beta_0) + (\sin T_0 - \kappa s_0) \sin(\beta - \beta_0)] \tan \varphi \equiv g \tan \varphi = \kappa s - f \quad (\text{B.9})$$

Note that again the function  $g$  is defined for brevity and that it is only a function of  $\beta$ . Equation B.9 represents the definition of the orientation angle in polar coordinates, which can be easily transferred to conical shell coordinates  $\{x, \theta\}$  through the usual transformations. However, some simplification can be performed first to illustrate the solution. Akin to the result displayed in (B.5), it is desirable to develop a solution for  $\sin \varphi$  for comparison purposes. This is most easily accomplished by combining (B.8) and (B.9) in the following manner:

$$\begin{aligned} g \tan \varphi = \kappa s - f & \Rightarrow \sin \varphi = \frac{\kappa s - f}{\sqrt{g^2 + (\kappa s - f)^2}} \\ g^2 + (\kappa s - f)^2 &= g^2 + f^2 + 2\kappa s_0 \sin T_0 - (\kappa s_0)^2 = 1 \\ & \Downarrow \\ \sin \varphi &= \kappa \left( \frac{s^2 - s_0^2}{2s} \right) + \frac{s_0 \sin T_0}{s} \end{aligned} \quad (\text{B.10})$$



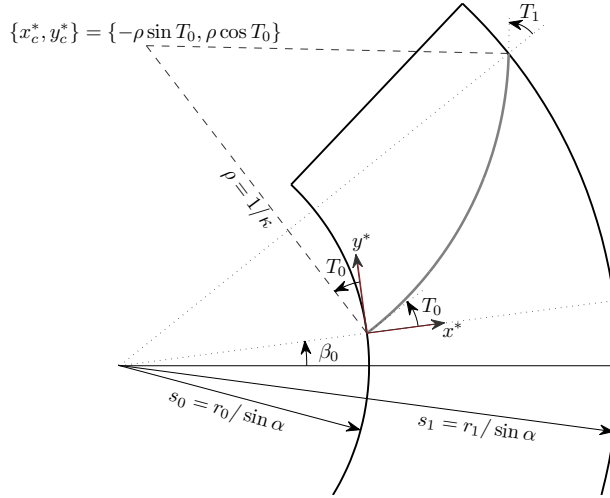


Figure B.1: 2D representation of the constant curvature path

As aimed for, this equation agrees exactly with the derivation based on integrating backwards from an assumed constant turning radius path on a conical shell surface, equation B.5. Therefore, the equations have shown that a constant curvature path in the unrolled configuration corresponds exactly to a constant turning radius path on the conical shell. Now the expressions for the fiber angle and the fiber path are found, it is useful to evaluate the value of the curvature  $\kappa$  as function of the orientation angles at the small and large radius of the cone ( $T_0$  and  $T_1$ , respectively). Therefore, if the desired fiber angle at the large radius is given a value  $T_1$ , equation B.5 yields:

$$\varphi(L) = T_1 \quad \Rightarrow \quad \kappa = \frac{r_1 \sin T_1 - r_0 \sin T_0}{L \left( \frac{r_1 + r_0}{2} \right)} \quad (\text{B.11})$$

Rearranging the equation for the orientation angle in terms of  $x$  and expressing it so that all values of the cone angle are immediately apparent yields the following equations for the curvature and fiber angle for the constant curvature path on a conical shell surface:

Curvature:	$\kappa = \left( \frac{r_1}{\bar{r}} \sin T_1 - \frac{r_0}{\bar{r}} \sin T_0 \right) \frac{1}{L} \quad \left[ \bar{r} = \frac{r_0 + r_1}{2} \right]$
Angle variation:	$\sin \varphi = \frac{r_0}{r(x)} \sin T_0 + \left( \frac{r_1}{\bar{r}} \sin T_1 - \frac{r_0}{\bar{r}} \sin T_0 \right) \frac{x}{L} \left[ 1 - \frac{x \sin \alpha}{2r(x)} \right]$

(B.12)



# Appendix C

## The Effect of Course Width Variation

The effective course width,  $w_e$ , depends on the fiber angle variation, as was explained in section 3.3.3. This can cause problems if the variation in fiber orientation is large. An explanation of these problems for constant-thickness laminates and overlap laminates will be given below.

### Course Width Variation for a Constant-Thickness Laminate

The effective course width should be constant for a constant-thickness laminate and equal to the course shift,  $\Delta x$ . This requires the width of the course,  $w$ , to vary accordingly, as shown in figure C.1.

The relation between the course width  $w$  and the effective course width  $w_e$  for the circumferential angle variation can be derived similar to the example in section 3.3.2. An approximation of the effective course width for the circumferential angle variation is:

$$w_e \approx \frac{w}{\sin \varphi} \quad (\text{C.1})$$

If the effective course width needs to be constant, the course width  $w$  is defined by the fiber angle  $\varphi$ :

$$w \approx w_e \sin \varphi \quad (\text{C.2})$$

The maximum course width that a fiber placement machine can lay down is 102 mm, or 32 tows. The minimum course width is determined by the ratio between the largest and the smallest fiber angle within a course:

$$\frac{w_{\min}}{w_{\max}} \approx \frac{w_e \sin \varphi_{\min}}{w_e \sin \varphi_{\max}} \quad (\text{C.3})$$

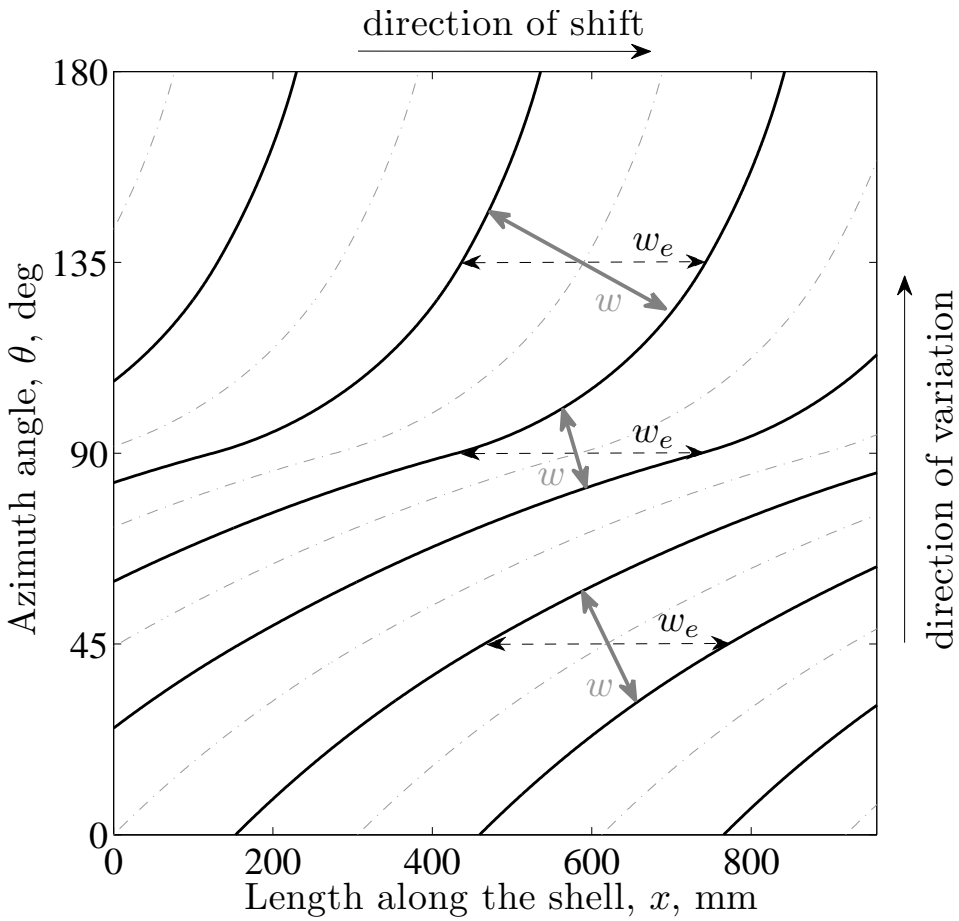


Figure C.1: Variation of the course width for a constant-thickness ply

Assuming the maximum fiber angle is  $90^\circ$ , the minimum course width becomes:

$$w_{\min} \approx w_{\max} \sin \varphi_{\min} \tag{C.4}$$

The course width becomes smaller than 18 mm, or less than 6 tows wide, if  $\varphi$  is smaller than  $10^\circ$ . In practice this would cause a large number of tow drops to occur in this region, which is undesirable from a strength point of view. Placing a small number of tows at a time also increases the production time, which is not desired either. Therefore manufacturing efficiency requires the fiber angle orientation to be at least  $10^\circ$ .

### Thickness Buildup

The course width is kept constant during the production of overlap laminates and courses within one ply are allowed to overlap. The amount of overlap  $O$  depends on the ratio be-

tween the largest effective course width and the smallest effective course width:

$$O = \frac{w_{e,\max}}{w_{e,\min}} \approx \frac{w \sin \varphi_{\max}}{w \sin \varphi_{\min}} \approx \frac{1}{\sin \varphi_{\min}} \quad (\text{C.5})$$

The overlap will be 5.8 if the largest fiber angle is  $90^\circ$  and the smallest fiber angle  $\varphi$  is  $10^\circ$ , which means that at some locations the ply will be 6 layers thick due to overlapping courses. The ply would locally be 12 layers thick if the smallest fiber angle is  $5^\circ$ , and at a minimum fiber angle of  $1^\circ$  it would be 58 layers thick. The overlap is smaller if the maximum fiber angle is smaller than  $90^\circ$ , but if for example  $\varphi_{\max} = 45^\circ$  and  $\varphi_{\min} = 1^\circ$ , the thickest part of the ply would be 40 layers thick. Allowing such a thickness variation within one ply would be undesirable in practice and therefore the smallest allowed fiber angle was set to  $10^\circ$ .



# Appendix D

## Bending Optimization Results

### Constant Thickness Laminates

#### Optimization Case 1

Table D.1: Optimum ply angles for constant-stiffness laminates, case 1

Laminate	$\phi_1$ ( $^\circ$ )	$\phi_2$ ( $^\circ$ )	$\phi_3$ ( $^\circ$ )	$\phi_4$ ( $^\circ$ )	$\phi_5$ ( $^\circ$ )
CS-1	8.4	41.1	89.8	73.1	48.0
CS-2	25.5	-	48.7	-	75.8
CS-3	-	42.5	-	66.6	-

Table D.2: Design variables for laminate VS-2, case 1

Ply	$T_0$ ( $^\circ$ )	$T_1$ ( $^\circ$ )	$T_2$ ( $^\circ$ )	$T_3$ ( $^\circ$ )	$T_4$ ( $^\circ$ )
$\varphi_1(\theta)$	1.0	1.0	1.0	27.0	67.9
$\varphi_3(\theta)$	1.0	3.1	1.0	41.7	72.3
$\varphi_5(\theta)$	1.0	8.4	1.0	76.3	64.9

Table D.3: Design variables for laminate VS-3, case 1

Ply	$T_0$ ( $^\circ$ )	$T_1$ ( $^\circ$ )	$T_2$ ( $^\circ$ )	$T_3$ ( $^\circ$ )	$T_4$ ( $^\circ$ )
$\varphi_2(\theta)$	1.0	1.0	1.0	27.5	61.8
$\varphi_4(\theta)$	1.0	6.3	1.0	39.5	66.2

Table D.4: Design variables for laminate VS-4, case 1

Ply	$T_0$ (°)	$T_1$ (°)	$T_2$ (°)	$T_3$ (°)	$T_4$ (°)
$\varphi_1(\theta)$	1.0	1.0	84.7	85.9	84.0
$\varphi_2(\theta)$	1.0	17.7	1.0	53.1	63.4

Table D.5: Design variables for laminate VS-5, case 1

Ply	$T_0$ (°)	$T_1$ (°)	$T_2$ (°)	$T_3$ (°)	$T_4$ (°)
$\varphi_1(\theta)$	1.0	1.5	37.1	71.0	77.3

## Optimization Case 2

Table D.6: Optimum ply angles for constant-stiffness laminates, case 2

Laminate	$\phi_1$ (°)	$\phi_2$ (°)	$\phi_3$ (°)	$\phi_4$ (°)	$\phi_5$ (°)
CS-1	26.0	30.2	10.7	90	74.4
CS-2	25.8	-	35.7	-	79.1
CS-3	-	35.5	-	63.3	-

Table D.7: Design variables for laminate VS-1, case 2

Ply	$T_0$ (°)	$T_1$ (°)	$T_2$ (°)	$T_3$ (°)	$T_4$ (°)
$\varphi_1(\theta)$	10.0	10.0	10.0	10.2	10.0
$\varphi_2(\theta)$	10.0	10.0	10.0	10.0	16.5
$\varphi_3(\theta)$	10.0	10.0	46.0	49.5	44.0
$\varphi_4(\theta)$	10.0	10.0	10.0	10.0	56.8
$\varphi_5(\theta)$	10.0	16.0	60.6	88.9	89.0

Table D.8: Design variables for laminate VS-2, cases 2 and 3

Ply	$T_0$ (°)	$T_1$ (°)	$T_2$ (°)	$T_3$ (°)	$T_4$ (°)
$\varphi_1(\theta)$	10.0	10.0	10.0	10.0	15.4
$\varphi_3(\theta)$	10.0	10.0	11.2	45.3	63.4
$\varphi_5(\theta)$	10.0	10.0	10.0	10.0	57.1



Table D.9: Design variables for laminate VS-3, cases 2 and 3

Ply	$T_0$ (°)	$T_1$ (°)	$T_2$ (°)	$T_3$ (°)	$T_4$ (°)
$\varphi_2(\theta)$	10.0	10.0	10.2	18.8	38.4
$\varphi_4(\theta)$	10.0	10.0	10.0	26.7	55.5

Table D.10: Design variables for laminate VS-4, case 2

Ply	$T_0$ (°)	$T_1$ (°)	$T_2$ (°)	$T_3$ (°)	$T_4$ (°)
$\varphi_1(\theta)$	10.0	10.0	10.0	10.0	27.0
$\varphi_2(\theta)$	10.0	10.0	56.3	74.2	89.0

Table D.11: Design variables for laminate VS-5, case 2

Ply	$T_0$ (°)	$T_1$ (°)	$T_2$ (°)	$T_3$ (°)	$T_4$ (°)
$\varphi_1(\theta)$	10.0	10.2	10.0	27.3	35.6

### Optimization Case 3

Table D.12: Optimum ply angles for constant-stiffness laminates, case 3

Laminate	$\phi_1$ (°)	$\phi_2$ (°)	$\phi_3$ (°)	$\phi_4$ (°)	$\phi_5$ (°)
CS-1	4.0	44.5	0	88.8	55.5
CS-2	22.1	-	30.2	-	70.5
CS-3	-	25.5	-	53.8	-

Table D.13: Design variables for laminate VS-1, case 3

Ply	$T_0$ (°)	$T_1$ (°)	$T_2$ (°)	$T_3$ (°)	$T_4$ (°)
$\varphi_1(\theta)$	10.0	10.0	10.0	10.0	10.0
$\varphi_2(\theta)$	10.0	10.0	10.0	10.0	10.0
$\varphi_3(\theta)$	70.2	75.4	89.0	89.0	89.0
$\varphi_4(\theta)$	10.0	10.0	10.0	10.0	59.1
$\varphi_5(\theta)$	10.0	10.0	10.0	35.2	61.2

## Overlap Laminates

### Optimization Case 1

Table D.14: Design variables for laminate VS<sup>o</sup>-1, case 1

Ply	$T_0$ (°)	$T_1$ (°)	$T_2$ (°)	$T_3$ (°)	$T_4$ (°)
$\varphi_1(\theta)$	10.0	25.0	85.0	10.0	10.0
$\varphi_2(\theta)$	89.0	80.0	85.0	10.0	10.0
$\varphi_3(\theta)$	10.0	36.9	89.0	10.0	10.0
$\varphi_4(\theta)$	62.8	89.0	89.0	10.0	10.0
$\varphi_5(\theta)$	10.0	36.9	89.0	10.0	10.0

Table D.15: Design variables for laminate VS<sup>o</sup>-2, case 1

Ply	$T_0$ (°)	$T_1$ (°)	$T_2$ (°)	$T_3$ (°)	$T_4$ (°)
$\varphi_1(\theta)$	10.3	89.0	87.4	10.0	10.0
$\varphi_3(\theta)$	10.0	31.1	89.0	10.0	10.0
$\varphi_5(\theta)$	22.8	89.0	89.0	10.0	10.0

Table D.16: Design variables for laminate VS<sup>o</sup>-3, case 1

Ply	$T_0$ (°)	$T_1$ (°)	$T_2$ (°)	$T_3$ (°)	$T_4$ (°)
$\varphi_2(\theta)$	10.0	28.5	89.0	10.0	10.0
$\varphi_4(\theta)$	89.0	87.8	89.0	10.0	10.0

Table D.17: Design variables for laminate VS<sup>o</sup>-4, case 1

Ply	$T_0$ (°)	$T_1$ (°)	$T_2$ (°)	$T_3$ (°)	$T_4$ (°)
$\varphi_1(\theta)$	10.0	36.9	89.0	10.0	10.0
$\varphi_2(\theta)$	62.8	89.0	89.0	10.0	10.0

## Optimization Case 2

*Table D.18: Design variables for laminate VS<sup>o</sup>-2, case 2*

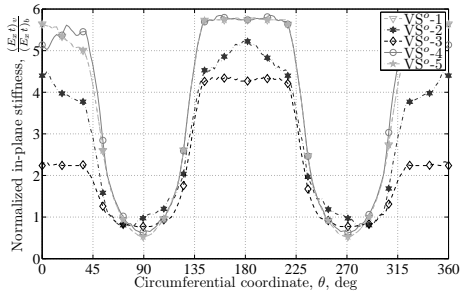
Ply	$T_0$ ( $^\circ$ )	$T_1$ ( $^\circ$ )	$T_2$ ( $^\circ$ )	$T_3$ ( $^\circ$ )	$T_4$ ( $^\circ$ )
$\varphi_1(\theta)$	10.0	10.0	59.1	10.0	10.0
$\varphi_3(\theta)$	10.0	58.6	24.8	16.2	10.0
$\varphi_5(\theta)$	10.0	10.0	57.4	11.9	10.0

*Table D.19: Design variables for laminate VS<sup>o</sup>-3, case 2*

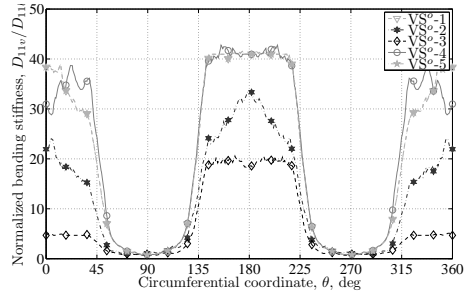
Ply	$T_0$ ( $^\circ$ )	$T_1$ ( $^\circ$ )	$T_2$ ( $^\circ$ )	$T_3$ ( $^\circ$ )	$T_4$ ( $^\circ$ )
$\varphi_2(\theta)$	10.6	10.6	58.1	10.0	10.0
$\varphi_4(\theta)$	87.8	86.8	58.8	10.0	10.0

*Table D.20: Design variables for laminate VS<sup>o</sup>-4, case 2*

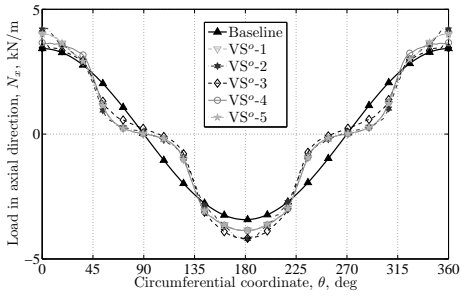
Ply	$T_0$ ( $^\circ$ )	$T_1$ ( $^\circ$ )	$T_2$ ( $^\circ$ )	$T_3$ ( $^\circ$ )	$T_4$ ( $^\circ$ )
$\varphi_1(\theta)$	10.0	10.0	30.2	10.0	10.0
$\varphi_2(\theta)$	12.3	10.0	49.1	10.0	10.0



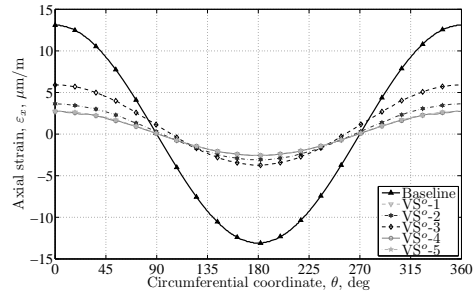
(a) In-plane laminate stiffness



(b) Laminate bending stiffness



(c) Load in axial direction



(d) Axial strains

Figure D.1: Optimization results for all variable-stiffness cylinders with overlap, optimization case 2

## Appendix E

# Strain-Equivalent Tsai-Wu Strength Constraint

The strain-equivalent Tsai-Wu strength constraint was developed by IJsselmuident et al. (2008). Here a summary of the derivation and use of the constraint in an optimization environment is given. The constraint was used in the cylinder optimization in chapter 5.

The Tsai-Wu failure criterion Jones (1999) is a first-ply failure criterion which is based on both material properties and explicit ply angles. IJsselmuident rewrote the criterion to derive a failure envelope based on the Tsai-Wu criterion which is independent of the stacking sequence and can be expressed in terms of strains. The Tsai-Wu failure criterion is defined by:

$$F_{11}\sigma_1^2 + F_{22}\sigma_2^2 + F_{66}\tau_{12}^2 + F_1\sigma_1 + F_2\sigma_2 + 2F_{12}\sigma_1\sigma_2 = 1 \quad (\text{E.1})$$

in which  $F_i$  and  $F_{ij}$  are defined by:

$$\begin{aligned} F_{11} &= \frac{1}{X_t X_c} & F_{22} &= \frac{1}{Y_t Y_c} & F_1 &= \frac{1}{X_t} - \frac{1}{X_c} \\ F_2 &= \frac{1}{Y_t} - \frac{1}{Y_c} & F_{12} &= \frac{-1}{2\sqrt{X_t X_c Y_t Y_c}} & F_{66} &= \frac{1}{S^2} \end{aligned} \quad (\text{E.2})$$

where  $X_t$ ,  $X_c$ ,  $Y_t$ ,  $Y_c$  and  $S$  are the failure stresses in tension, compression and shear in the principle material directions. The strength criterion can be rewritten in terms of strain:

$$G_{11}\varepsilon_1^2 + G_{22}\varepsilon_2^2 + G_{66}\varepsilon_{12}^2 + G_1\varepsilon_1 + G_2\varepsilon_2 + 2G_{12}\varepsilon_1\varepsilon_2 = 1 \quad (\text{E.3})$$

with:

$$\begin{aligned} G_{11} &= Q_{11}^2 F_{11} + Q_{12}^2 F_{22} + 2F_{12}Q_{11}Q_{12} \\ G_{22} &= Q_{12}^2 F_{11} + Q_{22}^2 F_{22} + 2F_{12}Q_{12}Q_{22} \\ G_1 &= Q_{11}F_1 + Q_{12}F_2 \\ G_2 &= Q_{12}F_1 + Q_{22}F_2 \\ G_{12} &= Q_{11}Q_{12}F_{11} + Q_{12}Q_{22}F_{22} + F_{12}Q_{12}^2 + F_{12}Q_{11}Q_{22} \\ G_{66} &= 4Q_{66}^2 F_{66} \end{aligned} \quad (\text{E.4})$$

The material strains  $\varepsilon_1$ ,  $\varepsilon_2$  and  $\varepsilon_{12}$  can then be expressed in terms of laminate strains  $\varepsilon_x$ ,  $\varepsilon_y$  and  $\varepsilon_{xy}$  by using the following transformation matrix on equation E.3:

$$\begin{bmatrix} \frac{1}{2}(1 + \cos 2\varphi) & \frac{1}{2}(1 - \cos 2\varphi) & \sin 2\varphi \\ \frac{1}{2}(1 - \cos 2\varphi) & \frac{1}{2}(1 + \cos 2\varphi) & -\sin 2\varphi \\ \frac{1}{2}\sin 2\varphi & -\frac{1}{2}\sin 2\varphi & \cos 2\varphi \end{bmatrix} \quad (\text{E.5})$$

The failure envelope is expressed in terms of laminate strains and ply angles:

$$F(\varepsilon_x, \varepsilon_y, \varepsilon_{xy}, \sin 2\varphi, \cos 2\varphi) = 0 \quad (\text{E.6})$$

By setting the derivative of this equation with respect to the fiber orientation  $\varphi$  to zero the failure envelope can be found within which no failure occurs regardless of the fiber orientation angle (for the derivation see reference IJsselmuiden et al. (2008)). The result yields two equations, representing a surface traced out by the failure criterion for all ply orientations:

$$4u_6^2 I_2^2 - 4u_6 u_1 I_2^2 + 4(1 - u_2 I_1 - u_3 I_1^2)(u_1 - u_6) + (u_4 + u_5 I_1)^2 = 0 \quad (\text{E.7})$$

and

$$u_1^2 I_2^4 - I_2^2 (u_4 + u_5 I_1)^2 - 2u_1 I_2^2 (1 - u_2 I_1 - u_3 I_1^2) + (1 - u_2 I_1 - u_3 I_1^2)^2 = 0 \quad (\text{E.8})$$

where  $I_1$  is the volumetric strain invariant and  $I_2$  is the maximum shear strain given by:

$$I_1 = \varepsilon_x + \varepsilon_y \quad I_2 = \sqrt{\left(\frac{\varepsilon_x - \varepsilon_y}{2}\right)^2 + \varepsilon_{xy}^2} \quad (\text{E.9})$$

The terms  $u_i$  are defined by:

$$\begin{aligned} u_1 &= G_{11} + G_{22} - 2G_{12} & u_2 &= \frac{G_1 + G_2}{2} \\ u_3 &= \frac{G_{11} + G_{22} + 2G_{12}}{4} & u_4 &= G_1 - G_2 \\ u_5 &= G_{11} - G_{22} & u_6 &= G_{66} \end{aligned} \quad (\text{E.10})$$

Equations E.7 and E.7 can be reformulated in terms of the safety factor  $\lambda$ , which is defined as:

$$\lambda = \frac{P_f}{P_a} \quad (\text{E.11})$$

where  $P_f$  is the failure load and  $P_a$  is the applied load. If the safety factor is implemented in the two failure equations they become:

$$\begin{aligned} f_1(\lambda) &= a_{12}\lambda^2 + a_{11}\lambda + a_{10} \\ f_2(\lambda) &= a_{24}\lambda^4 + a_{23}\lambda^3 + a_{22}\lambda^2 + a_{21} + a_{20} \end{aligned} \quad (\text{E.12})$$

where the coefficients are defined by:

$$\begin{aligned}
 a_{10} &= u_4^2 + 4u_1 - 4u_6 \\
 a_{11} &= -4u_2I_1(u_1 - u_6) + 2u_4u_5I_1 \\
 a_{12} &= 4u_6^2I_2^2 - 4u_3I_1^2(u_1 - u_6) - 4u_6u_1I_2^2 + u_5^2I_1^2 \\
 a_{20} &= 1 \\
 a_{21} &= -2u_2I_1 \\
 a_{22} &= -2u_3I_1^2 + u_2^2I_1^2 - I_2^2(u_4^2 + 2u_1) \\
 a_{23} &= 2u_2I_1^3u_3 - I_2^2(2u_4u_5I_1 - 2u_1u_2I_1) \\
 a_{24} &= u_1^2I_2^4 - I_2^2(u_5^2I_1^2 - 2u_1u_3I_1^2) + u_3^2I_1^4
 \end{aligned} \tag{E.13}$$

The failure index  $r(\bar{\varepsilon})$  is defined by:

$$r(\bar{\varepsilon}) = \frac{1}{\lambda^2} \tag{E.14}$$

where  $\lambda$  is the smallest positive real root obtained from equation E.12. Using the failure index, the strength constraint can be defined as:

$$r(\bar{\varepsilon}) - 1 \leq 0 \tag{E.15}$$





# Appendix F

## Miscellaneous Modal Test Results

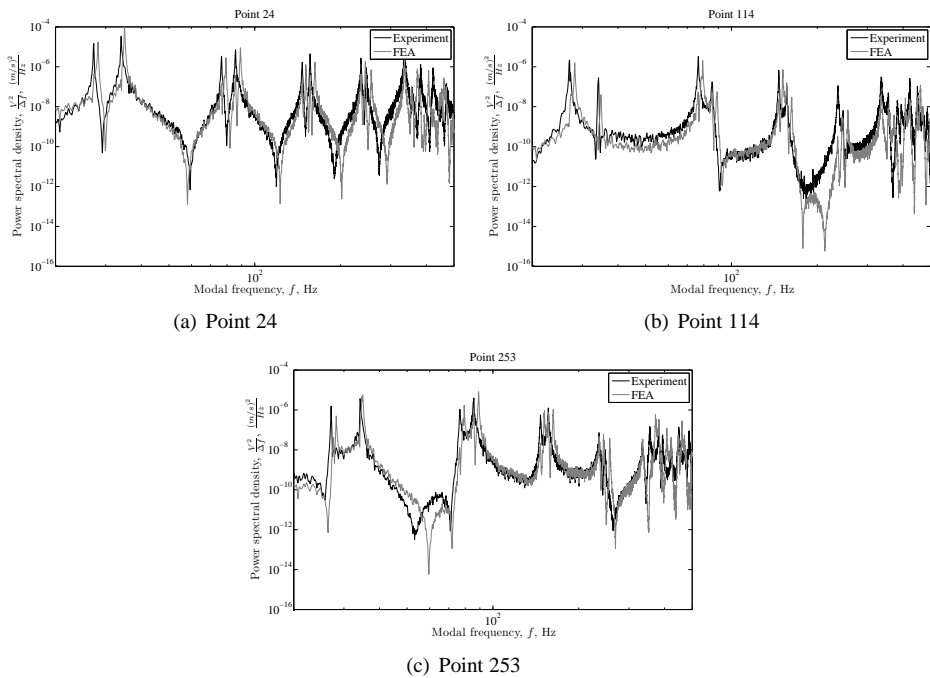


Figure F.1: Power spectral density for velocity of the steered cylinder

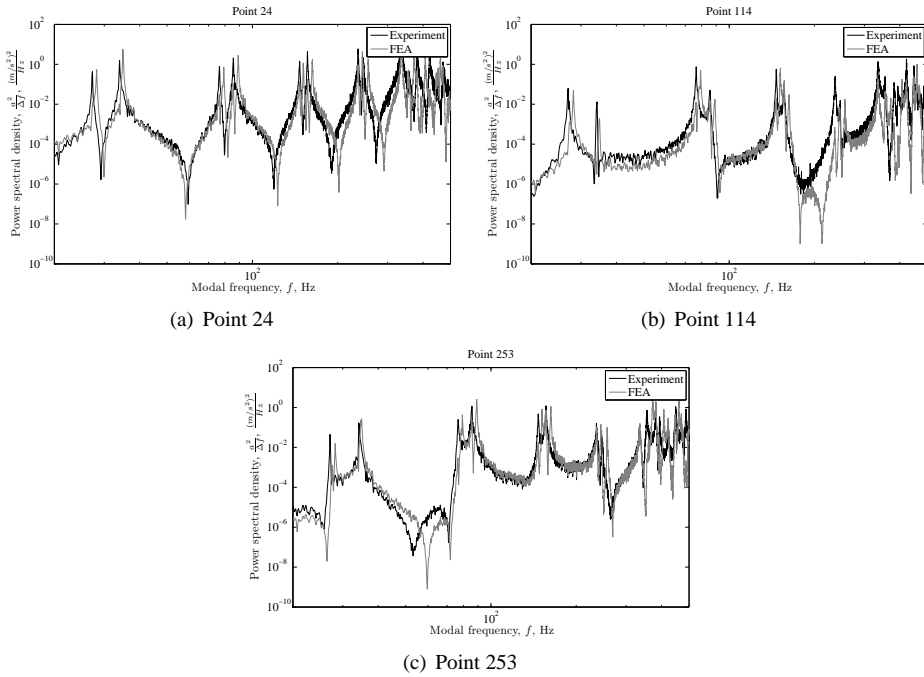


Figure F.2: Power spectral density for acceleration of the steered cylinder

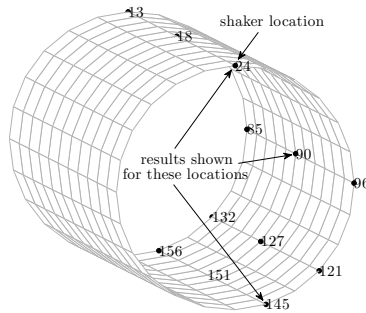


Figure F.3: Locations of points on the baseline cylinder for which responses are given

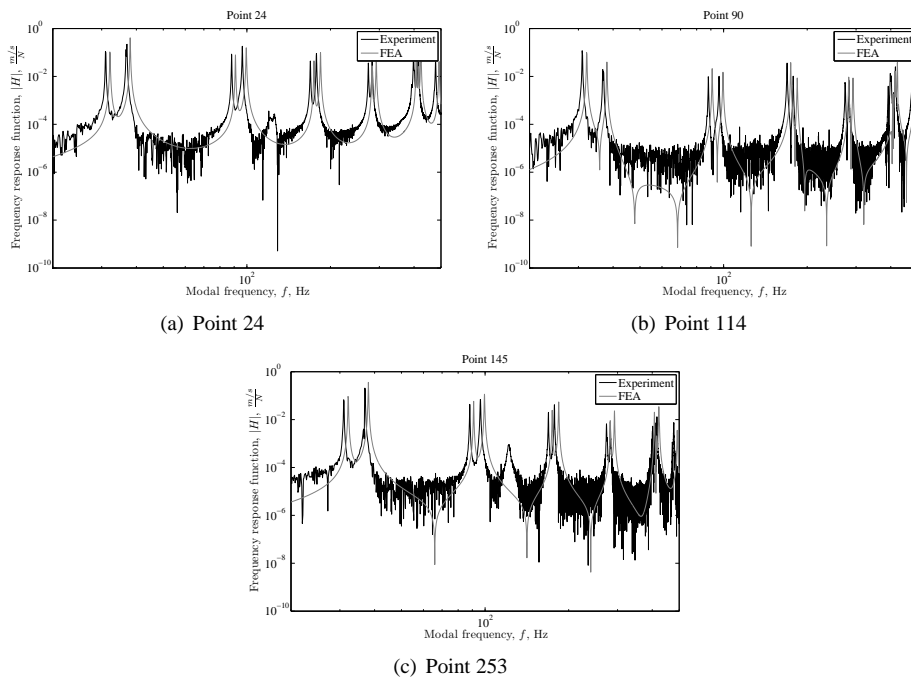


Figure F.4: Frequency response function of the baseline cylinder

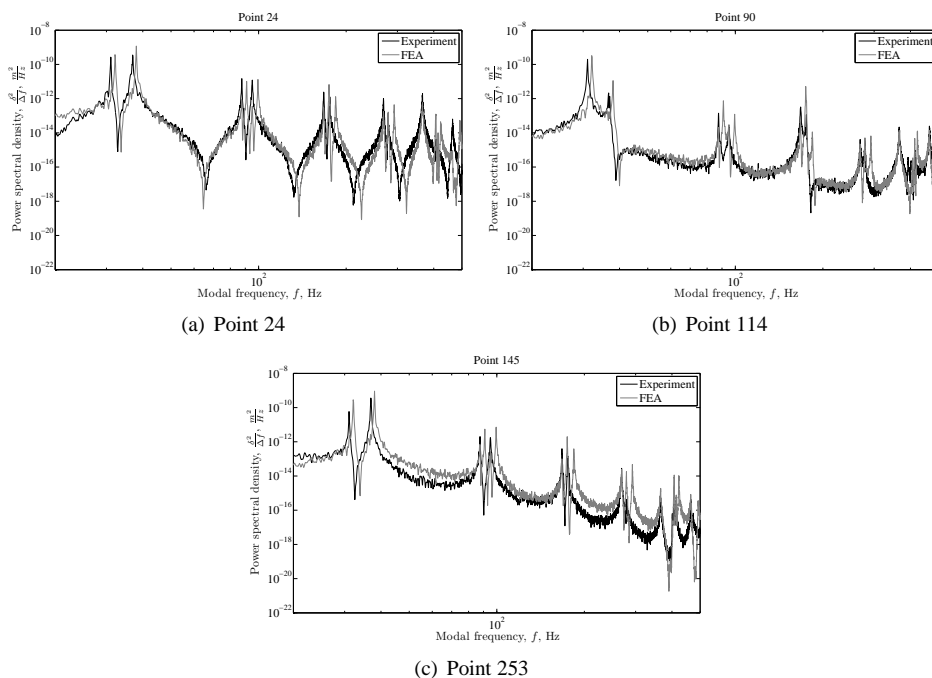


Figure F.5: Power spectral density for displacement of the baseline cylinder

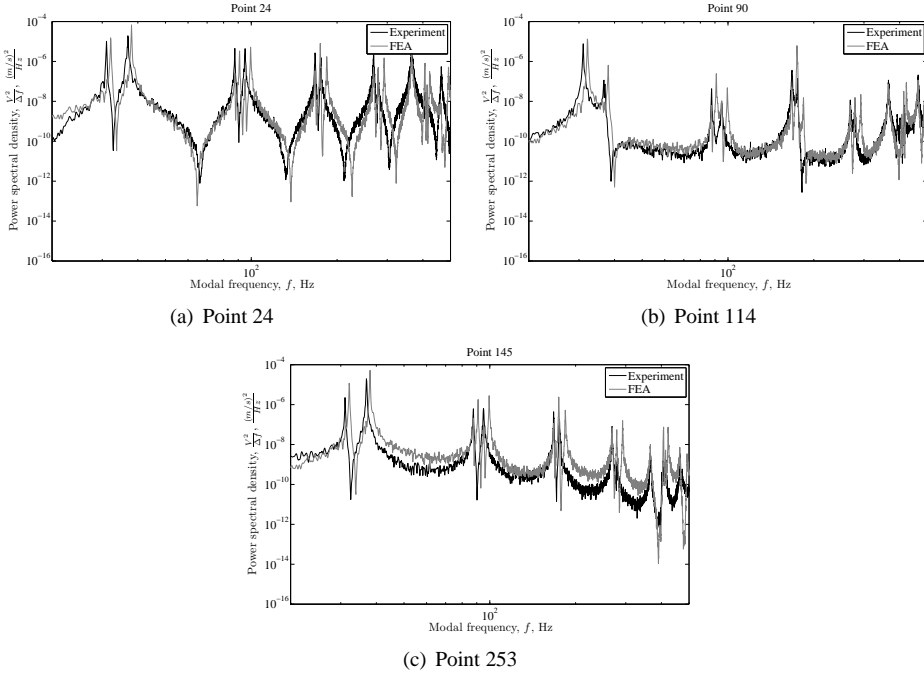


Figure F.6: Power spectral density for velocity of the baseline cylinder

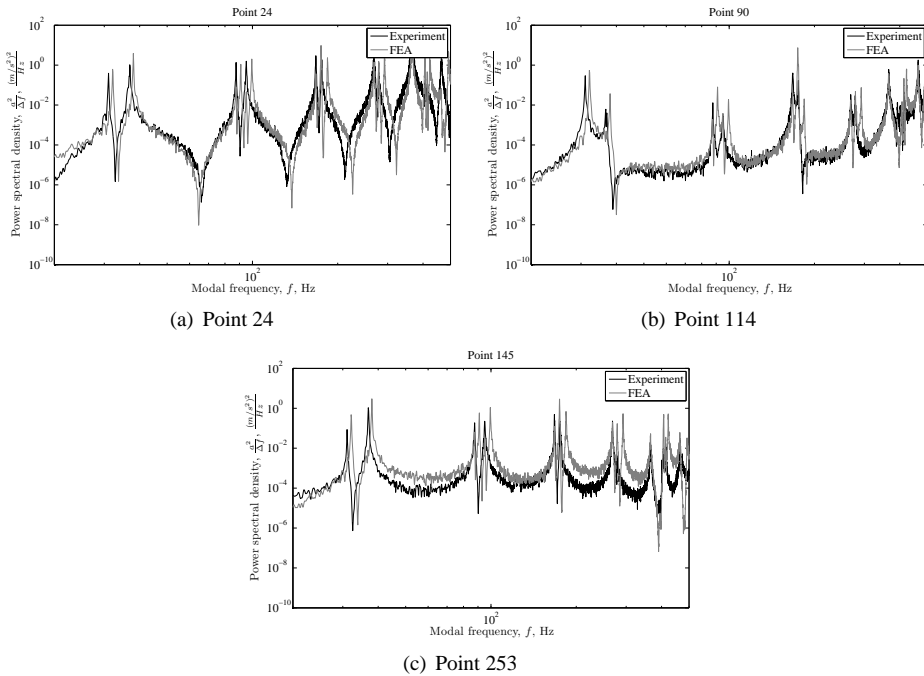


Figure F.7: Power spectral density for acceleration of the baseline cylinder

# Appendix G

## Test Mechanism Loads

Prediction of disturbing forces is based on a simplified model of the test mechanism as shown in figure G.1. All members are assumed rigid, except for the composite shell, which is modeled as a beam with longitudinal stiffness  $EA$  and bending stiffness  $EI$ , based on the baseline cylinder design. Furthermore hinges are included in locations 1, 2, 4 and 5 to connect the members, while the member that connects nodes 2, 3, 4 and 6 is a rigid part. The connection between the test setup and the shell at node 6 is also a rigid connection. The vertical plane passing through node 7 is a symmetry plane. The length of the members is given in table G.1.

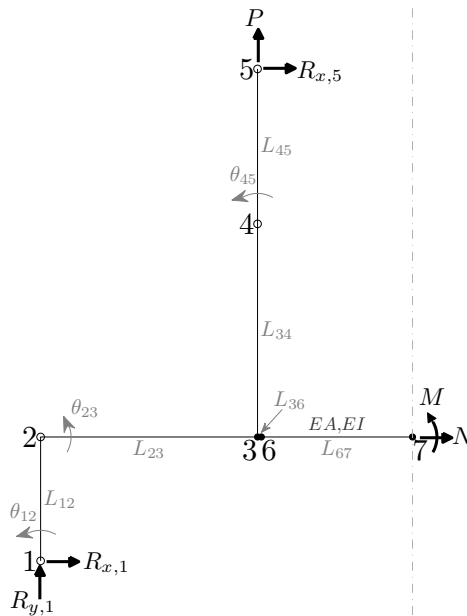


Figure G.1: Schematic of test mechanism

Table G.1: Length of the members of the test mechanism

member	$L$ , mm
$L_{12}$	406
$L_{23}$	711.2
$L_{34}$	698.5
$L_{45}$	508
$L_{36}$	12.7
$L_{67}$	495.3

Interconnectivity and equilibrium dictate the location of each node. The geometric relations are given in table G.3. Some nodes have additional constraints, as listed in table G.2

Table G.2: Compatibility equations

$x_1 = y_1 = 0$
$x_5 = L_{23}$
$x_7 = L_{23} + L_{36} + L_{67}$ (symmetry constraint)
$\theta_7 = \theta_{23} + \frac{ML_{67}}{EI} = 0$ (symmetry constraint)

Global equilibrium dictates that  $R_y, 1 = -P$ , because there is no vertical load in node 7 due to the symmetry plane. Subsequently local equilibrium of members 1-2 and 4-5 provide the horizontal reaction forces in nodes 1 and 5:

- $R_{x,1} = P \tan \theta_{12}$
- $R_{x,5} = -P \tan \theta_{45}$

Table G.3: Equations governing the location of the nodes

x-coordinate	y-coordinate
$x_1 = 0$	$y_1 = 0$
$x_2 = x_1 - L_{12} \sin \theta_{12}$	$y_2 = y_1 + L_{12} \cos \theta_{12}$
$x_3 = x_2 + L_{23} \cos \theta_{23}$	$y_3 = y_2 + L_{23} \sin \theta_{23}$
$x_4 = x_3 - L_{34} \sin \theta_{23}$	$y_4 = y_3 + L_{34} \cos \theta_{23}$
$x_5 = x_4 - L_{45} \sin \theta_{45}$	$y_5 = y_4 + L_{45} \cos \theta_{45}$
$x_6 = x_3 + L_{36} \cos \theta_{23}$	$y_6 = y_3 + L_{36} \sin \theta_{23}$
$x_7 = x_6 + L_{67} \cos \theta_{23} + \frac{NL_{67}}{EA}$	$y_7 = y_6 + L_{67} \sin \theta_{23} + \frac{ML_{67}^2}{2EI}$

Equilibrium of horizontal forces gives  $N$ :

$$N = -R_{x,1} - R_{x,5} = -P \tan \theta_{12} + P \tan \theta_{45} \quad (\text{G.1})$$

Finally, global moment equilibrium around node 7 results in the following equation:

$$\Sigma M_{7ccw} : 0 = M + PL_{23} + R_{x,1}(y_7 - y_1) - R_{x,5}(y_5 - y_7) \quad (\text{G.2})$$

such that the bending moment is:

$$M = -PL_{23} - P \tan \theta_{12}(y_7 - y_1) - P \tan \theta_{45}(y_5 - y_7) \quad (\text{G.3})$$

Looking at the equations in table G.3 and the equilibrium equations G.1 and G.3 it can be seen that it is a coupled system of equations, with the rotation angles  $\theta_{12}$ ,  $\theta_{23}$ , and  $\theta_{45}$  and loads  $N$  and  $M$  unknown. Applying the compatibility constraints of table G.2 the system of equations can be solved for a given load  $P$ , and the influence of the disturbing forces can be evaluated. At the maximum load  $P = 580$  kN, the deviation of the bending moment  $M$  from the ideal bending moment  $PL_{23}$  is less than 2 percent. The axial load that is generated at  $P = 580$  kN causes a compressive strain that is smaller than 0.25 percent of the maximum compressive strain caused by bending. Based on this approximation it can be concluded that the magnitude of disturbing forces is negligible for the current design of the test fixture. Furthermore, these disturbances will be smaller for the steered cylinder, since it is less compliant than the baseline cylinder.





## Appendix H

# Measurements of the End Rotations using DIC and LVDT's

A description of the end rotation measurements using DIC and a comparison with the end rotations measured using LVDT's are given in this appendix.

The cylinder deformations measured using the DIC system are shown in figure H.1. The colors in figure H.1 represent the axial displacement due to a bending moment of 415 kNm, shown both for the top part of the cylinder, which is in tension, and the bottom half of the cylinder, which is in compression. Points 1 and 2, shown in figures H.1(a) and H.1(b), were

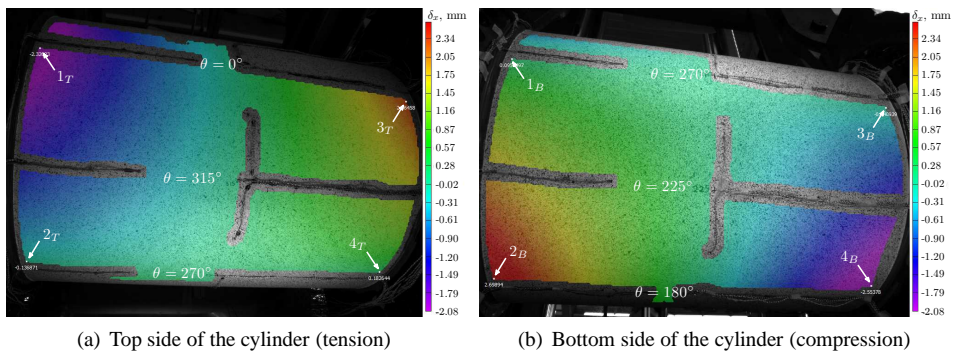


*Figure H.1: Displacements in longitudinal direction measured with DIC*

in one plane before any load was applied to the cylinder. Assuming points 1 and 2 in the top part remained in one plane, the end rotation  $\gamma$  could be calculated based on the vertical distance  $\Delta z$  between the points and the relative horizontal displacement  $\Delta \delta_x$ , which are related by:

$$\tan \gamma = \frac{\Delta \delta_x}{\Delta z} \quad (\text{H.1})$$

The same procedure can be followed for the bottom part of the cylinder. Subsequently, these two can be compared and a comparison can be made with the end rotation measured

by the LVDTs on the test structure, given in table H.1. Similarly, the end rotations at the other end of the cylinder can be calculated using points 3 and 4, see figures H.1(a) and H.1(b). The rotations measured by the LVDTs were larger than the rotations measured by the DIC system, which is an indication of flexibility in the interface between the cylinder and the support structure. Further, the rotations on the compression side were larger than the rotations on the tension side, which is in line with the strain distribution shown in figure 8.11(b).

*Table H.1: Displacement data of points measured with DIC*

Location	$\Delta z$ mm	$\Delta \delta_x$ mm	$\gamma_{DIC}$ deg	$\gamma_{LVDT}$ deg
(1-2) <sub>T</sub>	283.51	2.183	0.441	0.582
(1-2) <sub>B</sub>	290.74	2.604	0.513	0.582
(3-4) <sub>T</sub>	280.10	1.882	0.385	0.588
(3-4) <sub>B</sub>	279.67	2.413	0.494	0.588

## Appendix I

# Optimization of Boundary Conditions

The shell and the boundaries can be considered as springs in series, adding up to one spring with a stiffness  $k_t$ :

$$\frac{1}{k_t} = \frac{1}{k_c} + \frac{2}{k_s} \quad (\text{I.1})$$

where  $k_c$  is the spring stiffness of the composite laminate, calculated by:

$$k_c = \frac{E_c A_s}{L_c} \quad (\text{I.2})$$

and  $k_s$  is the spring stiffness of the boundary springs. A schematic representation is given in figure I.1. A total of 192 springs ( $N_s$ ) is included to account for the flexible boundary conditions, and therefore the spring area  $A_s$  is defined as:

$$A_s = \frac{2\pi R t}{N_s} \quad (\text{I.3})$$

Since the end plates are assumed to be rigid, the stress per spring element  $i$  is:

$$\sigma_i = \frac{M z_i}{I_y} \frac{k_{t,i}}{k_{t,avg}} \quad (\text{I.4})$$

where  $z_i$  is the vertical coordinate of the spring location, and  $I_y$  is the moment of inertia about the neutral  $y$ -axis of the cylinder (not necessarily located at  $z = 0$ ). The average spring stiffness is calculated by:

$$k_{t,avg} = \frac{1}{N} \sum_{i=1}^N k_{t,i} \quad (\text{I.5})$$

The load per element is then found by:

$$P_i = \sigma_i A_s = k_{t,i} u_{t,i} \quad (\text{I.6})$$

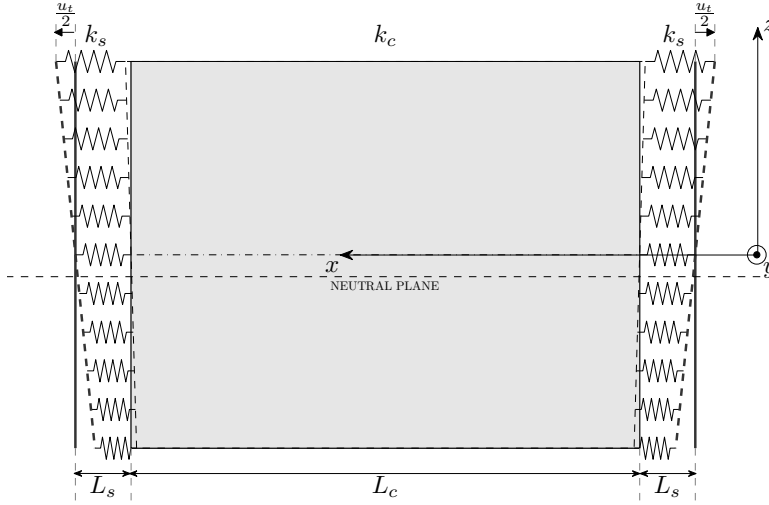


Figure I.1: Simplified model with flexible boundary conditions

such that the total displacement per element is:

$$u_{t,i} = \frac{\sigma_i A_s}{k_{t,i}} \quad (\text{I.7})$$

The rotation of rigid end plate can be calculated using the total displacements at  $z = -R$  and  $z = R$ :

$$\tan \gamma = \frac{\frac{1}{2}u_t(z=R) - \frac{1}{2}u_t(z=-R)}{2R} \quad (\text{I.8})$$

Ignoring other boundary condition effects the strain distribution around the circumference of the composite cylinder can be derived from the shell displacements:

$$\varepsilon_c = \frac{u_c}{L_c} = \frac{\sigma A_s}{k_c L_c} \quad (\text{I.9})$$

If the spring stiffness of the boundary springs is constant, the strains and end rotations vary linearly with the load. If the spring stiffness of all springs is equal the strain distribution with the height of the cylinder remains linear. Since the experimental results indicated that this is not the case, the spring stiffness is made dependent on the extension of the spring:  $k_s = k_s(u_s)$ . Considering the physics of the boundary conditions it is likely that springs in tension behave different from springs in compression. Therefore the spring stiffness is allowed to be discontinuous at  $u_s = 0$ . Furthermore a linear variation in spring stiffness is assumed, i.e.:

$$\begin{aligned} k_s &= a^+ + b^+ u_s & u \in [0, \infty] \\ &= a^- + b^- u_s & u \in [-\infty, 0) \end{aligned} \quad (\text{I.10})$$

As a consequence the location of the neutral axis changes, the responses are not linear with the load anymore, and the strain distribution is no longer linear with the  $z$ -coordinate.

The value of the  $a$  and  $b$  parameters are determined by a least-squares optimization using the solver add-in of Microsoft Excel, minimizing the difference between the measured and predicted end rotations and strains at 10 equally spaced load levels between 0 and  $3.56 \cdot 10^5$  Nm. The displacements are now calculated by:

$$u_t = \sum_{j=1}^{N_m} \frac{\Delta\sigma_j A_s}{k_{t,j}} \quad (\text{I.11})$$

where  $\Delta\sigma$  is the change in stress due to an increase in bending moment  $\Delta M$ . This optimization resulted in  $a^+ = 1.72 \cdot 10^7 \text{Nm}^{-1}$  and  $a^- = 1.19 \cdot 10^8 \text{Nm}^{-1}$ . The values for  $b^-$  and  $b^+$  were one order of magnitude smaller than  $a^-$  and  $a^+$ , and because the values of  $u_t$  are in the order  $10^{-4}$ , the linear part of the spring stiffness variation will be ignored. The spring stiffness can therefore easily be denoted as  $k_s^+ = a^+$  and  $k_s^- = a^-$ . After inspection, the spring stiffness of the compressive spring,  $k_s^-$ , is almost the same as the stiffness of the laminate segment enclosed by the end rings:

$$k_s^- \approx \frac{E_c A_s + E_{st} A_{st}}{L_s} \quad (\text{I.12})$$

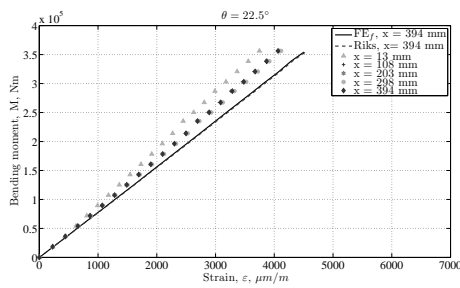
where the subscript  $c$  refers to the composite laminate and  $st$  refers to the steel tabs. This seems to correspond with the assumption that the load transfer on the compression side is through direct contact with the supporting back plate. The lower stiffness on the tension side is due to the load transfer through the bolted connection and through friction, which is less efficient than the load transfer on the compression side.

After optimizing the longitudinal spring stiffnesses using Excel, the springs are included in the ABAQUS model, and rotational springs are included as well. All rotational springs are assumed to have equal and constant stiffness. Three different stiffness values were evaluated, and the best matching stiffness was selected.

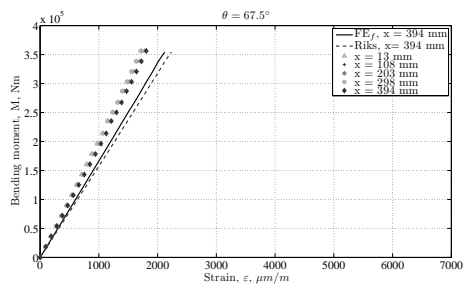


# Appendix J

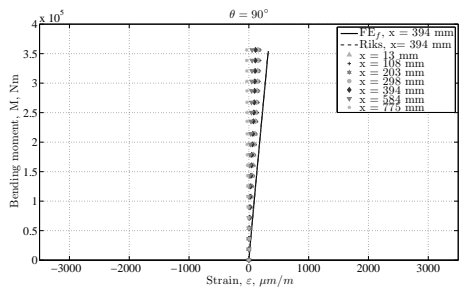
## Miscellaneous Bending Test Results



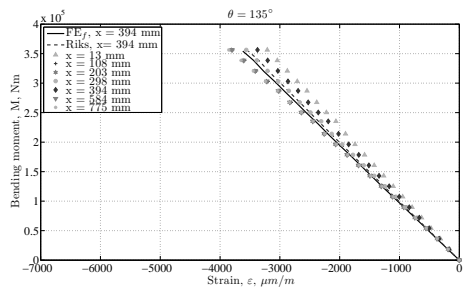
(a) Strains along  $\theta = 22.5^\circ$



(b) Strains along  $\theta = 67.5^\circ$

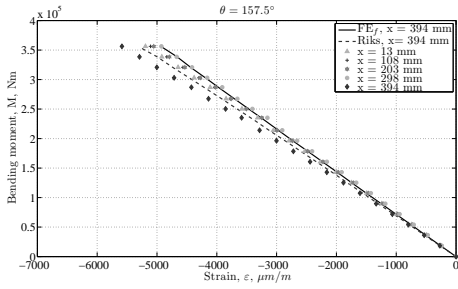


(c) Strains along  $\theta = 90^\circ$

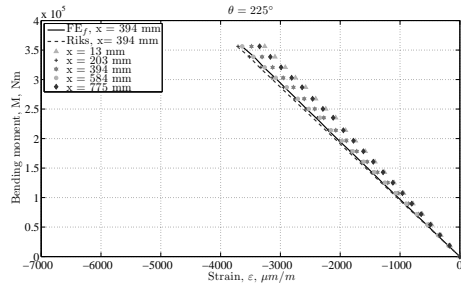


(d) Strain along  $\theta = 135^\circ$

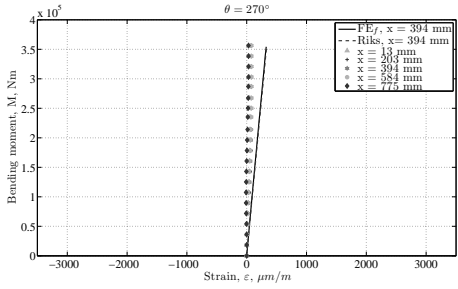
Figure J.1: Strains at different locations along the length of the baseline cylinder



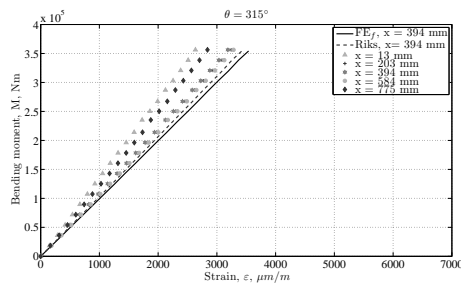
(e) Strain along  $\theta = 157.5^\circ$



(f) Strain along  $\theta = 225^\circ$

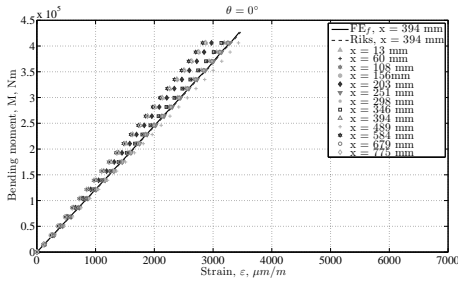


(g) Strain along  $\theta = 270^\circ$

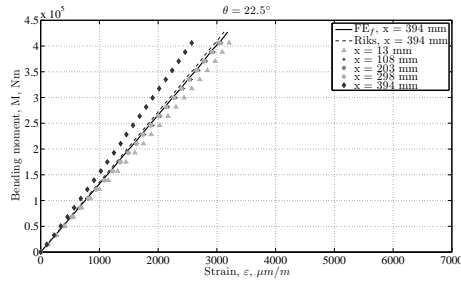


(h) Strain along  $\theta = 315^\circ$

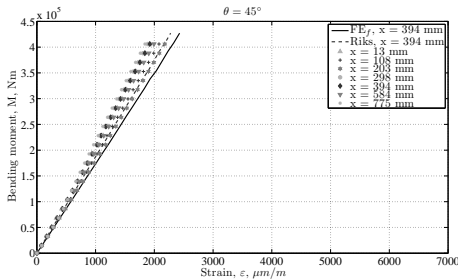
Figure J.1: Strains at different locations along the length of the baseline cylinder (cont'd)



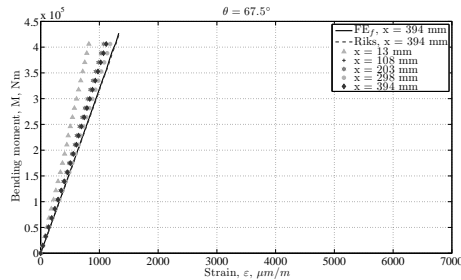
(a) Strains along  $\theta = 0^\circ$



(b) Strains along  $\theta = 22.5^\circ$



(c) Strains along  $\theta = 45^\circ$



(d) Strains along  $\theta = 67.5^\circ$

Figure J.2: Strains at different locations along the length of the variable-stiffness cylinder in the preferred orientation



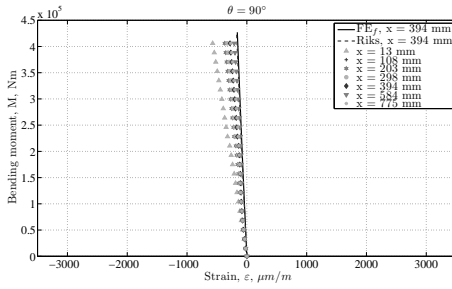
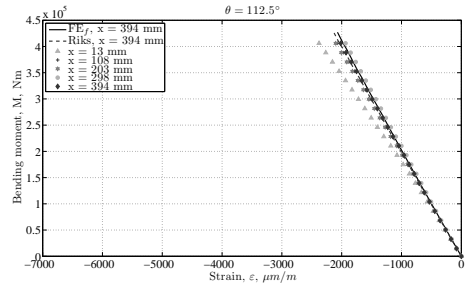
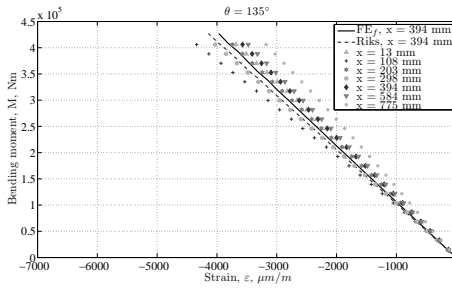
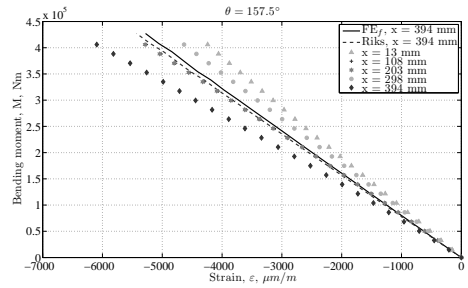
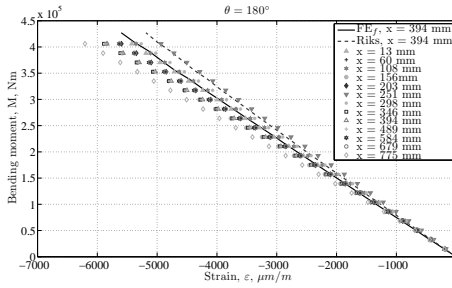
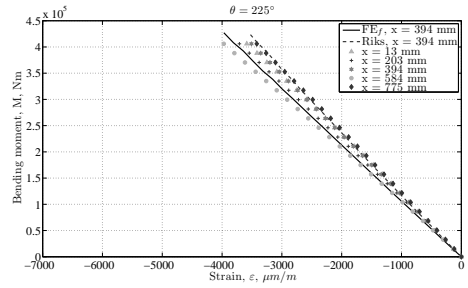
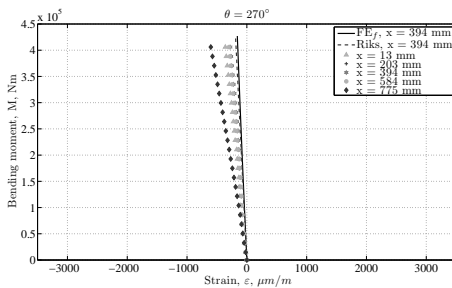
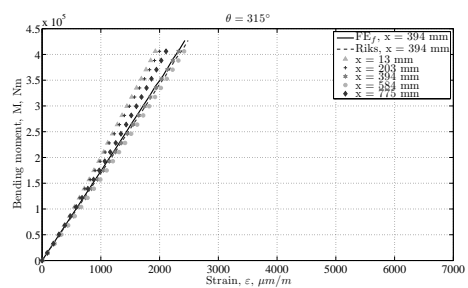
(e) Strains along  $\theta = 90^\circ$ (f) Strains along  $\theta = 112.5^\circ$ (g) Strain along  $\theta = 135^\circ$ (h) Strain along  $\theta = 157.5^\circ$ (i) Strain along  $\theta = 180^\circ$ (j) Strain along  $\theta = 225^\circ$ (k) Strain along  $\theta = 270^\circ$ (l) Strain along  $\theta = 315^\circ$ 

Figure J.2: Strains at different locations along the length of the variable-stiffness cylinder in the preferred orientation (cont'd)

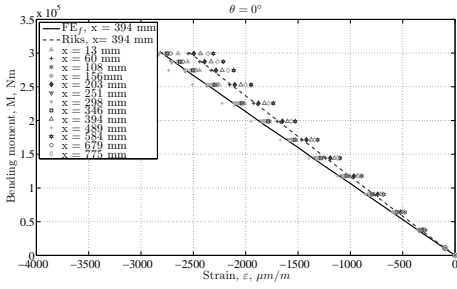
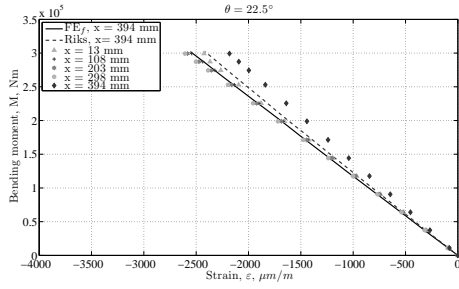
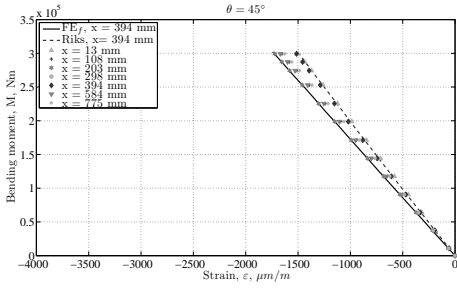
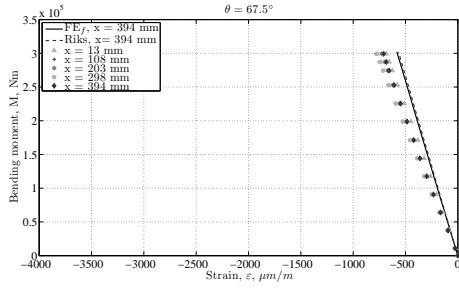
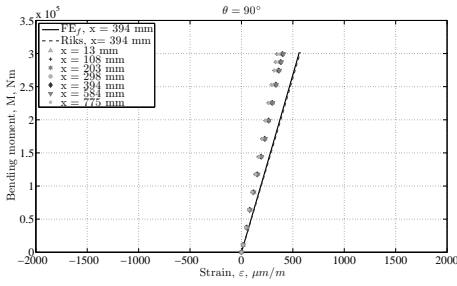
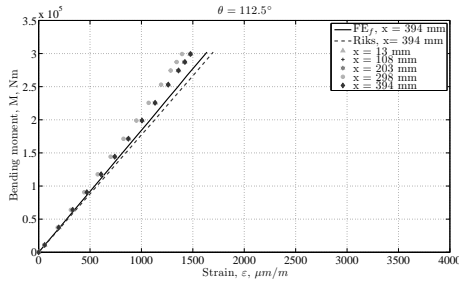
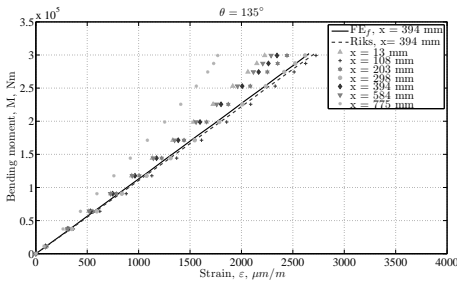
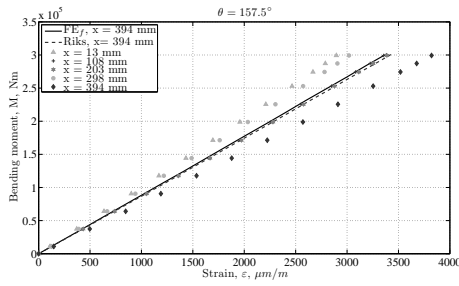
(a) Strains along  $\theta = 0^\circ$ (b) Strains along  $\theta = 22.5^\circ$ (c) Strains along  $\theta = 45^\circ$ (d) Strains along  $\theta = 67.5^\circ$ (e) Strains along  $\theta = 90^\circ$ (f) Strains along  $\theta = 112.5^\circ$ (g) Strain along  $\theta = 135^\circ$ (h) Strain along  $\theta = 157.5^\circ$ 

Figure J.3: Strains at different locations along the length of the variable-stiffness cylinder in the reversed orientation

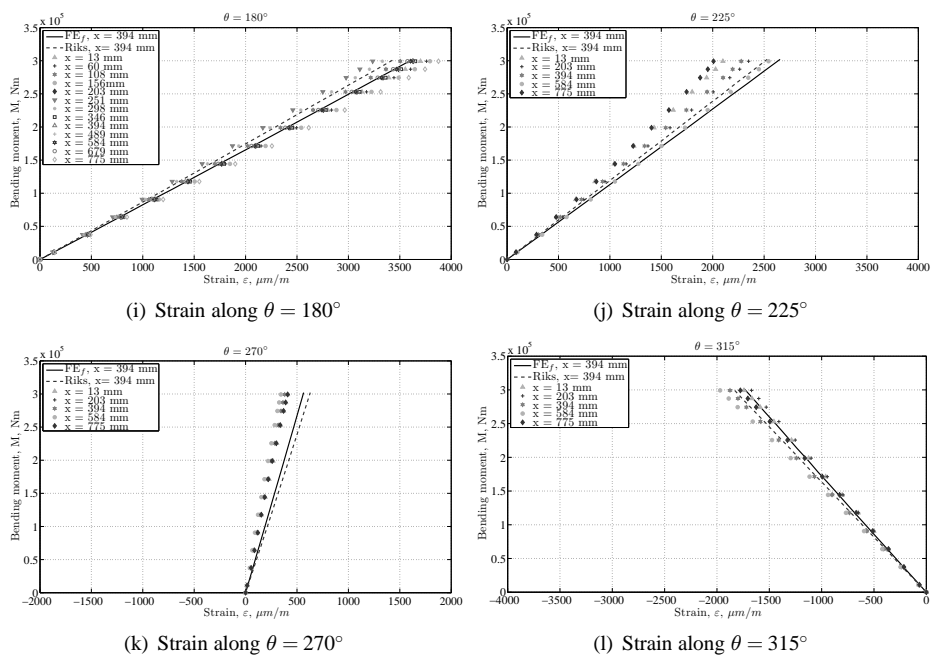
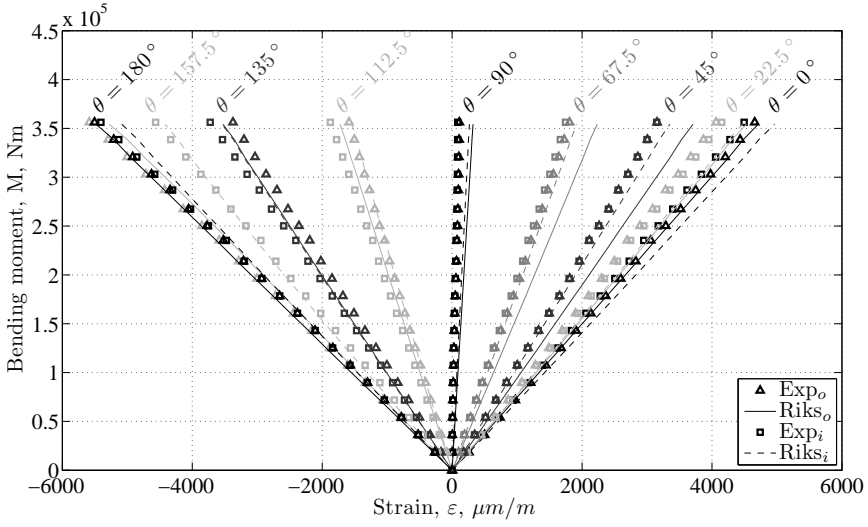
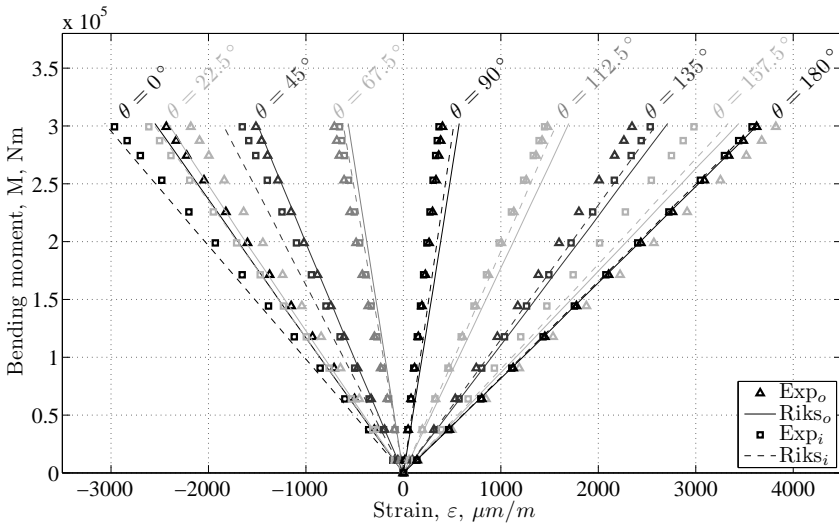


Figure J.3: Strains at different locations along the length of the variable-stiffness cylinder in the reversed orientation (cont'd)



(a) Baseline cylinder



(b) Variable-stiffness cylinder in the reversed orientation

Figure J.4: Back-to-back strain data

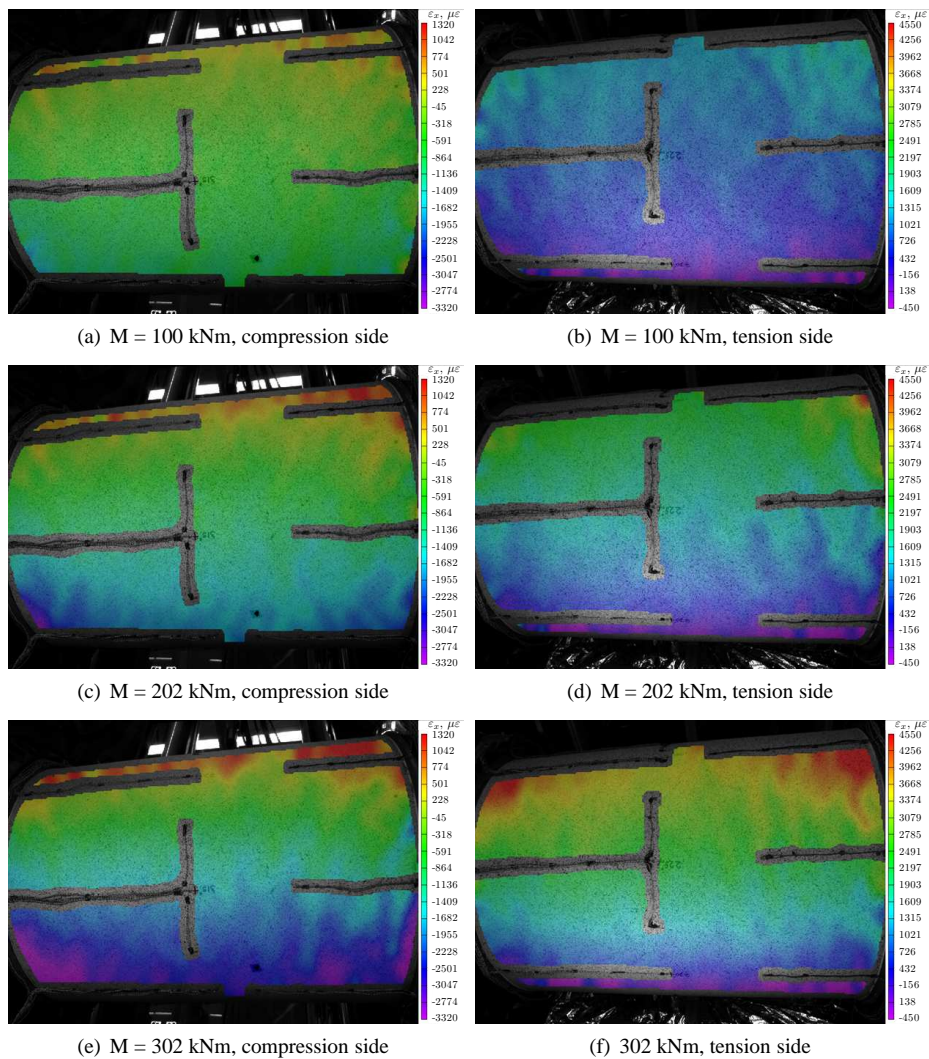


Figure J.5: Strains on the variable-stiffness cylinder in the reversed direction



# Bibliography

ABAQUS, Inc. *ABAQUS Version 6.7 User's Manual*. Pawtucket, RI, USA, 2005.

M. M. Abdalla, S. Setoodeh, and Z. Gürdal. Design of variable stiffness composite panels for maximum fundamental frequency using lamination parameters. *Composite Structures*, 81(2):283–291, 2007.

M. M. Abdalla, Z. Gürdal, and G.F. Abdelal. Thermomechanical response of variable stiffness composite panels. *Journal of Thermal Stresses*, 32(1-2):187–208, 2009.

A. Alhajahmad, M. M. Abdalla, and Z. Gürdal. Design tailoring for pressure pillowing using tow-placed steered fibers. *AIAA Journal of Aircraft*, 45(2):630–640, 2008a.

A. Alhajahmad, M. M. Abdalla, and Z. Gürdal. Optimal design of tow-placed fuselage panels with cutouts for maximum strength and buckling performance. In *Proceedings of the 2<sup>nd</sup> International Conference on Multidisciplinary Design Optimization and Applications*, Gijon, Spain, 2008b.

A. Alhajahmad, M. M. Abdalla, and Z. Gürdal. Optimal design of a pressurized fuselage panel with a cutout using tow-placed steered fibers. In *Proceedings of the International Conference on Engineering Optimization*, Rio de Janeiro, Brazil, June 2008c.

R.L. Anderson and C. G. Grant. Advanced fiber placement of composite fuselage structures. In *First NASA Advanced Composites Technology Conference*, volume 2, pages 817–830, 1991.

J. Arbocz and C.D. Babcock. The effect of general imperfections on the buckling of cylindrical shells. *Journal of Applied Mechanics*, 36(1):28–38, 1969.

C. Audet, J. E. Dennis, Jr., D. W. Moore, A. Booker, and P. D. Frank. A surrogate-model-based model for constrained optimization. In *Proceedings of the 8<sup>th</sup> AIAA/USAF/NASA/ISSMO Symposium on Multidisciplinary Analysis and Optimization*, Long Beach, CA, USA, Sept 2000.

M. Autio. Determining the real lay-up of a laminate corresponding to optimal lamination parameters by genetic search. *Structural and Multidisciplinary Optimization*, 20(4):301–310, 2000.

N. V. Banichuk, V. V. Saurin, and A. A. Barsuk. Optimal orientation of orthotropic materials for plates designed against buckling. *Structural Optimization*, 10(3-4):191–196, 1995.

- M. Baruch, J. Arbocz, and G.Q. Zhang. Laminated conical shells - considerations for the variations of the stiffness coefficients. In *35<sup>th</sup> AIAA/ASME/ASCE/AHS/ASC Structures, Structural Dynamics, and Materials (SDM) Conference*, pages 2505–2516, Washington, DC, USA, 1994.
- V. M. Benson and J. Arnold. Automated fiber placement of advanced materials. In *Proceedings of the SAMPE 2006 Conference*, 2006.
- S.B. Biggers and S.S. Pageau. Shear buckling response of tailored rectangular composite plates. *AIAA Journal*, 32(5):1100–1103, 1994.
- S.B. Biggers and S. Srinivasan. Compression buckling response of tailored rectangular composite plates. *AIAA Journal*, 31(3):590–596, March 1993.
- A. W. Blom, C. S. Lopes, P. J. Kromwijk, Z. Gürdal, and P. P. Camanho. A theoretical model to study the influence of tow-drop areas on the stiffness and strength of variable-stiffness laminates. *Journal of Composite Materials*, 43:403–425, 2009.
- A.W. Blom, M.M. Abdalla, and Z. Gürdal. Optimization of course locations in fiber-placed panels for general fiber angle distributions. *Composites Science and Technology*, 70(4): 564–570, 2010.
- B. Blonigen and B. Johnson. Fiber placing a composite aft pressure bulkhead. In *Proceedings of the SAMPE 2006 Conference*, Long Beach, CA, USA, 2006.
- A. J. Booker, J. E. Dennis, Jr., P. D. Frank, D. B. Serafini, V. Torczon, and M. W. Trosset. A rigorous framework for optimization of expensive functions by surrogates. *Structural Optimization*, 17(1):1–13, 1999.
- L. G. Brazier. On the flexure of thin cylindrical shells and other 'thin' sections. *Proc. Royal Society, series A*, 116:104–114, 1926.
- D. Buchanan, R. Alexander, and J. Thomas. Structural design of a fiber placed inlet duct. In *Proceedings of the 40<sup>th</sup> AIAA/ASCE/AHS/ASC Structures, Structural Dynamics, and Materials (SDM) Conference*, St. Louis, MI, USA, 1999. AIAA.
- B. Budiansky and J.W. Hutchinson. Dynamic buckling of imperfection sensitive structures. In *Proceedings 11<sup>th</sup> IUTAM Congress*, pages 636–651, Munich, 1964. Julius Springer-Verlag.
- R. Calawa and J. Nancarrow. Medium wave infrared heater for high-speed fiber placement. In *Aerospace Manufacturing and Automated Fastening Conference*, Los Angeles, CA, USA, 2007. SAE.
- century-of-flight website. *Development of Aviation Technology - Metal Skinned Aircraft*. <http://www.century-of-flight.net/Aviation%20history/evolution%20of%20technology-Metal-Skinned%20Aircraft.htm>, Jan 2010.
- M.A. Crisfield. A fast incremental/iterative solution procedure that handles "snap-through". *Computers and Structures*, 13:55–62, 1981.



- R. C. Davis. Buckling tests of a 3-meter-diameter corrugated graphite-epoxy ring-stiffened shell. Technical report, July 1982. NASA TP 2032.
- J. de Vries. *The Imperfection Data Bank and its Applications*. PhD thesis, Delft University of Technology, May 2009.
- R. Degenhardt, A. Kling, A. Bethge, J. Orf, L. Kärger, K. Rohwer, R. Zimmermann, and A. Calvi. Investigations of imperfection sensitivity of unstiffened CFRP cylindrical shells. *Composite Structures*, 92(8):1939–1946, 2010.
- R. DeVlieg, K. Jeffries, and P. Vogeli. High-speed fiber placement on large complex structures. In *Aerospace Manufacturing and Automated Fastening Conference*, Los Angeles, CA, USA, 2007. SAE.
- C.G. Diaconu, M. Sato, and H. Sekine. Layup optimization of symmetrically laminated thick plates for fundamental frequencies using lamination parameters. *Structural and Multidisciplinary Optimization*, 24(4):302–311, 2002.
- M.T. DiNardo and P.A. Lagace. Buckling and postbuckling of laminated composite plates with ply dropoffs. *AIAA Journal*, 27(10):1392–1398, 1989.
- G. Duvaut, G. Terrel, F. Léné, and V.E. Verijenko. Optimization of fiber reinforced composites. *Composite Structures*, 48(1-3):83–89, 2000.
- D. O. Evans, M. M. Vaniglia, and P. C. Hopkins. Fiber placement process study. In *Proceedings of the 34<sup>th</sup> International SAMPE Symposium*, 1989.
- D.O. Evans. Fiber placement. In D.B. Miracle and S.L. Donaldson, editors, *ASM Handbook*, volume 21: composites, pages 477–479. ASM International, 2001.
- H. P. Fuchs, J. H. Starnes, and M. W. Hyer. Collapse of composite cylinders in bending. In *Proceedings of the 38<sup>th</sup> AIAA/ASME/AHS/ASC Structures, Structural Dynamics and Materials (SDM) Conference*, Kissimmee, FL, US, Apr 1997. AIAA.
- Y. Goldfeld and J. Arbocz. Buckling of laminated conical shells given the variations of the stiffness coefficients. *AIAA Journal*, 42(3):642–649, 2004.
- Y. Goldfeld, J. Arbocz, and A. Rothwell. Design and optimization of laminated conical shells for buckling. *Thin-Walled Structures*, 43(1):107–133, 2005.
- C. G. Grant. Automated processes for composite aircraft structure. *Industrial Robot: An International Journal*, 33(2):117–121, 2006.
- C. G. Grant and V. M. Benson. Automated fiber placement - evolution and current demonstrations. In *Third NASA Advanced Composite Technology Conference*, pages 625–648, Long Beach, CA, USA, 1992.
- Z. Gürdal and R. Olmedo. In-plane response of laminates with spatially varying fiber orientations: Variable stiffness concept. *AIAA Journal*, 31(4):751–758, 1993.

- Z. Gürdal, B. F. Tatting, and K. C. Wu. Tow-placement technology and fabrication issues for laminated composite structures. In *Proceedings of the 46<sup>th</sup> AIAA/ASME/AHS/ASC Structures, Structural Dynamics and Materials (SDM) Conference*, Austin, TX, USA, Apr 2005. AIAA.
- Z. Gürdal, B. F. Tatting, and K. C. Wu. Variable stiffness composite panels; effects of stiffness variation on the in-plane buckling response. *Composites Part A: Applied Science and Manufacturing*, 39(5):911–922, 2008.
- R.T. Haftka and J. Starnes. Stiffness tailoring for improved compressive strength of composite plates with holes. *AIAA Journal*, 26(1):72–77, 1988.
- R.D. Hale and K. Schueler. Object-oriented design and analysis tools for fiber placed and fiber steered structures. In *Proceedings of the SAMPE 2002 Conference*, Long Beach, CA, USA, 2002.
- R.D. Hale, R.S. Moon, K. Lim, K. Schueler, A. Yoder, and H. Singh. Integrated design and analysis tools for reduced weight, affordable fiber steered composites. Technical Report N00014-00-1-0415, University of Kansas Center for Research, Inc., 2004.
- V.B. Hammer, M.P. Bendsoe, R. Lipton, and P. Pedersen. Parametrization in laminate design for optimal compliance. *International Journal of Solids and Structures*, 34(4):415–434, 1997.
- H.-T. Hu and S.-C. Ou. Maximization of the fundamental frequencies of laminated truncated conical shells with respect to fiber orientations. *Composite Structures*, 52(3):265–275, 2001.
- J. Huang and R. T. Haftka. Optimization of fiber orientations near a hole for increased load-carrying capacity of composite laminates. *Structural and Multidisciplinary Optimization*, 30(5):335–341, 2005.
- J. Huang, R. T. Haftka, and A. J. Rapoff. Optimization design of composite plates with holes for increased strength. In *Proceedings of the 44<sup>th</sup> AIAA/ASME/ASCE/AHS Structures, Structural Dynamics, and Materials (SDM) Conference*, Norfolk, VA, USA, 2003. AIAA.
- M. W. Hyer and R. F. Charette. Use of curvilinear fiber format in composite structure design. *AIAA Journal*, 29(6):1011–1015, 1991.
- M. W. Hyer and H. H. Lee. The use of curvilinear fiber format to improve buckling resistance of composite plates with central circular holes. *Composite Structures*, 18(3): 239–261, 1991.
- M. W. Hyer and J. C. Riddick. Internal pressure loading of segmented-stiffness composite cylinders. *Composite Structures*, 45(4):311–320, 1999.
- M.W. Hyer, R.J. Rust, and W.A. Waters. Innovative design of composite structures: Design, manufacturing, and testing of plates utilizing curvilinear fiber trajectories. Technical Report NASA-CR-197045, NASA, Nov 1994.

- S. T. IJsselmuiden, M. M. Abdalla, and Z. Gürdal. Implementation of strength-based failure criteria in the lamination parameter design space. *AIAA journal*, 46(7):1826–1834, July 2008.
- S.T. IJsselmuiden, M. M. Abdalla, and Z. Gürdal. Maximising buckling loads of variable stiffness shells using lamination parameters. In *50<sup>th</sup> AIAA/ASME/ASCE/AHS/ASC Structures, Structural Dynamics and Materials (SDM) Conference*, Palm Springs, CA, USA, 2009a. AIAA.
- S.T. IJsselmuiden, M. M. Abdalla, and Z. Gürdal. Thickness tailoring of variable stiffness panels for maximum buckling load. In W. Banks and M.R. Wisnom, editors, *17<sup>th</sup> International Conference on Composite Materials*, Edinburgh, 2009b. British Composites Society.
- S.T. IJsselmuiden, M. M. Abdalla, and Z. Gürdal. Thermo-mechanical design optimisation of variable stiffness composite panels for buckling. In *11<sup>th</sup> ECSSMMT Conference*, Toulouse, France, 2009c.
- S.T. IJsselmuiden, M. M. Abdalla, and Z. Gürdal. Optimization of variable-stiffness panels for maximum buckling load using lamination parameters. *AIAA Journal*, 48(1):134–143, 2010.
- L. Izco, J. Isturiz, and Motilva M. High speed tow placement system for complex surfaces with cut / clamp / restart capabilities at 85 m/min (3350 ipm). In *Aerospace Manufacturing and Automated Fastening Conference and Exhibition*, Toulouse, France, 2006.
- D. C. Jegley, B. F. Tatting, and Z. Gürdal. Optimization of elastically tailored tow-placed plates with holes. In *Proceedings of the 44<sup>th</sup> AIAA/ASME/ASCE/AHS/ASC Structures, Structural Dynamics and Materials (SDM) Conference*, Norfolk, VA, USA, Apr 2003. AIAA.
- D. C. Jegley, B. F. Tatting, and Z. Gürdal. Tow-steered panels with holes subjected to compression or shear loading. In *Proceedings of the 46<sup>th</sup> AIAA/ASME/AHS/ASC Structures, Structural Dynamics and Materials (SDM) Conference*, Austin, TX, USA, Apr 2005. AIAA.
- R. M. Jones. *Mechanics of Composite Materials*. Taylor and Francis, 2nd edition, 1999.
- S. E. Jones and M. J. Platts. Using internal fibre geometry to improve the performance of pin-loaded holes in composite materials. *Applied Composite Materials*, 3(2):117–134, 1996.
- C. Kassapoglou. Composite plates with two concentric layups under compression. *Composites Part A: Applied Science and Manufacturing*, 39(1):104–112, 2008.
- A. Khani, M. M. Abdalla, and Z. Gürdal. Maximum strength design of long composite non-circular cylinders. In *11<sup>th</sup> European Conference on Spacecraft Structures, Materials and Mechanical Testing*, Toulouse, France, 2009a.

- A. Khani, M. M. Abdalla, and Z. Gürdal. Circumferential stiffness tailoring of long composite non-circular cylinders. In *8<sup>th</sup> World Congress on Structural and Multidisciplinary Optimization*, Lisbon, Portugal, 2009b.
- K.N. Khatri and N.S. Bardell. The variation of the stiffness coefficients for laminated open conical shell panels. *Composite Structures*, 32(1-4):287–292, 1995.
- R.A. Kisch. Automated fiber placement historical perspective. In *Proceedings of the SAMPE 2006 Conference*, Long Beach, CA, USA, 2006.
- J.C. Klees, S.T. IJsselmuiden, M. M. Abdalla, D.H. Bassir, and Z. Gürdal. Fibre angle reconstruction for variable-stiffness panels including curvature constraints. In *11<sup>th</sup> EC-SSMMT Conference*, Toulouse, France, 2009.
- W. T. Koiter. The effect of axisymmetric imperfections on the buckling of cylindrical shells under axial compression. In *Proceedings Koninklijke Ned. Acad. Wetenschap*, volume 66 of B, pages 265–279, 1963.
- P.T. Langley. Finite element modeling of tow-placed variable-stiffness composite laminates. Master's thesis, Virginia Polytechnic Institute and State University, June 1999.
- R. Li, D. Kelly, S. Arima, R. Willgoss, and A. Crosky. Fiber steering around a cutout in a shear loaded panel. In *Proceedings of the SAMPE 2002 Conference*, Long Beach, CA, USA, 2002a.
- R. Li, D. Kelly, and A. Crosky. Strength improvement by fibre steering around a pin loaded hole. *Composite Structures*, 57(1-4):377–383, 2002b.
- C. S. Lopes, P. P. Camanho, Z. Gürdal, and B. F. Tatting. Progressive failure analysis of tow-placed, variable-stiffness composite panels. *International Journal of Solids and Structures*, 44(25-26):8493–8516, 2007. 10.1016/j.ijsolstr.2007.06.029.
- C. S. Lopes, Z. Gürdal, and P. P. Camanho. Variable-stiffness composite panels: Buckling and first-ply failure improvements over straight-fibre laminates. *Computers and Structures*, 86(9):897–907, 2008.
- J.P. Martin and C. Hennings. Affordable automation for engineered composite structures. In *Proceedings of the SAMPE 2008 Conference*, Long Beach, CA, USA, 2008.
- J.P. Martin, R.J. Langone, M.J. Pasanen, and J.A. Mondo. Cost-effective, automated equipment for advanced composite structure development and production, 1997.
- G. Matheron. *Les variables régionalisée et leur estimation*. Masson, Paris, France, 1965.
- D.A. McCarville, J.C. Guzman, and D.M. Rotter. Automated material placement - 2008 industry overview. In *Proceedings of the SAMPE 2008 Conference*, Long Beach, CA, USA, 2008.
- R. Measom and K. Sewell. Fiber placement low-cost production for complex composite structures, 1996.

- J.A. Mondo, M.J. Pasanen, R.J. Langone, and J.P. Martin. Advances in automated fiber placement of aircraft structures, 1997.
- B. Morey. Automating composites fabrication. *Manufacturing Engineering*, 140(4), 2008.
- M. Moruzzi, T. Oldani, B. F. Tatting, Z. Gürdal, and A. W. Blom. Tailoring of composite layups through tow-placement manufacturing techniques. In *Proceedings of the SAMPE 2006 Conference*, Long Beach, CA, USA, May 2006.
- A. Muc and A. Ulatowska. Design of plates with curved fibre format. *Composite Structures*, 92:1728–1733, 2010.
- S. Nagendra, A. Kodiyalam, J. E. Davis, and V. N. Parthasarathy. Optimization of tow fiber paths for composite design. In *Proceedings of the 36<sup>th</sup> AIAA/ASME/ASCE/AHS/ASC Structures, Structural Dynamics and Materials (SDM) Conference*, New Orleans, LA, USA, 1995. AIAA.
- N. Olhoff. Multicriterion structural optimization via bound formulation and mathematical programming. *Structural Optimization*, 1:11–17, 1989.
- R. Olmedo and Z. Gürdal. Buckling response of laminates with spatially varying fiber orientations. In *Proceedings of the 34<sup>th</sup> AIAA/ASME/ASCE/AHS/ASC Structures, Structural Dynamics and Materials (SDM) Conference*. AIAA, 1993.
- L. Papadopoulos and C. Kassapoglou. Shear buckling of rectangular composite plates with two concentric layups. *Journal of Reinforced Plastics and Composites*, 23(1):5–16, 2004.
- L. Papadopoulos and C. Kassapoglou. Shear buckling of rectangular composite plates composed of concentric layups. *Composites Part A: Applied Science and Manufacturing*, 38(5):1425–1430, 2007.
- L. Parnas, S. Oral, and U. Ceyhan. Optimum design of composite structures with curved fiber courses. *Composites Science and Technology*, 63(7):1071–1082, 2003.
- M.J. Pasanen, J.P. Martin, R.J. Langone, and J.A. Mondo. Advanced composite fiber placement process to application, 1997.
- P. Pedersen. On optimal orientation of orthotropic materials. *Structural and Multidisciplinary Optimization*, 1(2):101–106, 1989.
- P. Pedersen. On thickness and orientational design with orthotropic materials. *Structural Optimization*, 3(2):69–78, 1991.
- J. P. Peterson. Bending tests of ring-stiffened circular cylinders. Technical report, July 1956. NACA TN 3735.
- J. P. Peterson. Buckling tests of two integrally stiffened cylinders subject to bending. Technical report, June 1971. NASA TN D-6271.
- J. P. Peterson and J. K. Anderson. Bending tests of large-diameter ring-stiffened corrugated cylinders. Technical report, March 1966. NASA TN D-3336.

- R.L. Pinckney. Fabrication of the v-22 composite aft fuselage using automated fiber placement. In *The First NASA Advanced Composites Technology Conference*, volume 1, pages 385–397. NASA, 1991.
- G. Powell and J. Simons. Improved iteration strategy for nonlinear structures. *International Journal for Numerical Methods in Engineering*, 17:1455–1467, 1981.
- T. Rahman. *A Perturbation Approach for Geometrically Nonlinear Structural Analysis using a General Purpose Finite Element Code*. PhD thesis, Delft University of Technology, Dec 2009.
- C. C. Rankin, F. A. Brogan, W.A. Loden, and H.D. Cabiness. *STAGS Users Manual*. Lockheed Martin Missiles and Space Co., Inc., June 2000. Report LMSC P032594.
- J. C. Riddick and M. W. Hyer. Response of segmented-stiffness composite cylinders to axial end shortening. *Composite Structures*, 40(2):103–114, 1998.
- J. C. Riddick and M. W. Hyer. Influence of imperfections on buckling and postbuckling of segmented composite cylinders. In *43<sup>rd</sup> AIAA/ASME/ASCE/AHS/ASC Structures, Structural Dynamics, and Materials (SDM) Conference*, Denver, CO, USA, 2002. AIAA.
- J. C. Riddick and M. W. Hyer. Postbuckling behavior of segmented circular composite cylinders. *AIAA Journal*, 42(1):185–195, 2004.
- E. Riks. An incremental approach to the solution of snapping and buckling problems. *Int. J. Solids Structures*, 15:529–551, 1979.
- W. G. Roeseler, B. Sarh, and M. U. Kismarton. Composite structures: The first 100 years. In *Proceedings of the 16<sup>th</sup> International Conference on Composite Materials*, Kyoto, Japan, July 2007.
- D.T. Sandwell. Biharmonic spline interpolation of geos-3 and seasat altimeter data. *Geophysical Research Letters*, 14(2):139–142, 1987.
- K. Schittkowski. *NLPQLP: A Fortran implementation of a sequential quadratic programming algorithm with non-monotone line search - user's guide, version 2.0*. Department of Computer Science, University of Bayreuth, 2004.
- R. Schledjewski and A.K. Schlarb. Thermoplastic tape placement process challenges on the way to a fully automated lay-up of complex shaped parts. In *Proceedings of the SAMPE 2006 Conference*, Long Beach, CA, USA, 2006.
- K. Schueler, J. Miller, and R. Hale. Approximate geometric methods in application to the modeling of fiber placed composite structures. *Journal of Computing and Information Science in Engineering*, 4(3):251–256, 2004.
- P. Seide and V.I. Weingarten. On the buckling of circular cylindrical shells under pure bending. *Journal of Applied Mechanics*, 28:112–116, 1961.
- S. Setoodeh, Z. Gürdal, M. M. Abdalla, and L.T. Watson. Design of variable stiffness composite laminates for maximum bending stiffness. In *10<sup>th</sup> AIAA/ISSMO Multidisciplinary Analysis and Optimization Conference*, Albany, NY, USA, 2004. AIAA.

- S. Setoodeh, M. M. Abdalla, and Z. Gürdal. Design of variable-stiffness composite laminates for maximum in-plane stiffness using lamination parameters. In *46<sup>th</sup> AIAA/ASME/ASCE/AHS/ASC Structures, Structural Dynamics and Materials Conference*, Austin, TX, USA, 2005. AIAA.
- S. Setoodeh, M. M. Abdalla, and Z. Gürdal. Design of variable stiffness laminates using lamination parameters. *Composites, Part B: Engineering*, 37:301–309, 2006a.
- S. Setoodeh, A. W. Blom, M. M. Abdalla, and Z. Gürdal. Generating curvilinear fiber paths from lamination parameters distribution. In *Proceedings of the 47<sup>th</sup> AIAA/ASME/ASCE/AHS/ASC Structures, Structural Dynamics and Materials (SDM) Conference*, Newport, RI, May 2006b. AIAA.
- S. Setoodeh, Z. Gürdal, and L.T. Watson. Design of variable-stiffness composite layers using cellular automata. *Computer Methods in Applied Mechanics and Engineering*, 195 (9-12):836–851, 2006c.
- S. Setoodeh, M.M. Abdalla, S.T. IJsselmuiden, and Z. Gürdal. Design of variable-stiffness composite panels for maximum buckling load. *Composite Structures*, 87(1):109–117, 2009.
- J. Singer, J. Arobcz, and T. Weller. *Buckling Experiments, Experimental Methods in Buckling of Thin-Walled Structures*. John Wiley & Sons, Inc., West Sussex, England, 1998.
- P.J. Smith, L.B. Ilcewicz, and J.T. Olson. Advanced technology composite fuselage. In *Fifth NASA/DoD Advanced Composites Technology Conference*, Seattle, WA, Aug 1995. NASA.
- P. D. Soden, A. S. Kaddour, and M. J. Hinton. Recommendations for designers and researchers resulting from the world-wide failure exercise. *Composites Science and Technology*, 64(3-4):589 – 604, 2004. ISSN 0266-3538. doi: 10.1016/S0266-3538(03)00228-8. Failure criteria in fibre reinforced polymer composites Part C: Additional theories conclusions and recommendations.
- M. Sun and M.W. Hyer. Use of material tailoring to improve buckling capacity of elliptical composite shells. *AIAA Journal*, 46(3):770–782, 2008.
- B. F. Tatting. *Analysis and Design of Variable Stiffness Composite Cylinders*. PhD thesis, Virginia Polytechnic Institute and State University, Oct 1998.
- B. F. Tatting and Z. Gürdal. Design and manufacture of tow-placed variable stiffness composite laminates with manufacturing considerations. In *Proceedings of the 13<sup>th</sup> U.S. National Congress of Applied Mechanics*, 1998.
- B. F. Tatting and Z. Gürdal. Analysis and design of tow-steered variable stiffness composite laminates. In *American Helicopter Society Hampton Roads Chapter, Structure Specialists' Meeting*, Williamsburg, VA, USA, October 2001. American Helicopter Society.
- B. F. Tatting and Z. Gürdal. Design and manufacture of elastically tailored tow placed plates. Technical report, Aug 2002. NASA/CR-2002-211919.

- B. F. Tatting and Z. Gürdal. Automated finite element analysis of elastically-tailored plates. Technical report, Dec 2003. NASA/CR-2003-212679.
- H. Temmen, R. Degenhardt, and T. Raible. Tailored fibre placement optimization tool. In *25<sup>th</sup> Congress of International Council of the Aeronautical Sciences*, Hamburg, Germany, Sept 2006.
- M. W. Tosh and D. W. Kelly. On the design, manufacture and testing of trajectorial fibre steering for carbon fibre composite laminates. *Composites Part A: Applied Science and Manufacturing*, 31(10):1047–1060, 2000.
- S.W. Tsai and H.T. Hahn. *Introduction of Composite Materials*. Technomic, Lancaster, PA, USA, 1980.
- S.W. Tsai and N.J. Pagano. Invariant properties of composite materials. In *Composite Material Workshop*, pages 233–252, Lancaster, PA, USA, 1968. Technomic.
- J.M.J.F. Van Campen and Z. Gürdal. Retrieving variable stiffness laminates from lamination parameters distribution. In *50<sup>th</sup> AIAA/ASME/ASCE/AHS/ASC Structures, Structural Dynamics and Materials (SDM) Conference*, Palm Springs, CA, USA, 2009. AIAA.
- C. Waldhart, Z. Gürdal, and C. Ribbens. Analysis of tow placed, parallel fiber, variable stiffness laminates. In *Proceedings of the 37<sup>th</sup> AIAA/ASME/ASCE/AHS/ASC Structures, Structural Dynamics and Materials (SDM) Conference*, Salt Lake City, UT, USA, 1996. AIAA.
- G.S. Watson. Smoothing and interpolation by kriging and with splines. *Mathematical Geology*, 16(6):601–615, 1984.
- C.P. Wu and C.Y. Lee. Differential quadrature solution for the free vibration analysis of laminated conical shells with variable stiffness. *International Journal of Mechanical Sciences*, 43(8):1853–1869, 2001.
- K. C. Wu. Design and analysis of tow-steered composite shells using fiber placement. In *Proceedings of the American Society for Composites 23<sup>rd</sup> Technical Conference*, Memphis, TN, USA, 2008. DEStech Publications, Inc.
- K. C. Wu and Z. Gürdal. Thermal testing of tow-placed variable stiffness panels. In *Proceedings of the 42<sup>nd</sup> AIAA/ASME/AHS/ASC Structures, Structural Dynamics and Materials (SDM) Conference*, Seattle, WA, USA, Apr 2001. AIAA.
- K. C. Wu and Z. Gürdal. Variable stiffness panel structural analysis with material nonlinearity and correlation with tests. In *Proceedings of the 47<sup>th</sup> AIAA/ASME/ASCE/AHS/ASC Structures, Structural Dynamics and Materials (SDM) Conference*, Newport, RI, USA, 2006. AIAA.
- K. C. Wu, Z. Gürdal, and J.H. Starnes. Structural response of compression-loaded, tow-placed, variable stiffness panels. In *Proceedings of the 43<sup>rd</sup> AIAA/ASME/AHS/ASC Structures, Structural Dynamics and Materials (SDM) Conference*, Denver, CO, USA, Apr 2002. AIAA.



- K.C. Wu. Design and manufacturing of tow-steered composite shells using fiber placement. In *50th AIAA/ASME/ASCE/AHS/ASC Structures, Structural Dynamics and Materials (SDM) Conference*, Palm Springs, CA, USA, 2009. AIAA.
- K.C. Wu and Z. Gürdal. Evaluation of a highly anticlastic panel with tow overlaps. In *American Society for Composites Twenty-Third Technical Conference*, Seattle, WA, USA, 2007. DEStech Publications, Inc.
- J. Wyatt and H. Haj-Hariri. Atl design tool for tow path optimization. In *Proceedings of the SAMPE 2008 Conference*, Long Beach, CA, USA, 2008.
- S.S. Yau and T.W. Chou. Strength of woven-fabric composites with drilled and molded holes. *Composite Materials Testing and Design, ASTM STP-972*, pages 423–437, 1988.



# Curriculum vitae

Adriana W. (Agnes) Blom was born on March 16, 1982 in Leiderdorp, The Netherlands. She attended the "Christelijke Scholengemeenschap Groene Hart Lyceum" in Alphen aan den Rijn, the Netherlands, from which she received her gymnasium diploma in 2000. In September 2000 she started her Aerospace Engineering studies at Delft University of Technology in the Netherlands, from which she obtained both her BSc (2003) and MSc degree (2005) with honors. She did her internship with Boeing



Helicopters in Mesa, AZ. Her Master thesis with the title *Design of a Variable-Stiffness Cone, Tow-Placement Applied to a Section of the Apache Tailboom* was done under supervision of ir. Jan Hol and prof. Zafer Gürdal. She received the "prize for best final thesis work, awarded by the Dutch Association for Aeronautical Engineers (NVvL)". During her studies she worked as a student assistant at the university, with responsibilities varying from mentoring and guiding first year students, to teaching mechanics of materials, correcting exams and facilitating a project for 150 students participating in a 10 week project.

In the fall of 2005 she started her PhD studies with the Aerospace Structures group at the faculty of Aerospace Engineering of Delft University of Technology on the topic of fiber-placed, variable-stiffness conical and cylindrical shells. The first year of her PhD work was done in cooperation with the NLR (the Dutch National Aerospace Laboratory). In 2006 she was selected to participate in a one-year Boeing/Stork Fokker fellowship program, for which she spent a full year at Boeing in Everett, WA, working together with Boeing and Stork Fokker. There she completed the *Advanced Composite Structural Analysis and Design*, certificate program from the University of Washington and The Boeing Company in November 2007. After a fruitful first year the sponsorship by Boeing and Stork Fokker was extended until the end of her PhD project in 2010.

During her PhD studies Agnes received several recognitions for her work, among others the "Amelia Earhart Fellowship Award" in March 2006, the "Jefferson Goblet Award for best student paper at the 47th AIAA/ASME/ASCE/AHS/ASC Structures, Structural Dynamics, and Materials Conference, Newport, RI" in May 2006, the "Boeing Engineering Student of the Year Award" in July 2008, and the "First prize in student poster competition of the 1st joint American-Canadian Technical Conference on Composites, Newark, DE" in September 2009. In addition she was voted as one of the 400 Most Successful Women in the Netherlands by Viva magazine in September 2008, and she is listed in the 2010 edition of Marquis "Who's Who in the World".

